PROCEEDINGS OF THE FOURTEENTH SYMPOSIUM

ON

ELECTROMAGNETIC WINDOWS

June 21–23, 1978

DTIC
ELECTE
JAN 2 4 1996
G

Edited by

J. N. Harris

19951226 029

DEPARTMENT OF DEFENSE
PLASTICS TECHNICAL EVALUATION CENTER
ARRADCOM, DOVER, N. J. 07801

GEORGIA INSTITUTE OF TECHNOLOGY
ATLANTA, GEORGIA 30332

DTIC QUALITY INSPECTED 3

PLASTEC 35008

Add   AD295770 -
Add   AD295778

DEPARTMENT OF DEFENSE
PLASTICS TECHNICAL EVALUATION CENTER
ARRADCOM, DOVER, N. J.   07801

PROCEEDINGS OF THE FOURTEENTH SYMPOSIUM

ON

ELECTROMAGNETIC WINDOWS

June 21–23, 1978

Edited by

J. N. Harris

Accesion For		
NTIS CRA&I		☒
DTIC TAB		☐
Unannounced		☐
Justification		
By		
Distribution /		
Availability Codes		
Dist	Avail and / or Special	
A-1		

GEORGIA INSTITUTE OF TECHNOLOGY
ATLANTA, GEORGIA 30332

FOREWORD

The Fourteenth Electromagnetic Window Symposium marks 23 years of regularly scheduled symposia on electromagnetic windows. The first seven symposia were held at Ohio State. The Georgia Institute of Technology has hosted the symposia bienially since 1966, with the U. S. Air Force co-hosting the symposia of 1966, 1968 and 1972.

My sincere thanks go to the following individuals who served on the papers review committee and to their corresponding organizations which made their participation possible.

Mr. H. L. Bassett
Georgia Institute of
Technology

Mr. James Chesnut
Naval Air Systems
Command

Mr. Ken Letson
U. S. Army
MIRADCOM

Mr. A. E. Blume
U. S. Air Force
Avionics Laboratory

Mr. Donald Evans
U. S. Air Force
Materials Laboratory

Dr. G. P. Tricoles
General Dynamics
Electronics Div.

Mr. Vance Chase
General Dynamics,
San Diego

Mr. G. K. Huddleston
Georgia Institute of
Technology

Mr. E. A. Welsh
Martin Marietta
Orlando Div.

Some of the papers were not received in time for publication, but will be available during the meeting from the registration desk or from the author.

I would like to thank the authors for their contributions to the technical program and for their cooperation in our attempt to have the entire proceedings available at the time of the meeting. Finally, my sincere appreciation goes to H. L. Bassett and G. K. Huddleston for their diligent and cooperative efforts in handling many of the details required in organizing this symposium.

Joe N. Harris
Chairman

ii
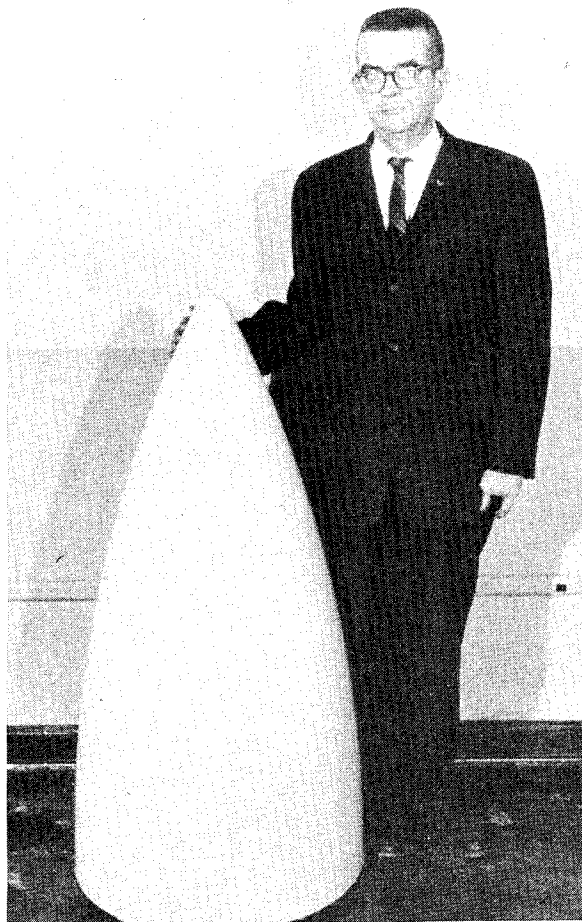
RICHARD A. IRELAND 1924-1978

This symposium is dedicated to the memory of Richard A. (Dick) Ireland who made numerous contributions to radome technology.

Dick was a Master Sergeant in the U. S. Air Force who had to retire because of a severe service incurred arm injury. After discharge, he worked for Wright-Patterson Air Force Base as a civilian for 20 years until his retirement in 1972. He was instrumental in the rewriting, publication and distribution of the radome handbook, and the conduct of numerous programs concerned with high speed, high temperature radomes and materials suitable for these applications. He was responsible for the Air Force co-sponsorship of the 1966, 1968 and 1972 EM Window Symposia held at Georgia Tech.

Dick's enthusiasm and dedication to the improvement of radome technology was rarely matched and he contributed much to meeting the needs of high performance radome systems. His contributions will become better known as the years pass. It is therefore fitting that we should remember him at this symposium.

TABLE OF CONTENTS

TABLE OF CONTENTS (Continued)

TABLE OF CONTENTS (Continued)

Broadband High Speed
Reinforced Plastic Radome*

Don Purinton
Texas Instruments, Inc.
Dallas, Texas

A high fineness ratio reinforced plastic radome is under development for applications requiring broadband transparency and environmental resistance for long range supersonic flight. Special environmental considerations include rain erosion and environments created by nearby thermonuclear devices.

The concept for a wall consists of a thick outer layer (.06 inches) of Duroid 5870 reinforced Teflon backed by a thin skinned "C" sandwich made of "quartz" reinforced polyimide laminate and polyimide fiberglass honeycomb. This wall design is shown in Figure 1.

The features of this approach are:

1. A thick outer layer of Duroid provides rain erosion resistance, thermal resistance and non charring ablation properties.

2. The low dielectric constant (2.35) of the thick Duroid provides broadband transparency, and electrical insensitivity to changes in thickness due to rain erosion and ablation.

3. The inner sandwich radome will be isolated from the exterior environment of heat and erosion and will provide structural support to the outer layer. Also the honeycomb sandwich construction will provide high thermal resistance to further isolate the seeker antenna from long term heating.

4. The thin skinned "C" sandwich will allow for broadband transparency.

Several areas of study have been completed toward validation of this radome approach. These areas are discussed in more detail below.

NUCLEAR ENVIRONMENT

The Teflon matrix for the Duroid outer shell is known for its relative susceptibility to radiation damage, especially when heated. Because the Duroid serves as a protective shell for the radiation resistant inner polyimide quartz sandwich shell, physical degradation of the Duroid material does not preclude successful completion of the mission by the radome. Radiation degradation of Duroid's dielectric properties were of some concern. However, since the dielectric constant of Duroid is low (2.35) and the shell is a small fraction of a wavelength thick, only severe changes in the dielectric properties would be detrimental. For very high radiation levels where the radome is heated, significant degradation in electrical properties may occur. Since no tests have been run under these conditions, an unknown degradation factor exists. However, since Teflon has a history of "electrically clean" degradation at temperature, it is expected that the degradation would remain clean even when it is accelerated by radiation.

RAIN EROSION

Tests on the sled track at Holloman Air Force Base have shown that Duroid 5870 is surprisingly resistant to rain erosion.[1,2] Several potential missile trajectories were analyzed for effects of rain erosion on the radome. A maximum erosion depth in to the Duroid was estimated to be .015 inches. This estimate was made using reference 1 and reference 3. Assumptions were that 5mm/hr rain represents a condition that presents the greatest potential for damage. Lower rain rates occur more frequently and over larger areas but produce less damage per second of exposure. Higher rates occur less frequently and in smaller cell sizes but produce more damage per second. For example a rain rate of 50mm/hr would be expected to produce only .011 inches of erosion and the probability of encouter is from 1/10 to 1/100 that for 5mm/hr rain. The cell size would be expected to be less than 10 km in diameter where rain at 5mm/hr may be expected over an area encompassing the complete trajectory of the missile. The occurence of rain at altitudes higher than 26,000 feet is relatively rare and is restricted to cells of very small diameters. Therefore rain above

[1] Velocity-Erosion Rate Relationships of Materials in Rain at Supersonic Speeds, George Schmitt and Allan Krapill, AFML-TR-70-44, Oct 1970.
[2] Aerothermal & Rain Erosion Sled Test Results on Radome Materials at Mach 5. Ken Letson & Phil Ormsby, Redstone Arsenal Tech Report TL-77-2, Feb 1977.
[3] Rain Erosion Behavior of Materials at 5500 Feet per Second. George Schmitt, Jr. AFML-TR-72-64, Sept 1972.

26,000 feet was not considered. Photographs of rain erosion tests on missile radomes have shown that the erosion is generally confined to a region extending from just behind the metal nose tip to 4 inches aft with the deepest erosion occurring just behind the tip. In fact all significant erosion occurs within 2 inches of the tip. Due to the high fineness ratio of the radome the nose tip is a considerable distance in front of the antennas. This distance reduces the effect of erosion on the electrical properties of the radome. In addition the radome is relatively insensitive to erosion of the Duroid shell because of its low dielectric constant and the non resonant nature of the radome wall design.

Statistical studies have shown that the probability of encountering rain during a missile flight to be on the order of 1 to 3 per cent. With such a low probability of encounter, consideration of rain erosion in a missile radome design may not be worthwhile because of the electrical penalties that nearly always accompany such consideration. However, it is felt that some rain erosion resistance is desirable to prevent susceptibility to rain erosion from being used as a counter measure.

THERMAL AND STRUCTURAL STUDIES

A thermal study has shown that the radome materials will experience temperature time profiles as shown in simplified form in Figure 2. The most significant stresses are produced by temperature gradients in the shell. Plastic yielding of the materials reduces peak stresses to acceptable levels. Because of the relatively high thermal expansion coefficient of Duroid the outer shell must experience considerable yielding during heating. Tests to date have shown that the use of a polyimide adhesive to bond the Duroid shell to the polyimide quartz laminate sandwich shell will ensure the unity and integrity of both shells throughout flight.

A white thermal control coating may be desirable for the outer surface of the radome to eliminate the small amount of ablation of the Duroid due to nuclear flash. Later studies will explore the effects of the assymetric removal of material on electrical boresight errors. If significant, a coating will be recommended.

A pressure wave from the presence of a nuclear blast will apply a large moment at the base of the radome. If the radome is attached to the missile by screws, the laminate at the base must be built up in thickness to handle the screw bearing stresses in the laminate. Other more complex attachment designs can be developed to eliminate this requirement.

3

Strength tests on the Polyimide quartz laminate material are being made at elevated temperatures using the time-temperature curves of Figure 2. This information will be used to verify data already published. Since strength degrades with time at temperature, tests for the exact time temperature combination are desirable.

It is planned to test the radome wall design on the hot gas facility at NWC China Lake to assure that the radome will withstand the required heating environments. During the test, electrical transmission through the wall will be measured to show the insensitivity of electrical transmission to heating

ELECTRICAL STUDY

The radome wall design has been optimized for transmission with a single frequency large aperture antenna operating simultaneously with a small aperture broadband antenna. Modification of wall design as a function of radome surface position may be desirable for reduction of boresight errors in the large antenna. Such phase tapering may be accomplished also with the use of low dielectric constant foam. Because of the non resonant nature of the radome wall, such tapering may be made without disturbing the broadband radome performance.

Calculations will be made to determine the performance of the large aperture antenna using a ray tracing program. Any phase correction schemes to reduce boresight error will be modeled by the program. To determine the performance of the broadband antenna, a radome will be fabricated of loaded plastic materials that simulates the dielectric properties of the designed radome. This radome will be tested on an antenna range to determine its performance.

Dielectric tests have been made on Duroid 5870 and quartz polyimide laminate during exposure to temperature time environments described by Figure 2. The tests show that only small changes in dielectric constant and loss tangent occur. Due to the nonresonant nature of the wall such small changes can be accommodated without any noticeable effect on performance.

SUMMARY

Development of a broadband reinforced plastic radome is underway. Work to date has shown this approach to be feasible. In addition, this development effort seems to promise fallout for radome designs not originally considered. For example, if the Duroid shell is increased in thickness to about .1 inches and the central layer of polyimide laminate is reduced from .04 to .02 inches, a K_a band radome wall design is accomplished. In addition, this wall has transparency at lower frequencies.

4
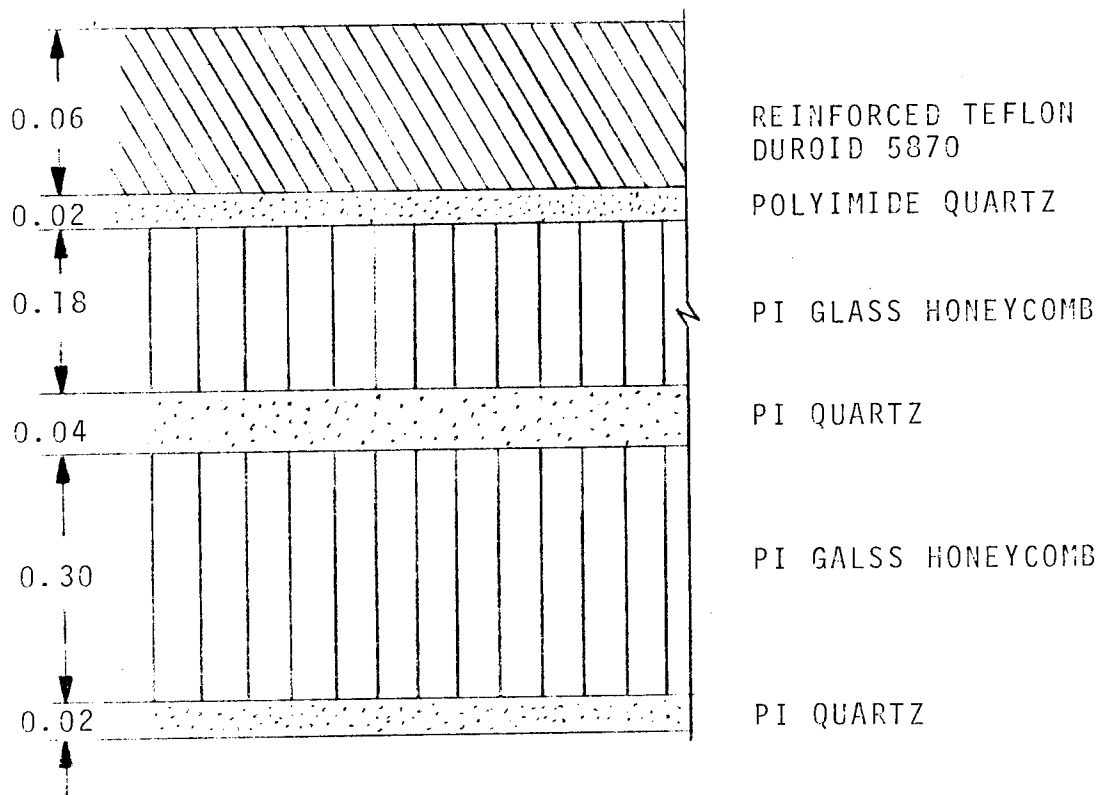
FIGURE 1   ENLARGED CROSS SECTION OF RADOME WALL
             SHOWING MATERIALS AND THICKNESSES
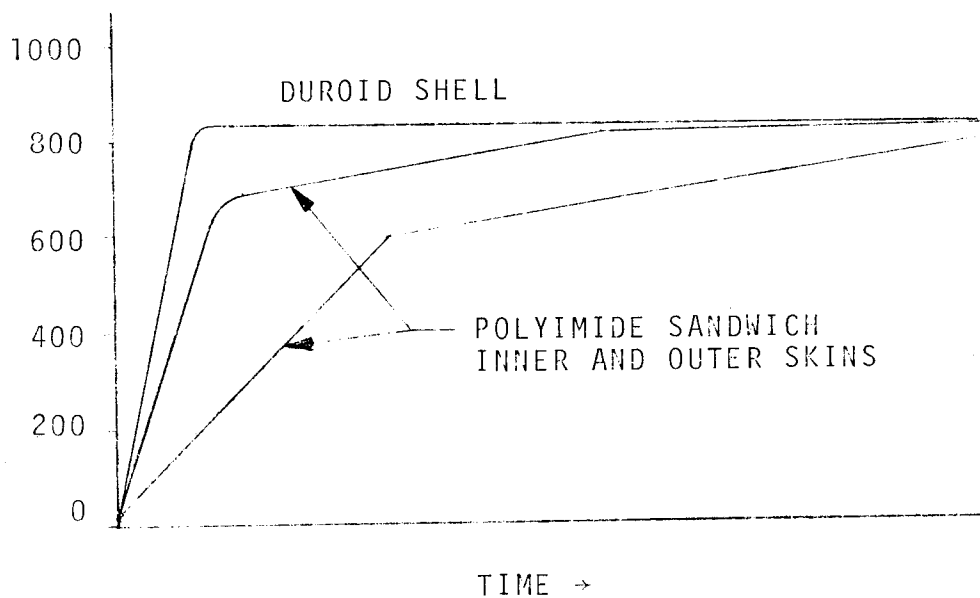
TIME →

FIGURE 2   TEMPERATURE-TIME OF RADOME SHELL

MULTI-LAYERED TANGENT POWER SERIES
RADOME WITH INTEGRATED LENS

F.D. Groutage and D.E. Smith

Naval Ocean Systems Center

INTRODUCTION

The essence of this paper is to present an overview of a technology being developed at the Naval Ocean Systems Center, San Diego, relative to the design of a *low cost* broad- band radome for a guided missile application. Traditionally, radomes for high performance missiles have been manufactured from ceramic type materials which even in high volume production are in the two to five thousand dollar per copy cost range. Modern technology has addressed the reduction of electrical component costs which make up the guidance system; therefore, the cost of the radome is becoming a higher percentage of the total guidance system package for the advanced guidance systems on the modern missiles.

This development effort is centered around a baseline configuration which is a multi-layered dielectric, tangent power series radome with lens integrated into one of the dielectric layers in the nose section of the radome. The design approach is based on an analytical/hardware development.
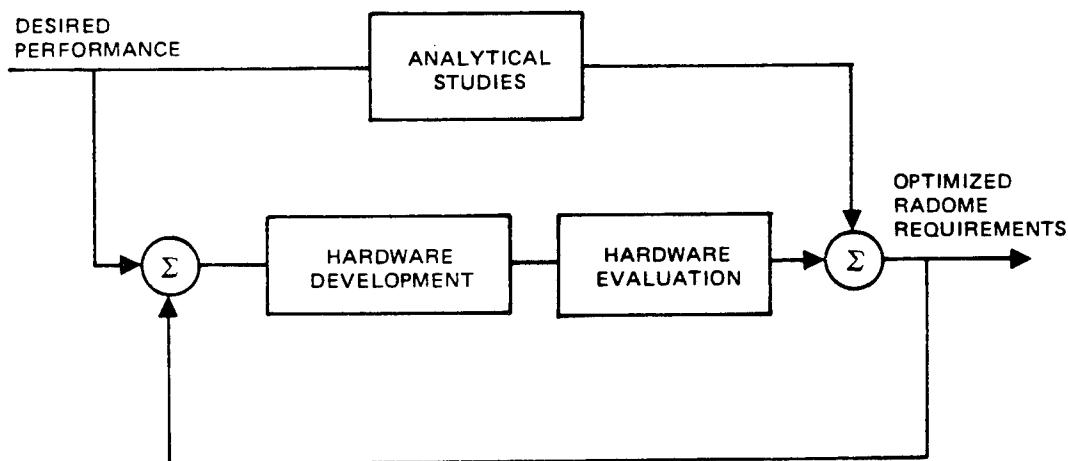
Figure 1. Methodology for establishing radome performance requirements.

Radome requirements (aerodynamic/structural, and electrical) are the main outputs of the development program. The remainder of this paper will address the analytical aspects of formulating a radome configuration to meet the desired performance.

AERODYNAMIC/STRUCTURAL

The primary consideration under the aerodynamic aspects of radome requirements is the drag. The parameter which has the greatest impact on drag is the shape. Not only does the shape affect the drag, it impacts the electrical characteristics of the radome performance. Also affected are the configuration, size, weight and shape of the sensor system housed within the radome. A radome shape selected as the baseline was the tangent power series*. Figure 2 presents a comparison of three radome shapes. The zero lift drag for the three shapes of Figure 2 is presented in Figure 3.

*A tangent power series differs from the conventional power series in that the base of the radome is tangent to the missile body where as the conventional power series joins the missile body with a discontinuity.
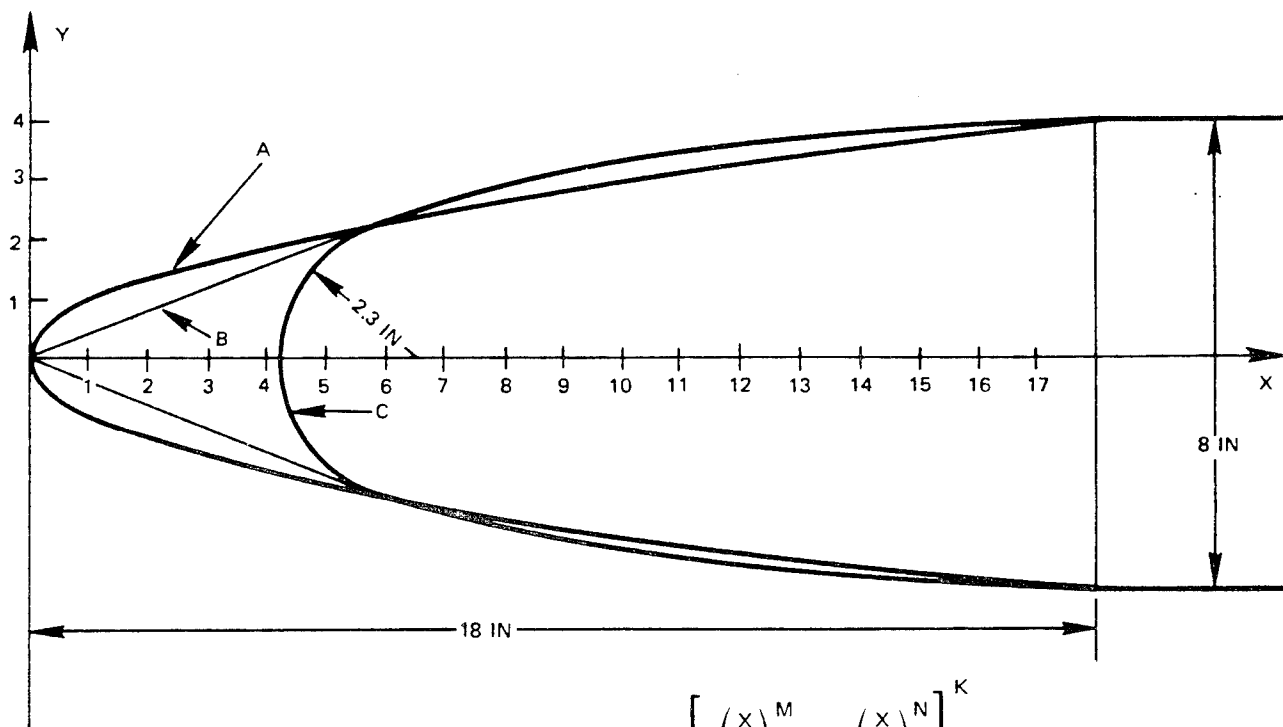
A TANGENT POWER SERIES RADOME: $Y = R\left[C\left(\dfrac{X}{L}\right)^M - D\left(\dfrac{X}{L}\right)^N\right]^K$ WHERE R = 4,

C = 1.02, M = 0.5, D = .02, K = 1.0, L = 18.0, N = 25.5

B TANGENT OGIVE: $Y = \sqrt{R^2 - (L - X)^2} - a$ WHERE $R = Y_B/2 + 2L^2/Y_B$ and $a = R - Y_B/4$

C HEMI-OGIVE: TANGENT OGIVE BLUNTED WITH 2.3-IN RADIUS HEMISPHERE

Figure 2. Comparative radome shapes
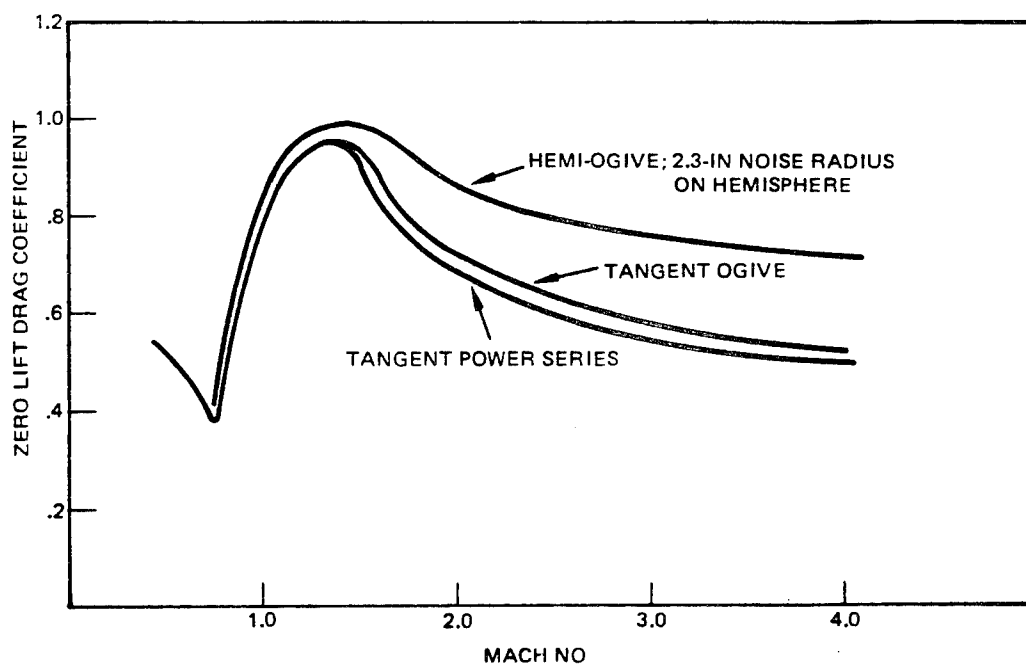
Figure 3. Zero lift drag coefficients for 2.5:1 L/D tangent
ogive, hemi-ogive, and tangent power series radomes.

8

The structual aspects of the radome are aerodynamic heating, rain erosion, and dynamic pressure. These aspects are all addressed in the references provided and will not be covered in this paper.

ELECTRICAL

The electrical aspects of the radome performance are the transmissivity and the boresight error. Both of these items are functions of many parameters, and both have dominate impact on the sensor type and quality of guidance information. Both of these areas were analyzed using mathematical models on a digital computer.

Transmissivity is a function of the following parameters:

> Frequency
> Wall Construction
> Incident Angle
> Polarization

The parameters that the designer has little control over are the incident angles, frequencies, and impinging energy polarizations. That leaves wall construction as the variable parameter. The wall construction encompasses the number of layers, dielectric constant of each layer, and layer thickness. The technique that was used to achieve the broadband coverage was an impedance matching technique. The outside is a thin, low-dielectric layer. Succeeding layers have dielectric constants of increasing value. This is analogous to a transmission line, as shown in Figure 4, where a multi-stage impedance transformer is used to minimize reflection.
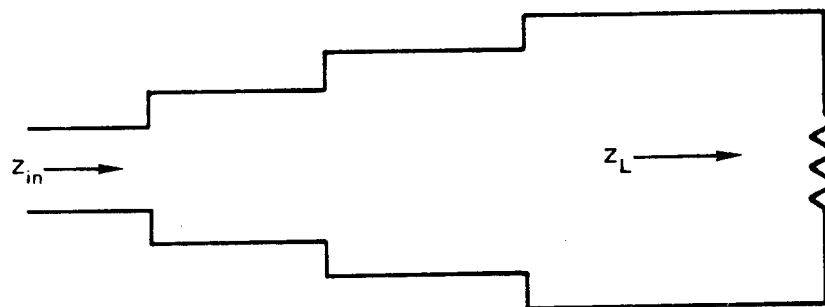
Figure 4. Multistage impedance matching transmission line transformer.

Boresight error is a function of even more variables than transmissivity, including:

> Antenna station
> Antenna aperture
> Nose shape
> Rf energy
> > Frequency/polarization
> Wall construction
> > Layer thicknesses and dielectric constants
> Phase compensation
> > Lens shape
> > Lens dielectric constant

Candidate radomes which could be constructed from a low cost manufacturing process were analyzed to establish electrical performance. Two computer programs were used to investigate the boresight error/boresight error slope aspects of the candidate radomes. One program was a two dimentional optical ray trace (2 DORT) and other a three dimentional electromagnetic surface integration (3 DEMSI) program. The 2 DORT program being very inexpensive to run was used to conduct a variation of parameter study to establish a design point. The 3 DEMSI program was used to validate the design point. The 3 DEMSI program is quite expensive to run and was used for final design excursion runs.

SUMMARY

A low cost radome design technique using a molding process to construct the multilayer radome wall with an integrated lens in the nose section of the dome has been validated in a design study. Hardware development and testing is currently underway to substantiate the analytical effort. The shape of the radome is tangent power series described by the formula:

$$Y = R \left[C \left(\frac{X}{L} \right)^M - D \left(\frac{X}{L} \right)^N \right]^K$$

Where at $X = L$, $Y = R$

and at $X = L$, $\frac{dy}{dx} = 0$

Which results in $\qquad$ $C - D = 1$

and $\qquad$ $CM = DN$

As C increases, the radome cross-sectional diameter increases at all points except those close to the tip. Setting $K < 1.0$ results in a blunting of the nose, whereas setting $K > 1.0$ yields a sharper nose. Figure 5 shows three possible candidates for lensing the low cost radome.

Representative boresight error data for the low cost lensed radome is shown in Figure 6. This figure presents comparative data for a lensed and non-lensed radome from both the 2 DORT and 3 DEMSI computer program.

10
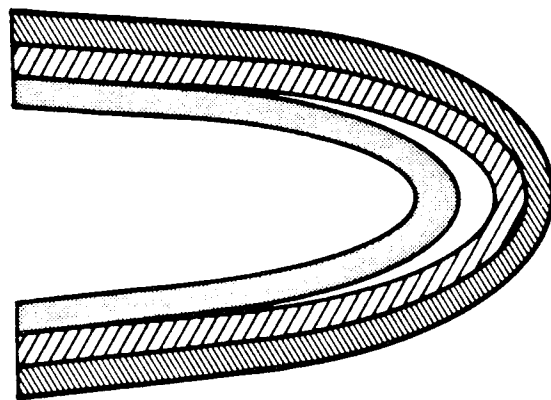
lens integrated between layers
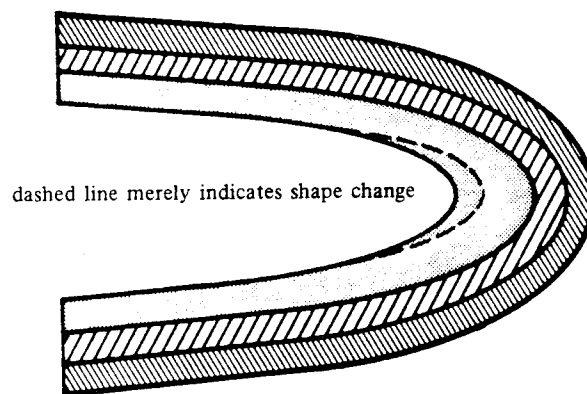
dashed line merely indicates shape change

lens integral part of support layer
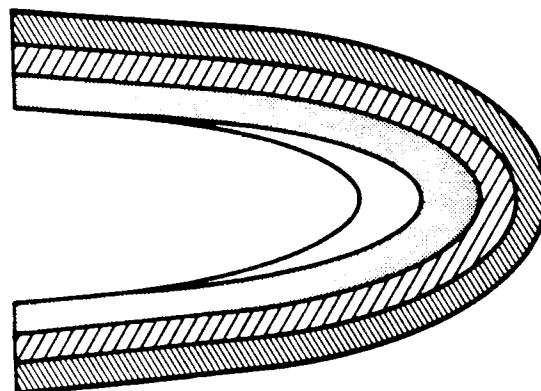
lens molded to inner surface

Figure 5. Lensing options.

11
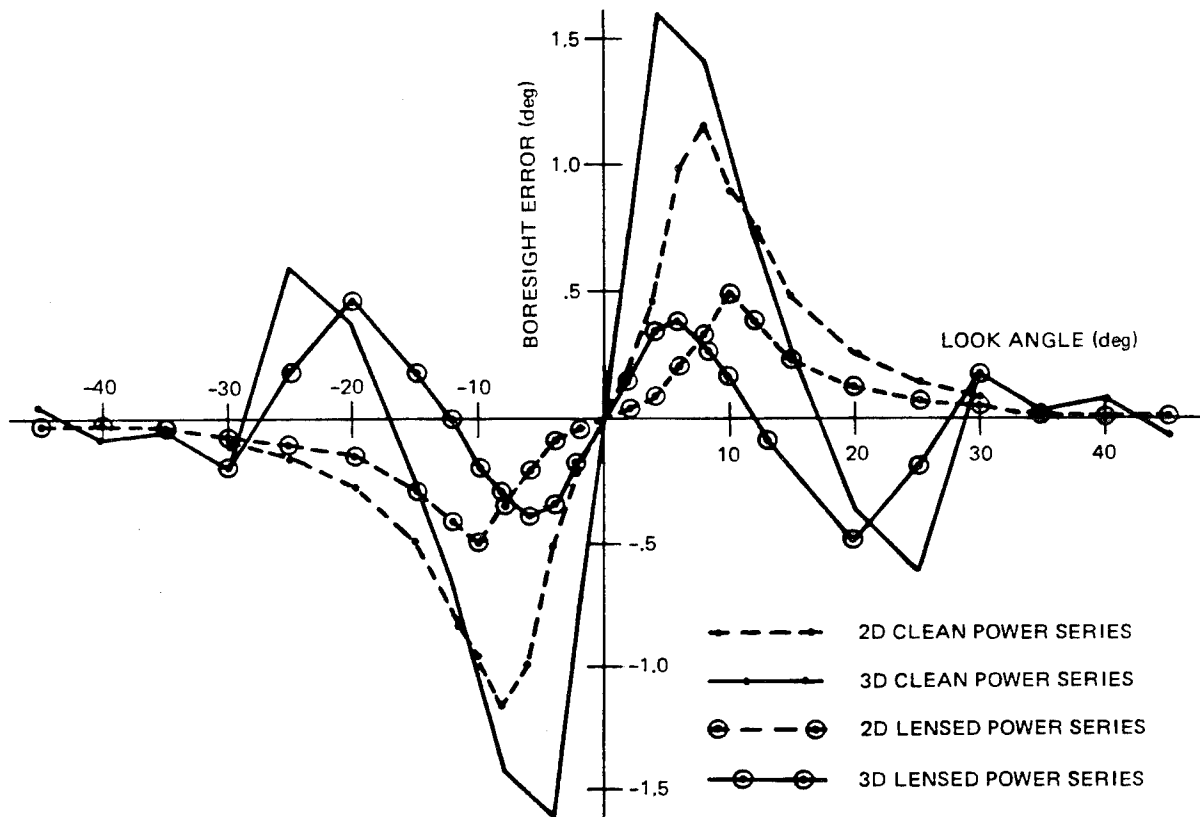
Figure 6. Boresight error vs gimbal angle.

POTENTIAL FOR CHEMICALLY VAPOR DEPOSITED SILICON NITRIDE AS A MULTIMODE ELECTROMAGNETIC WINDOW (VIS, IR, RF)

R. A. Tanzilli, J. J. Gebhardt, J. O. Hanson

General Electric Co. (RESD)
P. O. Box 7560
Philadelphia, Penna. 19101

INTRODUCTION

During the past year under ONR sponsorship,[1] the basic processing outlines for the fabrication of crystalline α-Si_3N_4 plate and dome geometries by the chemical vapor deposition (CVD) method have been defined. Physical property evaluations of deposits on this program when combined with earlier property data (shown in Table 1) continue to be supportive of the premise that high-purity, crystalline α-Si_3N_4, as prepared by the CVD method, may be useful as a high-performance ceramic component in advanced DoD missile systems. Of particular interest to this Symposium are the electromagnetic transmittance properties (Category 1 and 2, Table 1) of CVD α-Si_3N_4 which suggest its potential application as a multiple-frequency window material for missile systems utilizing combinations of active and semi-active microwave and millemeter wave antennas and passive IR (or optical) sensors for target acquisition and tracking.[2]

PROCESS DESCRIPTION

The general procedure for forming CVD Si_3N_4 consists of passing a mixture of vapor-borne precursors into a chamber, hot wall or cold wall, within which the precursors react and form deposition species. These then adhere to the heated substrate and crystallize. The process is continued until desired thicknesses are achieved. The chemistry and detailed transformation processes (deammination, crystal growth, etc.) involved in formation of deposits of certain characteristics are at present inferred primarily through analysis of the materials and correlation with the deposition conditions (temperature, pressure, gas feed rate and concentration, gas flow dynamics, substrate characteristics, etc.).

Silicon nitride can be formed from the vapor phase by interaction of ammonia and a silicon halide (e.g., silicon tetrachloride, -fluoride or -bromide), a silane derivative (e.g., chlorosilane SiH_xCl_y (x + y = 4), or silane itself (SiH_4). Typical gross reactions are:

$$3\ SiCl_4 + 4NH_3 \longrightarrow Si_3N_4 + 12\ HCl$$
$$3\ SiF_4 + 4NH_3 \longrightarrow Si_3N_4 + 12\ HF$$
$$3\ SiH_4 + 4NH_3 \longrightarrow Si_3N_4 + 12\ H_2$$
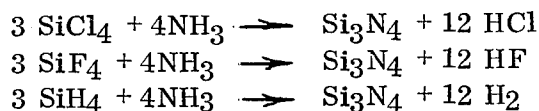
Table 1. Physical Property Trends for CVD α-Si_3N_4

Category	Supporting Data	Source
1. Visible/Infrared Transmittance	Ground and polished translucent flat plate and dome geometries exhibit a transmittance window from 0.20 to 5.0 μm. (Conventional Si_3N_4 is opaque in this wavelength range.)	Reference 1
2. Radar Transmittance	High–purity deposits show a loss tangent at X–band approximately an order of magnitude lower than conventional Si_3N_4.	Reference 1
3. Oxidation Resistance	Oxidation studies monitored by weight gain measurements show a rate of $10^{-4}kg/m^2s^{1/2}$ at 1450°C, or about 10 times less than Si_3N_4 hot–pressed with 5% MgO and tested at 1100°C.	Reference 3
4. Creep Behavior	Creep experiments in three point bending at 1540°C showed essentially no deflection after 7 x 10^5 sec. at 70 MPa. The material exhibited an upper creep rate at least 5 orders of magnitude less than that expected for hot–pressed Si_3N_4 containing MgO, based on extrapolation of published data.	Reference 3
5. Flexure Strength	Although room temperature flexure strength of CVD α-Si_3N_4 (at its current development stage in our laboratory) is approximately 1/3 that of hot–pressed Si_3N_4, its invariancy after a 100 hr. exposure at 1400°C is far superior to hot–pressed Si_3N_4 which generally exhibits a 50% reduction in flexure strength under similar aging conditions.	Reference 1
6. Microhardness	Crystalline CVD α-Si_3N_4 has a hardness level superior to common abra–sives ranking it in third place behind diamond and cubic boron nitride; amorphous CVD α-Si_3N_4 has a hardness level comparable to α-Al_2O_3.	References 1 and 4
7. Thermal Stress Resistance	Using standard thermal–stress resistant figure–of–merit parameters, Si_3N_4 is predicted to have good thermal stress resistance. Of course, its actual performance will depend upon specific operational environ–ments and component configuration.	Reference 5

14

In this work, α-Si$_3$N$_4$ was prepared (using the above reactions) in dynamic, hot-wall, low-pressure, reactors with hot-zone diameters of 2.54 and 10.16 cm, respectively. The reactors are equipped with conventional gas handling facilities including mass flowmeters, cold traps and high-capacity vacuum pumps. Table 2 is an overview of the CVD process-parameter ranges investigated (with each reactant combination) including diagnostic data and interpretive remarks which will be important when addressing the problem of process scale-up feasibility, control, and finished costs.

Table 2. CVD α-Si$_3$N$_4$ Process-Parameter Ranges

	SiCl$_4$	SiF$_4$	SiH$_4$
Temperature ($^\circ$C)	1450 – 1500	1425 – 1450	1400 – 1450
Pressure (torr)	5 – 10.5	3.5 – 10.0	0.5 – 2.0
N:Si Ratio	0.5 – 12.5	0.7 – 0.9	180 – 640
Deposition Rate (mm/hr)	0.20 – 0.64	0.025 – 0.10	0.005 – 0.010
Percent Si Conversion	40.3 – 100	13.5 – 21.7	---
Remarks:	• lowest raw material cost • highest deposition rate and conversion • roughest last deposited surface • solid byproducts clog furnace	• intermediate raw material cost • low deposition rate and conversion • smooth last deposited surface	• highest raw material cost • lowest deposition rate

Material characterized in this work was prepared using the SiCl$_4$ and SiF$_4$ precursors in conjunction with NH$_3$.

PHYSICAL PROPERTIES

Optical/Infrared Properties

Visual color variations have been observed within and between deposits evaluated in this work. These include: shades of brown, green and white including regions of near water clarity. Analysis of the extreme color variations show correlation with O$_2$ content and unit cell dimensions as shown below:

Color	O_2 Content (w/o)*	a-Spacing ($\overset{\circ}{A}$)	c-Spacing ($\overset{\circ}{A}$)	Vol. of Unit Cell ($\overset{\circ}{A}$)
White	1.07	7.7562	5.6179	292.69
Brown	0.36	7.7646	5.6219	293.53

*Fast Neutron Activation Analysis

Figures 1 and 2 compare the hemispherical and near-normal specular transmittance of polished translucent white and brown α-Si$_3$N$_4$, respectively. The transmittance spectrum of brown α-Si$_3$N$_4$ shows significant absorption in the ultraviolet-blue wavelength region accounting for the dominance of a brown color. On the other hand, the white α-Si$_3$N$_4$ shows comparatively little absorption over the same wavelength range. Both types of α-Si$_3$N$_4$ (at the current stage of development) exhibit poor imaging capability as indicated by their relatively low specular transmittance levels. For non-imaging visible applications, both types of material would be usable with the water-clear crystalline material being favored where sensitivity to ultraviolet-blue transmitted energy is desired. Scattering in the visible wavelength range is traceable, in part, to at least the following defects: porosity, disregistry of columnar growth nodules resulting in microcracks and possibly intrinsic crystal index of refraction anisotropy (birefringence).

In the near infrared wavelength region extending up to its transmittance cut-off, a relatively high specular transmittance level (compared to the visible spectrum) exists for both types of α-Si$_3$N$_4$. Figure 3 shows both the hemispherical and specular transmittance spectrum for near water-clear α-Si$_3$N$_4$. The transmittance spectrum for brown material is virtually identical to Figure 3. Also noteworthy is the reduced degree of scattered transmitted energy in the infrared compared to that in the visible spectrum. Calculations of intrinsic spectral absorption coefficients are premature at this time since this property has yet to be systematically studied and optimized. Current optical quality material would be unacceptable as an imaging infrared window unless a maximum-thickness constraint on the order of fractions of a millimeter were tolerable for the particular window design.

Microwave Properties

A resonant cavity technique[6] was developed to permit accurate measurement of the dielectric properties of CVD α-Si$_3$N$_4$ on specimens of limited size. The technique was calibrated using dielectric-constant standards from Custom Materials, Inc. Figure 4 is a schematic of the laboratory set-up used for recording data from which the room temperature dielectric constant and loss tangent were computed in the X-band frequency range (9-10GHz). The electric field vector coincided with the plane of deposition of the specimen. A summary of room temperature dielectric data for translucent brown and white material is given below:

Specimen Color	Dielectric Constant	Loss Tangent	O_2 Content
Brown	7.90	< 0.0002	0.36
White	7.66	< 0.0006	1.07

It should be noted that the loss tangent data for CVD α-Si$_3$N$_4$ is an order of magnitude lower than literature data on hot-pressed (HPSN) and reaction-sintered (RSSN) modifications of Si$_3$N$_4$. If this trend continues at elevated temperatures, CVD α-Si$_3$N$_4$ would provide a significant advantage over HPSN and/or RSSN for high-temperature microwave window applications.

Mechanical Properties

Four-point flexure strength measurements (4 specimens – 50.80 x 5.64 x 1.27mm) at room temperature averaged 218.22 MN/$_m$2 (31.6 ksi) with an associated average failure strain of 0.07 percent and an average Young's modulus of 312.14 GPa (45.26 x 10^6 psi). Subsequent three-point flexure strength measurements (4 specimens) at NRL on similar quality material showed an average tensile strength of 164.09 MN/$_m$2 (23.8 kpsi). Additional flexure specimens were heat treated by NRL at 1430°C for 100 hrs. yielding an average room temperature flexure strength of 218.56 MN/$_m$2 (31.7 ksi). The fact that the strength did not decrease after this heat treatment is significant since over 50 percent drops in strength have been observed on commercial hot pressed Si$_3$N$_4$ after similar heat treatments.

Figure 5 summarizes Knoop hardness measurements on crystalline α-Si$_3$N$_4$ at 100, 500 and 3000gm loads. The data indicates that crystalline CVD α-Si$_3$N$_4$ has hardness levels superior to common abrasives (α-Al$_2$O$_3$, B$_4$C, SiC) ranking it in third place behind diamond and cubic boron nitride.

The critical stress intensity factor of current generation CVD α-Si$_3$N$_4$ has been found to be comparable to hot-pressed Si$_3$N$_4$ using the NRL grooved double-cantilever beam method (K$_c$ = 4.3 MPa $\sqrt{m}$), but somewhat lower than hot-pressed Si$_3$N$_4$ using the indentation toughness method (K$_c$ = 3.2 MPa $\sqrt{m}$). The relatively high hardness of crystalline α-Si$_3$N$_4$ coupled with its moderate critical stress intensity factor suggests erosion performance superior to current generation electromagnetic window materials.

SUMMARY

Processing research on the preparation and associated property characterizations of CVD α-Si$_3$N$_4$ has resulted in the identification of several unique intrinsic properties which indicate potential for improved performance in many applications where the more conventional forms of Si$_3$N$_4$ are being considered. For some advanced missile systems, in particular, which will require wide-band electromagnetic transmittance capability in addition to good thermal shock and erosion resistance, CVD α-Si$_3$N$_4$ appears to be a potential candidate window material. Continued processing

research focussing on scale-up feasibility and optimization of physical properties through microstructural control is currently being pursued.[7]

ACKNOWLEDGEMENTS

REFERENCES

1. R. A. Tanzilli, et al., "Chemical Vapor Deposition of Silicon Nitride", GE-RESD Final Report No. 77SDR2257, September, 1977 (ONR Contract No. N00014-76-C-0547).

2. D. L. Loyet, "Multiple Frequency Radomes", Proceedings of the Fourteenth Symposium on Electromagnetic Windows, September 1976, pp. 149-153.

3. C. Greskovich, J. H. Rosolowski and S. Prochazka, "Ceramic Sintering", DARPA Final Technical Report, No. SR-75-084, 1975 (ONR Contract No. N00014-74-C-0331.

4. K. Niihara and T. Hirai, "Chemical Vapour-Deposited Silicon Nitride - Part 4. Hardness Characteristics", Journal of Materials Science, Vol. 12, 1977, pp. 1243-1252.

5. MCIC-HB-07, "Engineering Property Data on Selected Ceramics, Vol. 1, Nitrides", March, 1976, p. 5.3.3-28.

6. ASTM D2520-70, "Complex Permittivity of Solid Electrical Insulating Materials at Microwave Frequencies and Temperatures to 1650°C."

7. "Renewal Program on CVD Si_3N_4", ONR Contract N00014-78-C-0107, in progress.
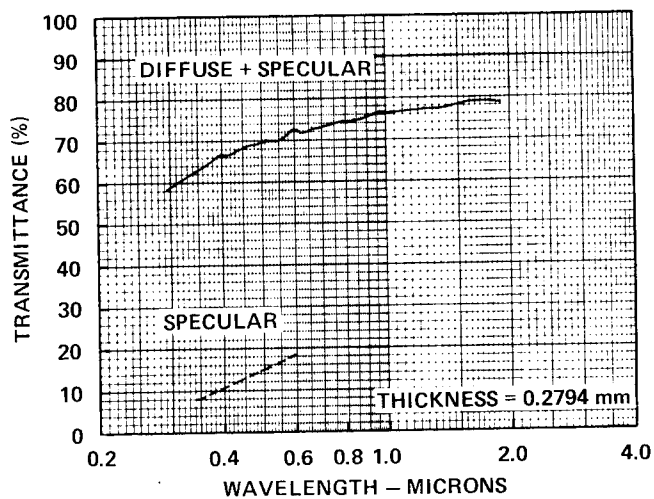
Figure 1. Hemispherical and Specular Visible Transmittance of Polished Flat Plate α-Si3N4 (Water Clear)
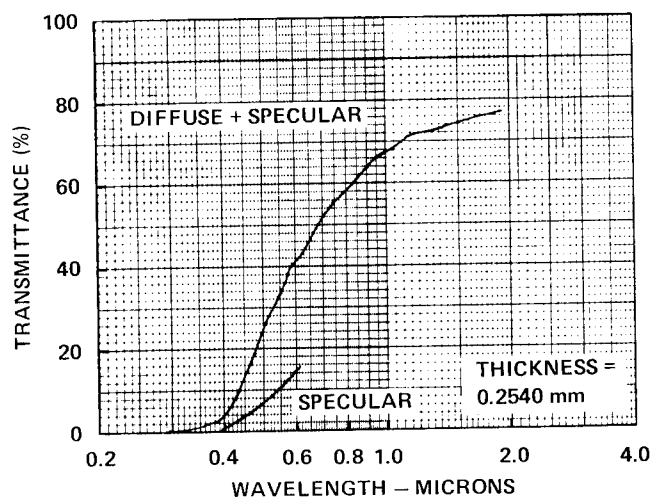
Figure 2. Hemispherical and Specular Visible Transmittance of Polished Flat—Plate α-Si3N4 (Brown)
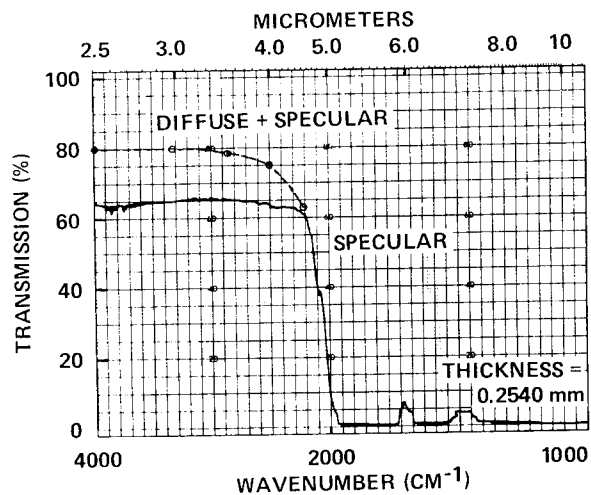
Figure 3. Hemispherical and Specular Infrared Transmittance of Polished Flat Plate α-Si3N4 (Water Clear)

19
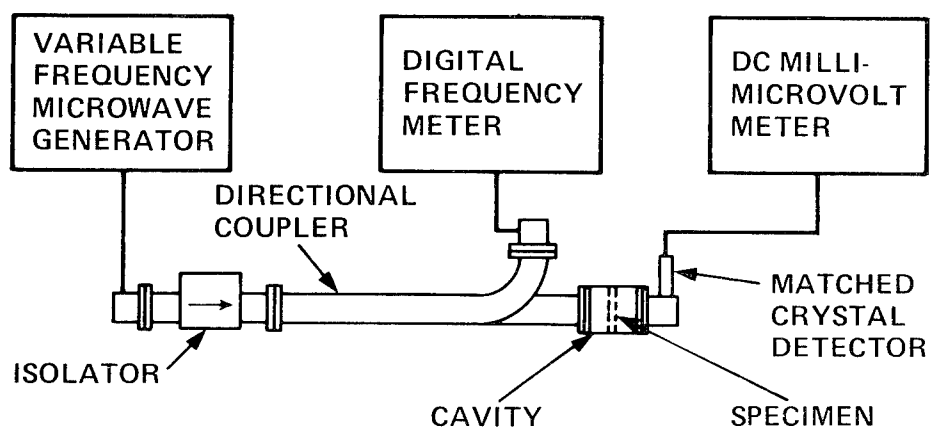
ADVANTAGES

- SMALL SPECIMEN SIZE

- CLOSE SPECIMEN TOLERANCES NOT REQUIRED

- GOOD ACCURACY FOR LOW LOSS MATERIALS

Figure 4. Schematic of Resonant Cavity Apparatus
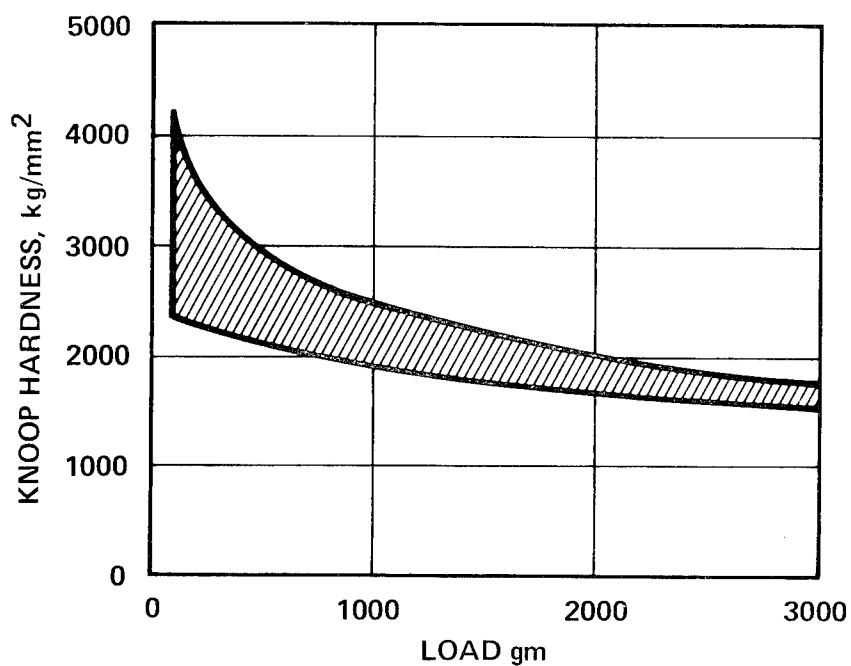
Figure 5. Knoop Microhardness Versus Identor Load for Crystalline
CVD α-Si$_3$N$_4$

20

PARAMETRIC INVESTIGATION OF RADOME ANALYSIS METHODS

G. K. Huddleston, H. L. Bassett, and J. M. Newton
Georgia Institute of Technology
School of Electrical Engineering and Engineering Experiment Station
Atlanta, Georgia   30332

Numerous methods of radome analysis have been developed [1-9], and some comparisons of theoretical and measured results have been made for specific radome/antenna combinations [2,5,7,8]; however, no attempt has been made to define the ranges of antenna and radome parameters over which any given method of analysis yields acceptably accurate results.

This paper describes some early results of an investigation recently undertaken to determine the accuracies of various radome analysis methods under controlled conditions of antenna size and placement, wavelength, and radome size and shape. To carry out valid comparisons of various methods, a fundamental theory of radome analysis has been developed and is presented below. All existing methods, as well as some new ones, can be formulated in terms of the basic theory. Comparisons of computed results obtained for two methods of analysis are also presented. No experimental results are available at this time, but rather extensive measurements involving antennas and radomes of various sizes are planned.

Theory

The Lorentz reciprocity theorem [11] is a starting point for the formulation of a basic theory of radome analysis. Field equivalence principles [12] are also important in suggesting approximate methods of obtaining the fields called for in the reciprocity theorem; more importantly, such theory is needed to obtain the transmitting formulation for radome analysis.

Consider the antenna/radome combination shown in Figure 1 where the surface S encloses the antenna. Let a plane wave be incident on the radome from the direction K_A expressed in the antenna coordinate system (X,Y,Z). Then application of the reciprocity theorem results in the following expression for the voltage produced at the antenna terminals by the incident field:

$$V_R \; (\hat{K}_A) \; = \; C \int \int_S (\underline{E}_T \; \times \; \underline{H}_R \; - \; \underline{E}_R \; \times \; \underline{H}_T) \; \cdot \; \hat{n} da \qquad (1)$$

where C is a complex constant and where

$\underline{E}_T, \underline{H}_T$ = the electric and magnetic fields produced on S when the antenna is transmitting (and no fields are incident on the radome from the outside)

E_R, H_R = the electric and magnetic fields produced on S when the plane wave is incident (and the antenna is passive or in the receive mode)

$\hat{n}$ = unit vector pointing out of the volume V enclosed by S

da = element of area on the surface S

The fields $(\underline{E}_R, \underline{H}_R)$ and $(\underline{E}_T, \underline{H}_T)$ are the total fields produced in each case and would correctly include incident and all scattered components. The voltage given by Equation (1) is exact and serves as a basic tenet of radome analysis theory. The surface S may be any conveniently chosen closed surface. Linear, homogenous, isotropic media are assumed. Time variations of the form $e^{j\omega t}$ are understood and suppressed.

The selection of the surface S and the approximations used to determine the fields $(\underline{E}_T, \underline{H}_T)$ and $(\underline{E}_R, \underline{H}_R)$ on this surface are the parameters which differentiate the various methods of radome analysis which are based on a receiving formulation. For example, Tricoles [5] and Huddleston and Joy [10] chose a planar surface coinciding with the antenna aperture for the surface S, ignoring the contribution of that portion of the surface needed to completely enclose the antenna. Huddleston and Joy used ray tracing to approximate the fields $(\underline{E}_R, \underline{H}_R)$ on S. Tricoles used field equivalence and induction theorems to determine these fields on S. Huddleston and Joy used the primary transmitting fields of the antenna to approximate $(\underline{E}_T, \underline{H}_T)$. Tricoles used measured values of antenna response.

Other approximate methods based on the receiving formulation in Equation (1) are obvious. Consider the surface S which coincides with the inner surface of the radome. The fields $(\underline{E}_T, \underline{H}_T)$ on S may be approximated using modal expansions such as the PWS [8], a spherical wave expansion [13], or from theoretical analysis [14]. These fields should correctly contain reflected components which may be approximated using plane sheet transmission coefficients and Poynting's vector. The fields $(\underline{E}_R, \underline{H}_R)$ on S may be approximated using plane sheet transmission coefficients and ray tracing. The voltage received could then be obtained by performing the surface integration over the inside surface of the radome indicated by Equation (1).

22

The effects of reflections may also be included in the analysis. Let $(\underline{E}'_T, \underline{H}'_T)$ represent the transmitting fields on the surface S which coincides with the inner radome surface. Then at a point P on the inner surface, the fields at all other points contribute components due to reflections given by [15]

$$\underline{E}_p = \frac{1}{4\pi} \iint_S [-j\omega\mu \, \psi \, (\hat{n} \times \underline{H}'_T) + (\hat{n} \times \underline{E}'_T) \times \nabla\psi + (\hat{n} \cdot \underline{E}'_T)\nabla\psi]dS \qquad (2)$$

$$\underline{H}_p = \frac{1}{4\pi} \iint_S [j\omega\varepsilon(\hat{n} \times \underline{E}'_T)\psi + (\hat{n} \times \underline{H}'_T) \times \nabla\psi + (\hat{n} \cdot \underline{H}'_T)\nabla\psi)]dS \qquad (3)$$

where

$$\psi = \frac{e^{-jkr}}{r} \qquad (4)$$

and where r is the distance from P to any other point on S. The importance of the contributions of first and higher order reflections has not been established.

A second generalized approach to radome analysis uses a transmitting formulation which does not consider explicitly the fields produced by an incident plane wave. Instead, the tangential fields produced by the antenna on a closed surface outside the radome are used to determine the fields anywhere in the unbounded, homogenous medium outside this surface. Equations (2) and (3) are the basic equations which apply, where the point P is at a great distance from S so that $\underline{E}_p, \underline{H}_p$ become the far zone fields $\underline{E}_{Tff}, \underline{H}_{Tff}$ radiated by the antenna in the presence of the radome. Selection of the surface S and the approximations used to find the fields $(\underline{E}_T, H_T)$ on S are the parameters which, again, differentiate the various methods of radome analysis based on a transmitting formulation.

The voltage that would be received by the antenna which produces far zone fields $\underline{E}_{Tff}, \underline{H}_{Tff}$ is given by [23]

$$V_R(\hat{K}_A) = C \, \underline{E}_{Tff} \cdot \hat{n}_b \qquad (5)$$

where C is a complex constant and $\hat{n}_b$ is a generally complex vector which describes the orientation and polarization of an infinitesimal current element located in the direction given by $\hat{K}_A$. Note that the current element would produce an

23

incident plane wave on the radome having the same polarization as that indicated by $\hat{n}_b$; hence, Equation (5) provides the connection between the receiving and transmitting formulations and is a third facet of a basic theory of radome analysis.

The above equations combine to form a fundamental theory of radome analysis. All existing analysis methods, as well as some new ones, can be cast in terms of this theory. The theory provides a rigorous framework in which the approximations which may be used in any analysis method can be clearly seen and their effects on predicted results assessed. Comparisons of the various methods in terms of speed of computations and accuracy can also be made.

All radome analysis methods of practical interest entail approximations of one form or another. Consequently, the only satisfactory way to determine the accuracy of any method is by comparison with experimental data. To cover the broad range of parameters that may be encountered in practice, combinations of radomes and antennas of various sizes should be carefully selected for measurement to yield the most useful true data for assessing the accuracies of different methods of analysis.

Application

A computationally fast method of radome analysis based on a receiving formulation [10] results when the surface S in Equation (1) is chosen to coincide with the planar aperture of the antenna whose radiating characteristics are represented using the plane wave spectrum formulation [17]. The difference receiving pattern in the azimuth plane for a vertically polarized monopulse antenna with square aperture (corners removed) of dimensions $4.3\lambda \times 4.3\lambda$ is shown in Figure 2 for the case of a Pyroceram radome of wall thickness d = .22λ. The tangent ogive radome with fineness ratio L/D = 2.25 gimballed so that its tip is positioned at $+12^{\circ}$ in the azimuth plane of the antenna. Execution time to generate this pattern and three others like it was 104 seconds (CDC Cyber 70).

For comparison, the pattern obtained for the same values of radome and antenna parameters when a transmitting formulation [9] is used is shown in Figure 3. In this method, a PWS representation is used to describe the antenna, and rays representing each plane wave are used to construct an equivalent aperture which includes the effects of the radome on each plane wave in the spectrum. The execution time to generate this pattern and three others was 60 seconds on the same computing system.

Other methods of analysis which utilize integration on the surface of the radome for both receiving and transmitting formulations are currently being implemented. Computed results obtained using these methods will be presented at the symposium. The

24

experimental procedures being used will also be described.

Summary

A fundamental theory of radome analysis, which embodies all existing methods as well as some new ones, is presented. Computed results using two different methods of analysis have been obtained as preliminary data. Computed results obtained using additional methods of analysis will be presented at the symposium.

References

1. "Microwave Antenna Theory and Design," edited by Samuel Silver, McGraw-Hill Book Company, Chapter 14, 1949.

2. N. R. Kilcoyne, "An Approximate Calculation of Radome Boresight Error," Proceedings of the USAF/Georgia Institute of Technology Symposium on Electromagnetic Windows, pp. 91-111, June 1968.

3. O. Snow, "Discussion of Ellipticity Produced by Radomes and Its Effects on Crossover Point Position for Conically Scanning Antennas," U. S. Naval Air Development Center, Report E15108, 1951.

4. P. I. Pressel, "Boresight Prediction Technique," Proceedings OSU-WADC Radome Symposium, 1956.

5. G. Tricoles, "Radiation Patterns and Boresight Error of a Microwave Antenna Enclosed in an Axially Symmetric Dielectric Shell," J. Optical Soc. of America, 54, No. 9, pp. 1094-1101, September 1964.

6. M. Tavis, "A Three-Dimensional Ray Tracing Method for the Calculation of Radome Boresight Error and Antenna Pattern Distortion," Report No. TOR-0059(56860)-2, Air Force Systems Command, May 1971.

7. D. T. Paris, "Computer-Aided Radome Analysis," IEEE Transactions, AP-18, No. 1, pp. 7-15, January 1970.

8. D. C. F. Wu and R. C. Rudduck, "Application of Plane Wave Spectrum Representation to Radome Analysis," Proceedings of the Tenth Symposium on Electromagnetic Windows, pp. 46-49, July 1970; also Final Technical Report 2969-4 (AD 722 634), March 1971.

9. E. B. Joy and G. K. Huddleston, "Radome Effects on Ground Mapping Radar," Contract DAAH01-72-C-0598, U. S. Army Missile Command, March 1973.

10. G. K. Huddleston and E. B. Joy, "Development of Fabrication and Processing Techniques for Laser Hardened Missile Radomes: Radome Electrical Design Analysis," MMC Purchase Agreement No. 573712, Martin Marietta Aerospace, March 1977.

11. R. E. Collin and F. J. Zucker, "Antenna Theory, Part 1," Section 4.2, McGraw-Hill Book Company, New York, 1969.

12. Ibid., Section 3-3.

13. A. C. Ludwig, "Near-Field Far-Field Transformations Using Sperical Wave Expansions," IEEE Transactions, AP-19, No. 2, pp. 214-220, March 1971.

14. D. T. Paris, "Digital Computer Analysis of Aperture Antennas," IEEE Transactions, AP-16, pp. 262-264, March 1968.

15. Silver, op. cit., Section 3-8, Equations (108)-(109).

16. Collin and Zucker, op.cit., Section 4.5.

17. H. G. Booker and P. C. Clemmow, "The Concept of an Angular Spectrum of Plane Waves, etc.," Proceedings IEE, 97, Part III, p. 11-17, 1950.
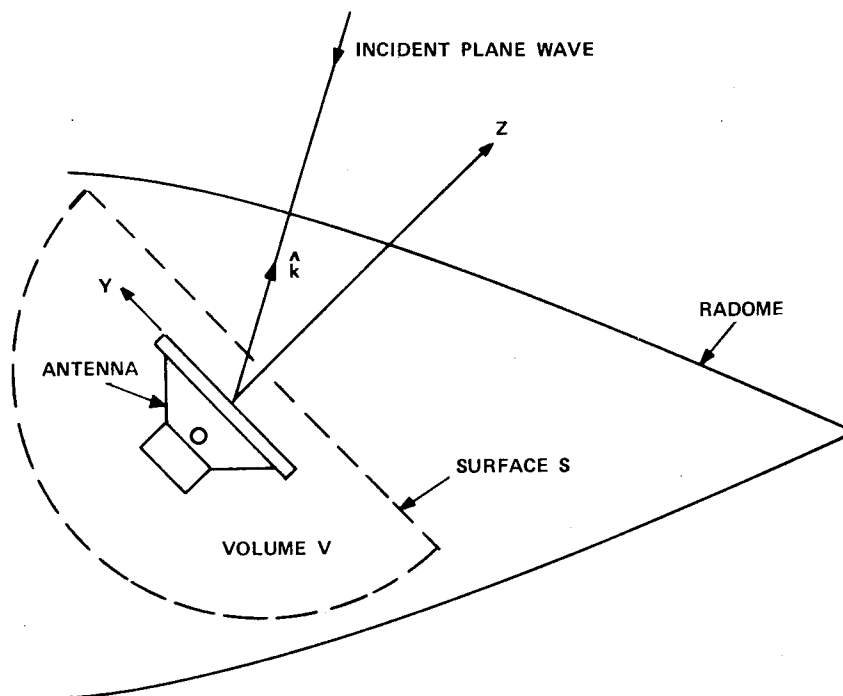
FIGURE 1. ANTENNA/RADOME GEOMETRY FOR ANALYSIS.
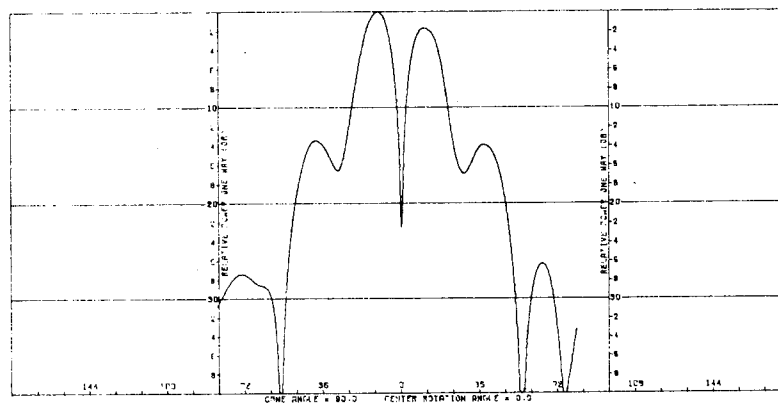
FIGURE 2. AZIMUTH PATTERN FOR RECEIVING FORMULATION.
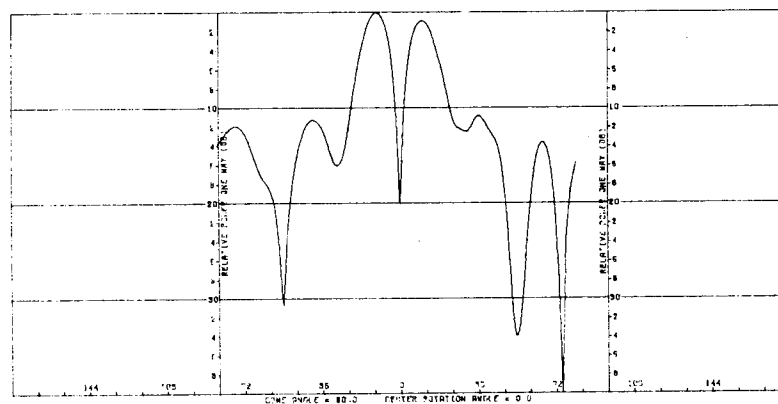
FIGURE 3. AZIMUTH PATTERN FOR TRANSMITTING FORMULATION.

27

DESIGN OF AN ABLATIVE MISSILE RADOME
FOR USE WITH A SHAPED BEAM ANTENNA

D.J. Kozakoff and A. Ossin

Martin Marietta Corporation, Orlando Division
Orlando, Florida 32855

INTRODUCTION

A feasibility study was performed considering use of an ablative radome concept for use with a Ku-band circularly polarized shaped beam ground mapping radar antenna. Acceptance of the concept depended on the degree of antenna pattern distortion which could be tolerated by the guidance system; a ±1 dB departure from the theoretical cosecant mapping pattern was taken as the criterion. Antenna patterns for various fiberglass core materials and ablator material and thickness combinations were computed. The aggregate ablation among all missile trajectories based on thermal analysis were compared to the range of ablator thicknesses which yielded acceptable pattern distortions to identify an acceptable "window" and nominal design thickness. Fabrication and testing of a selected fiberglass Duroid concept demonstrated acceptable pattern distortions as predicted by the theory.

RADOME CONCEPT

The radome is a complex cone-tangent ogive shape; the wall construction, radome and antenna geometry are illustrated in Figure 1. Here, the core material acts as the structural portion, while the outer material must provide for ablation and insulation requirements on all missile trajectories. In the initial design tradeoffs, various core materials such as fiberglass epoxy and fiberglass silicone, and ablator materials such as Duroid 5650 and Avcoat 8027 were considered. Electrical properties of candidate materials are summarized in Table I.

TABLE I

Electrical Properties of Candidate Radome Materials

Material	Dielectric Constant	Loss Tangent
Duroid 5650	2.6	0.0035
Fiberglass Epoxy (30% Resin)	4.1	0.0150
Fiberglass Silicone (30% Resin)	3.0	0.0015
Avcoat 8027	2.9	0.0300
Slip Cast Fused Silica (SCFS)	3.33	0.004
Fiberglass Epoxy (18% Resin)	5.0	0.015
Fiberglass Silicone (18% Resin)	5.0	0.006

ABLATION ANALYSIS

The ablation analysis of various material combinations was accomplished using the Martin Marietta Fϕ-110 computer code. This program is capable of computing the effects of aerodynamic heating on heat shield-type materials.

It includes the effects of both equilibrium and rate controlled chemical ablation, as well as in-depth pyrolysis. In this case, a rate-controlled analytical model, using Teflon and Duroid ablation data, was used to describe the ablation phenomena of Duroid (reference 1).

Figure 2 shows Duroid recession as a function of altitude for the two worst case trajectories that yielded maximum ablation. The net aggregate ablation is significant, in that it defines the size of the electrical window in which acceptable pattern distortions must be found. In the event that the electrical window is less than the net aggregate ablation, the window may be enlarged by rolling the missile or accepting larger pattern distortions.

ELECTRICAL ANALYSIS

Elaborate plane wave spectra techniques have been applied to compute broad beam antenna patterns in the presence of a radome (reference 2). In the analysis herein, a simple 2-dimensional ray trace method was employed because of its low cost and the availability of the RADEP2 computer program. In RADEP2, the antenna terminal voltage due to a single plane wave incident from direction θ-degrees (measured from the antenna normal) is computed by a backward ray trace similar to that employed in reference 3. Describing N-sample points over the antenna aperture (see Figure 3), the received voltage is given by the numerical integration:

$$V = \frac{\sum_{i=1}^{N} \cos(\theta) \, T_i \, A_i \, \exp[-j \, \psi_i(\theta)]}{\sum_{i=1}^{N} A_i \, \exp[-j \, \psi_i(0)]} \tag{1}$$

where, T_i = complex radome transmission coefficient for the ith ray

A_i = aperture weighting coefficient

$\psi_i(\theta)$ = spatial phase constant of the ith ray in the θ direction.

Aperture Weighting

The ground mapping radar antenna has a shaped beam power gain pattern given by the formula

$$G(\theta) = \csc^2\theta \sqrt{\cos \theta} \tag{2}$$

where the defined mapping region corresponds to values of θ from 25 thru 55 degrees. For an antenna having such vertical dependence with depression angle, Silver (reference 4) has shown that equal received power would be produced by a ground target at any elevation angle in the mapping region of the antenna.

Determination of the aperture weighting coefficients, A_i, corresponding to the cosecant antenna pattern, was accomplished by a Woodwards synthesis (reference 5). The far-field pattern in the mapping region is approximated by the sum of M-beams, each of which is generated by a uniform aperture and of the

characteristic Sin X/X form. Beams are equispaced in sine space, and the net pattern given by

$$G(\theta) = \csc^2\theta \sqrt{\cos\theta} = \sum_{j=1}^{M} B_j \left\{ \frac{\sin(\theta - \theta_j)}{(\theta - \theta_j)} \right\}^2 \qquad (3)$$

where B_j is the relative weight of jth beam as determined by emperical fit to the ideal pattern. The mapping region was approximated within ±0.5 dB by 20-beams spaced 0.026 apart in sine space. The A_i's are taken as the vector sum of the j uniform illumination.

Verification of Approach

RADEP2 was used to predict the performance of a slip cast fused silica (SCFS) radome since a SCFS concept was already designed and extensively tested electrically. Figure 4 depicts measured and predicted patterns demonstrating reasonable correlation. The patterns indicate considerable degradation when the tip shadow falls into the mapping region, a phenomena that has indeed been a problem, based on actual experience.

Concept Tradeoffs

Hundreds of antenna patterns were computed with various core and ablator material and thickness combinations. Calculations were performed for vertical and horizontal linear polarizations. In each case, the departure of the computed pattern from the ideal mapping pattern in dB ripple was noted as ablator thickness varied. Table II summarizes the result. Best performance was noted for a 0.16-inch fiberglass epoxy core with a 0.36-inch Duroid ablator (case 10 in Table II). The pattern ripple versus ablator thickness for this case is shown in Figure 5. An electrical window of 60-mils is noted; the window opens up rapidly with small increases in the amount of ripple acceptable.

MEASURED DATA

A radome based on the 0.16-inch fiberglass core and 0.36-inch Duroid ablator was fabricated and electrically tested to verify the pattern ripple predictions. Figure 6 illustrates a measured antenna pattern with and without radome. Although the overall radome loss was higher than anticipated in almost all cases, the measured distortion of the antenna patterns was less than predicted, indicating the analysis was conservative.

CONCLUSIONS

A simple 2-dimensional worst case analysis was employed to evaluate the feasibility of an ablative radome concept for use with a shaped beam antenna pattern. The criterion for acceptance was a maximum ±1 dB departure of the antenna pattern from the ideal pattern in the mapping region. Various combinations of fiberglass core thicknesses with Duroid ablators were noted to have favorable windows. No window was found for Avcoat 8027 ablator. This phenomenon was probably due to the fact that the Avcoat material loss tangent was over 10 times greater than the Duroid.

31

Electrical tests conducted on a prototype fiberglass/Duroid radome as designed showed small pattern distortions over the mapping region, as predicted. This test data validates the analysis approach.

TABLE II

Summary of Results

Case Number	Core Material	Core Thickness, t_2 (inches)	Core Dielectric Constant, ϵ_2	Core Loss Tangent, $\tan \delta_2$	Ablator Dielectric Constant, ϵ_1	Ablator Loss Tangent, $\tan \delta_1$	Comments
1	Fiberglass/ Silicone	0.14	3.0	0.0015	2.6	0.0035	Window found at 1 dB
2	Fiberglass/ Silicone	0.18	3.0	0.0015	2.6	0.0035	Window found at 1 dB
3	Fiberglass/ Silicone	0.23	3.0	0.0015	2.6	0.0035	Window found at 1 dB
4	Fiberglass/ Silicone	0.28	3.0	0.0015	2.6	0.0035	No window
5	Fiberglass/ Epoxy	0.14	4.1	0.015	2.6	0.0035	Window found at 1 dB
6	Fiberglass/ Epoxy	0.23	4.1	0.015	2.6	0.0035	No window
7	Fiberglass/ Silicone	0.16	5.0	0.006	2.6	0.0035	Window found at 1 dB
8	Fiberglass/ Silicone	0.23	5.0	0.006	2.6	0.0035	No window found
9	Fiberglass/ Silicone	0.3	5.0	0.006	2.6	0.0035	Window found at 1 dB
10	Fiberglass/ Epoxy	0.16	5.0	0.015	2.6	0.0035	Window found at 1 dB Selected concept with 0.36 inch Duroid/.16 inch fiberglass
11	Fiberglass/ Epoxy	0.30	5.0	0.015	2.6	0.0035	Window found at 1 dB
12*	Fiberglass/ Epoxy	0.14	4.1	0.015	2.9*	0.03	No window found

*Case 12 ablator was Avcoat 8027

REFERENCES

1. "Aerodynamics Heating and Heatshield Design," A. Ossin, Martin Marietta Report OR 12,029, Orlando, May 1972.

2. "Final Report on Radome Effects on Performance of a Ground Mapping Radar," E.B. Joy and G.H. Huddleston, MICOM study DAAH01-72-C-0598, RF Guidance Technology Branch, Advanced Sensor Division; report by Geo. Inst. of Technology, Atlanta, March 1973.

3. "Radome Boresight Error and Its Relation to Wavefront Distortion," R.A. Hayward, E.L. Rope and G. Tricoles, Proc. of 13th Symposium on EM Windows, Geo. Inst. of Technology, Atlanta, 1976.

4. "Microwave Antenna Theory and Design," S. Silver, McGraw Hill Book Company, New York, 1949.

5. "Antenna Engineering," W.L. Weeks, McGraw Hill Book Company, New York, 1970.
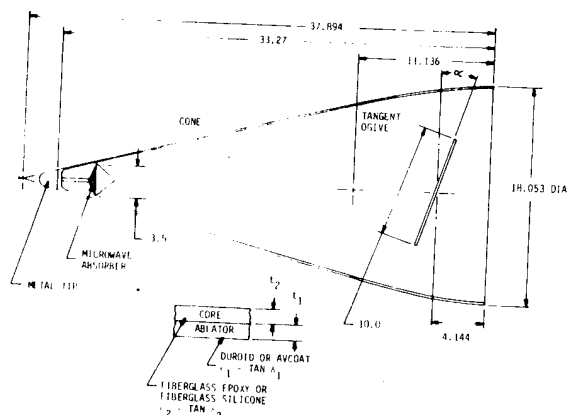
Figure 1. Radome and Antenna Geometry
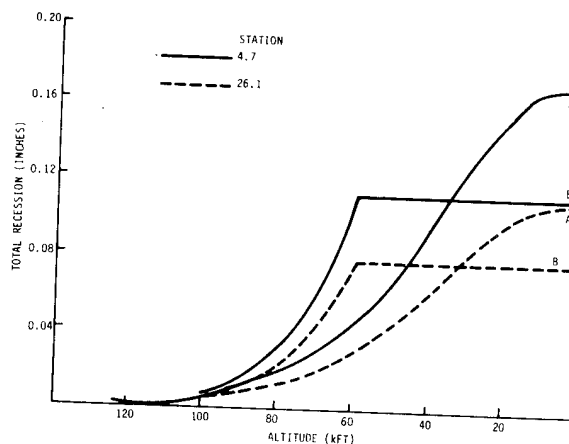
Figure 2. Duroid Recession Versus Altitude for the Two Worst Case Trajectories
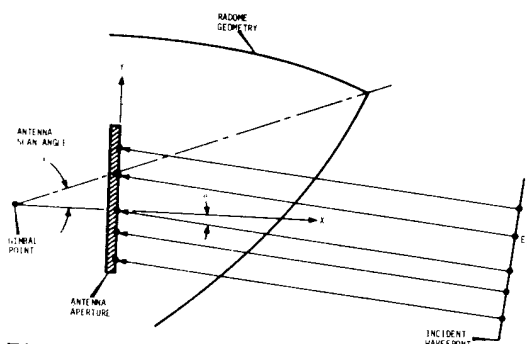
Figure 3. Incident Plane Wavefront E_I Propagating Through Radome Wall and Impinging on Antenna Aperture
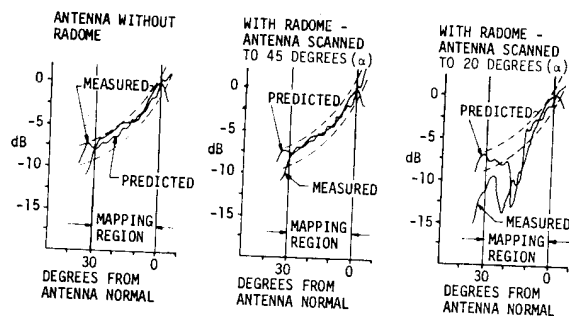
NOTE: DOTTED LINES REPRESENT SPECIFICATION LIMITS

Figure 4. Comparison of Measured and Predicted Mapping Patterns SCFS Radome Based on RADEP-2 Code

33
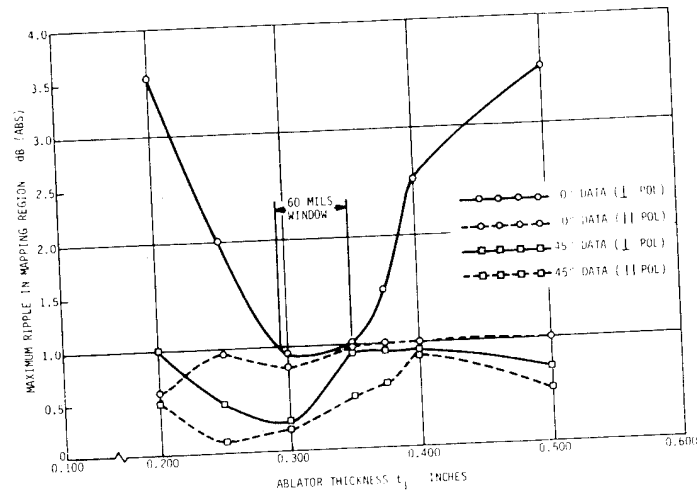
Figure 5. Ripple Versus Ablator
Thickness: Case 10
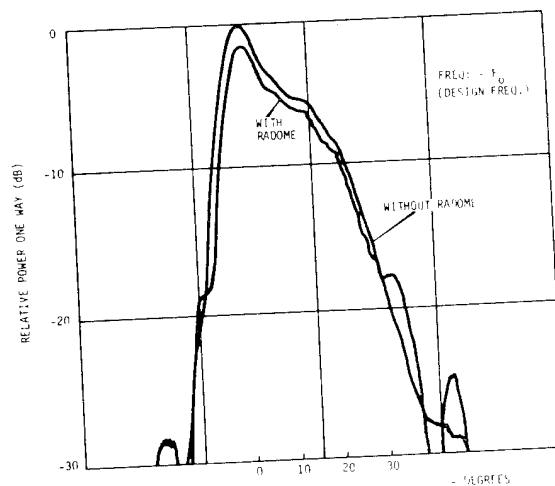
Figure 6. Antenna Patterns With and
Without Radome; Antenna Scan Angle
70-Degrees (Case 10)

34

Near Field Antenna Range
For Radome Nose Tip Problems

Don Purinton and Dean Hofer
Texas Instruments, Inc.
Dallas, Texas

The metal tip and the dielectric region around it produce severe radome distortion at X and K_u band frequencies. Near Field measurements can be used as a tool to provide compensation for this distortion.

For a broadbeam broadband antenna, measurements were made in the plane of the antenna aperture without the presence of the antenna. The field probe was illuminated from the far field with a plane wave. Figure 1 shows measurements made with and without the presence of the radome. The nose of the radome has the effect of retarding the energy received at the center of the antenna aperture. This retardation produces "focusing" of the far field antenna pattern at boresight as is shown in Figure 2. The "focusing" occurred only at the highest operating frequencies of the radome and antenna.

Foam inserts as shown in Figure 3 were experimentally fashioned to reduce the effect of the nose tip. Polyethylene foam having a nine (9) pound density was used. The thickness of the foam was chosen to provide the approximately 10^0 of phase shift needed to retard the incoming wave surrounding the nose tip region. With the proper foam thickness the near field measurements showed the phase to be flat across the aperture as if the radome were not present. As a result, the antenna pattern produced with the compensators in place looked like that of an antenna without the radome. This pattern is shown in Figure 4. When the foam compensator was made too thick, the phase at the center of the antenna aperture was advanced with respect to that at the edge and the far field antenna pattern appeared as shown in Figure 5.

The foam compensator was found to provide pattern improvement at the highest operating frequencies where the "focusing" problem appeared. At lower frequencies the compensator had no effect on radome performance as was desirable since compensation was not needed.

Since the dielectric constant of the foam was low in value, the foam was essentially transparent and without reflections. It produced a phase delay corresponding to the difference in index of refraction between the foam and air.

Because polethylene has a limited temperature capability, a syntactic foam was developed that had a dielectric constant of 1.2. This foam was made using 3M microballoons and Colorado Chemical Ricon 1595 butadiene resin. This foam was found to withstand the temperature time profile of Figure 6 without significant degradation. It is not known whether the above specific use of a foam phase corrector has application to the more general radome nose tip problem. Near Field range measurements are being made for various sizes of radome nose tips to determine their forward scattering characteristics. Efforts will be made to develop a class of foam phase compensators to reduce the effect of the nose tip for radomes used with narrow beam scanning antennas.

SUMMARY

For a specific case of a non-scanning broadbeam broadband antenna placed behind a radome, near field measurements have helped to develop a phase compensator that reduces distortion due to the nose tip. It is planned to extend this work to large narrow beam scanning antennas placed behind radomes. Foam phase correctors have the advantage of allowing the radome wall to be maximized for transmission independently of phase considerations needed to counter the distortion effects of radome tips and radome geometry.
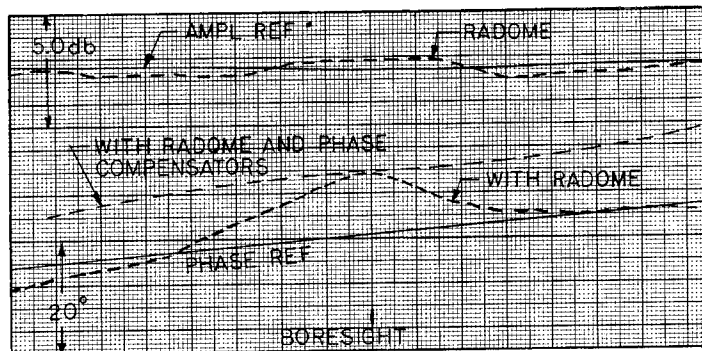
FIGURE 1. PHASE AND AMPLITUDE
MEASUREMENTS MADE AT ANTENNA
APERTURE
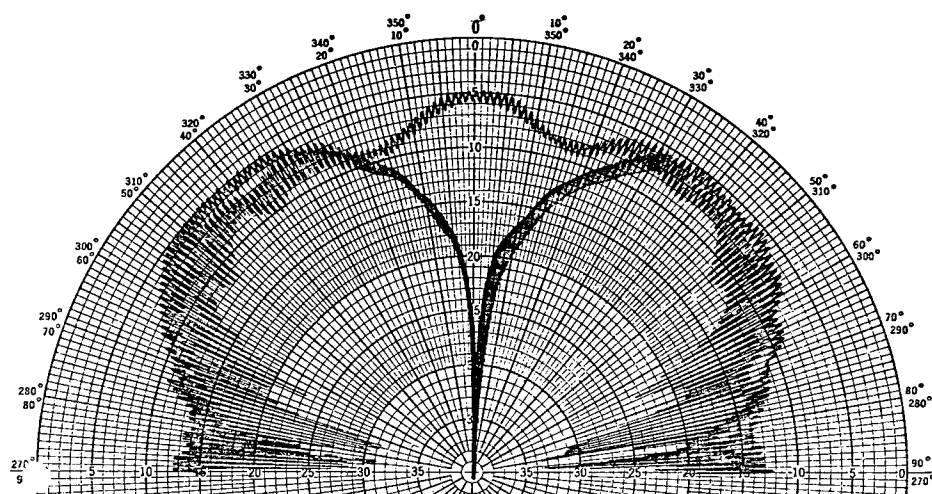
FIGURE 2. ANTENNA PATTERN WITH RADOME
IN PLACE WITHOUT A FOAM COMPENSATOR
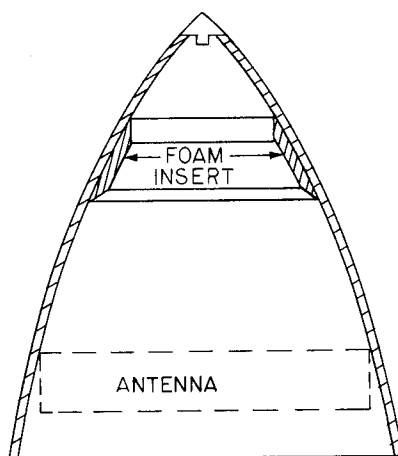
FIGURE 3. CROSS SECTION OF RADOME
SHOWING FOAM PHASE SHIFTERS

37
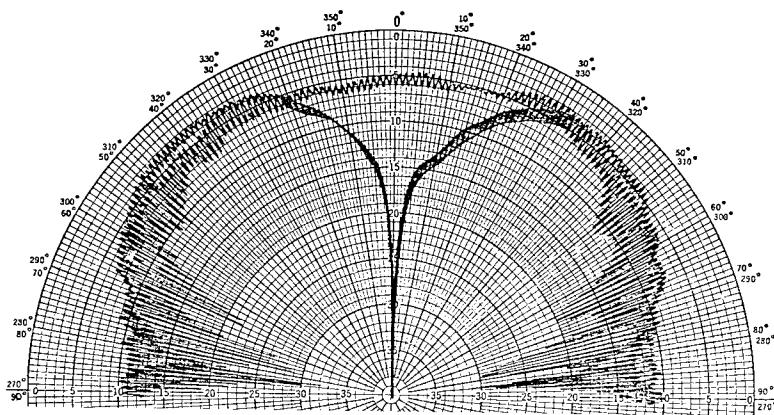
FIGURE 4. ANTENNA PATTERN WITH RADOME
AND FOAM COMPENSATORS
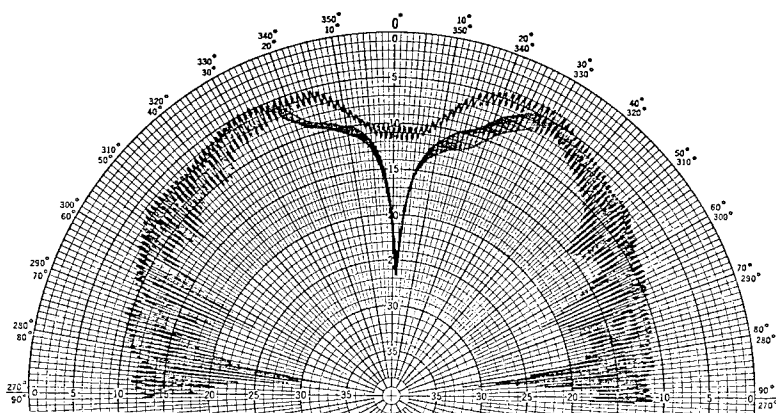
FIGURE 5. ANTENNA PATTERN WITH RADOME
AND EXCESSIVE FOAM COMPENSATION
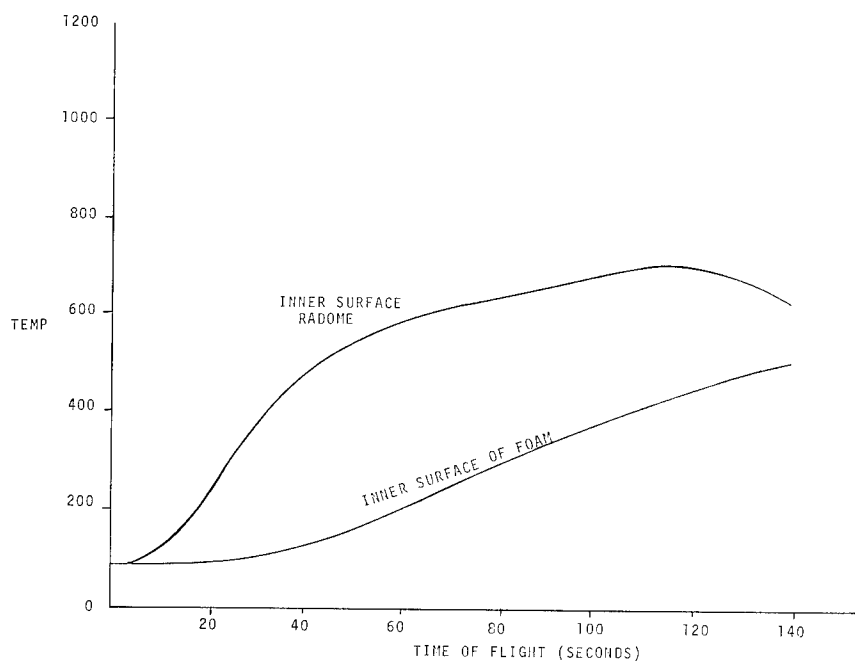
FIGURE 6 TEMPERATURE VS TIME OF FOAM COMPENSATOR

38

C.N. TOWER MICROWAVE RADOME

Milton B. Punnett, P.E.
Chief Engineer, Birdair Structures, Inc.
2015 Walden Ave., Buffalo, N.Y. 14225

INTRODUCTION. In June 1973, Birdair Structures was contacted by the architects of the CN Tower in Toronto, Canada regarding the feasibility of enclosing the microwave communications level of the record height tower with an air-inflated radome. It was recognized that exposed antennas mounted outboard around the base of the "skypod," as shown in artists' concepts of the tower, were not practical. Birdair's proposal was a simple inflated torus section (Fig. 1), completely encircling the section. The unique, 360°, RF transparent enclosure not only appealed to the aesthetic and progressive concepts of the architects, it also promised performance otherwise unobtainable, including:

A. Complete protection for equipment and servicing at 1200 ft. above street level.

B. Flexibility for future changes with uninterrupted viewing and a minimum degree of frequency dependence.

C. Smooth exterior to prevent significant ice or snow accumulation, especially critical, as failing ice which might form on irregular antenna and feed structures would present an extreme hazard to people in the area below.

GEOMETRY. Detail dimensions of the 138 ft. diameter radome are shown in the cross section, Fig. 2. The antenna mounting plane was dictated by the dimensions of the tower "skypod." The 25' 6" height of the enclosure was selected to allow variable mounting of antenna at least 12 ft. diameter. The vertical curvature and outer diameter were then a function of space required and skin stresses. The rooms behind the antenna are for the electronic gear. Individual angular sectors are leased to tenant clients. The entire level (which is not part of the area open to the public) is pressurized, eliminating the need for seals between equipment and antennas. The inflation system is under the equipment deck in unused space.

WIND TUNNEL TESTING. Concern as to wind turbulence factors and the exact effect of the tower geometry resulted in testing at the Boundary Layer Wind Tunnel at the University of Western Ontario. A special 1/120th inflatable model with a 0.001" skin was used (Fig. 3) to measure skin deflection and pressure distribution under varying turbulence. Results were used to establish wind distortion, pressure distribution for calculating stresses, operating inflation levels, and optimum location of the air intakes.

PRESSURIZATION. Even though the radome is retained by clamping rings at top and bottom, the envelope depends upon inflation pressure for the pretensioning which provides shape and stability. The inflation system is based upon the trouble-free, 210 ft. diameter Telstar radome design. One of three pressure levels is automatically selected in accordance with ambient wind. Seven blowers are used in a redundant design. Under normal conditions only one 5 HP blower is required, running at 5 amps and delivering 2800 cfm at 3 inches water pressure. Maximum pressure is sufficient for gradient wind velocities exceeding 120 mph (a 10^{-4} time probability level derived statistically by the

University of Ontario researchers). The system is split between the two standby emergency power sources in the tower.

CALCULATED LOADS. Stresses in the tensioned skin of the radome are variable, reaching a peak under aerodynamic loading in the area of minimum negative pressure. The principal stress is in the vertical, clamp-to-clamp direction and may be conservatively calculated by assuming the entire pressure load is reacted in this direction. Maximum loads in the envelope reach 100 lb./in. at a yaw angle of 150° with 110 mph winds. The design safety factor is then six. Under normal inflation the skin is only stressed to 20 lb./in.

MATERIAL. The radome material chosen is a recently developed coated fabric, combining superior electrical and physical characteristics. Beta glass yarn is woven into an 18 oz./sq. yd. structural base fabric. This is coated with TFE and FPE "Teflon" resin to a total weight of 47 oz./sq. yd. and thickness of 0.038". Tested strip tensile strength is 935 x 860 lb./in. Measured water absorption is less than 0.1% after 24 hours total immersion. Accelerated weathering tests show the coating to have excellent resistance to weathering or aging and it naturally resists adherence of ice and dirt. Variations of the same material are being used in many architectural applications (such as the Pontiac, Michigan "Silverdome") where it is taking the air structure from a temporary concept to a permanent design.

RF PROPERTIES. Transmission losses have been conservatively measured at less than 0.2 db at 7.5 GHz, increasing to 0.4-0.5 db at 15 GHz. The radome is considered satisfactory for operation up to 20 GHz. Precise dielectric measurements (per ASTM-2520) of a similar material are shown in Table I. The obtaining of a dielectric constant less than 2.1 and loss tangent less than 0.0025 required special care in compounding. Pure Teflon has a ϵ = 2-2.1 and loss tangent of 0.00015. The Beta fiberglass is based upon the "E" or electrical composition having a dielectric in the order of six and loss tangent of 0.002. Presumably the Teflon is the predominate component in what is essentially a non-homogenious composite. Some work has been done on alternate structural base fabrics, specifically the Aramids, NOMEX, and Kevlar ($\epsilon \approx 3.0$), but only the fiberglass yarns have shown sufficient resistance to the sintering temperatures presently required for the Teflon.

INSTALLATION. The radome was prefabricated in three 120° segments, each weighing 1500 lbs. The antenna hoisting ring on the tower just below the upper clamp was also used to install the radome. Temporary lifting clamps secured the accordian-folded radome to roller trolleys on the ring much like a shower curtain (Fig. 4). It was then spread open and clamped top and bottom around the skypod. Fiberglass clamps are used to join the sections together at the three vertical joints, which were pre-located to minimize interference with the antenna patterns. Once clamping was completed, the envelope was pressurized. The envelope was uncrated, deployed, secured, and inflated in one day.

DESIGN FEATURES. The radome is fabricated of 90 identical vertical panels joined with 3" wide thermal weld lap joints. Although the joint contains no metal and is RF transparent, it does present a double thickness. A sample joint was tested by the Canadian National Research Council who concluded they would have no significant effect upon total RF performance. The three sectionalized field joints are made by clamping overlapped roped edges. The clamp members are extruded 3" fiberglass channels with 3/8" diameter stainless steel bolts. Beaded edges, top and bottom, are clamped to the steel tower rings with 5/8" diameter stainless steel bolts at 17" spacing.

A unique feature is the method of adding or removing full size antenna. The 8 ft. wide base deck of the radome is actually a series of 3' x 5' hatch plates. By using an electric winch on the hoisting ring and removing the plates directly under the antenna position, a reflector may be hoisted directly from the ground 1200 ft. below. Two high volume blowers (10 HP, 50,000 cfm) maintain radome inflation while the hatch is open.

CONCLUSION. The CN Tower radome is a good example of the flexibility in design concepts possible with an air-inflated structure. It vividly illustrates that shapes other than a simple sphere are possible. The Teflon-Fiberglas, which was first accepted as a structural material due to its long life and excellent fire resistance, has great promise for many radome applications. It is already used on several large sports stadiums up to 10 acres in size and is the primary candidate for a 100-acre structure to be erected in Saudi Arabia. Work is continuing on the high-tenacity Aramids which show strength/density ratios better than the glass (or steel). Unfortunately, and most surprising, the architects, and not the electronic engineers, have become the most progressive and creative in the field and seem to be the leaders in the development of new concepts.

Photo credits: CN Foundation, Robertson Corp., Panda Associates

TABLE I

Microwave Dielectric Measurements

Specimen No.	Frequency Gigahertz	Dielectric Constant	Dissipation Factor
1, dry	10.036	1.96	0.0015
2, dry	10.028	2.02	.0023
1, dry	8.654	1.95	.0010
2, dry	8.647	2.01	.0018
1, wet	10.033	2.00	.0046
2, wet	10.024	2.06	.0043
1, wet	8.646	2.05	.0038
2, wet	8.643	2.06	.0040

Material: G12T28, t = 0.028", wt = 27.4 oz./sq. yd.

Wet: After 48 hours immersion in water at 23C.

Test Per: ASTM-2520 (Method B).

FIGURE 1. CN TOWER
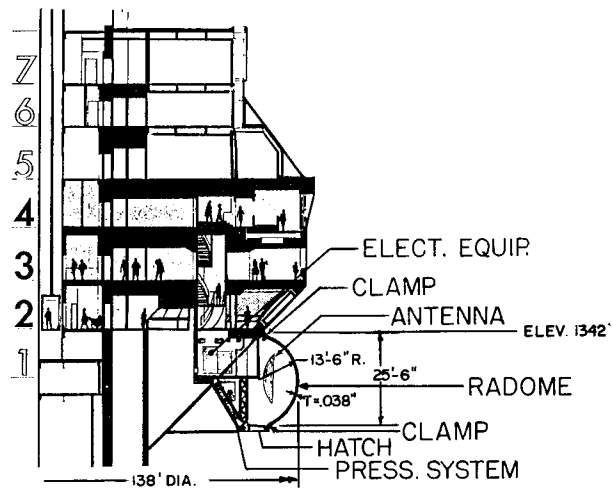
FIGURE 2.   "SKYPOD" CROSS–SECTION
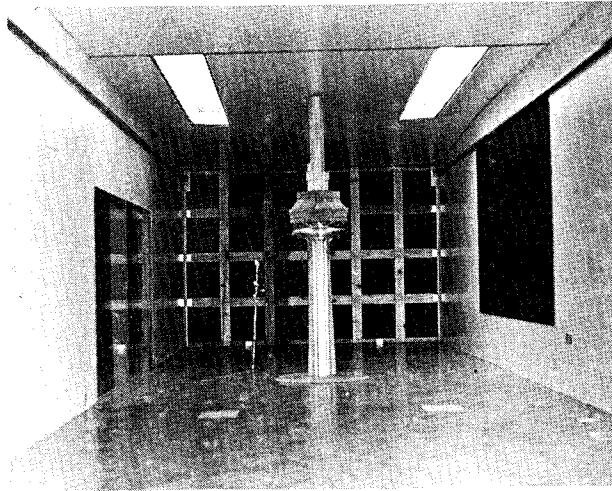
FIGURE 3.   WIND TUNNEL MODEL

FIGURE 4.   RADOME INSTALLATION

43
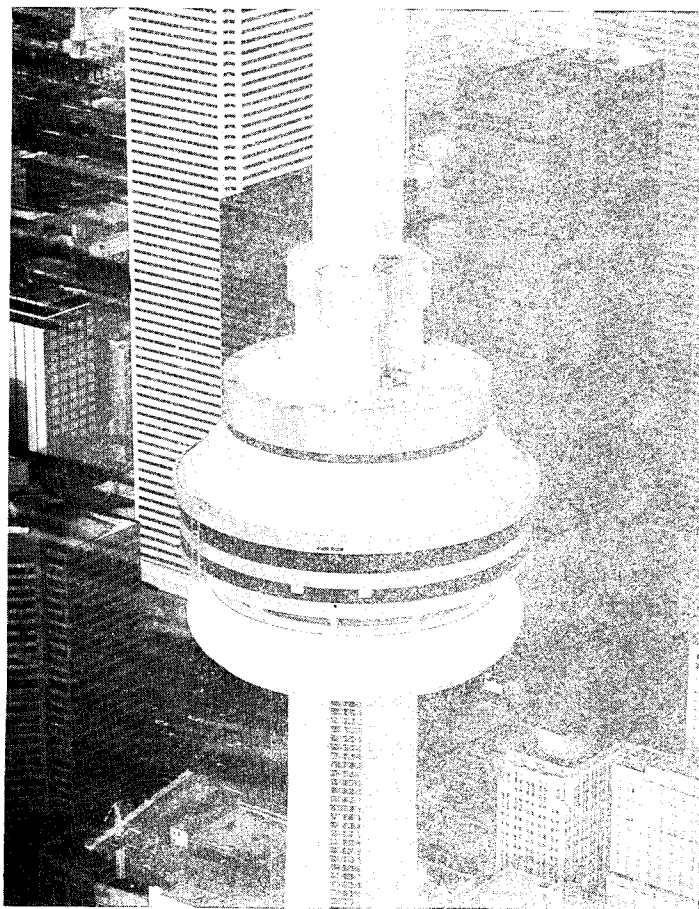
FIGURE 5.   TOWER "SKYPOD" WITH
COMPLETED RADOME
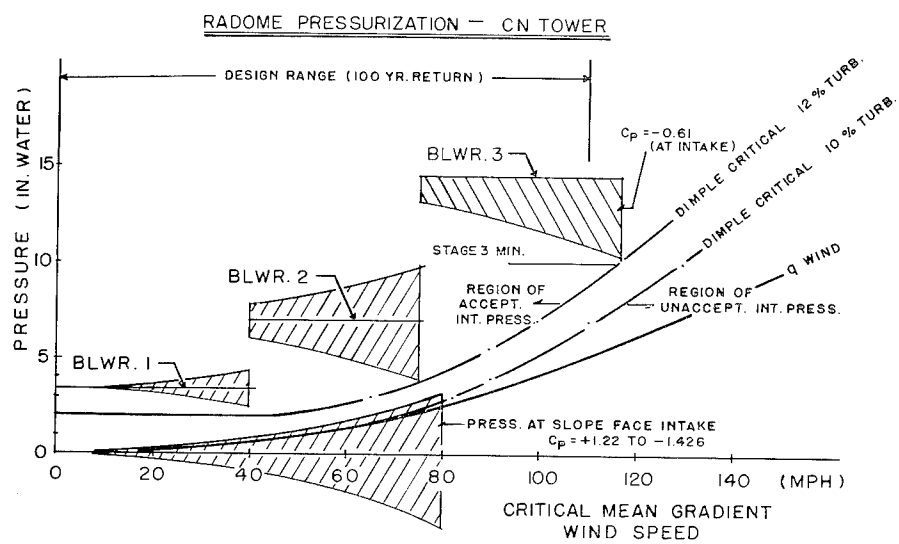
FIGURE 6.   RADOME PRESSURIZATION

44

AERODYNAMIC HEATING EFFECTS ON RADOME BORESIGHT ERRORS

by

L. B. Weckesser, R. K. Frazer, D. J. Yost and B. E. Kuehne
of The Johns Hopkins University Applied Physics Laboratory
and G. P. Tricoles, R. Hayward and E. L. Rope
of General Dynamics Electronics Div.

Introduction

For supersonic homing missiles whose mission includes attack of super-sonic-maneuvering targets at high altitude, there is a severe demand on the guidance system for high accuracy. As a result, the guidance engineer places a stringent requirement on the allowable boresight errors (BSE) caused by the radome. In the past, the radome designer has worked diligently to provide radomes that would meet this requirement at room temperature and has given little consideration to the effect of aerodynamic heating. An analytical investigation has been carried out to determine this effect on a Pyroceram 9606 radome.

The investigation described herein was carried out in four phases: (1) The missile radome was "tuned", using special fiberglas correction tape to minimize BSE's. It's BSE's versus look angle were then measured in an antenna range at every 22.5° around its circumference. The radome was then flown in a missile flight test against a drone target. (2) The radome was mathematically modeled and a thermal analysis was carried out to define the hot radome electrical properties and its wall dimensions. (3) Analyses were carried out to define BSE's versus look angle in the E and H planes for both the room temperature and hot radome. (4) Missile dynamic performance predictions were made considering the effect of the hot radome BSE's and these results were compared to flight test data. This paper will report on Phases 2, 3 and 4 giving the principal results obtained in each phase without going into the detailed analysis procedures. These procedures are reported in other papers elsewhere in these proceedings.

Discussion

The guidance system requirements for the radome considered in this study place a stringent restriction on the allowable radome BSE's. For this reason each radome is prescription ground by the radome fabricator and then "tuned" in an anechoic chamber prior to installation on the missile airframe. Following this tedious procedure, a complete boresight error map of the radome is prepared. Measurements of BSE versus look angle are made at every 22.5° around the axis of the radome. Thus, a full microwave performance definition of the radome is documented before it is flown.

A sketch of the particular radome considered in this study is shown in Fig. 1. The tuning is accomplished by placing layers of a special fiber glass tape with mastic circumferentially around the inside surface as indicated in the figure. Also, 2" wide strips oriented along a meridian were located in the areas shown. To analytically model the radome and tape required the comprehensive breakup shown in Fig. 1. Twelve axial sections were considered and each section was divided into a variable number of circumferential sectors. The sectors were chosen according to the wall thickness and number of tape layers. As noted in the figure,

each sector was divided into as many as nine elements composed of two fortification layers (one on each side of the wall), six dense Pyroceram elements and one correction tape element, as required. Variations in the wall thickness were accounted for in the dense Pyroceram elements. The final dielectric model of the radome consisted of a total number of 700 individual elements.

At one point during this study, the elevated temperature adhesive qualities of the correcting tape were questioned. A simple peal test was carried out on a small piece of Pyroceram exposed to simulated flight temperatures. The test consisted of hanging a 20 gram weight from a loose edge of tape stuck to the back side of the Pyroceram test section. This section was heated by quartz heat lamps to a maximum hot surface temperature of $670°F$. Observations of the tape during the test showed that it did not pull loose. The only degradation noted was a slight discoloration of the tape which is undoubtedly a reaction in the adhesive caused by the elevated temperature.

The altitude and velocity histories of the flight test vehicle were used to predict the aerodynamic heating and resulting temperatures throughout the radome using the method described in Ref. 1. Also, a companion paper in these proceedings (Ref. 2) describes the use of the computer code to obtain radome performance data. Since the time of most interest was during the terminal homing phase of the missile flight, the temperatures at a time near the mid point of this phase were noted. For these temperatures, the dielectric constant (ϵ), loss tangent (δ) and element thickness (considering thermal expansion and thermal stress restraint) were defined for all 700 elements.

Some typical results of the thermal analysis are shown in Figs. 2 and 3. Fig. 2 presents the temperature distribution, ϵ and δ through the wall for section 12 at a time during the terminal phase of flight. Note the highest temperature is at the inner surface which is due to the radome cooling at this time in the missile flight. Also, note the variation in ϵ from the room temperature value which, when combined with the wall thickness change, (for this section, the total wall thickness increase was 0.0008") causes a change in the electrical wall thickness which affects the radome microwave performance. Longitudinal variations in the radome wall temperature may have a larger effect on BSE than temperature changes that are uniform over the entire radome. Fig. 3 shows the radome external surface longitudinal temperature variation at a time during the terminal phase. Note the lower temperatures on the aft part of the radome, which is due to the lower angle of incidence to the air stream and the thickening boundary layer.

Prior to carrying out the boresight error calculations, several characteristics of the radome wall had to be determined. Even though the number of layers of glass tape were known, its thickness and dielectric constant were not known. A series of tests and calculations were carried out to determine the best values to use. Insertion phase delay (IPD) was measured on one to thirteen layers of tape using a microwave interferometer at normal incidence. Flat panel calculations were made for several thicknesses and dielectric constant combinations centered about the approximate values estimated for the tape. These calculations included cases where the tape layers were separated by a thin layer of air as might be the case for the glue layer with a dielectric constant of 1.0. When the calculated results were compared with the measured IPD values, a good match was obtained for a tape thickness of 0.007 and dielectric constant of 3.1 with no air gaps.

46

The Pyroceram 9606 radomes are structurally improved by a fortification process which results in the surface (both inside and outside) layers being somewhat porous. The thickness of these layers can vary from .005" to .020". Based on observations made by a dye drop test and microscopic examination of broken radome pieces, the fortification layer thickness was chosen as 0.010" for both the inside and outside layers. To obtain the dielectric constant of the fortified layers, exact calculations of IPD were made for flat sheets using a three layer model and taking the dielectric constant of the unfortified Pyroceram 9606 at 5.575. The dielectric constant of the fortified layers was theoretically varied until a match was obtained with an IPD of 131.9 degrees which was measured for parallel polarization on the flight radome. Good agreement was found when the dielectric constant of the fortified layers was assumed to be 4.60.

In-plane boresight error calculations were carried out for both the room temperature radome and the hot radome. The primary method of calculation used was the direct ray method; however, errors for the room temperature radome were also computed using the surface integration method. Discussion of these methods and evaluation of their accuracy is reported in another paper in these proceedings (Ref. 3).

All of the boresight error data is presented in Fig. 4. This figure is somewhat cluttered but study of the various curves on a comparative basis will allow the reader to better understand these results. As may be noted from the solid lines, the measured data shows the radome to be of very low errors which makes accurate prediction of such errors difficult. On a percent basis, the predicted room temperature BSE's are not in good agreement with those measured. When the surface integration method was used (this method samples the incoming wavefront over an area for each point on the antenna) to compute these BSE's, no better correlation to the measured data was obtained. The multiple changes of sign in the measured BSE slope suggests the presence of surface wave phenomena which were not treated in the computer simulation. A search was made for reflected rays in the test set-up, but none were located.

The analytical model of the hot radome was used to calculate the dashed curves shown in Fig. 4. Comparing these results to the calculated room temperature values, it may be seen that little effect is experienced in the H-plane but rather large changes in BSE occur in the E-plane. This amount of change is somewhat surprising when one considers the small change in ϵ and δ noted in Fig. 2. Since there was a large percentage difference between the measured and predicted room temperature BSE's, an adjustment was made to the predicted hot radome BSE's. To obtain the adjusted elevated temperature values shown in Fig. 4, the difference between the predicted room temperature and elevated temperature BSE's was added to or subtracted from the measured room temperature values. These data were then used in the dynamic analysis reported on next.

As mentioned previously, a specific missile flight test has been considered throughout this analytical study program. A portion of this missile's terminal guidance phase exhibited oscillations of the guidance command and response functions. Fig. 5 shows the single plane acceleration command profile as recorded for this flight. Here the dependent variable is presented as the time from start of the terminal phase of flight. Until 16 sec. the missile's guidance computer had a Roll-Yaw-Pitch (RYP) limiter which restricted

the command accelerations. Also, a 4 sec. guidance filter was removed at 8 sec. which allowed the oscillation to start. In the 16 to 18 sec. period the oscillation diminished but when it started building up again, it was no longer limited to the RYP limit value. In this final period prior to intercept, the accelerations built up to a substantial level.

A digital simulation has been developed which contains a three-dimensional, six degree-of-freedom representation of the rigid body characteristics of the missile under study. Specifically, the simulation contains 3-D aerodynamics, terminal homing guidance equations, a model of the autopilot, a model of the seekerhead and track loop including radome induced error and a maneuvering point mass target. A discussion of a generalized version of the simulation used in this study is given in Ref. 4 and a companion paper (Ref. 5) in these proceedings describes some general results obtained from exercising this computer code.

Even though the flight results presented above were for a single plane, the oscillatory motion of the missile was not confined to a plane but rather a coning motion. Hence, the look angle did not lie totally in either the E or H-plane but varied between these two directions. For this reason it was necessary to model the heated radome BSE's over the entire radome surface. Since data were available in only the E and H-planes, an approximation was made to describe the errors over the entire radome. Using the adjusted hot radome BSE values calculated for the E and H-planes and the room temperature BSE's measured at every 22.5° around the radome, an algorithm was empirically derived for in-plane errors of the entire hot radome.

$$\epsilon_I = \epsilon_{I-RT} + 0.127 \left(e^{-0.14\beta_T} - e^{-0.28\beta_T} \right) \left[1 + 2 \cos(2\Phi) \right]$$

where:

ϵ_I = Hot radome BSE at β_T and Φ

ϵ_{I-RT} = Room Temperature Radome BSE at β_T and Φ

β_T = $\tan^{-1} \left[\left(\tan^2\beta_A + \tan^2\beta_B \right)^{\frac{1}{2}} \right]$ = Seeker look angle

β_A & β_B = Seeker look angle in A and B planes

Φ = $\tan^{-1} \left(\dfrac{\tan \beta_B}{\tan \beta_A} \right) + 315°$

This approximation of the hot radome errors gives good agreement with the adjusted values shown in Fig. 4 for the E and H-planes. Also, the assumption was made that the cross plane BSE's of the hot radome were the same as those measured for the room temperature radome.

With the above radome model and with the simulation initialized so that it would follow the missiles terminal homing trajectory, calculations were carried out of the guidance computer output acceleration commands. The results for the A-plane are shown overlayed on the flight measurements in Fig. 5. Since the oscillation did not decrease in the simulation between 16 and 18 sec. to allow the RYP limit to be removed, this limit was removed artifically in the simulation at 19 sec. The decrease in the oscillation

48

observed during flight may have been due to a detail on the radome error surface which was not modeled by the algorithm. Considering the complexity of the entire calculation process, the simulation results are in reasonable agreement with those measured. These results point to the heated radome boresight errors as the explanation for the noted flight oscillations and raise a flag to indicate the need for further study of this potential problem.

Conclusions and Recommendation

A three part study has been performed to analytically define an aerodynamically heated radome, compute the boresight error change resulting from heating the radome and finally, calculate the dynamic response of a homing missile resulting from the increased boresight errors. The results of this study were found to agree quite well with measured acceleration command data taken during a flight test. Since good agreement was obtained between prediction and flight data, it could be concluded that an analysis procedure is in hand to predict the effect of aerodynamically heated radomes on flight performance. The writers feel that there are several questionable areas in the procedures however and a strong recommendation is made to perform ground tests to generate experimental data for evaluating the predictive methods used in this study.

Undoubtedly, the most important conclusion to be derived from this work is that there is likely to be a hot radome problem for high speed missiles that have a tight BSE requirement (i.e. homing missiles whose primary mission is to kill supersonic high altitude targets). Little consideration has been given to this problem in the past but with missiles flying at higher speeds, provision will be necessary to account for radome characteristic changes resulting from aerodynamic heating. Most likely, new radome correction procedures will have to be developed to account for changes in BSE in flight.

References

1. R. K. Frazer, "URLIM - A Unified Radome Limitations Computer Program, Vol. 1 - Theoretical Background", APL/JHU TG-1293A, July 1976.

2. R. K. Frazer, "Use of the URLIM Computer Program for Radome Analysis", Proceedings of the 14th EM Window Symposium held at Georgia Institute of Technology, June 21-23, 1978.

3. R. A. Hayward, E. L. Rope and G. Tricoles, "Accuracy of Two Methods for Numerical Analysis of Radome Electromagnetic Effects", Proceedings of the 14th EM Window Symposium, June 21-23, 1978.

4. P. J. Voss and B. E. Kuehne, "Stochastic Missile Simulation Development at the Applied Physics Laboratory of the Johns Hopkins University", 9th Annual Pittsburgh Conference on Modeling and Simulation, Pittsburgh, Pa., April 28, 1978.

5. B. E. Kuehne and D. J. Yost, "When are Boresight Error Slopes Excessive?", Proceedings of the 14th EM Window Symposium, June 21-23, 1978.
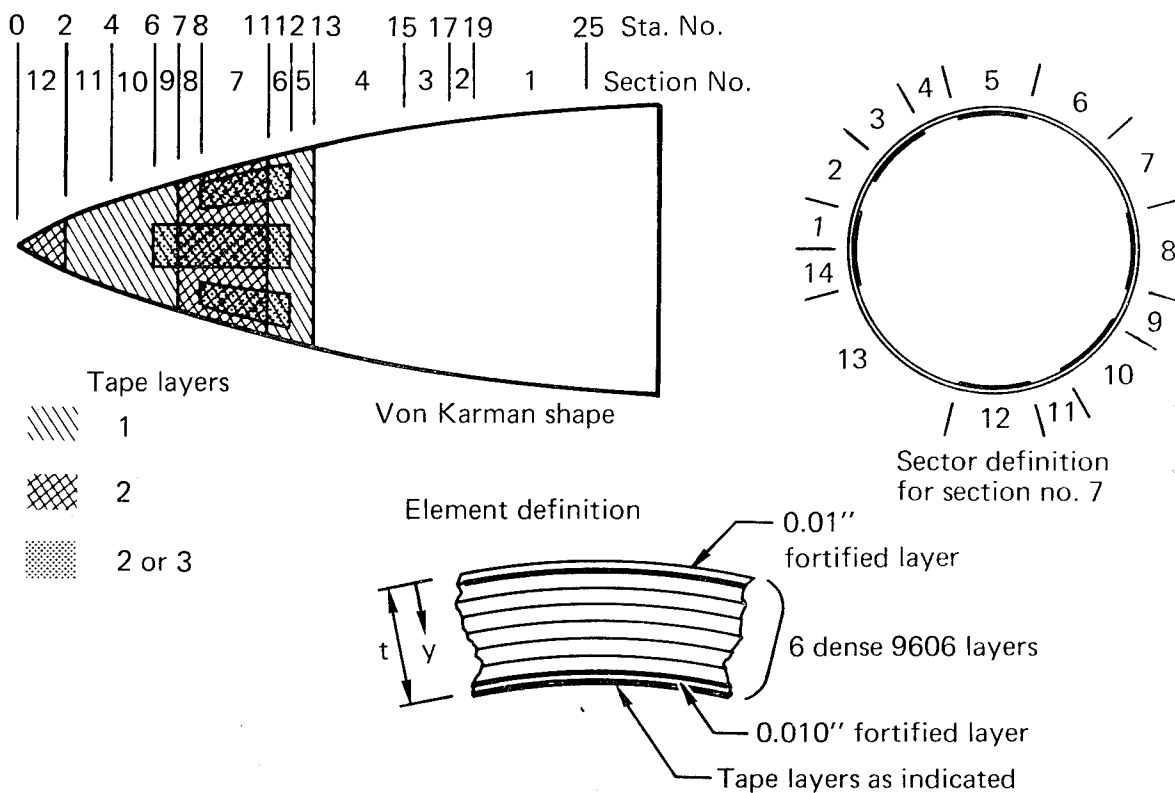
Fig. 1 Pyroceram 9606 Radome Considered in Study
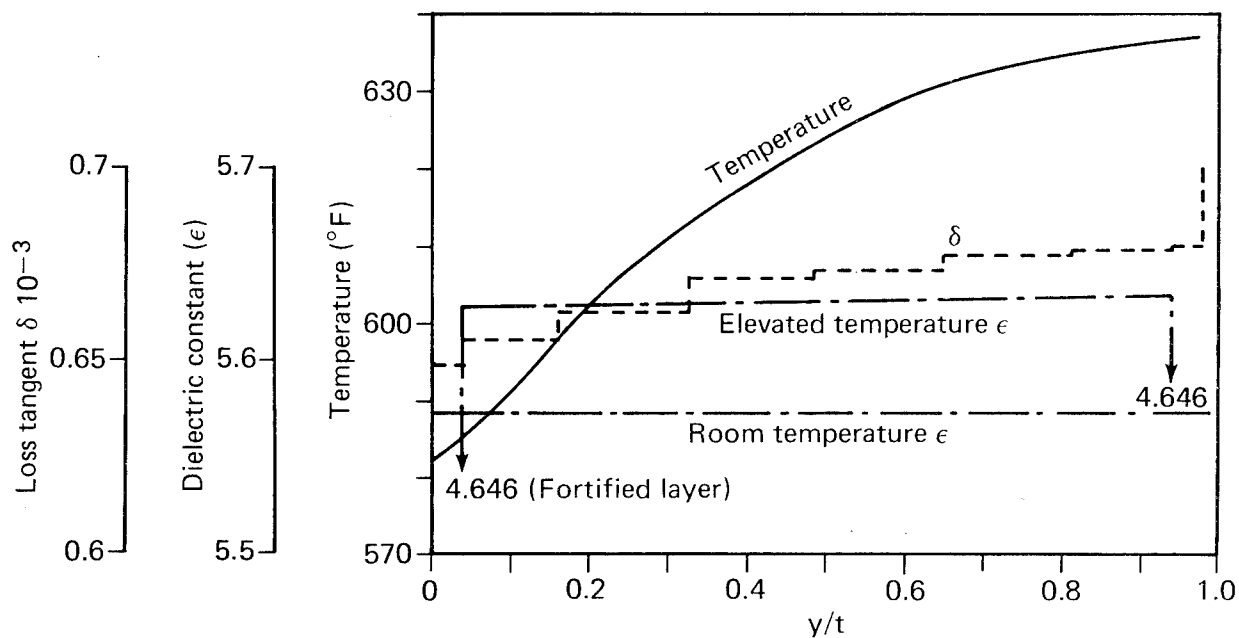
Fig. 2 Temperature, Dielectric Constant and Loss Tangent Variation Through Radome Wall at Section 12

50
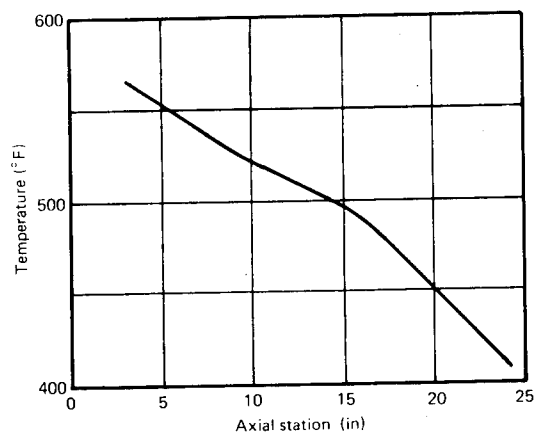
Fig. 3   External Surface Temperature versus Axial Station
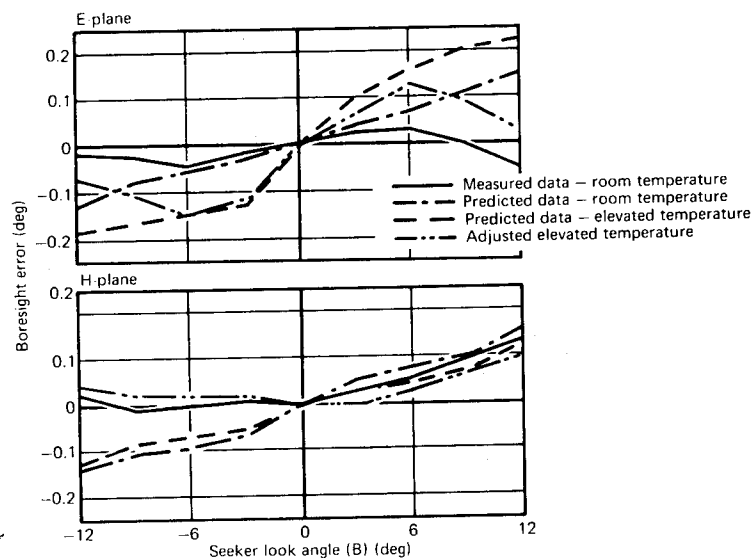
Fig. 4   In Plane Boresight Error versus Look Angle Predictions and Measurements
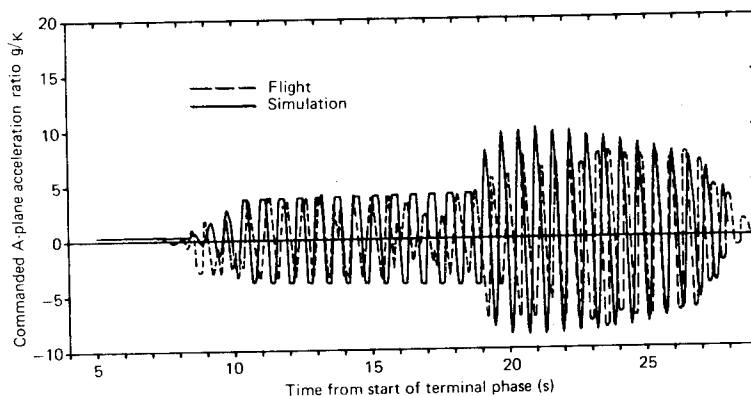
Fig. 5   Measured Flight Accelerations Compared to Prediction

51

ACCURACY OF TWO METHODS FOR NUMERICAL ANALYSIS OF RADOME ELECTROMAGNETIC EFFECTS

R. A. Hayward, E. L. Rope, and G. Tricoles

General Dynamics Electronics Division
P. O. Box 81127
San Diego, CA 92138

INTRODUCTION

Although several methods have been developed for radome analysis, results for most methods have been compared with measured data for only a restricted range of the variables that influence numerical predictions.[1-8] The variables are the size, shape, thickness, and constitutive parameters of the radome; the size, aperture distribution, and polarization of the antenna enclosed by the radome; the position and orientation of the antenna; and the wave frequency. The large number of variables means that a comprehensive evaluation of accuracy is an extensive task. Further, a numerical method must predict several quantities, namely transmittance, antenna sidelobe levels, and the components of boresight error.

This paper summarizes an evaluation of two numerical methods. Both methods assume receiving operation, and compute the farfield patterns of the enclosed antennas. Boresight error is obtained from the patterns as the shift that a radome causes in the direction of a tracking null, and transmittance is intensity reduction at the beam maximum. Sidelobe levels are the levels of subsidiary maxima of the patterns.

Computations and measured data are given for three ceramic radomes with the dimensions and configurations shown in Figure 1. All radomes had Von Karman shapes; their thicknesses were approximately a half wave length. Each radome was utilized with its own antenna; diameters were appropriate to each radome. Boresight error data are presented, and phase data inside radome-bounded regions are given as a diagnostic quantity that reveals sources of inaccuracy.

THEORY

Both methods compute patterns in two steps. The first step is computation of the complex-valued field in the radome bounded region for a plane wave, externally incident in an arbitrary but fixed direction. The data describe the wavefront propagated through the radome. The second step is integrating the wavefront data over the antenna. For a scalar field component u we represent the received amplitude as

$$u = \int T u^I F \, dA \qquad (1)$$

where u^I is the incident plane wave function; T is the complex valued transmittance, and F is the receiving nearfield distribution of the antenna. The integration extends over the region for which F has appreciable magnitude.

The two methods differ in the computation of T. One method is relatively simple; it is illustrated in Figure 2a. A single ray describes the field at each point of the aperture. This ray has phase and amplitude determined by a flat sheet tangent to the radome where the incident ray through the aperture point intersects the radome. Thus, the ray is the sum of multiple internal reflections, those for a flat sheet that locally approximates the radome. The approximating sheets depend on position, and they also depend on the direction of the incident wave.

The second method utilizes a surface integration over the incident wavefront to compute T; see Figure 2B. This method also approximates the radome locally with flat sheets.

The aperture distribution F is determined by processing phase and intensity data measured in the nearfield of the antenna. An open-end waveguide scans a plane that is a few wavelengths from antenna. The separation reduces scattering between the probe and the antenna; it also reduces the sampling interval because evanescent waves are negligible. The measured data are Fourier transformed, and the transform is propagated to the aperture plane, where the inverse transform gives the aperture field. This backward propagation technique is necessary because the distribution F must fit within the radome, even for non-zero gimbal angles, which are ϕ and θ in Figure 3.

COMPUTED AND MEASURED DATA

This section gives some typical data. Figure 4 shows in-plane error computed by the direct ray method for Radome 1 of Figure 1. The calculations were done first with an experimentally determined aperture distribution, and additional calculations were done with a distribution that had uniform amplitude but phase reversal on opposite halves. It is clear that the measured distribution gives smaller discrepancies between theoretical and measured boresight error.

Figure 5 shows in-plane boresight error for the smallest radome, Radome 3. Calculations are given for both the direct ray and the surface integration method. It is clear that the direct ray method fails, but surface integration is accurate. This conclusion agrees with an earlier result obtained for a small antenna by integrating over the radome surface, see Reference 4.

54

To examine the source of discrepancies we measured and computed the phase and intensity in the radome bounded regions. Figure 6 shows a typical result. The data are for Radome 2. It is clear that the surface integration is more accurate than the direct ray method.

ACKNOWLEDGMENT

REFERENCES

1. O. J. Snow, U. S. Naval Air Development Center Report No. EL 5108, 13 Nov. 1951.

2. G. Tricoles, J. Opt. Soc. Am., 53 pp 545-557 (1963); 54 pp 1094-1101 (1964).

3. N. R. Kilcoyne, The Ohio State University Electro Science Lab Report 4767-2, 2 Oct. 1969.

4. E. L. Rope and G. Tricoles "The Fresnel-Kirchoff Formula as a Basis for Radome Design", Georgia Institute of Technology, Proceedings Electromagnetic Window Symposium, 1968.

5. D. T. Paris, IEEE Trans., AP-22, pp 7-15 (1970).

6. D. C. F. Wu and R. C. Rudduck, Digest 1971 G-AP Symposium p 157; see also IEEE Trans. AP-22, pp 497-500 (1974).

7. R. A. Hayward and G. Tricoles, Digest 1975, AP-S Symposium, pp 61-63, (1975).

8. R. A. Hayward, E. L. Rope and G. Tricoles, Digest 1977, AP-S Symposium, pp 1-4 (1977).

RADOME 1

● DENOTES GIMBAL POINT

2

RADOME	LENGTH	DIA. AT BASE
1	24.14 λ_0	11.55 λ_0
2	14.17 λ_0	6.73 λ_0
3	10.64 λ_0	4.73 λ_0

3
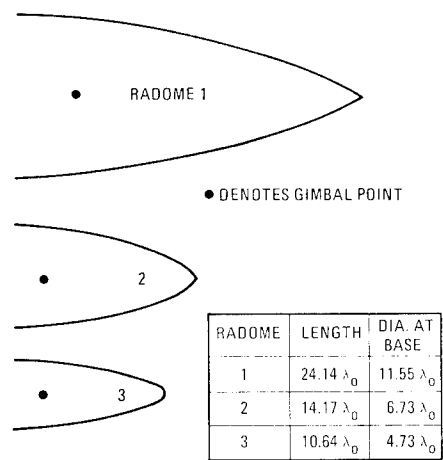
Figure 1. Three Radome Configurations. All radomes had dielectric constant value 5.55.

A. DIRECT RAY METHOD

B. SURFACE INTEGRATION
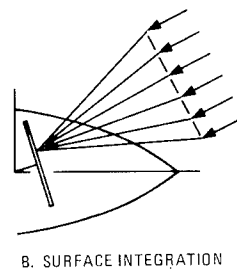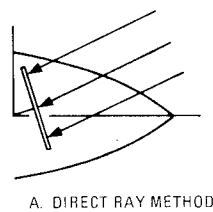
Figure 2. Two Methods for Computing Transmittance

Z_A

Z_R

INCIDENT RAYS

X_A

ϕ_R

ϕ

X_R

$P_A (X'_A, Y'_A, Z'_A)$

$P_R (X'_R, Y'_R, Z'_R)$
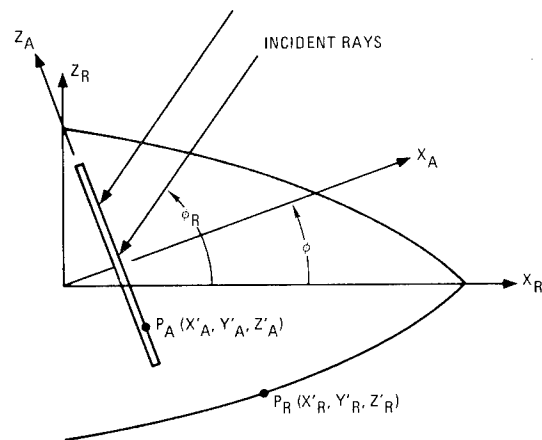
Figure 3. Co-ordinate System

56
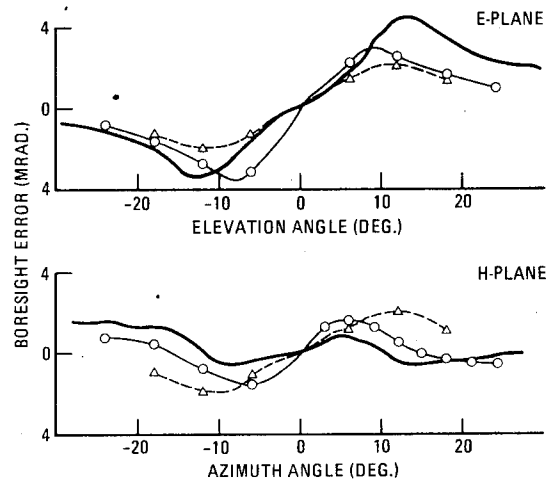
Figure 4. Inplane Boresight Error, Radome 1 Measured (—); Computed, Uniform Aperture Amplitude (△); Computed Measured Aperture Distribution (○).
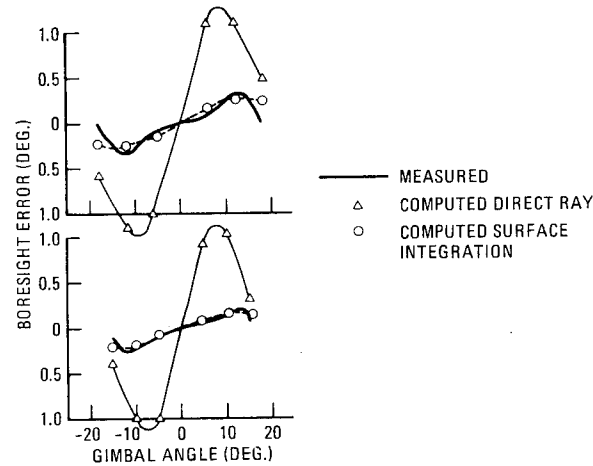
Figure 5. Boresight Error, Radome 3
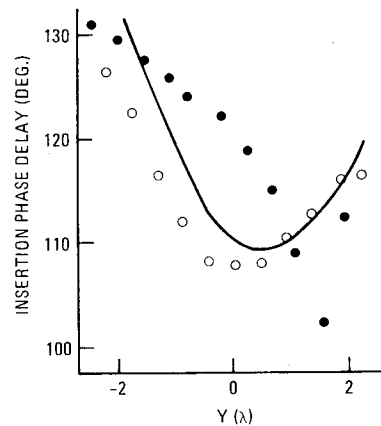
Figure 6. Insertion Phase Delay of Radome 2. Horizontal Polarization, Measured (—); Direct Ray Calculation (●); Surface Integration (○).

WHEN ARE BORESIGHT ERROR SLOPES EXCESSIVE?

B. E. Kuehne and D. J. Yost

The Johns Hopkins University
Applied Physics Laboratory
Laurel, Maryland 20810

INTRODUCTION

For at least two decades a fundamental consideration for designers of homing missile guidance systems has been that of establishing boresight error (line-of-sight tracking error) requirements. Due to the functional dependence of this error on the seeker look angle, an undesirable feedback path is closed about the missile guidance loop, with the resulting feedback gain equal to the slope of the boresight error with respect to look angle. The missile guidance system response characteristics are effected, and if the magnitude of the boresight error slope is large enough, an oscillatory guidance system instability can result.

The question that must be addressed during missile guidance system design is: When are boresight error slopes too large for effective target engagement? Many design criteria have been employed in the past in attempts to provide answers to that question, however most were based on small signal stability characteristics of the missile guidance system. As will be shown, this traditional approach to the problem has severe limitations when applied to many future missile systems. Hence, a more viable approach to setting boresight error slope requirements must be found.

TRADITIONAL APPROACH TO BORESIGHT ERROR COMPENSATION

The traditional philosophy behind compensation for the boresight errors associated with narrowband radomes is generally to assure that the missile guidance system will be stable over the entire range of expected in-flight boresight error slopes. Two avenues of approach are used to accomplish this goal. First, extensive tailoring (e.g., prescription grinding, etc.) of the radome is performed during fabrication to reduce boresight error slopes as much as is reasonably possible. Using current radome fabrication technology, boresight errors for a narrowband radome can be reduced to quite small values, even if the radome is highly streamlined. Figure 1 illustrates the boresight errors associated with the tailored narrowband radome of a typical high performance surface-to-air missile. Note that boresight error slopes are less than .02 degrees/degree.

Second, the missile's guidance filtering is adjusted to stabilize the missile guidance system with respect to the residual boresight error slopes (in this case, those of .02 degrees/degree or less). There are several parameters which impact the missile stability region. The principal ones are the aerodynamic lift per degree angle-of-attack, the control moment per degree tail deflection (both characteristics of the missile aerodynamic configuration, and hence highly dependent on dynamic pressure), the missile guidance gain (which is a function of the missile/target closing velocity), and the missile guidance system time constant. However, of these parameters only the guidance filter time constant can be somewhat arbitrarily varied for the purpose of boresight error compensation. Generally as this time constant is increased, the size of the missile stability region also increases.

In addition, the guidance filtering is often designed to be a function of dynamic pressure and closing velocity to counteract changes in the other three principal parameters influencing missile stability with respect to boresight errors.

Guaranteeing missile stability by increasing guidance filtering has been a satisfactory approach to boresight error compensation in previous missile designs. However, future mission requirements may cause this design philosophy to be taxed beyond its limits. For instance, several surface-to-air missiles have been proposed with the capability of passively homing on more than one RF frequency. Current radome tailoring techniques lose their effectiveness when the radome is not tailored for a specific frequency. Hence, multiband or broadband radomes typically have boresight error slopes substantially larger than those associated with present state-of-the-art narrowband radomes. As a second example, the current trend for future moderate and long range homing missiles has been toward increased velocities. However, high missile velocities cause increased radome temperatures due to aerodynamic heating. Large in-flight changes in the radome temperature can cause substantial detuning of the radome, negating to a great extent the effects of pre-flight radome tailoring. This effect has even been observed with near term, lower velocity missiles (see for example, Reference (1)).

Increasing guidance filtering to assure stability in the presence of these increased boresight error slopes decreases missile responsiveness, hence decreasing missile effectiveness. Consequently, the traditional design philosophy for boresight errors results in a paradox. To guarantee missile stability for the increased boresight error slopes associated with future missions requires a considerable increase in guidance filtering; but successful intercept of future high altitude, high performance air targets precludes any significant increase in missile time constant.

INADEQUACY OF THE SMALL SIGNAL STABILITY ANALYSIS

Figure 2 illustrates the boresight error surface for a typical narrowband radome. Shown is the component of the boresight error resulting from resolving the error along one of the missile's two orthogonal control planes. The center of the surface coincides with the centerline of the radome, and the surface extends outward to approximately 36° in look angle. An alternate representation of the same data is shown in Figure 3, where the data is plotted as a contour plot. Lines of constant boresight error are drawn over the radome surface. Again, the radome centerline passes through the center of the figure.

It should be clear from these figures that the regions of high boresight error slopes do not extend over large sections of the radome but rather are confined to small regions of the error surface. For instance, with the large slopes occurring in the center-right of Figure 3 (around $\beta_p = -15$, $\beta_y = 0$), the various established slopes extend over less than 10° in look angle. This type of characteristic is represented in Figure 4a, which shows a single plane cut from a hypothetical boresight error surface. Note that in the vicinity of the look angle labeled β_o, the boresight error slope is .1 degrees/degree. If such a slope were expected in flight, missile guidance system designers employing the traditional approach to boresight error compensation would increase guidance filtering during missile design to assure stability in the presence of a slope of .1 degrees/degree. However let us assume for the moment that the guidance system designer did not want to incur

the general penalty in missile response time resulting from such an increase
in guidance filtering. Consequently he sets the guidance filtering only high
enough to assure missile stability for slopes of .03 degrees/degree or less.
With this design approach, if the .1 degrees/degree slope at β_0 is encountered
during flight, the missile guidance system will indeed become unstable and the
missile will begin to develop an increasingly oscillatory motion. However, as
the oscillation in look angle continues to grow, an amplitude will be reached
at which the average boresight error slope impacting the missile guidance
system is only .03 degrees/degree, as is illustrated in Figure 4b. Any fur-
ther increase in the oscillation amplitude causes the average slope to be less
than the unstable value of .03 degrees/degree and hence the oscillation de-
creases until the average slope is .03 degrees/degree again. Consequently,
a stable limit cycling motion occurs, and the oscillation does not continue
to grow, but becomes bounded. In addition, the frequency of the oscillation
is often high, or due to changing missile/target geometry the look angle is
only in unstable slope regions for a short time, so that consequently little
or no actual trajectory deviation may occur due to the bounded oscillation.
If the slope were negative rather than the positive slope assumed here, the
frequency of the instability would be lower, resulting in a much larger traj-
ectory deviation for a given oscillation amplitude. However, even though tol-
erance to a low frequency instability is reduced, averaging effects still apply.

This averaging effect could be analyzed more quantitatively through
the use of describing function analysis, but that is not the intent of the
present discussion. What is important is the idea that look angle magnitude
and direction variations, as well as any rapid time variations in the error
occurring due to in-flight changes in the radome environment, can lead to an
averaging of the boresight errors perceived by the missile. And even if an
instability does occur, the resulting oscillation, since it is bounded, does
not necessarily result in a catastrophic performance degradation. These ef-
fects should be taken into account when setting boresight error slope re-
quirements.

EXAMPLES ILLUSTRATING THE CONCEPT
Two examples will be discussed that illustrate how the traditional
philosophy concerning what constitute excessive boresight error slopes results
in overly stringent boresight error requirements. Both of these examples
present data generated with a digital simulation of a typical high performance
surface-to-air missile. The simulation which was used contains a detailed
three dimensional, six degree-of-freedom representation of the rigid body
characteristics of the missile, along with its control loops, during the
terminal homing portion of flight. Except for the presence of the boresight
error, the missile is assumed to be operating in a noise-free environment.
The autopilot, guidance computer, and seeker models contained in the simula-
tion are of course dynamically valid over a frequency range sufficient to
accurately model any instability due to excessive boresight error slopes.
Since averaging of the boresight error is an important consideration, accur-
ate models representing entire boresight error surfaces were implemented in
the simulation.

As a first example, the error shown on Figures 2 and 3, along with
its companion orthogonal component, was increased by a factor of four and
implemented in the simulation. Performance runs were made against medium
altitude, constant velocity targets. The missile/target relative geometry
was varied to exercise various high positive and negative slope regions of
the radome. For the set of runs simulated, the boresight error slope over

look angle regions of approximately 8° was on the average nearly four times greater than the largest value permissible for stability. However the largest miss distance simulated was still within the performance specification for the missile in question, and the average miss was well within the required specification. This was in spite of the fact that bounded oscillations occurred due to the large boresight error slopes encountered. In addition, it should be noted that the oscillation amplitude often decreased during a given simulation run when missile motion caused by the effects of the oscillation resulted in the look angle leaving the region of the large slopes.

As a second example, a surface representation of the boresight error data from Reference (1), in which aerodynamic heating of the radome caused the error slopes to increase to 2-1/2 times the maximum values for stability, was implemented in the simulation. Performance runs were simulated both with this heated radome model and with no boresight error against medium and high altitude weaving targets. Though the increased boresight errors resulting from radome heating caused a guidance system instability, the peak miss distance against these highly maneuvering targets typically increased by less than 30% when the heated radome model was included in the simulation.

The boresight error slopes simulated in both of these examples are clearly "excessive" in the context of the traditional approach to boresight errors and the required guidance system compensation. And yet, boresight error slopes were increased over present requirements by factors of from 2 to 4 without serious degradation in missile homing performance, raising the suspicion that the traditional concept of "excessive" boresight error slopes is substantially more stringent than necessary. Present boresight error requirements used in missile design could be relaxed considerably if requirements were to result from a criterion based on performance rather than the classical stability criterion. However, in developing such a set of requirements, the accurate modeling of representative boresight errors over the surface of the radome is a critical element that must be considered.

SUMMARY

Boresight error slopes associated with future surface-to-air missiles with multiband or broadband radomes will be substantially larger than those of current narrowband radomes. In addition in-flight errors may be larger than expected even for narrowband radomes due to aerodynamic heating. However, this paper has presented evidence that missile instability due to these large slopes may not necessarily result in significant performance degradation if the large slopes are confined to small regions of the radome. Consequently, missile boresight error requirements should not be based on a criterion of stability but rather on one of maintaining a given level of performance.

REFERENCE

(1) L. B. Weckesser, R. K. Frazer, D. J. Yost, B. E. Kuehne, G. B. Tricoles, and R. Hayward, "Aerodynamic Heating Effects on Radome Boresight Errors", Preceedings of the 14th Symposium on EM Windows, June, 1978.

Figure 1

63
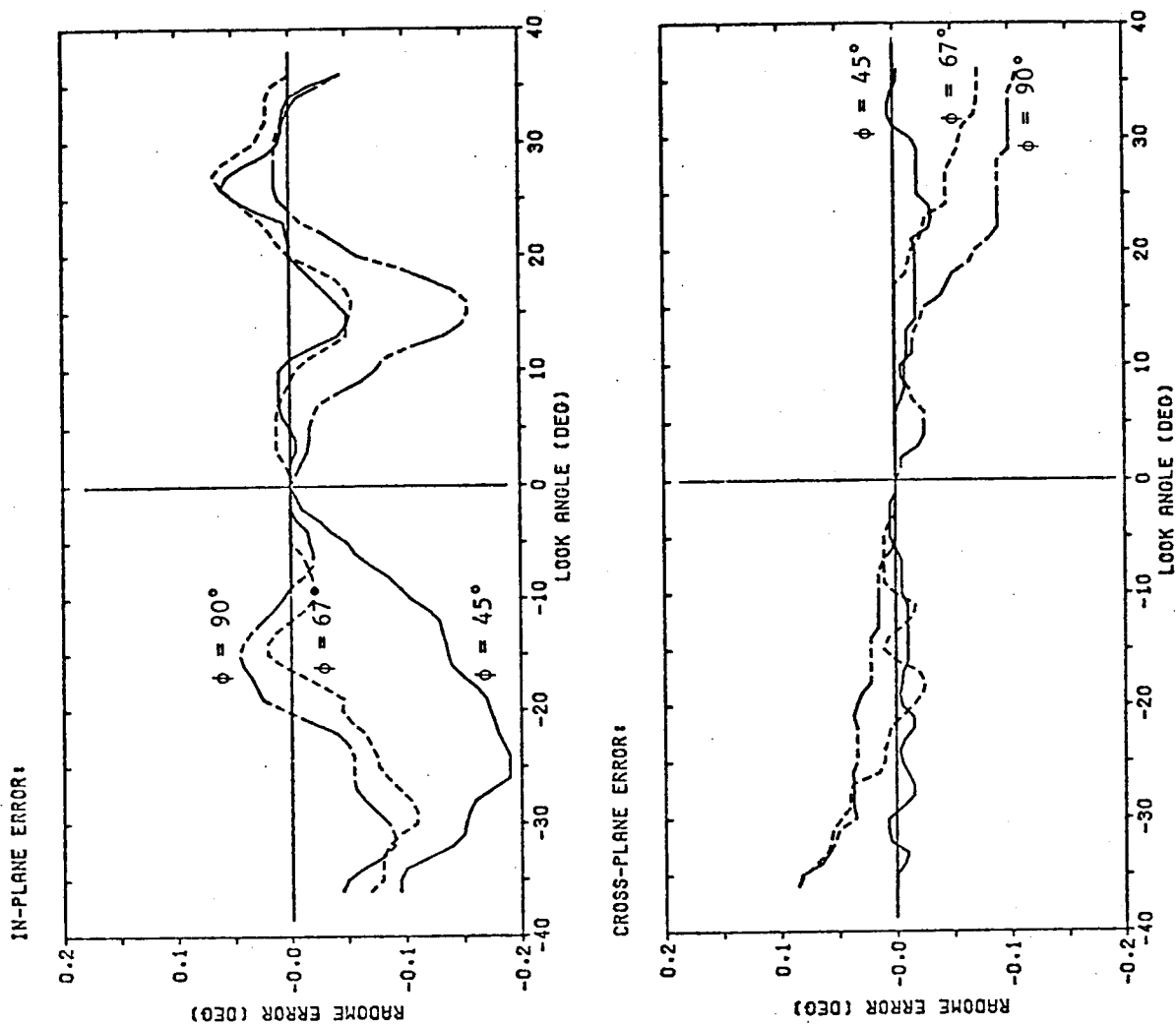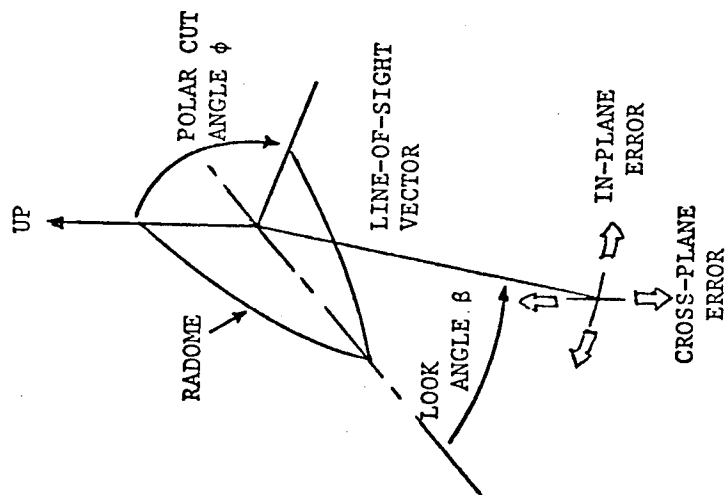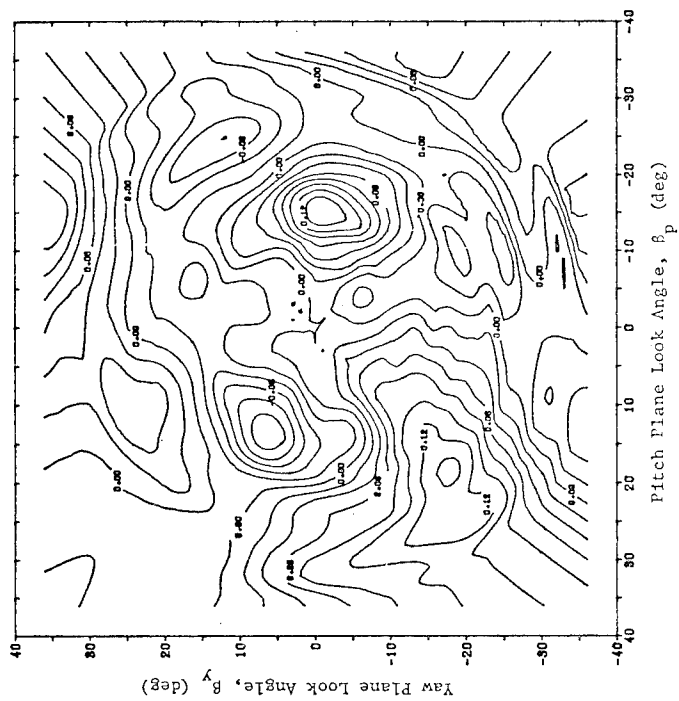
Figure 3: PITCH PLANE COMPONENT OF BORESIGHT ERROR
(Contour Plot Representation)

Figure 4a: RADOME WITH LARGE BORESIGHT ERRORS
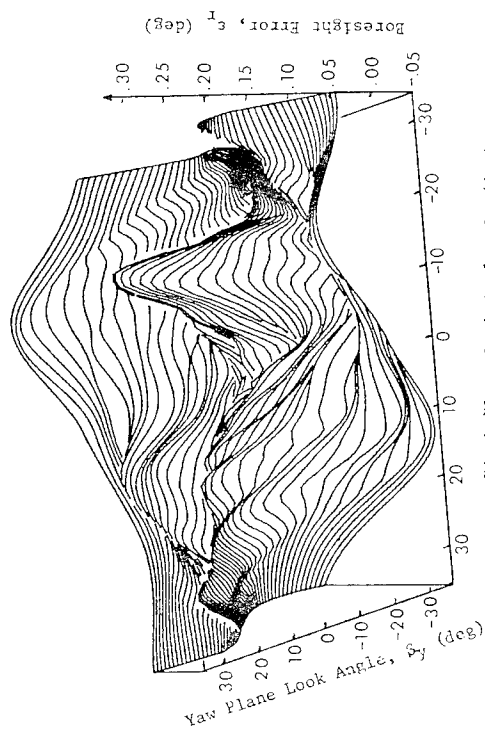
Figure 2: PITCH PLANE COMPONENT OF BORESIGHT ERROR
(3-Dimensional Plot Representation)
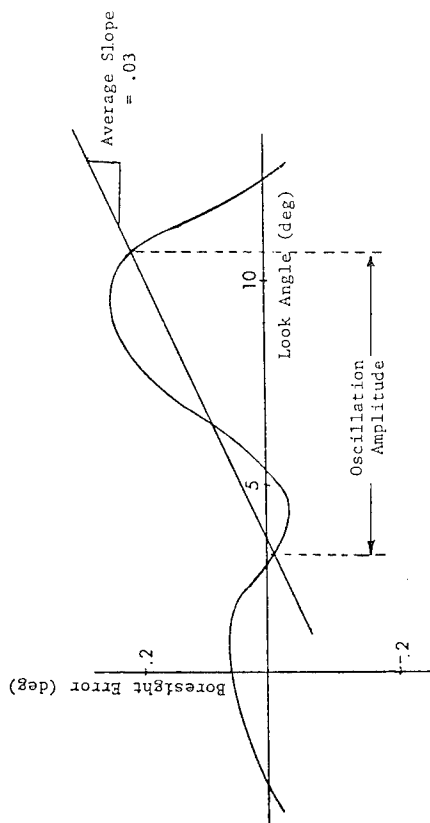
Figure 4b: AVERAGING OF LARGE BORESIGHT ERRORS

Use of the URLIM Computer Program
for Radome Analysis

R. K. Frazer
Johns Hopkins University Applied Physics Laboratory
Laurel, Maryland

The Unified Radome Limitation (URLIM) computer program has been described in the two previous Electromagnetic Window Symposia and is fully presented in Ref. 1. The program has been developed over a number of years through the sponsorship of Lionel Pasiuk at the Naval Sea Systems Command. This paper will briefly discuss the general applicability of the URLIM code and then present the highlights of three analyses that used URLIM. These studies include: (1) evaluating the comparative performance of reaction sintered silicon nitride (RSSN), hot pressed silicon nitride (HPSN), and slip cast fused silica (SCFS) when used on two tactical surface-to-air trajectories; (2) estimating the capability of the Arnold Research Organization's APTU wind tunnel to simulate flight-level thermal stresses in Pyroceram 9606; and (3) providing a detailed three-dimensional model of the dielectric properties of a Pyroceram 9606 radome during flight. This latter effort supports an investigation of the adverse effects of aerodynamic heating on radome boresight error slopes and the attendant guidance set performance. This later work is further reported by Weckesser, et. al. in another part of these proceedings (Ref. 2).

Introduction

The URLIM computer program fundamentally solves transient heat transfer problems. It provides a means of numerically modeling three-dimensional structures of arbitrary shape that are subjected to a variety of boundary conditions. Among these boundary conditions is a model of forced convective heating that is used extensively to calculate supersonic aerodynamic heat transfer. These two fundamental capabilities of aerodynamic heating simulation and transient thermal response prediction are used to calculate missile structural temperatures as functions of flight time. In the case of radomes, the URLIM program can calculate thermal stresses, incipient melting, and the dielectric properties of the radome wall as they vary with temperature (i.e. flight time). An added feature of the program is the ability to estimate the bending stresses at the base of the radome due to aerodynamic pressure and maneuver (i.e. inertial) forces. These four secondary radome material responses (thermal stress, melting, dielectric change and maneuver loads) are the primary failure modes associated with radar frequency (RF) electromagnetic windows. All four are calculated by URLIM vs. trajectory time for a given radome material and can thereby be used to estimate the missile's performance boundaries due to the radome material selection. URLIM, when used in this manner, is a valuable analysis tool that can be readily used in the preliminary design of radome/missile systems. The comparative analysis described next is an example of this sort of study.

Radome Material Comparisons

Three materials have recently emerged as leading candidates for high speed (M4 and greater) tactical missile applications. These materials are slip cast fused silica, reaction sintered silicon nitride and hot pressed silicon nitride. While various uncertainties remain about the properties, capabilities, and manufacturability of these materials, sufficient data now exist to make preliminary studies. Table I presents an abstract of the material properties that were used for the evaluations made here. Two trajectories were considered as representative of future tactical surface-to-air missions - the first is the result of applying upgraded propellant technology to existing rocket systems and the second assumes supersonic ramjet propulsion is used.

In order to employ URLIM for this study the trajectory parameters (i.e. velocity and altitude vs. time) must be supplied along with the material properties and geometric specifications of the radome. When these data are used with the URLIM code, results as shown in Figure 1 are obtained. This figure shows a comparative plot of the four materials' thermal stress and boresight error sensitivity parameter. This latter calculated parameter is not the change in boresight error slope for the radome; rather it is a measure of the change in electrical wall thickness of a section of the radome near the nose. Relating this single spot calculation to the boresight error slope changes occurring over the entire radome surface is probably impossible - however, it is felt that comparisons among materials of this parameter will indicate which is most sensitive to boresight errors induced by aerodynamic heating. Figure 1 shows how the four materials compare on the same trajectory - the thermal stresses are normalized to the maximum allowable design stress and the electrical sensitivity parameter again is for comparative purposes only. Both silicon nitride materials are comfortably below their design level stresses while the Pyroceram 9606 shows very little safety margin. Conversely, the HPSN shows the highest sensitivity to changes in electrical performance. Overall, the SCFS material performs best with regard to thermal stress and electrical sensitivity. To fully evaluate the silicon nitride materials would require a more refined boresight error analysis.

For the supersonic burning ramjet flight, extremely high temperatures become the main concern. Figure 2 shows the temperatures experienced on the hypersonic flight for the silicon nitride and SCFS materials. The radome in this case is assumed to be a $9\frac{1}{2}°$ semi-vertex angle cone with a base diameter of 6.75". While melting of the materials would not appear to be a limitation, certainly the seeker and other electronic components that are housed within this radome would need to be protected from the 2200°F radiation environment.

Wind Tunnel Thermal Shock Simulations

An essential part of the full scale development of any weapon system is the testing of prototype production components. In the case of a ceramic radome it must be demonstrated that it can withstand the rigors of flight, that is, endure the thermal stresses generated by rapid aerodynamic heating. The URLIM program was recently used to determine if the APTU facility at the Arnold Research Organization,

66

Tullahoma, Tennessee is capable of generating thermal stresses comparable to those indicated in Fig. 1. The APTU facility has three nozzles that are large enough to provide uniform flow over a full size radome. These are a 38" dia. and 24.8" dia. nozzle operating at M4.1, and a 38" dia. nozzle operating at M2.55. The facility is capable of supplying air to these nozzles at total pressures (P_t) up to 1500 psia and total temperatures (T_t) up to 2900°R. Using this information, five different total temperature values between 1500° and 3000°R and five total pressure values between 100 and 2000 psia were paired in 20 different combinations for the two Mach number nozzles. Each pairing of P_t and T_t would result in a particular flow condition for the radome. It was assumed that the radome could be inserted into this stream in 0.5 sec. The URLIM program was then set up to simulate these 20 different aerodynamic conditions. Each simulation then produced a thermal stress history and, in particular, a maximum thermal stress level. The stress levels were then compared to the expected flight level stress of 17,600 psi and also to levels at 125% and 150% of this value.

Fig. 3 presents a plot of the net results of this study. The figure shows first the P_t and T_t requirements for a M4.1 nozzle to provide thermal stress levels at 100%, 125% and 150% of the design limit. Also shown in comparison to these curves are the APTU facility capabilities for the two M4.1 nozzles. These facility curves assume that the test lasts 30 sec. Inspection of the figure will show that the 24.8" nozzle curve of capability intersects all three requirement curves. Furthermore, the intersection points represent the P_t and T_t combination appropriate for the particular stress level. In fact any point on the three "Requirements" curves that also lies below and to the left of the "Capabilities" curves will be a suitable test condition. It was therefore concluded that the APTU facility was capable of generating flight level as well as 25% and 50% over flight level thermal stresses in this particular full size Pyroceram 9606 radome.

Dielectric Modeling of a Radome During Flight

The paper presented at this meeting by Weckesser et. al. (Ref. 2) discusses an effort to predict the boresight error slopes and attendant missile performance that resulted when a Pyroceram 9606 radome was heated during a flight test. The prediction methods of Hayward (Ref. 3) and Kuehne (Ref. 4) require that the radome be defined electrically over its entire surface. The URLIM program was used to provide this information. The radome in question was a von Karman profile with a base diameter of 13.5" and a 2.1 fineness ratio. The radome was prescription ground and tuned to a very low boresight error characteristic by the selective placement of fiberglass tape segments on the inner wall surface. Figure 1 of the paper by Weckesser shows the precise locations of all the tuning tape. As can be seen in this figure the entire inner surface from the tip of the radome to station 13 was covered with a single tape layer. Two more bands of tape were applied from Sta. 0.0 to Sta. 2.0, and from Sta. 7.0 to Sta. 11.0. Six longitudinal strips 2" wide were also placed as shown. In addition to the tuning tape, the Pyroceram 9606 radome was fortified by a chemical etching process that leaves the inner and outer surface of the radome slightly porous and less likely to have strength

reducing cracks. Dielectrically, this radome is seen as a composite wall of three different materials whose exact dimensions vary radially, circumferentially, and longitudinally. Figure 1 of Ref. 2 also shows how the radome was divided up for computational purposes. There are 12 longitudinal sections each of which is divided into circumferential sectors as required by the tape placements. Each sector is in turn divided into two fortification layers, one tape layer (of the appropriate thickness) and six dense Pyroceram "core" layers. Small variations in the Pyroceram wall thickness as measured by the inspectors of the Corning Glass Works were accounted for in the sector thicknesses as required. Specifying the dielectric properties of this radome then amounts to giving the dielectric constant (ϵ_d), loss tangent (tan δ), and thickness of each element just described. In all, the model contains 700 elements.

The temperature dependent dielectric properties of the dense Pyroceram are given in Figure 4. Weckesser describes procedures that were used to determine the dielectric properties of the fortification layer ($\epsilon_d \cong 4.6$) and tuning tape ($\epsilon_d \approx 3.1$). The thicknesses of these layers are 0.010" and 0.007" respectively (c.f. Fig. 1, Ref. 2). All of these values were used as input to the URLIM program along with the velocity and altitude histories of the test flight. The aerothermal analysis carried out by URLIM had the following assumptions included: (1) the aerodynamic flow and attendant heating is assumed axisymmetric and non-axisymmetric features of the radome (i.e. slight thickness changes and tape placements) do not significantly alter the circumferential symmetry of the temperature distribution; (2) the fortification layers are thin enough so that they behave thermally like the dense Pyroceram; (3) the axial variation in aerodynamic heating can be represented by nine different flow regimes.

Typical thermal and dielectric property results from this study are given briefly in Figs. 2 and 3 of Weckesser's paper and will not be discussed again here. These results were formatted upon output so as to be directly usable by Hayward et. al. in their boresight error predictions. In summary, the URLIM program proved to be invaluable in determining the hundreds of values necessary to properly define the radome. Without a tool like the URLIM code, this level of thoroughness would not have been possible.

Conclusions

The utility of the URLIM program for radome analysis has been demonstrated in this paper by three examples. These examples, while very different in terms of the results provided, were all modeled effectively through the facilities of the URLIM code. Furthermore, the program's usefulness is not restricted to radome technology as shown here but to any structure whose transient thermal response is required.

References

1. R. K. Frazer, "URLIM - A Unified Radome Limitations Computer Program", APL/JHU TG-1293, July 1976.

2. L. B. Weckesser, et. al. "Aerodynamic Heating Effects on Radome Boresight Errors", Proceedings of the 14th EM Window Symposium, Georgia Institute of Technology, Atlanta, Georgia, June 21-23, 1978.

3. R. A. Hayward, E. L. Rope, G. Tricoles, "Accuracy of Two Methods for Numerical Analysis of Radome Electromagnetic Effects, Ibid.

4. B. E. Kuehne, D. J. Yost, "When are Boresight Error Slopes Excessive", Ibid.

Table 1

Radome Material Properties

Material	Elastic Modulus (10^6psi)		Expansion Coefficient (10^{-6}/°F)		Thermal Conductivity (Btu/ft-hr °F)		Dielectric Constant		Loss Tangent		Maximum Use Temp (°R)	Bending Strength (psi)
	RT	1500°F	RT	1500°F	RT	1500°F	RT	1500°F	RT	1500°F		
HPSN ρ=3.2 gm/cc	43.5	43.5	1.77	1.77	12.1	9.0	7.59	8.55	.00275	.0065	3870	58,000
RSSN ρ=2.4	15.0	15.0	1.1	2.05	5.4	4.05	5.56	6.1	0.005(?)	0.005(?)	3870	20,000
SCFS ρ=1.926	8	10	0.45	0.175	0.31	0.40	3.4	3.5	.0014	.003	3600	4,000
Pyroceram 9606 ρ=2.6 gm/cc	16.5	16.8	2.5	3.0	2.2	1.74	5.575	5.805	.0003	.01	2930	22,500
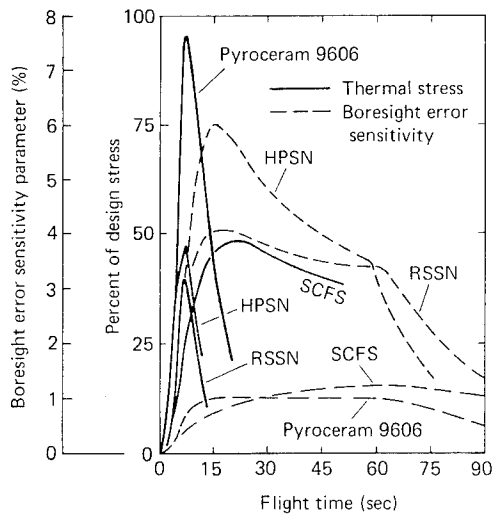
Fig. 1   Radome Material Comparisons for Thermal Stress and
Boresight Error Sensitivity
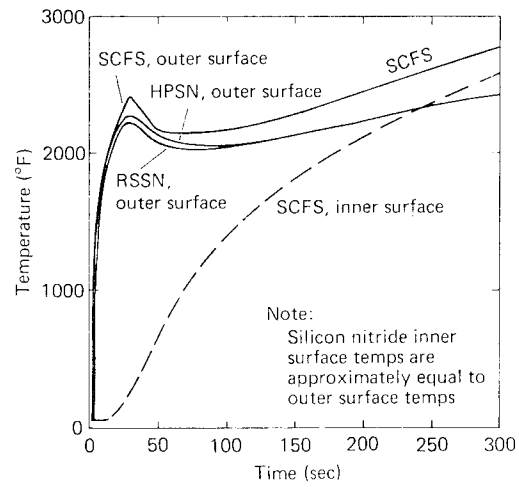
Fig. 2   Wall Temperature Histories Hypersonic Tactical Missile with Ramjet
Propulsion
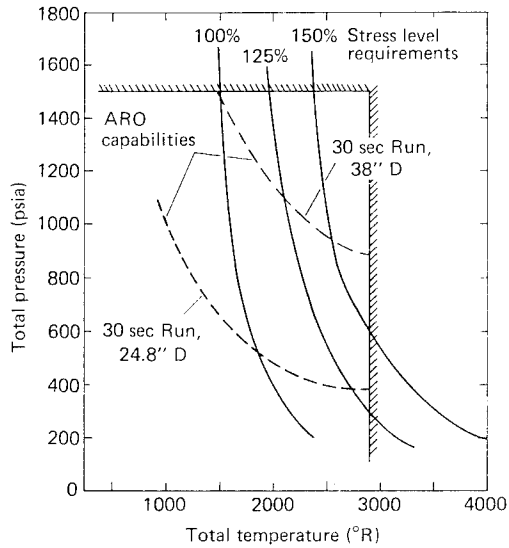
Fig. 3   Comparison of Required to Available Conditions for
a Mach 4.1 Freejet
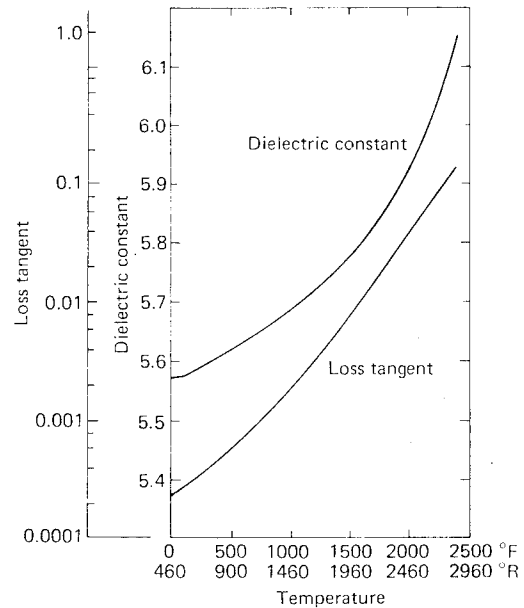
Fig. 4   Dielectric Constant and Loss Tangent versus Temperature for
Pyroceram 9606

70

NUMERICAL ASPECTS OF RADOME BORESIGHT ERROR ANALYSIS

K. Siwiak, T. Dowling, and L. R. Lewis

Raytheon Company, Missile Systems Division
Bedford, Massachusetts 01730

The boresight error induced by a missile radome is computed as the analog of the antenna difference port to sum port voltage ratio for fields incident from the assumed boresight direction. The antenna port voltages are computed as the reaction between this excitation and the radiated fields of the antenna over the radome inner contour. The reaction integral is specified over a surface which is the inner contour of the radome in the forward halfspace of the seeker antenna along with the plane of the seeker antenna. Both the radome shadow region (that portion of the radome not directly illuminated by the incident planewave) on the radome and the antenna reflection contributions to the integral are taken into account. A high degree of accuracy is achieved for a relatively coarse point sampling in the numerical integral.

One approach to boresight error computation [1] is a pattern analysis where boresight shift is determined by farfield sum pattern peak location. This involves a mechanization of a pattern search procedure which requires the computation of several pattern points for the determination of a single boresight error value. An alternate method [2] correlates difference pattern null shift with average wavefront tilt at the plane of the seeker antenna. The radome shadow regions are usually ignored as are antenna reflections.

The method presented here derives boresight error in the same manner defined by a monopulse seeker system. For a reasonable angle excursion off the antenna electrical axis, the boresight error ϵ is proportional to the antenna difference port to sum port voltage ratio.

$$\epsilon = \text{Real} \left\{ \frac{V_\Delta / V_\Sigma}{C} \right\} \tag{1}$$

where C is the monopulse antenna sensitivity computed in the absence of the radome. The antenna port voltages V_Δ and V_Σ are found using a reaction integral,

$$V = \frac{1}{I_b} \iint (\underline{E}^a \cdot \underline{J}^b - \underline{H}^a \cdot \underline{M}^b) \, dS \tag{2}$$

$\underline{E}^a$ and $\underline{H}^a$ are the electric and magnetic nearfields of the seeker computed at the radome inner contour. $\underline{J}^b$ and $\underline{M}^b$ are planewave excited equivalent electric and magnetic currents on this contour and I_b is the farfield current amplitude. The antenna port voltages V_Δ and V_Σ are computed for sum and difference seeker illuminations.

The surface S includes the inner contour of the radome forward of the antenna and the plane formed by the antenna surface. A set of equivalent currents corresponding to the dielectric-air boundary are assumed along the radome inner contour. The plane of the antenna surface is considered a perfect electric conductor.

Figure 1 shows the geometry of the seeker antenna and radome. The antenna is rotated with respect to the radome along a set of specified pitch and yaw directions. A planewave is incident from infinity along the z direction. A shadow region not directly illuminated by the planewave is identified as the shaded portion of the radome. The antenna nearfields $\underline{E}^a$ and $\underline{H}^a$ are computed at the radome inner contour using the vector potential formulation for the fields. $\underline{J}^b$ and $\underline{M}^b$ are planewave excited equivalent currents on the same contour. These currents have two components, one due to direct plane-wave transmission through the radome wall, the second from reflection off the seeker antenna surface. This reflection contribution is approximated using the ray path along the z direction for each point on the inner contour and amplitude weighted by the average transmission through the radome. In the shadow region the currents are approximated by optical ray tracing from the lit region.

The numerical techniques used tend to cancel radome grid point spacing granularity errors. Figure 2 illustrates the rapid convergence of this method. Boresight errors in the two principal gimbal planes are shown for calculations using 1, 1.3 and 5 radome grid points per wavelength. Also shown for reference are the corresponding measured curves. The integration is seen to converge for a radome grid point density as coarse as 1.3 points per wavelength.

The reaction integral approach to BSE computation is numerically imple-mented on a CDC 6700 computer by a collection of FORTRAN coded subpro-grams which through a keyword system adhere to a structured programming [3] philosophy. The inherent program flexibility allows for the definition of many generic radome shapes including tangent ogives, von Karman contours and multifaceted pyramid radomes. The seeker antenna is described by a planar array of arbitrarily excited modal elements.

An extensive program of measurements paralleled the analytical and numerical aspects of the development of the approach. Basic measurements and calculations of the antenna response to planewave excited simple struc-tures gimbaled in front of the antenna were used to verify the approach. One such structure was a large (4 ft by 8 ft) plexiglass sheet of 0.40 in. thickness gimbaled in the H-plane 12.3 in. in front of a 6 wavelength diameter X-band antenna. The gimbal center was 2 in. behind the antenna. Two thickness perturbations in the form of 2 in. wide fiberglass tape were added symme-trically to the sheet along the E-plane. The edges of the tape were 2 in. apart and the thickness was varied using 0.03, 0.06 and 0.09 in. of tape. The computed (solid line) and measured (dashed line) results are shown in Figure 4 where the antenna difference to sum port amplitude and phase are plotted as a function of gimbal angle. The agreement is excellent both in phase and amplitude.

Comparisons of measured and computed boresight errors are shown in Figure 3 for the E and H planes (pitch and yaw respectively) of a missile radome. The measurements and computations were made at X-band for a monolithic half wave constant wall thickness tangent ogive shaped radome. This radome is 16 wavelengths long, has a base diameter of 6.5 wavelengths with a dielectric constant of 5.7. The agreement at two frequencies over a 2.5 percent bandwidth was achieved using a radome grid density of 2.5 points per wavelength.

Figure 5 compares the measured and computed boresight errors of a similar size radome with a dielectric constant of 9.3 and with a complex wall thickness prescription. The comparison is over more than a five percent bandwidth at X-band. Again the radome was modelled by a grid density of 2.5 points per wavelength.

References

[1]   The Exact Analysis of Radome Boresight Errors, Ohio State University Electro-Science Laboratory Report 2485-3, 28 August 1968.

[2]   Radome Boresight Error and Wavefront Deformation, R.A. Haward, E.L. Rope, G. Tricoles, 1977 IEEE/AP-S Symposium, IEEE Catalog No. 77CH1217-9 AP.

[3]   Structured Programming, O.-J. Dahl, E.W. Dijkstra, C.A.R. Hoare, Academic Press, 1972.
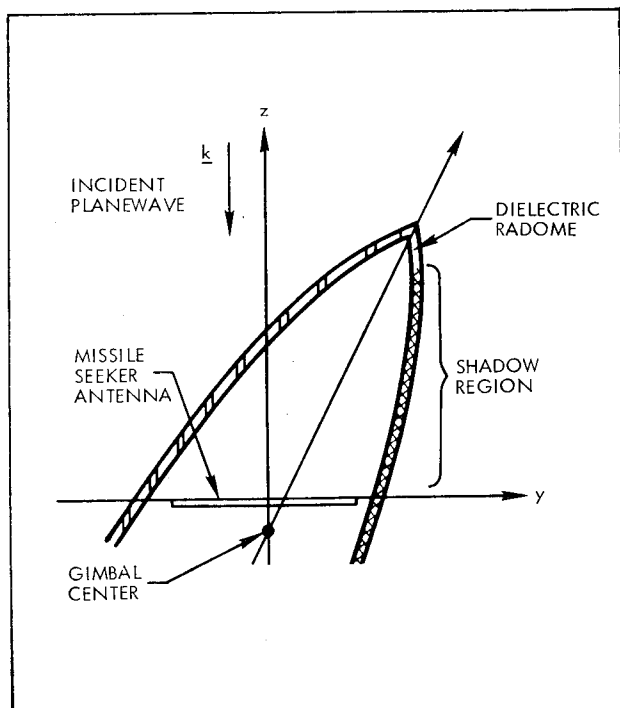
Figure 1 - Radome - Antenna Geometry Showing the Shadow Region and the Incident Plane-Wave Direction
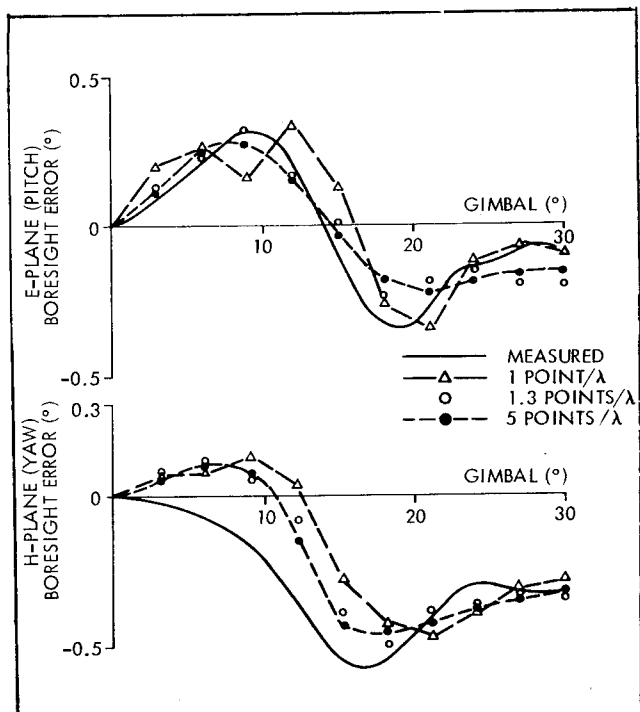
Figure 2 - Boresight Error for Various Radome Grid Point Spacings
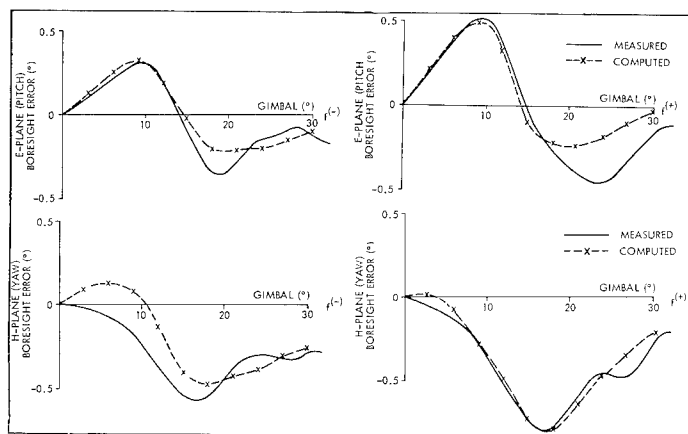
Figure 3 - Computed and Measured Boresight Errors at Two X-Band
Frequencies in a 2.5% Band for a Missile Radome with 5.7 Dielectric Constant
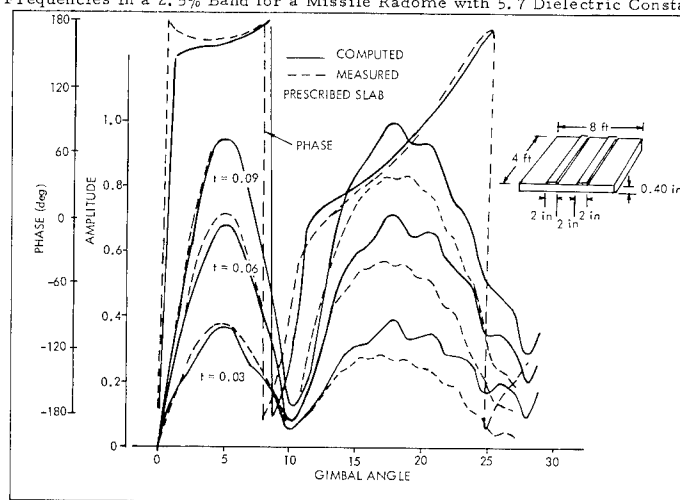
Figure 4 - Antenna Response for a Gimbaled Prescribed Slab
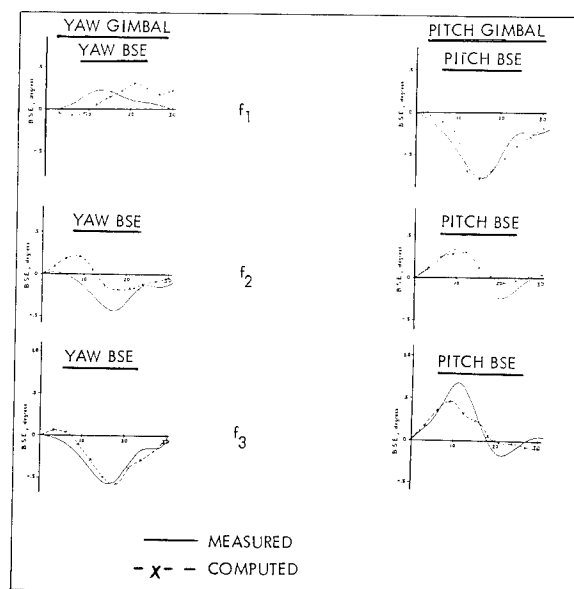
Figure 5 - Computed and Measured Boresight Errors
at Three X-Band Frequencies Across a 5% Band for
a Missile Radome with 9.3 Dielectric Constant

RADOME BORESIGHT ERROR REDUCTION
WITH DIELECTRIC TUNED PERFORATED METAL
PLATES

T.E. Fiscus, C.J. Meierbachtol

General Dynamics Electronics Division
San Diego, California

INTRODUCTION

In numerous cases the radome designer needs a tuning device other than ordinary dielectrics such as sheets, lenses, and anisotropic gratings to achieve desired electrical performance. In particular, control of the insertion phase delay (IPD) of the radome as a function of incidence angle, polarization and frequency is necessary to minimize radome boresight error magnitude and slope.

Recently, a metallic tuning device was used to reduce boresight error of a ogival shaped half-wave ceramic radome. These devices were dielectric coated perforated metallic plates, where the perforations are circular apertures. Perforated metallic plates were selected because they have inductive characteristics as compared to dielectric materials which are capacitive in nature. The dielectric coated perforated metallic plate, when properly tuned, is capable of advancing or retarding the phase of electromagnetic waves, while dielectrics alone can only retard phase. This paper describes the electrical characteristics of perforated metallic plates and how this type of tuning device can be used to lower the boresight error characteristics of radomes which had been tuned for minimum boresight error using dielectric tuning methods only.

PERFORATED METALLIC PLATES

The phase and transmittance characteristics of perforated metallic plates with circular and tripole aperture shapes laid out in hexagonal, square and rectangular lattices were determined by computation and measurement. It was determined that circular aperture shapes arranged in hexagonal lattice patterns provided the optimum characteristics for varying polarization, range of incidence angle and operating frequency band. A test panel with circular apertures arranged in a hexagonal lattice pattern is shown in Figure 1. The diameter of each aperture is approximately $0.4\lambda_0$ where λ_0 is the wavelength at the center frequency of the operating band. Spacing between the centers of adjacent apertures is approximately $0.5\lambda_0$. The

final dimensions of aperture size and spacing can be determined from experimental data. The thickness of the metal is not critical since dielectric materials added to the surface(s) of the perforated plate can tune the plate for desired electrical characteristics over the frequency band of interest.

The phase and amplitude characteristics for the panel of Figure 1 are shown in Figures 2 and 3. Figure 2 shows these characteristics for the perpendicular polarization case and the parallel case is shown in Figure 3. The data of Figures 2 and 3 are for the circular aperture perforated metallic panel tuned with dielectric to maximize transmittance in the frequency band. The data is plotted as a function of panel gimbal angle with ends of the frequency band as the parameter. Frequency, F_o, represents the center frequency and the bandwidth is approximately 7 percent. It should be noted that the change in phase of the plate is leading at the low frequency and lagging at the high frequency. It is this phase characteristic which is desirable for improving the boresight error magnitude and slope of radomes, particularly at the edges of the operating frequency band. The transmittance characteristics of the panel is better than 0.5 dB for both parallel and perpendicular polarization. The difference in phase between the high and low frequencies for the perpendicular polarization case at the larger angles of incidence is important for streamlined shaped radome boresight error reduction, because of the rapidly changing angle of incidence of these type radomes which results in large delta IPD.

RADOME CORRECTION WITH METALLIC PLATES

The boresight error magnitude and slope values of a half-wave wall ceramic radome with 2:1 fineness ratio were reduced by use of the perforated metallic dielectric tuned plates. The size and shape of this radome is shown in Figure 4.

Tuning plates were cut from perforated metallic flat panels for use within the radome. These plates had dimensions of approximately one wavelength and were placed within the radome bounded region forward of the antenna. Figure 5 shows tuning plates as typically installed within a radome. The plates were positioned so that portions of the antenna aperture as projected on the interior radome surface were shadowed by the plates. As the antenna scans past the plates the phase characteristics of the plates reduces the IPD variation of the radome wall which results in reduced boresight error. Plate position, angle and phase shift were adjusted by analyzing radome boresight error data of the radome which had been previously tuned by using dielectric materials.

76

RESULTS

Boresight error magnitude and slopes were reduced for both inplane and crossplane errors using the metallic plates. The most dramatic reduction in boresight error occurs at the ends of the operating frequency band with polarization parallel to the wall normal. Boresight error at the intermediate frequencies are essentially unaffected by the plates since the phase is constant as a function of angle of incidence.

The inplane error of the radome shown in Figure 4 is plotted as a function of radome look angle in Figure 6. The inplane error characteristics with and without the metallic plate are shown for F_O -325 MHz in Figure 6A while the F_O +325 MHz data is plotted in Figure 6B; the system and source antennas are aligned colinearly and the polarization is parallel.

The data shows that the error magnitude has been reduced at both ends of the frequency band by up to 25 percent with the use of the perforated metallic tuning plates as compared to dielectric tuning only. Crossplane error reduction with the plates were greater than the inplane case. The error data shown is for a monopulse antenna and radome. Similar results, although not shown, were obtained with a conical scan antenna of equivalent size to the monopulse antenna.

Transmittance characteristics of the radome with the perforated plates were virtually unaffected as compared to the without plate case. One would expect this to be the case since the transmittance of the plates is so good as shown in Figures 2 and 3.
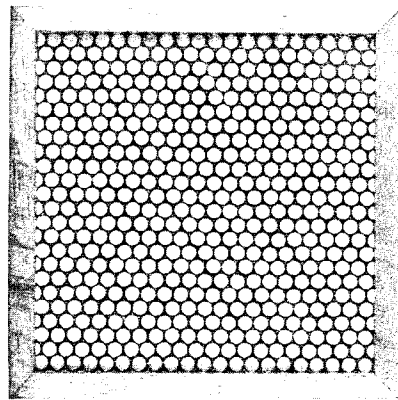
Figure 1. Perforated Metallic Flat Panel
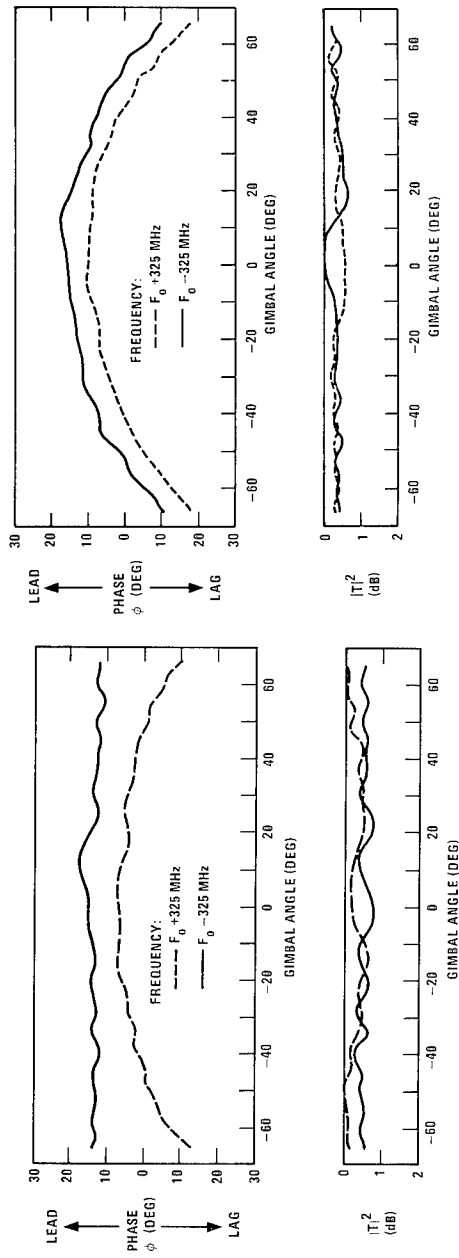
Figure 2. Phase and Amplitude of Panel With Circular Apertures (Figure 1) for Perpendicular Polarization.
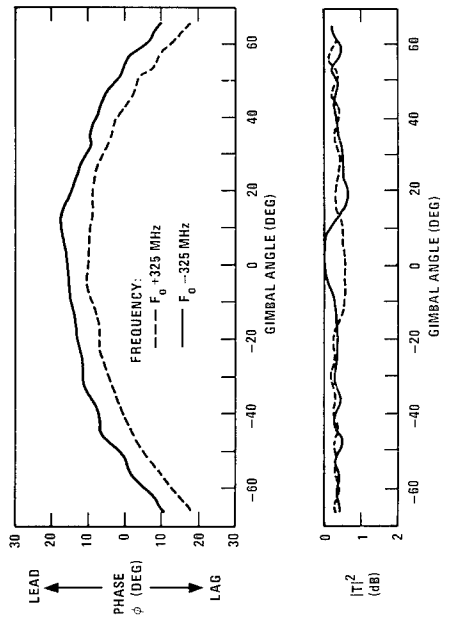
Figure 3. Phase and Amplitude of Panel With Circular Apertures (Figure 1) for Parallel Polarization.

78

Figure 6. Boresight Error
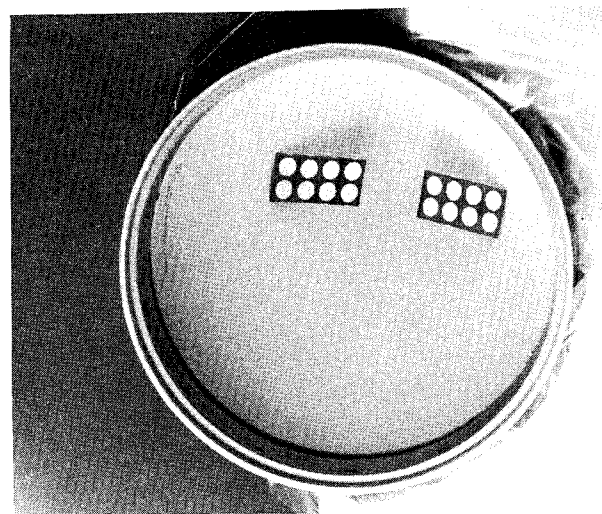
Figure 5. Plates Installed in a Radome
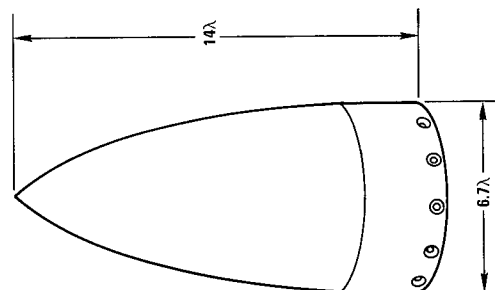
Figure 4. Ogival Shaped Radome
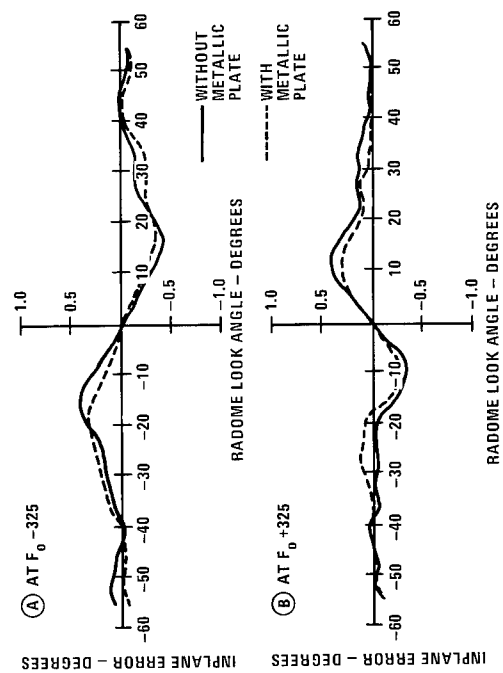
AN INVESTIGATION OF RADOME ERROR SLOPE DEGRADATION

D. E. Barb

General Dynamics Pomona Division

P. O. Box 2507

Pomona, CA. 91766

INTRODUCTION

Radome error slopes are a critical parameter in missile performance. Excessive slope magnitudes can cause missile instability or excessive miss distances. The need for maximum radome error slopes of .02 degree/ degree required an investigation of possible sources of error slope degradation. The radome tip assembly and trapped waves in the radome wall are two such sources. The tip assembly mass causes a wave front phase distortion while the trapped waves reradiate to modify the amplitude pattern of the antenna. The radome in case is a half wave wall Von Karman shape radome made from Pyroceram[R] 9606. The length is 24.8 wave lengths with a base diameter of 11.8 wave lengths. The following text details the empirical approach used to further reduce the radome error slope magnitudes after final tailoring. Final tailoring is defined as the maximum reduction of error slopes possible by the stragetic placement of glass tape rings along the radome wall.

MEASUREMENT SYSTEM AND PARAMETERS

The radome error slopes are measured with a automatic null seeking system utilizing an monopulse receiving antenna. A closed loop servo system maintains the transmitting horn in the antenna pattern null. The error slopes are plotted explicitly as a function of the antenna gimbal angle. Error slope measurements are made for eight radome roll angles (every 22.5°), three frequencies covering a 1.5 percent operating band and for three signal conditions, right circular, left circular, and linear polarization. The mean error slope magnitudes in the text are calculated using the combined slopes of the three signal conditions.

TIP CONFIGURATION VS. ERROR SLOPES

The initial steel tip assembly (Figure 1) generated error slopes which, after final radome tailoring, would not meet the error slope limits of Table 1. Radome tailoring which reduced the slopes (Figure 3) at $\pm10°$ for the steel tip assembly at f_L increased the slope from $+5°$ to $-5°$ at f_H. The effective tip cross-section area was reduced approximately 50 percent by removing the screw, silastic rubber insert and washer (Figure 1, items 2 & 3). The mean radome error slope magnitudes decreased 60 percent without further radome tailoring. To eliminate tip blockage and scattering effects the steel tip (Figure 1, item 1) was replaced with a tip made from dielectric material (K=5). The mean radome error slope magnitudes (Figure 5) decreased an additional 10 percent without further tailoring. Similar tips made from Pyroceram[R] 9606 and Beryllium did not change the error slope magnitudes. A Pyroceram tip (Figure 1, item 1) bonded in place with ceramic cement did not change the error slopes from those of the Pyroceram[R] 9606 tip without the cement.

A tip assembly (Figure 2) incorporating a mechanical locking feature was made from dielectric material (K = 5). The mean error slope magnitudes (Figure 4) increased 65 percent over those of the tip (Figure 1, item 1) made of the same dielectric material (K = 5). The large increase in error slope magnitudes had not been expected since the tip assembly was made from dielectric material. Evidently the extended tip shaft plus the washer caused wave front phase distortion either by excessive phase delay or by scattering due to the high incident angles seen along the tip shaft. Since the bonded Pyroceram[R] tip had a minimum effect on the radome error slopes, it was selected as a possible flight tip and has since been flown on missile rounds.

TRAPPED WAVES VS. ERROR SLOPES

A ceramic tip radome was taped to a guidance shell with a ring of Eccosorb SF-10 resonant absorber as an interface between the radome base and the guidance shell. The .050 inch thick absorber has a normal incidence reflectivity of -17 to -20 dB in the radome operating frequency band. The absorber ring width matched the radome base wall thickness. Error slopes were measured after final tailoring. The absorber ring was removed and the error slopes measured again. The mean radome error slope magnitudes (Figure 6) increased by 9 percent when the absorber ring was removed. The slope degradation occurred within $\pm15°$ of the 0° antenna gimbal angle. The greatest slope magnitude increase (15 percent) occurred for the right circular polarized signal.

DISCUSSION OF RESULTS

The primary purpose of the investigation was the reduction of error slopes. Therefore no effort was made to correlate the change in error slopes for the different tip configurations to possible changes in the near field phase contours. In all cases the cross-plane error slope data was unchanged by changes in the tip configurations or by the trapped waves effect. Although the degradation in radome error slopes due to trapped waves is minor at ambient temperatures, an increase in the trapped waves magnitude and its effect on error slopes is possible under flight conditions.

There was no appreciable change in mean error slope magnitudes for any change in signal condition (i.e., right circular, left circular, or linear polarization).

REFERENCES

1. J. D. Walton, Jr., "Radome Engineering Handbook, Marcel Dekker, Inc., New York, 1970.

2. J. D. Walton, Jr., "Techniques for Airborn Radome Design", Volume I & II, Air Force Avionics Laboratory, Wright-Patterson Air Force Base, Ohio, 1966.

Table 1

Examine the record for in-plane slopes equal to or greater than 0.02 degree per degree. A total of 40 is allowed for any one radome, allocated as follows:

Magnitude	Quantity allowed			Window size allowed
0.02 to 0.25 degree per degree				5 degrees, maximum, except that 2 windows at each test frequency may be 7 degrees, maximum
0.025 to 0.03 degree per degree		16	40	4 degrees, maximum, except that 1 window at each test frequency may be 5 degrees, maximum
0.03 to 0.04 degree per degree	3			3 degrees, maximum except that 1 window at each test frequency may be 5 degrees, maximum

Examine the record for crossplane slopes greater than 0.01 degree per degree. A total of 36 is allowed for any one radome, allocated as follows:

Magnitude	Quantity allowed			Window size allowed
0.01 to 0.015 degree per degree				7 degrees, maximum, except that 4 windows at each test frequency may be 10 degrees, maximum
0.015 to 0.02 degree per degree		11	36	5 degrees, maximum, with no exceptions allowed
0.02 to 0.03 degree per degree	7			3 degrees, maximum, except that 1 window at each test frequency may be 4 degrees, maximum

84
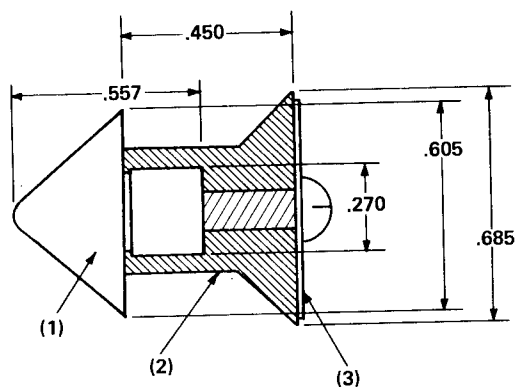
FIGURE 1

(1) Steel

(2) Silastic Rubber

(3) Steel
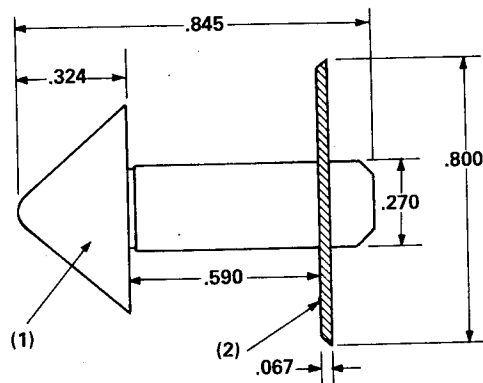
FIGURE 2

(1) "HI—K" Dielectric Material (K = 5.0)

(2) Teflon Washer
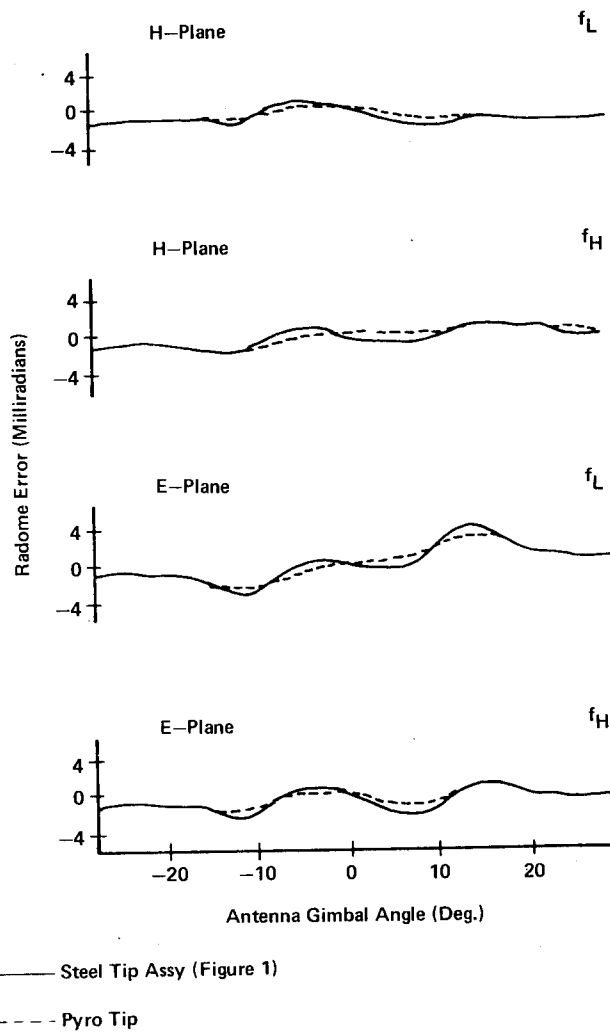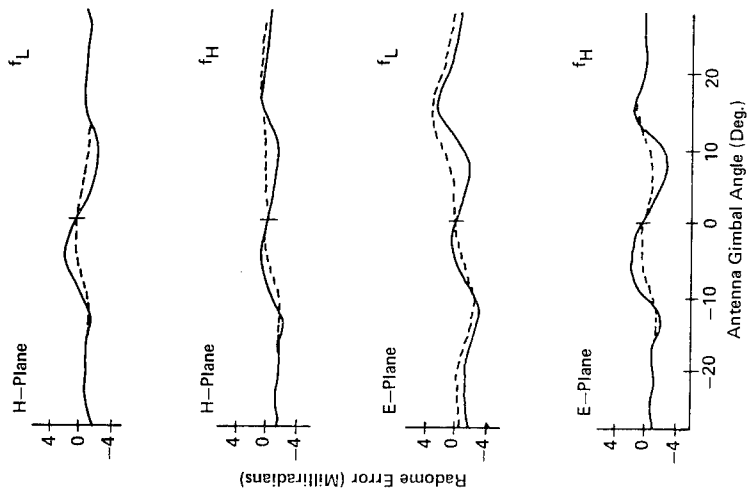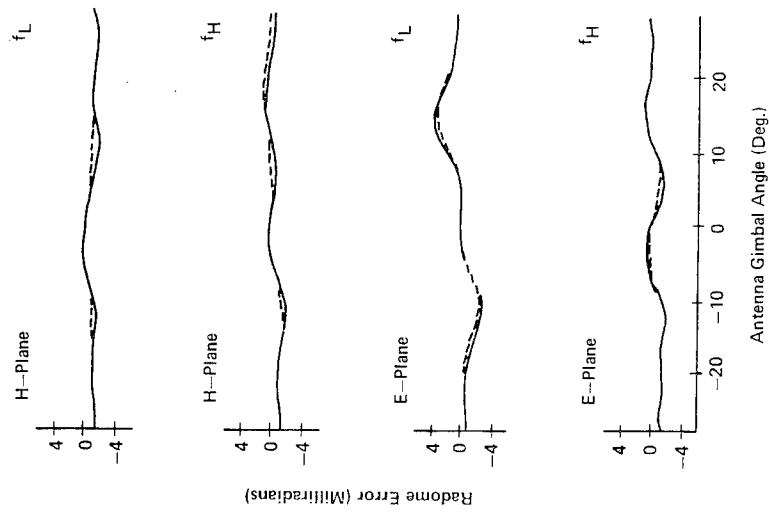
Antenna Gimbal Angle (Deg.)

—— Steel Tip Assy (Figure 1)

- - - - Pyro Tip

FIGURE 3

85
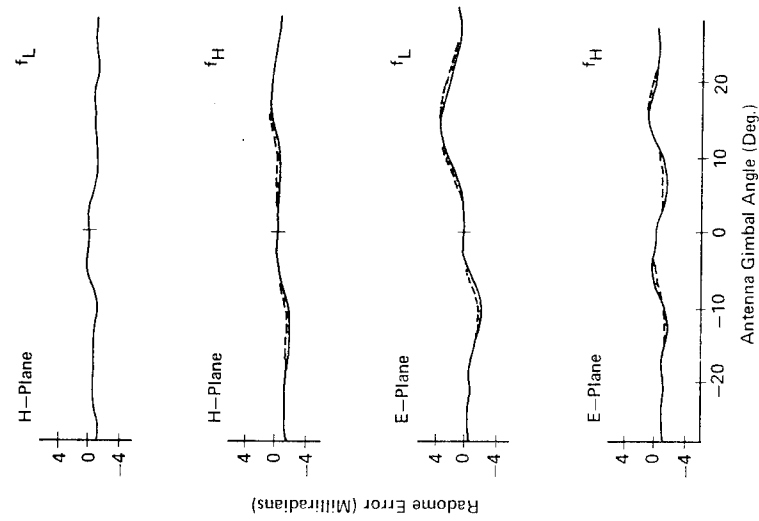
FIGURE 4

FIGURE 5

FIGURE 6

86

Supersonic Rain Erosion Behavior of Ablative Fluorocarbon Plastic Radome Materials

by

George F. Schmitt, Jr.
Air Force Materials Laboratory
Wright-Patterson Air Force Base, Ohio

Introduction

The utilization of cast or molded plastic thermal protection materials for tactical missile radomes is receiving increasing emphasis because of their features of low cost, handleability and ease of fabrication. These materials which ablate cleanly leaving little, if any, char residue are an attractive alternative to the monolithic ceramics which have been used for high Mach number missile systems. They change wall thickness as they ablate and, of course, that change must be accounted for in the electrical design.

As with any tactical radome material, the requirement for all weather operation dictates that rain erosion performance must be assessed. Two groups of ablative plastic materials were investigated. The first was the Duroid fiber reinforced tetrafluoroethylene (Teflon*) materials from Rogers Corporation. Materials reinforced with glass fibers (Duroid 5870) which had been prepared by molding, laminating and a complex molding with special orientation of the fibers and one material reinforced with aluminum silicate (Duroid 5650) were tested.

The other group of ablative plastics were the Avcoat materials from Avco Corporation which consisted of Avcoat 8027, a cast epoxy-polyurethane, Avcoat 8028, a fluoroelastomer compounded with filler, and Avcoat 8029-1, -2, and -3, Teflon with three levels of a proprietary particulate filler loading.

The purpose of this investigation was to characterize the erosion behavior of these ablative plastics in a supersonic (Mach 4) rain encounter and more particularly, to determine the influence of types of reinforcement (fibers vs. particulate) and processing (laminated vs. molded) on their rain erosion resistance.

*Trademark, E.I. duPont de Nemours & Co.

Experimental Technique

The supersonic rain erosion wedge described in Reference 1 was designed for multiple specimen testing of materials at velocities up to Mach 4.0. Forty-eight total specimens (1.25" x 1.25" x 0.50") of materials are mounted on both the left and right sides with 12 each at the following angles: 13.5, 30, 45, 60 degrees.

The Holloman rocket sled track is 50,000 ft long with 18,000 ft equipped with nozzles for rain simulation; 12,500 ft. are available for acceleration and 19,500 ft. for braking. Monorail sleds are used for rain erosion tests with braking accomplished by waterfilled polyethylene bags or frangible plastic water trays laid directly on the track.

For the Mach 4.0 runs with the wedge, the rainfield was limited to 2000 ft., and a velocity profile which peaked out at Mach 4.0 as the sled entered the rainfield and decreased from there was utilized. Satisfactory velocity profiles were achieved at these Mach numbers through proper selection of firing points, staging and combinations of booster and sustainer motors.

The rainfield at Holloman was completely reconstructed in 1974 with the rain spray nozzles being mounted on standpipes immediately above the track rather than on risers out to each side of the track. This has enabled the rainfall to be reduced from 5.5-6.5 inches per hour with a 1.9mm dia mean drop size to 2.5-3.5 inches per hour ($3g/m^3$) a 1.37 mm dia mean drop size. These tests utilized the new rainfield entirely.

Description of Materials and Results

A. Duroid 5870 Laminated, Molded and Complex Molded Glass-Reinforced Teflon and A-56 Duroid 5650 Molded Aluminum Silicate-Reinforced Teflon

The three Duroid 5870 glass reinforced materials which exhibited excellent erosion performance compared to the other ablative plastics and in comparison to many monolithic ceramics or other reinforced constructions differed in the method of manufacture-molding versus lamination and in the orientation of the reinforcing glass fibers relative to the exposed surface. These orientations were as follows(X and Y refer to directions in the plane of the sample surface and Z refers to the in-depth direction through the sample):

88

	Axis I to Surface	Axis II to Flow
A-53 Duroid 5870 Laminated	Y	Z
A-54 Duroid 5870 Molded	X	Z
A-55 Duroid 5870 Complex Molding	Z	X
A-56 Duroid 5650 Molded	X	Z

In the laminated material, the relative percentage of fibers perpen-- dicular to surface is much reduced compared to the molded materials and the molded material exhibited greater erosion resistance (less MDPR) than did the laminated material.

The glass reinforced molded material (A-54) was clearly superior to the aluminum silicate-reinforced molded material (A-56). The complex molding process in which the relative amount of fiber ends at the surface was increased compared to the standard molding in which the X and Y direction fiber percentages are the same and greater than the Z direction did not offer increased erosion performance at high or low angles.

B. Avcoat 8027 Epoxy Polyurethane, 8028 Elastomeric Fluorocarbon and 8029-1, -2, and -3 Teflon with Particulate Loading

The Avcoat 8027 epoxy-polyurethane ablative plastic material has received consideration for thermal protection on a number of missile system radomes and was previously investigated in this series (Reference 6). It was included as a reference material in these runs although thermal effects were expected to be more pronounced on it compared to the other fluorocarbon-based Avco plastic materials. This was experienced and dis- coloration and mass loss were three to five-fold greater than the other materials.

The Avcoat 8028 fluorocarbon elastomeric material is prepared by conventional rubber compounding techniques and is based on the same starting materials as the fluoroelastomer radome coatings which have proven so successful for thermal flash environments and prolonged thermal exposure (Reference 2). This material obviously would require a sub- structure such as quartz polyimide or other laminate to be used in tactical missile radomes as it has no structural capability, but that is true (at least for larger radomes) for most of these ablative plastic materials. The low angle performance at 30° was the best of the Avcoat materials.

C. Rankings of Materials

Based upon the exposure at a velocity of 1300 m/s in the 3 g/m^3 rain environment, the ranking of these materials is as follows for the 60° impingement angle:

	MDPR(cm/sec)$^{@}$ Mach 4.0, 60°
A-53 Duroid 5870 laminated	0.10425
A-63 Avcoat 8029-1 Teflon/5 pts filler	0.11200
A-62 Avcoat 8028 Fluorocarbon	0.11457
A-54 Duroid 5870 molded	0.11649
A-55 Duroid 5870 complex molding	0.13938
A-51 Avcoat 8027 Epoxy polyurethane	0.25199**
A-64 Avcoat 8029-2 Teflon/7.5 pts filler	0.2402
A-65 Avcoat 8029-3 Teflon/10 pts filler	0.26341

**Based on run 30R-M6A in June 76

The rankings change slightly if the data at lower impingement angles is compared. In general, the glass fiber-reinforced Teflon materials exhibited considerably less mass loss at the 13.5° and 30° angles than did the particulate-loaded Teflon materials. The elastomeric fluorocarbon-based material also exhibited good performance while the aluminum silicate fiber-reinforced Teflon and the cast epoxy-polyurethane exhibited poorer performance in part because of ablation material losses.

The 30°, 1300 m/s and 13.5°, 1300 m/s rankings are summarized below:

	*MDPR (cm/sec)$^{@}$ Mach 4.0, 30°
A-54 Duroid 5870 molded	0.01347
A-53 Duroid 5870 laminated	0.01807
A-55 Duroid 5870 complex molding	0.01883
A-63 Avcoat 8028 cast fluorocarbon/filler	0.02909
A-56 Duroid 5650 molded	0.04278
A-62 Avcoat 8029-1 Teflon/filler	0.04511
A-51 Avcoat 8027 Epoxy polyurethane	0.11851

	*MDPR (cm/sec) Mach 4.0, 13.5°
A-54 Duroid 5870 molded	0.00395
A-53 Duroid 5870 laminated	0.00491
A-55 Duroid 5870 complex molding	0.00798
A-63 Avcoat 8029-1 Teflon/filler	0.01144
A-56 Duroid 5650 molded	0.01758
A-51 Avcoat 8027 Epoxy polyurethane	0.05143

*Others not run at these conditions

Discussion

The excellent erosion performance of the fiber reinforced Teflon Duroid materials and the elastomeric fluorocarbon Avcoat 8028 from Avco has demonstrated a new class of materials for primary thermal protection of tactical missile radomes. Common practice in the past has utilized the high density, thermally resistant monolithic ceramics for this thermal protection. Electrical considerations require new techniques for analysis and design of missile guidance with a changing wall thickness but this has been accommodated in reentry vehicle antenna window design for many years and is not a serious consideration. Obviously determination of the ablation behavior of these materials becomes a necessary element of their characterization.

The variation in erosion mean-depth-of-penetration-rate for the four Duroid materials is shown in Figure 1 as a function of the sine of the impact angle. As can be seen, essentially one curve could be drawn through the laminated and molded glass fiber-reinforced tetrafluoroethylene data and perhaps extended to include the complex molding as well. The aluminum silicate fiber reinforced tetrafluoroethylene on the other hand exhibited a greater MDPR at each angle although its dependence on angle was approximately the same.

A log-log plot of MDPR vs. $\sin\theta$ is shown in Figure 2 for the laminated Duroid 5870L and the velocity exponent on $\sin\theta$ as 2.62 which is somewhat higher than has previously been determined for bulk plastic erosion as a function of angle. In References 1, 3 and 4, a sine squared relationship was found to best fit the data for polyphenylene oxide, Teflon)TFE), Kydex acrylic and other laminates and bulk plastics. This slightly higher dependence is most likely because the data were at only one velocity whereas the work in References 1, 3 and 4 also utilized the 13.5° and 30° cone fixtures at Mach 5.0

as well as the wedge at lower velocities (Mach 1.5, 2.0, 2.5 and 3.0). The higher erosion rate-angle dependence may also be due in part to the presence of the fiber-reinforcement and its influence on the behavior at higher angles.

The particulate loaded tetrafluoroethylene, Avcoat 8029 series, was less erosion resistant than the fiber reinforced materials with erosion resistance decreasing as the amount of filler increased. Variation of the erosion rate of all Avcoat materials is shown in Figure 3 as a function of the sine of the angle. The Avcoat 8027 epoxy-polyurethane was much less resistant at all angles in keeping with its increased ablation and erosion under these test conditions. The MDPR vs. $\sin\theta$ dependence was similar for all Avcoat materials except the Avcoat 8028 elastomeric fluorocarbon which exhibited a linear dependence through $60°$ based upon only 3 data; no specimen was run at $13.5°$ angle and low angle data might change the linear dependence.

A log-log plot of MDPR vs. $\sin\theta$ is shown in Figure 4 for the Avcoat 8029-1 particulate-reinforced tetrafluoroethylene; the velocity exponent is determined to be 2.08 for $\sin\theta$ in keeping with results from previous investigations (References 1, 3 and 4) which indicated sine squared to provide the best fit of the data.

The less the amount of particulate filler loaded into the tetrafluoroethylene the more erosion resistant was the resulting material. However, these tests indicate that the fiber-reinforcement imparts more resistance than does the particulate reinforcement. Teflon materials, because they are by nature an agglomeration of polymer particles (globules), erode by chunking out of pieces from the surface. The fiber reinforcement inhibits this chunking and results in better erosion performance, whereas the particulate reinforcement does not result in any improvement.

A comparison of mean depths of penetration from the U. S. Army MIRADCOM tests (References 5 and 6) on $22.5°$ cones at Mach 5.0 at Holloman through a nearly identical rainfield with the results from these tests is shown in Table 1. As can be seen, the velocity is the most important influence with the MDP increasing by an order of magnitude with a 25% increase in velocity. Note however, the rankings of the four ablative plastics would be the same from either series of tests and the relative magnitude of the erosion is similar under any set of velocity and angle conditions.

It is clear that the potential offered by the ablative plastic radome materials must be exploited because of the fabricability, ease of handling, low cost and design flexibility which they possess. Erosion resistance and ablation characteristics appear adequate for many systems applications.

However, a commitment must be made on the part of missile development agencies to learn how to design with them, how to accommodate structural requirements with substructures or other means, and which thermal ablation characterization tests are essential and accepted for design data for these ablating materials.

Conclusions

1. Fiber-reinforced tetrafluoroethylene ablative plastic materials offer considerable promise for rain erosion and thermal protection of tectical missile radomes. These materials can be prepared by molding or laminating processes and offer improved erosion performance over unreinforced Teflon.

2. Particulate-reinforced tetrafluoroethylene and epoxy-polyurethane ablative plastics offer somewhat less erosion resistance than the fiber-reinforced materials but still have application in supersonic rain environments.

3. Thick sections of elastomeric fluorocarbons compounded with fillers exhibit excellent erosion resistance even at 1300 m/s if utilized in thicknesses of 0.5 inch. Dimensional stability/structural considerations will require substructures.

4. Erosion rate dependence with these ablative plastic materials was found to vary with the 1.5 to 2.0 power of the sine of the impact angle and the 2.7 to 3.5 power of the normal velocity component.

REFERENCES

1. G. F. Schmitt, Jr., "Influence of Density and Porosity on the Supersonic Rain Erosion Behavior of Silicon Nitride Radome Materials," Proceedings of the Thirteenth Electromagnetic Window Symposium, Georgia Institute of Technology, Atlanta, Ga., 21-23 September 1976, pp 37-44.

2. J. F. Moraveck, "Rain Erosion Resistant Fluoroelastomer Radome and Antenna Coatings," Proceedings of the Thirteenth Electromagnetic Window Symposium, Georgia Institute of Technology, Atlanta, Ga., 21-23 September 1976, pp 29-36.

3. G. F. Schmitt, "On the Dependence of Materials Erosion on Environmental Parameters at Supersonic Velocities," Journal of Aircraft, Vol. 10, No. 12, December 1973, pp 705-709.

4. G. F. Schmitt, Jr., "Erosion Behavior of Materials in Rain at High Velocities," High Temperatures - High Pressures, 1974, Vol. 6, pp. 177-188.

5. K.N. Letson and P. A. Ormsby, Aerothermal and Rain Erosion Sled Test Results on Radome Materials at Mach 5, U.S. Army MIRADCOM Technical Report TL-77-2, Redstone Arsenal, Ala., 1 February 1977.

6. W. G. Burleson, Evaluation of Aerothermal Ablation and Rain Erosion Results for Plastic Radome Materials Tested on Sleds at Mach 5, U. S. Army MIRADCOM Technical Report RL-77-3, Redstone Arsenal, Ala., 10 December 1976, AD No. B017-703L.

Note

The discussion of materials by brand names or suppliers in this report is in no way to be taken as an endorsement or criticism by the Government. They were selected as representative of certain classes of materials and their names are a convenient way of handling and discussing them. The Government incurs no liability or obligation to any supplier of materials from the information included in this report. The author expresses his appreciation to those individuals and companies who supplied materials specimens for this study.

TABLE 1

COMPARISON OF CONE AND FLAT SPECIMEN
SLED RESULTS ON ABLATIVE PLASTIC RADOME MATERIALS

AFML No.	Material	Letson Results MDP, mm [1]		Schmitt Results MDP, mm [2]
		22.5°	13.5°	30°
A-51	Avcoat 8027 Epoxy Polyurethane	3.43	0.22	0.524
A-62	Avcoat 8028 Elastomeric Fluorocarbon	1.65	--	0.200
A-56	Duroid 5650 Aluminum-Silicate Fibers/Teflon	0.41 - 1.36	0.08	0.19
A-53	Duroid 5870 Glass Fibers/Teflon	0.63	0.02	0.07

1. Reference 5, 5500 fps, 22.5° cones.

2. 4200 fps, 13.5° and 30° specimens, these tests.

95
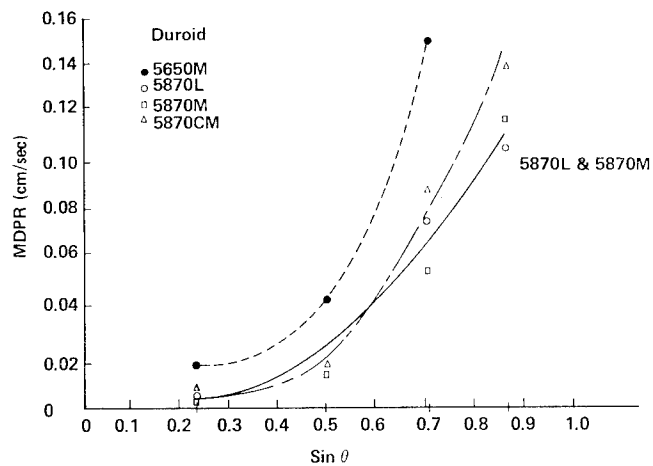
FIGURE 1. Mean Depth of Pentration Rate vs. Sine of
the Impact Angle for Fiber—Reinforced
Tetrafluoroethylene Materials
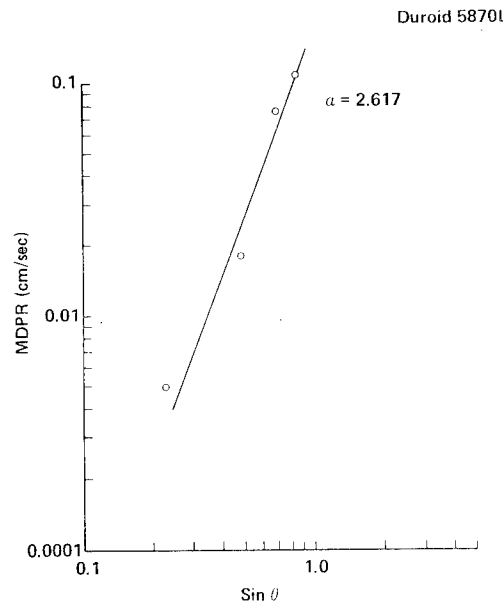
FIGURE 2. Log MDPR vs. Log Sin θ for Duroid 5870L Material
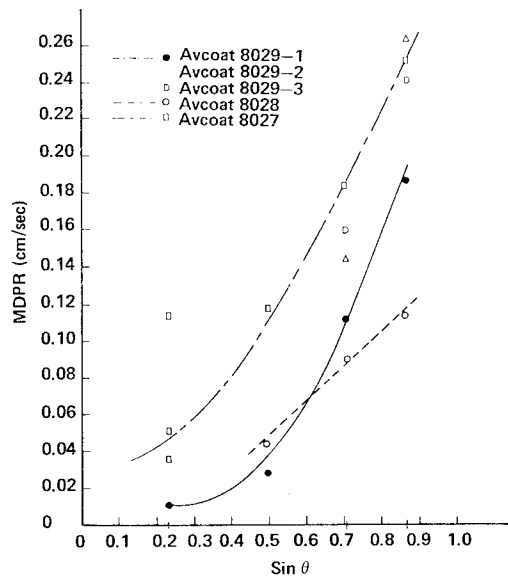
FIGURE 3. Mean Depth of Penetration Rate vs.
Sine of the Impact Angle for Particulate—
Reinforced Tetrafluoroethylene and
Other Avcoat Materials
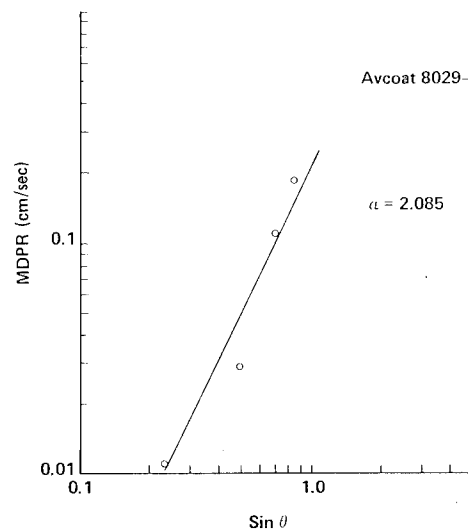
FIGURE 4. Log MDPR vs. Log Sin θ for
Avcoat 8029—1 Material

AEROTHERMAL AND ELECTRICAL EFFECTS OF RAIN EROSION
FOR A SLIP-CAST FUSED SILICA RADOME

by D.L. BALAGEAS, J. CASSAING & A. SARREMEJEAN*

Office National d'Etudes et de Recherches Aérospatiales (ONERA)
92320 Châtillon (France)
* *ONERA, Centre de Toulouse (France)*

♦

Abstract

Rain erosion has two important consequences on radome behaviour during a mission. On the one hand, the surface roughness created by erosion may noticeably increase the convective heat transfer within the boundary layer and hasten the laminar-turbulent transition, which restricts the safety margin of structural resistance, and on the other hand, the modification of the thickness law and the new surface state entails modifications of the radome electrical characteristics.

Both phenomena, increase of convective heat flux, and deterioration of electrical performance, have been experimentally studied in the case of a slip-cast fused silica radome having been subjected to non-symmetrical erosion in a hypersonic wind tunnel. An increase of near 20% of convective heat flux has been recorded, and an increase of several milliradians of boresight error has been measured after the erosive test. These results are compared to aerothermal and electrical evaluations, taking into account the variations of radome thickness and the mean roughness created.

It is concluded that, if the three dimensional electrical theory is adequate for boresight error increase prediction, presently available rough wall heat transfer theories seem not well adapted to small radius anti-erosion caped radomes.

Introduction

To-day slip-cast fused silica is in fact the unique radome material adapted to flight conditions above Mach 5 with a well established technology leading to reproducible properties. Slip-cast fused silica unfortunately has a poor erosion resistance. This phenomenon has been studied for some years as it may lead to catastrophic failure [1, 2, 3]. Furthermore, even when radome survives hydroerosive environments (rain or snow precipitation, high altitude cirrus), secondary effects of erosion exist that can decrease system efficiency. In effect modification of the thickness law may break down the radioelectrical performance of the radome, and the roughness created by erosion can noticeably increase the convective heat transfer within the boundary layer and hasten the laminar-turbulent transition. So it is interesting to study these effects and to take them in account in previsional evaluation.

Hydroerosion simulation on full-scale radome

It is very difficult to simulate by ground tests the hydroerosion of a full-scale slip cast fused silica radome. Practically the unique facility that allow this is the S3-MA wind tunnel of the ONERA at Modane (France), where a rain field is created in a Mach 0.83 air flow [4]. Unfortunately, due to relatively low speed, erosion is low and producing noticeable erosion depth on the entire structure is a time consuming operation.

The S4-MA blowdown hypersonic wind tunnel of ONERA, which allows to study the aerothermal behaviour of full-scale radomes at Mach 6 (see photograph on figure 1), has given the opportunity to produce realistic simulation on the entire structure. This facility, described in ref. [5], includes a heater containing 12 tons of alumina pebbles heating the quantity of air necessary for a run up to 1850 Kelvin. With such a pebble-bed heater, dust exist in the air flow. This dust, generated by the successive thermal cycles acting on the alumina pebbles and the refractory brick layer, has no effect on metallic models generally used in wind tunnels.

97

On the other hand, with a poor erosion resistant material such as silica, important erosion can be obtained. This effect which may be troublesome in some cases, allows here a simulation of hydroerosion on the full-scale radome.

The present study was performed with an ogival SCFS radome which was successively run for 22 s at Mach 6 (stagnation temperature : 1650 K, stagnation pressure : 2.5 MPa) without incidence and 33 s in the same conditions with an angle of attack of $15°$. These conditions reproduce flight environment of Mach 6 at an altitude of 30 km. The aspect of the surface in the windward region is shown by the photograph of figure 2. The radome was dimensionally and radioelectrically checked before and after the wind tunnel runs.

Radome post-test analysis

A post-test analysis of the radome allowed to determine, for the windward and the leeward lines the mean erosion depth and the mean roughness height. The distribution of these two parameters along the two meridians is given on figure 3. No erosion is obtained on the tip region, for a hot pressed silicon-nitride rain erosion cap was mounted on the radome, as described in ref. [2]. The erosion is more important for the windward meridian than for the leeward region. In this last case the erosion was essentially done during the first run with zero angle of attack. The erosion on the windward meridian reaches near 0.20 mm just behind the erosion cap and less than 0.1 mm on the symmetrical region of the leeward meridian.

To give an idea of the importance of this erosion, referring to charts presented in [2, 3], one can consider that it is equivalent, for instance, to the erosion resulting from two successives flights : seven hours at Mach 1 without incidence through a 4 mm.hr^{-1} rain and the encounter, at Mach 4, with an angle of attack of $15°$, of a 400 meters thick high altitude cirrus with 0.1 g.cm^{-3} water concentration.

Aerothermal effects of erosion

Erosion has aerothermal consequences for the radome. The surface roughness characterized here by a mean roughness height, k, increases the convection heat transfer and can hasten the transition.

For laminar boundary layer, the correlation of Phinney [6] is generally used :

$$(1) \qquad \frac{Ch_r}{Ch_s} = 1 + \sqrt{\frac{\rho_\infty . V_\infty}{\mu_2}} \; . \; R_N \; . \; f\left(\frac{k}{\delta}\right)$$

where Ch_r and Ch_s are the heat transfer coefficients for rough and smooth surfaces, R_N the nose radius, δ the boundary layer displacement thickness, ρ_∞ and V_∞ respectively the density and velocity of free stream, and μ_2 the dynamic viscosity beyond normal shock. The function f is :

$$f\left(\frac{k}{\delta}\right) = 0.00166 \; . \; \frac{k}{\delta} \quad \text{if } \left|\frac{k}{\delta}\right| \leqslant 2.41 \qquad \text{and} \qquad f\left(\frac{k}{\delta}\right) = 0.004 \quad \text{if } \left|\frac{k}{\delta}\right| > 2.41.$$

For turbulent heat transfer, various types of correlations have been proposed, [7, 8]. They introduce "equivalent sand grain roughnesses", but recent works such as [9 and 10], seem indicate that average peak height yields better agreement with experience.

At last, many authors indicate that the transition is hasten by roughness. For Wilcox [11], the transition occurs if the Reynolds number related to the boundary layer momentum thickness verifies the relation :

$$(2) \qquad Re_\theta \geqslant 275 \; . \; \frac{T_p}{T_e} \; . \; \left(\frac{\theta}{k}\right)^{2/3} \; .$$

A similar expression results from PANT wind tunnel data.

Thermal measurements were made during the runs : inner temperatures were obtained from 18 thermo-couples and an IR pyrometer gave the outer superficial temperature at a location defined by an axial distance of 40 mm from the tip and a meridian angle $\phi = 250°$ ($\phi = 0°$ being windward meridian and $\phi = 180°$ leeward meridian). During the second run, thermocouple measurements indicated that no transition occurs even on the windward meridian where Re_θ reaches the value 600 at the base of the radome. The relation (2) for rough transition lead to very small transitional Reynolds number Re_θ on the windward meridian, which is in contra-diction with the experiment. This inadequacy of rough transitional criteria may be attributed to the fact that in the present case of an erosion-cap-equipped radome the roughness is negligible in the nose region.

From pyrometer data it appears that the heating rates at the end of the second run where significantly higher than smooth surface laminar heat transfer theory indicates. A value of 1.18 was deduced for the ratio Ch_r/Ch_s which is higher than the evaluation made with correlation (1) presented on figure 4. Here the discre-pancy may be explicated by the fact that all theories developed for rough heat transfer are specially suited for reentry shapes with more important nose radii (at least 10 mm against 1 mm in the present case).

Electrical effects of erosion

The boresight error and the transmission efficiency of the radome were measured, in X band, before and after the wind tunnel runs. The relative positions of windward and leeward meridians and E and H planes during the electrical measurements are defined on figure 5.

Transmission efficiency is not significantly affected by erosion, but boresight error is notably modified (see figure 6). The absolute value of this increase is of the same order of magnitude than the non-eroded-radome boresight error. For E plane scan angles, the modification in boresight error is not symmetrical. Conver-sely , it is symmetrical for H plane scan angles. This trend is related to the fact that, for electrical measure-ments, E plane was identical to the erosion symmetry plane. In conclusion, erosion destroyed the electrical symmetry of the radome and strongly degradated its electrical performance.

The experimental results have been compared to theory. The theoretical evaluation is done using a three dimensional method described in reference [12]. Starting from the evaluation of the near field of the antenna at the inner surface of the radome, the radome influence is approximated by computing the geometrical optics transmission and reflection coefficients. These coefficients are multiplied by the incident field to obtain the transmitted field. The far field is derived by numerically integrating on the surface of the radome the corres-ponding tangential field on the outer surface. The transmission efficiency is found by comparing far-field am-plitudes as calculated with and without radome. The boresight error is evaluated in this analysis by the devia-tion of the beam maximum. This method was applied with the dimensional characteristics —shape and thickness law— of the radome, measured before and after the erosion. The increase in boresight error is deduced directly from these two evaluations and compared to measured values on figure 6. A good agreement between experi-mental and theoretical values is found. A similar evaluation performed with a three dimensional ray tracing gives very close results.

Conclusion

Dust erosion of SCFS radome produced in an hypersonic wind tunnel allowed the study of aerothermal and electrical effects of erosion.

An increase in laminar convective heat transfer has been verified, but the ratio of rough wall to smooth wall heat transfer coefficient is higher than rough wall heat transfer theory predictions. On the other hand, in contradiction with empirical rough wall transition criteria, no transition was recorded. These discrepancies bet-ween experiments and theory may be attributed to the fact that recent developments in this area concerned re-entry shapes with more important nose radii than the studied radome nose and that in the present case rough-ness was non existent on the tip (presence of an anti-erosion cap). Therefore, it may be concluded that there is a need for further work leading to erosion-roughness aerothermal effect modelization more specially adapted to high-speed radomes.

For a SCFS radome with small boresight error, non symmetrical erosion leading to mean erosion depth lower than 0.2 mm, may substantially alter electrical performance in such a way that this phenomenon cannot be neglected when evaluating the system efficiency. In the present case, electrical effects are well predicted by the three-dimensional theory when introducing post-erosion thickness law as given by post-test analysis.

References

[1]   K.N. LETSON & P.A. ORMSBY, "Rain erosion testing of slip-cast fused silica at Mach 5", ASME Publication n° 76-ENAs-6, July 1976.

[2]   D.L. BALAGEAS & A. HIVERT, "Rain erosion : a serious problem for slip-cast fused silica radomes", Proceedings of the XIIIth Symposium on Electromagnetic windows, Atlanta, September 1976. Also : ONERA TP n°1976-98.

[3]   D.L. BALAGEAS, "Prediction of the rain erosion of slip-cast fused silica radomes for high velocity missiles", La Recherche Aérospatiale, 1977-3, p. 133-137. Also : ESA TT 415.

[4]   G. FASSO, G. LECLERE & M. PLETIN, "Etude en soufflerie de l'érosion due à la pluie sur des éléments d'avion ou de missiles volant à grande vitesse", La Recherche Aérospatiale, n° 119, 1967.

[5]   C. SOULIER & J. LAVERRÉ, "Using the ONERA S4-MA hypersonic wind tunnel for supersonic combustion ramjet tests", Supersonic Tunnel Association, 35th Meeting, Dallas, March 1971. Also ONERA TP n° 924 (1971).

[6]   R.E. PHINNEY, "Mechanism for heat transfer to a rough blunt body", Letters in Heat and Mass Transfer Journal, vol. 1, n°2, p. 181-186, 1974.

[7]   R.B. DIRLING, "A method for computing roughwall heat transfer rates on reentry nosetips", AIAA paper n° 73-763, 1973.

[8]   R.M. GRABOW & C.O. WHITE, "Surface roughness effects on nosetip ablation characteristics", AIAA Journal, vol. 13, n° 5, p. 605-609, May 1975.

[9]   G.L. DENMAN, "Turbulent boundary layer rough surface heat transfer on blunt bodies at high heating rates", phD Dissertation, Ohio State University, 1976.

[10] D.E. NESTLER, "High pressure arc test performance of carbon-carbon nosetips", AIAA Paper n° 77-771, 1977.

[11] D.V. WILCOX, "Turbulent model transition prediction", AIAA Journal, vol. 13, n° 2, February 1975.

[12] A. DELFOUR, J.F. DUPUTZ & A. SARREMEJEAN, "Nouvelle méthode de calcul des aberrations d'un radôme", Third International Conference on Electromagnetic Windows, Paris, 1975.
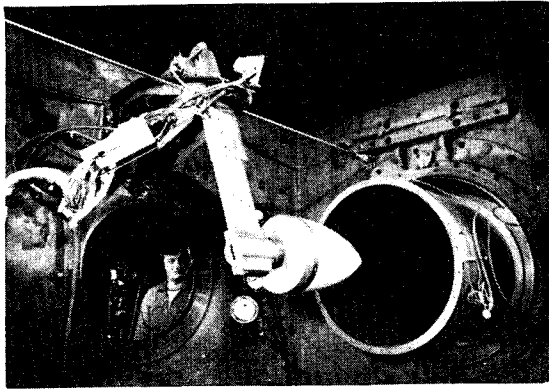
Fig. 1 — Slip-cast fused silica radome assembly in the
S4-MA hypersonic wind tunnel of ONERA at Modane.
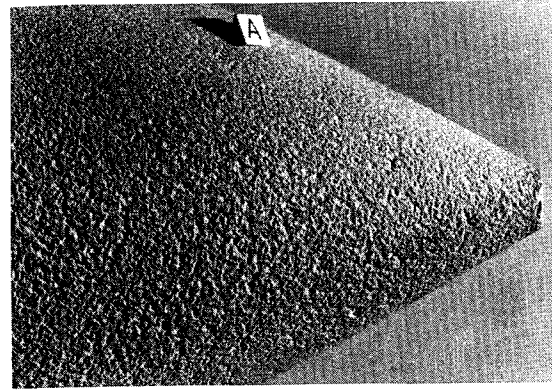
Fig. 2 — Surface aspect of windwardregion of slip-cast
fused silica radome after 33 s test in the wind tunnel.
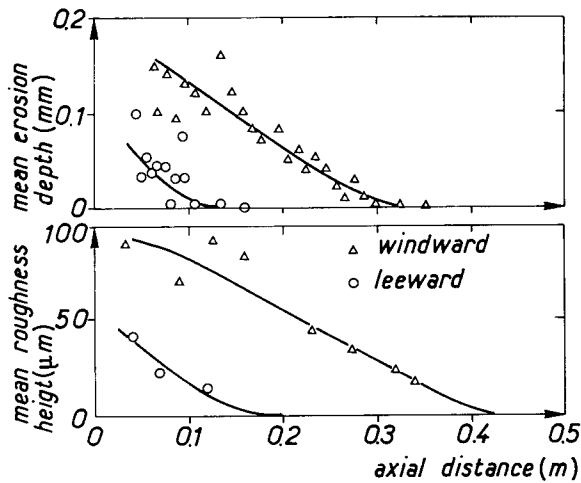
Fig. 3 — Radome post test analysis : mean erosion
depth (up) and mean roughness height (down)
versus axial distance.
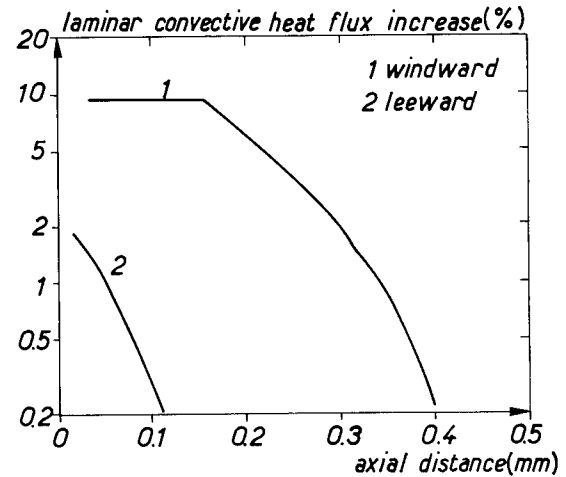
Fig. 4 — Laminar convective heat flux increase due to
roughness for wind conditions (M_∞= 6, P_{stag} = 25.10^5
Pa, T_{stag} = 1650 K) at the time t= 30 s.
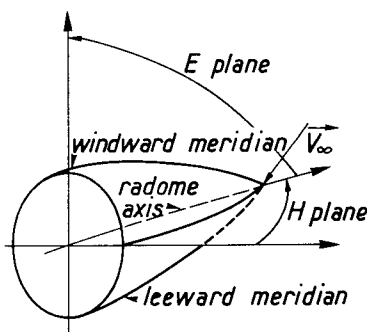
Fig. 5 — Relative position of wind-
ward and leeward meridians, and
E and H planes.
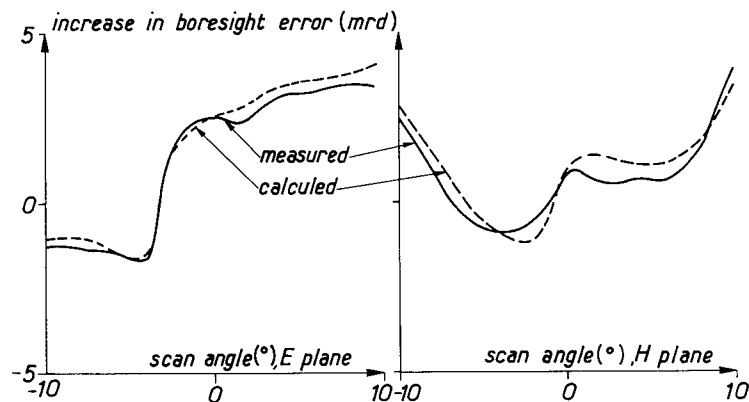
Fig. 6 — Increase in boresight error due to erosion versus scan angle, in E plane
(left) and H plane (right).

101

MACH-4 RAIN EROSION TEST OF SINTERED β-SIALON

by

Peter L. Land
Air Force Materials Laboratory
Wright Patterson AFB, Ohio 45433

Introduction

This paper describes the results of rain erosion testing of sintered β-sialon, a compound described chemically as $Si_{6-x}Al_xO_xN_{8-x}$, which was formed by reacting Si_3N_4 with equal molar parts of Al_2O_3 and AlN in a nitrogen atmosphere, 25 psi, at about $1775^{\circ}C$. The crystallographic structure of β-sialon is the same as that of $\beta-Si_3N_4$ and the properties are similar, which makes β-sialon a candidate radome material. The main advantage of β-sialon is that it can be sintered to about 98% of the theoretical density without pressure, whereas the sintering of Si_3N_4 has until recently required both sintering aids and pressure.

The powder mixtures used in fabricating the test specimens were prepared by Gatti and Noone of the General Electric Company under an Air Force contract. The three compositions used are GE-128 (65 w/o Si_3N_4), GE-129 (84 w/o Si_3N_4) and GE-130 (87 w/o Si_3N_4). (1) The specimen densities ranged from 2.94 to 3.34 gm/cm^3, both below and above the theoretical density which for this composition is between 3.10 and 3.17 gm/cm^3. (2)

Additional tests and evaluation results on β-sialon are contained in the following paper and in Reference 3.

Experimental Conditions

The rain erosion tests were performed at Holloman Air Force Base under the direction of G. F. Schmitt of AFML/MBE, who has previously described in detail procedures and results of this kind of testing. (4) The test conditions were: rain rate 2.52 in/hr, mean drop size 1.37 mm diameter, average velocity 4213 FPS for a period of 0.44 seconds and the rain field length was 2000 feet. The samples were tested at the most severe of the four available conditions, GE-128 at 60°, GE-129 at 45 and 60°, and GE-130 at 45 and 60° angle of incidence, because it was expected that the material could withstand the conditions.

Fracture of Rain Erosion Specimens

Unfortunately all of the specimens failed by fracture, resulting from vibrations set up in the samples by the rain field or the sled. There was, however little or no erosion except in areas where edges were provided by fracture or by scratches in the sample surfaces. The largest amount of erosion not ascribable to edge chipping occurred on the lowest density sample for a 60° angle of incidence as would be expected.

Figures 1-4 constitute a study of the fracture of GE-129-1 which was tested at a 45° angle of incidence. The numbers 1, 2 and 3 are placed near the first and subsequent points of fracture initiation. The first fracture, which branched at the point marked Br, is identifiable as the first by the continuity of the fracture markings and the fact that the subsequent fractures terminate in the first fracture surface. Fractures 1 and 2 clearly originated at subsurface processing flaws. According to the fracture markings, fracture 3 also occurred at a subsurface flaw, at about the same depth as fracture 1, but the origin was eroded away by rain.

103

The fracture markings shown in Figures 1-4 diverge from the subsurface processing flaws. Each fracture surface exhibits characteristics which suggest that the crack front advanced under the influence of an oscillating intensified tensile stress. (The intensification at the crack front results because the fractured zone cannot transmit tensile stress.)

The fracture origins 1 and 2 in GE-129 are a 300 micron diameter pull-out or pore and a 170 X 670 micron inclusion pull-out. Scanning electron microscope in conjunction with energy dispersive analysis by X-rays showed the flaw causing the first fracture to be an iron inclusion. The nature of the second fracture was undermined because half of the fracture origin was missing. Both fractures had steps in the fracture radiating from the flaw which suggest that the fracture initiated at several locations on the flaw perimeter.

Three of the five rain erosion samples have fracture surfaces like those shown in Figures 1-4. In all cases there is an undulating concentric fracture pattern consisting of smooth and sharply curved ridges and valleys. At the sharply curved locations, the crest of a ridge or the bottom of a valley, radiating steps or ridges frequently occur. The sharp ridges and valleys are probably a result of crack arrest and recurrance where the critical stress recurred across a differently oriented surface and where the crack growth conformed to the new stress situation in a very short distance. The radiating steps or ridges, called hackel or lances, are probably a result of rotation of the principal tensile stress in the plane normal to the general direction of crack propagation at that location. (5)

The fracture features observed here are unusual, but they are not unique. Behat has observed very similar features which occurred during the third stage of a thermally induced fracture of glass. (6) In that case the second stage fracture induced vibrations into the fragments which subsequently fractured in concentric undulating patterns centered on damaged areas where the glass contacted the alumina crucible in which it was cooling. Similar features can be seen on reaction sintered Si_3N_4 and pyroceram fractured in an earlier rain erosion test but the fracture features were not discussed at that time. (4)

Figures 5 and 6 show samples GE-130-1 and GE-130-2 which were exposed at 45 and 60° angles of incidence, respectively. Both have fracture features like those already shown. In each case the eroded area is shown to be contiguous with a fracture or to be associated with surface scratches which indicates that undamaged surface does not erode appreciably under the test conditions, with the possible exception of GE-130-2 at 60° angle of incidence. These figures also show that the samples fractured under the retainer as a result of either vibration or crack branching.

Strength and Fractography of 4-Point Bend Specimens

Six flexure samples, 1/8 X 1/4 X 1 inch, were taken from each of the blocks of GE sialon prepared for rain erosion testing. Two of each set of six were tested at AFML. The remaining samples were sent to IIT Research Institute where the high temperature strength will be measured and documented.

The room temperature strength data can be summarized as follows: For 4 bars of GE-128 the average strength was 23,000 psi and the range was 13,000 to 33,000 psi. For 8 bars of GE-129 the average strength was 32,200 psi and the range was 19,000 to 50,000 psi. For 10 bars of GE-130 the average strength was 35,200 psi and the range was 21,000 to 48,000 psi. The average strength of the

GE-129, and probably that of the GE-130, was substantially lowered by scratches which occurred while the specimens were being ultrasonically machined. It is expected that fine grinding to remove scratches would have increased the average strength substantially. For example, Wills et al, found that the average strength of 50 m/o Si_3N_4 β-sialon increased from 50,000 to 70,000 psi when samples were finely ground. (5)

The fracture surfaces of the flexure bars were examined in order to locate and characterize the fracture origins. In only one case out of 22 was the origin a large flaw comparable to those shown on the fracture surfaces of GE-129-1. Large flaws increasingly dominate fracture as the stressed volumn increases. The difference in observation frequency of large flaw induced fracture can be explained by the decrease in tensile stress with depth in flexure bars and the contribution of surface damage, which typically biases fracture to within 100 microns of the surface, whereas the typical depth of the fracture origins of the rain erosion samples was more than 1000 microns below the exposed surface.

Conclusions

The most important conclusion from these observations is that the samples failed from vibration rather than from erosion. A more nearly representative test for erosion might result if compliant material such as lead foil were utilized as a gasket between the sample and the mount in order to dampen sample vibrations. Since the samples failed from vibration it seems likely that radomes may fail in a similar manner. A study of fracture surfaces of radomes might reveal features likes those observed here in which case measures to dampen vibrations would be in order.

The samples tested contained large processing flaws which caused failure at stress levels estimated to be below 10,000 psi. Since radomes are required to survive stresses greater than 10,000 psi it is essential that large processing flaws be eleminated before sialon can be utilized.

The conclusion from these tests is that sintered sialon having near theoretical density can survive a mach 4 rain field as described with little or no erosion when the finish is good, and when there are no exposed edges. This is consistant with other work to be presented by Meyer et al. at this conference, where sialon survived 600 meters of mach 5.5 rain at a 22.5° angle of incidence with no apparent damage.

References

1. A. Gatti and M. J. Noone, "Methods of Fabricating Ceramic Materials," Final Report AFML-TR-77-135 (1977).

2. P. L. Land, J. M. Wimmer, R. W. Burns and N. S. Choudhury, " Compounds and Properties of the System Si-Al-O-N," J. Am. Ceramic. Soc. 61, No. 1-2, 56-60 (1978).

3. P. L. Land and S. Holmquest, "Evaluation of β-Sialon for Radome Application," AFML-TR-78-79 (1978).

4. G. F. Schmitt, Jr., "Influence of Porosity and Density of the Supersonic Rain Erosion Behavior of Silicon Nitride Radome Materials," pp 37-44 in the Proceedings of the Thirteenth Symposium on Electromagnetic Windows, Sept. 21-23, 1976, Edited by H. L. Bassett and J. M. Newton, Georgia Institute of Technology, Atlanta, Georgia.

5. F. Kerhoff, "Wave Fractographic Investigations of Brittle Fracture Dynamics," pp. 3-35 in Dynamic Crack Propagation, Edited by G. C. Sih, Noordhoff, Leyden, The Netherlands (1972).

6. D. Behat, "Thermally Induced Wavy Hertzian Fracture," J. Am. Ceramic Soc., 60, No. 3-4, 118-120 (1977).

7. R. R. Wills, Private Communication, and "Sintered Silicon Nitride Based Ceramics, Processing and Engineering Properties," In the Proceedings of the 2nd Conf. on Composites and Advanced Material, Cocoa Beach, Fla, January (1978)
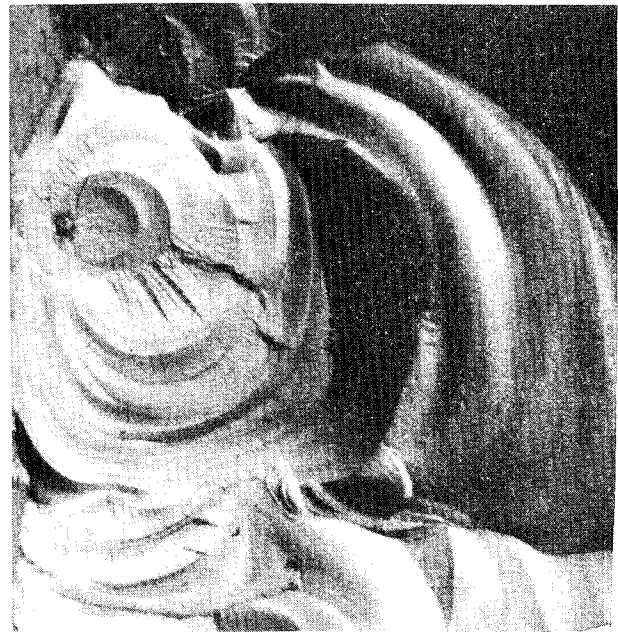
Figure 1.   GE-129-1, Rain at 45°, 3.5X   Figure 2.   GE-129-1, 2nd Fracture, 12X
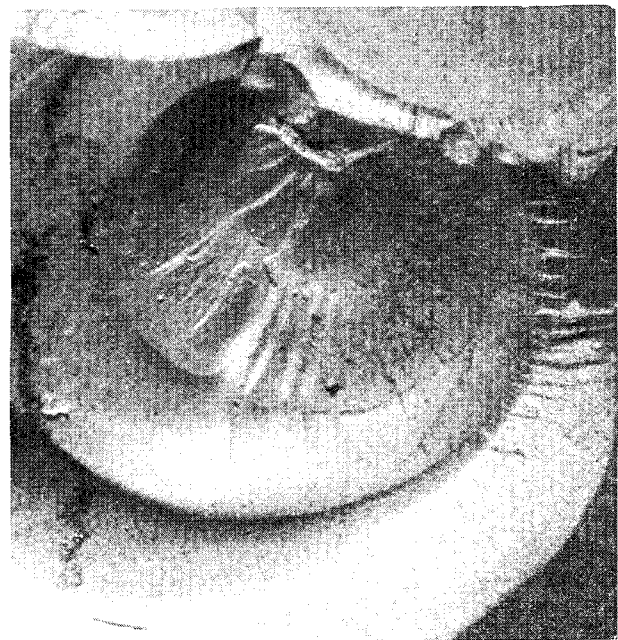
Figure 3.   GE-129-1, 1st Fracture, 4X   Figure 4.   GE-129-1, 1st Fracture, 16X

Figure 6. GE-130-2, Rain at 60°, 3.5X

Figure 5. GE-130-1, Rain at 45°, 3.3X

RAIN EROSION AND AEROTHERMAL SLED TEST RESULTS
ON RADOME MATERIALS

K. N. Letson, W. G. Burleson, and P. A. Ormsby

US Army Missile Research and Development Command

ABSTRACT

A summary of the results of the US Army MIRADCOM sled test program to characterize the rain erosion behavior of slip-cast fused silica and candidate plastic radome materials at supersonic velocities is presented.

INTRODUCTION

Twelve sled tests involving seven samples per test have been performed at the Holloman Sled Test Track to characterize the rain erosion behavior of ceramic and plastic radome materials. Tests were run at velocities that varied from Mach 3.7 to Mach 5 with samples that had half-angles ranging from 15- to 30-deg. The artificial rainfield had a mean rain rate of 67 mm/hr.

The MIRADCOM effort was initiated to evaluate the rain erosion behavior of natural high purity slip-cast fused silica (SCFS) as a function of velocity and angle of incidence for short times. Because SCFS has low fracture toughness and relatively poor rain erosion resistance the sled test program was enlarged to include other candidate ceramic and plastic radome materials in the interest of finding a tougher structure.

Two of the tests, which included ceramics other than SCFS, were a joint effort between MIRADCOM and the Army Materials and Mechanics Research Center (AMMRC). Results on ceramics, other than SCFS, from these tests are reported separately.

Because plastics aerothermally ablate at velocities near Mach 5, it was necessary to determine the thermal ablation component of recession in the rain erosion tests. To aid in doing this a test without rain was run.

Materials for which results are summarized include SCFS (with and without coatings and impregnants), cast epoxy polyurethane (AVCOAT 8027), a cast elastomeric fluorocarbon (AVCOAT 8028), laminated glass-polyimide, glass-silicone, Teflon, laminated fiber-reinforced Teflon (Duroid 5650 and 5870), molded fiber-reinforced Teflon (Duroid 5650M, 5650D and 5870M), and molded particulate-loaded fluorocarbon (AVCOAT 8029).

The sample carrier vehicle was designed to carry seven cone frusta that simulate actual radome shapes and to permit the testing of different shapes simultaneously.

Results from the tests of SCFS indicate that rain erosion varies as the normal component of velocity from a threshold value between 475 and 525 m/sec.

Results for the plastics show that aerothermal ablation was responsible for mass loss in the rain erosion tests that ranged from a high of 95% for the AVCOAT 8027 to a low of 30% for the Duroid 5650. The rain erosion performance of all plastics tested was superior to that of SCFS. However some of the plastics ablated excessively or formed a significant char thickness.

EXPERIMENTAL PROCEDURE

The MIRADCOM rain erosion test vehicle (Fig. 1) was designed for use in testing seven cone frusta at velocities up to Mach 6. This vehicle consists of a hollow steel cone frustum with a 15-deg half-angle. Six struts are welded into slots through the cone wall. Pads welded to the front of the struts serve as base mounts to which sample subassemblies are attached. The seventh sample subassembly is mounted to the front of the center cone frustum. The sample subassembly (Fig. 2) consists of the material specimen held between a stainless steel raincap and base.

The Holloman rocket sled track is 15500 m long, of which 5500 m is equipped with nozzles for rain simulation. Monorail sleds are used for rain erosion tests. All rain erosion tests utilized 610 m of the available rainfield except two of the early tests of SCFS. Test No. 2 utilized 1100 m and Test No. 3 utilized 850 m. The artificial rainfield provided a mean liquid water content (density) of 3.1 gm/m^3, a mean rate of 67 mm/hr and a mass median drop diameter of 1.37 mm. Satisfactory velocity profiles, with peak velocity occurring at the midpoint of the rainfield, were achieved for each test through proper selection of firing points, staging, and combinations of rocket propulsion units.

TEST RESULTS FOR SCFS

In the early tests (1,2)*, mass loss to some of the SCFS samples was caused by a combination of sled vibration and rain impact at sample edges. Mass loss due to these causes is not included in the results reported. Changes made to sample base and mounting procedure successfully eliminated mass loss due to these spurious causes.

To prevent moisture absorption and its attendant effects upon dielectric constant and structural response, SCFS radomes are usually coated or impregnated with solvented silicone resins such as DC808 or GE SR80. Two samples that were impregnated with GE SR80 resin experienced erosion that fell slightly above the upper bound of the scatter of data obtained for bare SCFS. One sample of SCFS that was coated with DC808 showed no significant difference in erosion from that experienced by bare SCFS.

*Denotes references.

110

However, the normal component of velocity for this sample was below the threshold. Measurable but minimal erosion occurred on samples tested at velocities below this threshold.

Rain erosion results from tests of thirty eight SCFS samples including those coated and impregnated with silicone resins discussed above are presented in Fig. 3. All samples had a density of 1.95 ± .03 gm/cc. Maximum and mean depth of erosion were determined for each sample. Maximum erosion rate for each of the thirty eight samples is presented (Fig. 3) as a function of the normal component of velocity (V sin θ), where V is the average velocity in rain and θ is the angle of incidence (sample half-angle). The data from samples with significant erosion are bounded by two line segments that show the scatter of data differs by less than a factor of 3. This variation is considered normal due to the low fracture strength of SCFS and the variability of the rainfield. These line segments intersect the abcissa at 475 and 525 m/sec and indicate that the rain erosion threshold or a discontinuity in the rain erosion rate occurs in this neighborhood. Fig. 4.a. is a photograph of a 15 deg half-angle sample of SCFS that was tested at Mach 5 (V sin θ = 450 m/sec (<Threshold Velocity)). As shown, minimal erosion occurred. The sample shown in Fig. 4.b. experienced rain at a normal component of velocity (495 m/sec) near the erosion threshold. A few pits resulted. Fig. 4.c. shows the result for a normal component of velocity (650 m/sec) which would clearly cause catastrophic failure of a radome. This sample did not disintegrate because of special mounting techniques (2).

Because SCFS has low fracture toughness and its erosion rate proceeds in an exponential manner after reaching the threshold velocity, the risk of catastrophic failure of SCFS radomes is considered unacceptably high at any velocity above this threshold.

TEST RESULTS FOR PLASTICS

Analysis of the rain erosion behavior of plastics at a velocity of Mach 5 is complicated by the loss of material due to aerothermal ablation. To separate the mass loss due to each of these causes, a sled test without rain was run, also, to provide data on aerothermal ablation (3).

Table 1 lists results for candidate plastic radome materials that were tested in the supersonic sled tests. Data presented are for samples with cone half-angles of 22.5-deg that were tested at a nominal velocity of Mach 5 either through 610 m of rain or without rain. Aerothermal analyses of sample behavior in the "dry" test were performed, and the math model was modified to obtain agreement between calculated and measured ablation (4). These data and procedures were then used to determine the separate effects of aerodynamic heating and rain erosion on material mass loss.

The tabulated data show that the AVCOAT 8027 has excellent rain erosion resistance but thermally ablated excessively, that glass-polyimide and glass-silicone have good rain erosion resistance but form a carbonaceous surface char, that AVCOAT 8028 and AVCOAT 8029 (Fig. 5) have good combined ablation and erosion resistance, and that the best performance (noncharring, and minimum ablation and rain erosion) was by the fiber-reinforced Teflon materials (Duroid 5650, 5870, 5650M, 5870M). Duroid 5650 (laminate) and 5650M (molded) contain alumina silicate reinforcing fibers. Duroid 5870 (laminate) and 5870M (molded) contain glass reinforcing fibers. Duroid 5650 (Fig. 6.a.) exhibited the greatest resistance to aerothermal ablation while Duroid 5870 was more resistant to rain erosion and combined rain erosion and aerothermal ablation. All materials with reinforcement were tested with the direction of reinforcement being normal or nearly normal to the outside surface except sample No. 9 - 7 which had the reinforcing fibers oriented normal to the base and sample No. 12 - 7 which had laminae parallel to its surface. While the molded Duroid materials, 5650M (Fig 6.b.) and 5870M, were not tested without rain, their performance was similar to that of the laminated Duroids. The low pressure molding, Duroid 5650D, did not perform as well as the high pressure moldings, 5650M or 5870M, and also had a delamination that occurred during manufacture. Teflon was tested primarily as a reference material.

CONCLUSIONS

1. The rain erosion threshold or discontinuity in the erosion rate profile for high purity SCFS (Density = 1.95 $\pm$ .03 gm/cc) occurs at a normal component of velocity between 475 and 525 m/sec for rainfields equivalent to the artificial rainfield at Holloman.

2. At a normal component of velocity above the threshold point, the risk of catastrophic failure of a SCFS radome is unacceptably high.

3. Silicone resin moisture sealants DC808 and GE SR80 probably do not significantly affect the rain erosion behavior of SCFS. (More test data is needed). However, conclusion 2 makes this information of academic interest only.

4. All plastics tested possess superior rain erosion resistance to that of SCFS.

5. All plastics tested will experience significant aerothermal ablation at Mach 5.

6. The high pressure molded and laminated reinforced Teflon materials gave the best performance (noncharring and minimum ablation and rain erosion) of all materials tested.

REFERENCES

1. Letson, K. N. and Ormsby, P. A., "Hypersonic Multi-Sample Testing of Ceramic Radome Materials in Simulated Rain," Proceedings of the Third International Conference on Electromagnetic Windows, Paris, France, 10-12 Sep 1975.

2. Letson, K. N. and Ormsby, P. A., Rain Erosion Testing of Slip Cast Fused Silica at Mach 5," ASME Paper 76-ENAs-6, April 1976.

3. Letson, K. N., Burleson, W. G., and Ormsby, P. A., "Aerothermal and Rain Erosion Behavior of Selected Candidate Plastic Radome Materials in Mach 5 Sled Tests," ASME Paper 77-ENAs-16, 25 March 1977.

4. Burleson, W. G., "Evaluation of Aerothermal Ablation and Rain Erosion Results for Plastic Radome Materials Tested on Sleds at Mach 5," MICOM Technical Report RL-77-3, 10 Dec 1976.

NOTE: The discussion of materials by brand names or suppliers in this report is in no way to be taken as an endorsement or criticism by the Government. The use of brand names is the most convenient way of identifying them. The Government incurs no liability or obligation to any supplier of materials from the information included in this report. The authors express their appreciation to those individuals and companies who supplied materials for testing.

TABLE 1. Performance of Plastics in Mach 5 Sled Tests[a]

Material	Test No.-Sample No.	Material Density (g/cm³)	Pretest Sample Weight (g)	Weight Loss (g)	Maximum Depth of Penetration (mm)	Average Depth of Penetration (mm)	Calculated Aerothermal Ablation (%)	Sample Supplier Or Manufacturer
Teflon	4[b]-7	2.15	97.34	14.98	4.06	1.66	52	MIRADCOM
	6-5		96.96	8.87	1.30	1.01	100	MIRADCOM
AVCOAT 8027	6-1	1.3	60.94	21.02	3.55	5.10	100	AVCO, Inc.
	7-1	1.3	61.04	19.68	3.32	3.56	95	AVCO, Inc.
AVCOAT 8028	7-5	2.05	91.83	14.60		1.70	100	AVCO, Inc.
AVCOAT 8029	9-6	2.15	107.12	13.17	2.39	1.46		AVCO, Inc.
Glass-Polyimide	6-6[c]	1.8	80.40	2.31	0.79+.7 char	0.31+.7 char	100	Texas Instruments, Inc.
	7-6[c]		80.25	9.13	1.91+.5 char	1.21+.5 char	30	
Glass-Silicone	12-7[d]	1.8	52.60	10.34	1.50+.89 char	1.37+.89 char		MIRADCOM
Duroid 5650	6-3	2.15	99.25	3.65	0.58	0.40	100	Rogers, Inc.
	7-3		98.97	11.98	1.63	1.36	30	
	9-1		103.85	9.76	1.60	1.08	30	
Duroid 5650M	9-3	2.15	110.40	10.87	1.27	1.20	30	Rogers, Inc.
Duroid 5650D	9-5	2.15	103.72	12.61	2.79	1.40		Rogers, Inc.
Duroid 5870	6-4	2.15	96.70	5.58	0.96	0.62	100	Rogers, Inc.
	7-4		97.18	7.46	1.12	0.83	70	
	9-2		106.26	6.05	1.02	0.67	70	
	9-7[e]		106.89	6.29	1.63	0.70	70	
Duroid 5870M	9-4	2.15	107.30	8.00	1.12	0.89	70	Rogers, Inc.

NOTES: a. All samples had a cone half-angle of 22.5-deg.
　　　　 b. Rainfield length was 610 m for all tests except test 6 which was run without rain.
　　　　 c. Fiber laminae were oriented normal to sample surface.
　　　　 d. Fiber laminae were oriented parallel to sample surface.
　　　　 e. Fiber laminae were oriented normal to sample base.
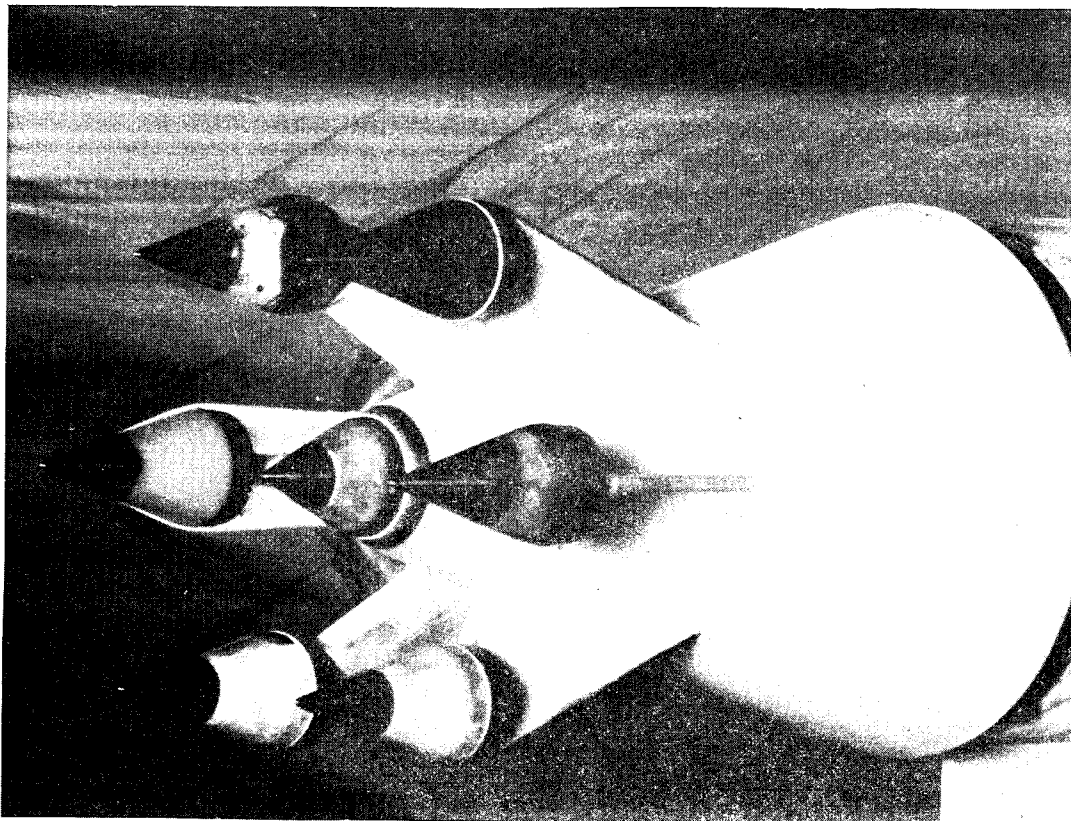
FIGURE 1. MIRADCOM RAIN EROSION TEST VEHICLE WITH SAMPLES IN SUPERSONIC SLED TEST

114
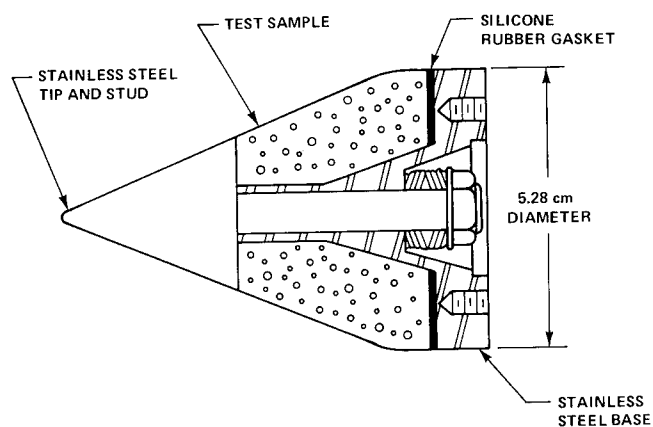
FIGURE 2. SAMPLE SUBASSEMBLY
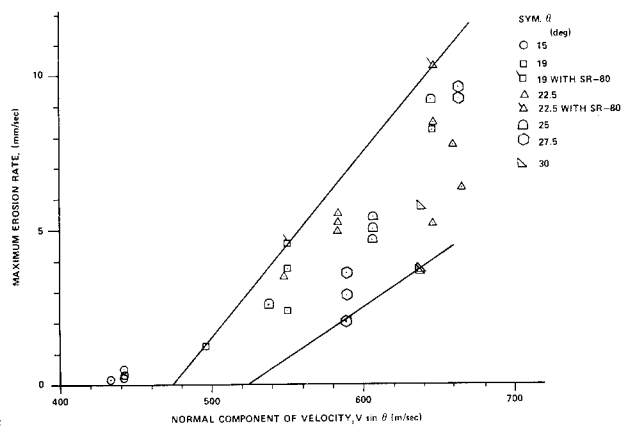
FIGURE 3. MEASURED MAXIMUM EROSION RATE OF SCFS
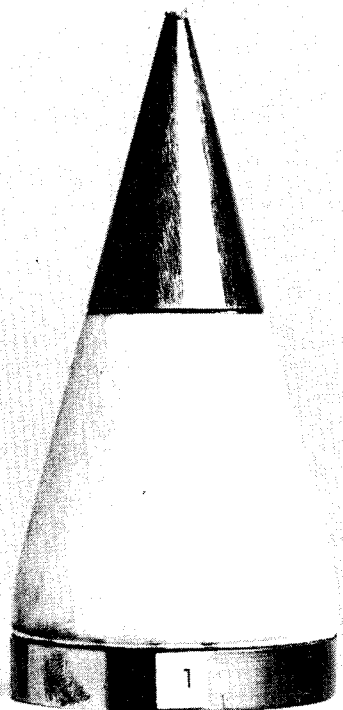
FIGURE 4a. SCFS AS TESTED IN RAIN AT
Vsin θ = 450 m/sec (< THRESHOLD VELOCITY)
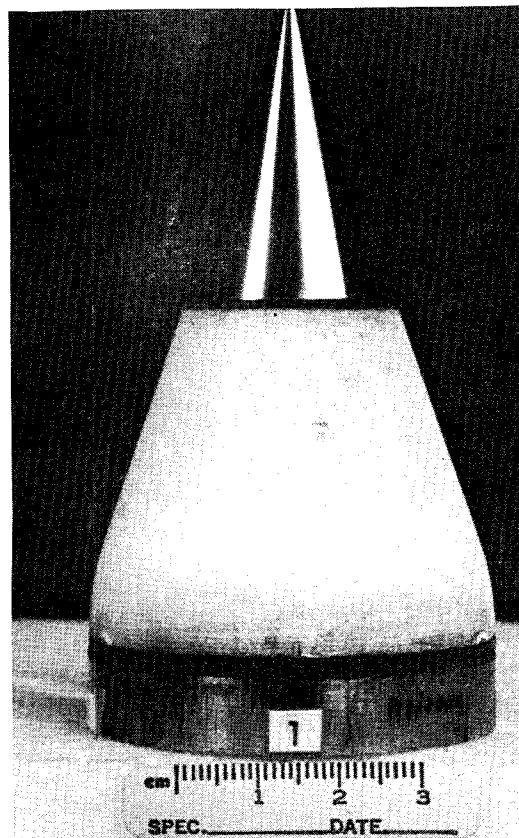
FIGURE 4b SCFS AS TESTED IN RAIN AT Vsin θ = 495 m/sec ($\geq$ THRESHOLD VELOCITY)

115
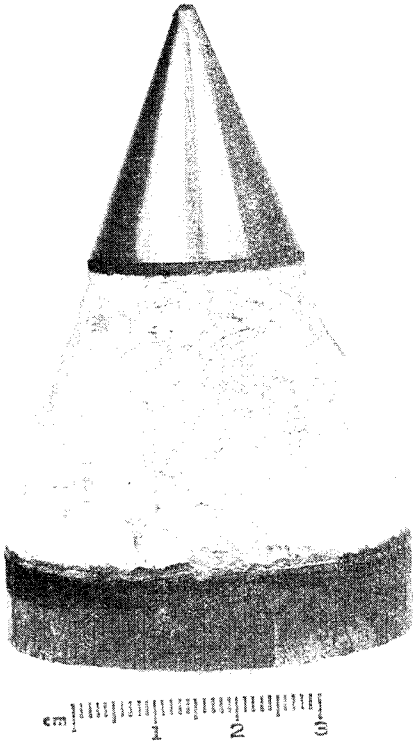
FIGURE 4C. SCFS AS TESTED IN RAIN AT Vsin θ = 660 m/sec (> THRESHOLD VELOCITY)
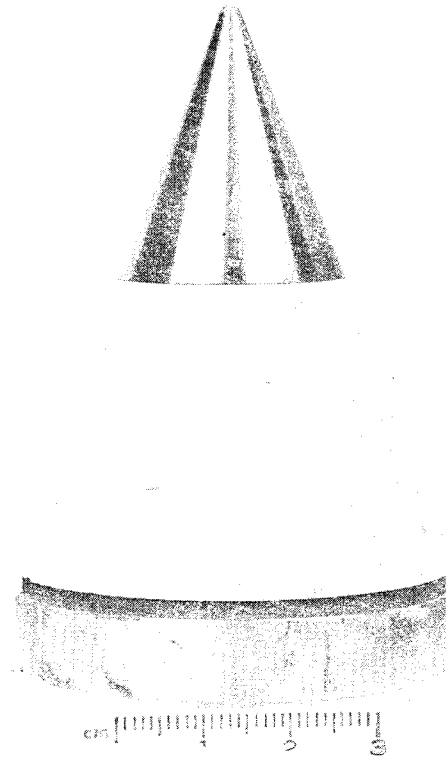
FIGURE 5. AVCOAT 8029 AFTER RAIN EROSION AND AEROTHERMAL ABLATION
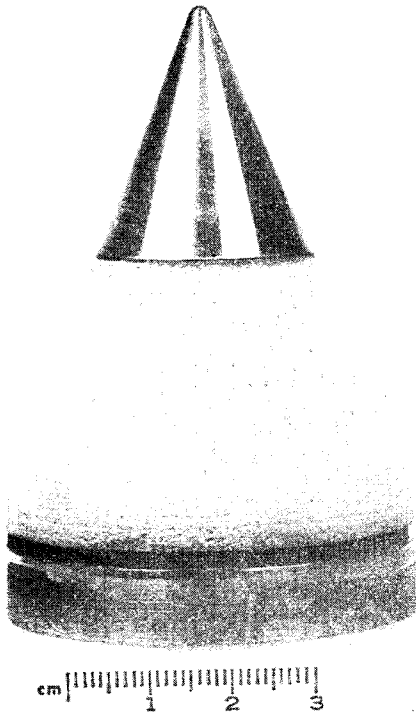
FIGURE 6b. DUROID 5650M AFTER RAIN EROSION AND AEROTHERMAL ABLATION
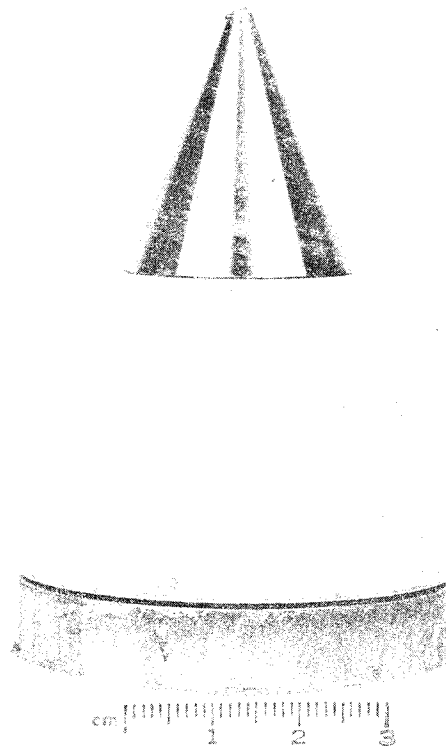
FIGURE 6a. DUROID 5650 AFTER AEROTHERMAL ABLATION

116

Evaluation and Testing of New Ceramic Radome Materials

by

F. P. Meyer

U. S. Army Materials & Mechanics Research Center
Watertown, Massachusetts

&

P. A. Ormsby & K. N. Letson

U. S. Army Missile Research & Development Command
Redstone Arsenal, Alabama

INTRODUCTION

During a recent detailed study of the rocket sled rain erosion testing of slip cast fused silica (SCFS) by Letson and Ormsby (1) it was determined that for a cone half-angle of 19° or more, severe damage was suffered by SCFS at MACH 5. Even for a radome with a 15° half-angle it will incur this damage as it turns and maneuvers during flight through a rain cloud. A preliminary sled test sample of hot pressed silicon nitride (HPSN) run by Letson and Ormsby however exhibited excellent erosion resistance. At MACH 5.5 thru 610 meters of rain there was no surface erosion of the sample whatsoever. This was the best erosion resistance exhibited by any material tested to-date. The high costs associated with fabricating and machining HPSN led to a program to test and evaluate other new state-of-the-art ceramic materials for application as tactical missile radomes.

PROCEDURE

The principal objective of this program was to test and evaluate a series of nitrogen-based ceramics for radome applications. These included not only the HPSN but also the newer sintered silicon nitrides (SSN) and also a silicon aluminum oxynitride (SiAlON). A sample of reaction sintered silicon nitride was also obtained for this study as this material has received much attention in the past two years. Additionally, two samples of hyper-pure SCFS were obtained; this material has recently been developed as a reflective heat sheild for re-entry vehicles (2). Table I. lists the materials tested, their fabrication processes and some physical properties.

Each of the materials used in this study were supplied as small radome frustra suitable for mounting on the MIRADCOM rocket sled test fixture at Holloman, AFB, New Mexico for rain erosion testing at MACH 5.5. Whenever possible additional samples were obtained for dielectric constant and loss tangent measurements from room temperature to $1230^{\circ}C$. All dielectric measurements were made by Microwave & Electronics Consultants of Atlanta, GA. at 9.375 GHz by the shorted wave guide technique.

Each of the samples were also measured for bulk density and powder patterns run to determine the principal phases present. Some of the data on these samples is considered company confidential and has been omitted from the table.

RESULTS and DISCUSSION

The dielectric constant and loss tangent data from room temperature to $1230^{\circ}C$ are plotted in Figures 2 & 3. Both samples of sintered silicon nitride and the SiAlON sample show fairly low and very stable dielectric constants over the temperature range. The loss tangents are also low and very temperature stable. The data for HPSN has previously been reported by Messier and Wong (3) as well as much data on reaction sintered material. The HPSN samples exhibited a slightly higher dielectric constant over the temperature range that did the SiAlON or sintered materials, however, the HPSN was less lossy.

For the sintered silicon nitride materials, Gazza (4) gives an excellent review of the techniques and additives used to get high fired densities and strengths in this material. In particular, up to 20 w/o of certain additives are needed to obtain a density level of above 90% of theoretical in the final piece. Although the exact additive and level of addition is not known in each case at least the dielectric constant data shows that relatively large amounts of additions can be tolerated and still yield rather low and very stable dielectric properties in sintered silicon nitride.

Reaction sintered silicon nitride was shown by Messier and Wong (3) to be suitable for radome applications with its dielectric properties. The material used in this study was not submitted for dielectric testing but these properties have been compiled by Waugh (5).

Similarly, the hyper-pure fused silica material was not tested for dielectric properties here but this data is compiled by Ruhmann (6).

Results of the rocket sled rain erosion testing of these materials is shown in Figures 1,4,5 and 6. All samples were run at Holloman AFB attaining a maximum speed of 1772 meters per second, approximately MACH 5.5, and were subjected to 610 meters of rain. The rain rate was 67 mm/hr with an average rain drop size of 1.37 mm. A very thorough description of the test facility is given by Letson and Ormsby (1).

For HPSN two samples were run, the first a 22.5° radome frustrum and the second a full scale rain cap configuration (also 22.5° cone angle) as shown in Figure 1. The radome frustrum showed no surface

erosion whatsoever. The rain cap sample had a maximum depth of erosion of approximately 3.8 mm at the area of normal impact. The rain cap sample had previously been subjected to an aerothermal heating run in which it was sled tested at MACH 5.5 but without rain. This was done to determine the effects, if any of the aerodynamic heating or ablation that might take place. There was no effect on the sample.

The SiAlON material also exhibited no surface erosion whatsoever. Its erosion resistance was equal to the HPSN and both are outstanding. This was also a 22.5° radome frustrum configuration.

Although the two samples of sintered silicon nitride showed very little if any surface erosion, Figure 6, each did crack during the sled test. High speed photographs taken just before entrance into the rain field by the rocket sled show both samples intact so each cracked while in the rain field. All cracks extended completely through the thickness of the sample and it was the sample holder that kept the large sections of material from being lost. The only surface erosion evident was a small amount that occurred at the crack surfaces. The sample of SSN with a rare earth sintering aid had two cracks each of which extended from the tip of the sample to ite base. The SSN with MgO as an additive had one circumferential crack approximately half way down with two longitudinal cracks extending from the tip of the sample down only to the circumferential crack. The entire lower half of this sample was crack and erosion free. Again, the only surface erosion occurred after the cracks had formed and at the surface of the cracks. It is possible that vibrations from the sled could have cracked the samples but this has not as yet been confirmed. Further investigation of the failure mechanism will be done but the fact still remains that there was no surface erosion on these samples except when the cracks occurred. Without cracking the erosion resistance of these two materials would have equalled HPSN and SiAlON.

The sample of reaction sintered silicon nitride was severely eroded and 37.3% of the total sample was lost during the test. This sample had a density of 2.30 g/cc and had not been surface sealed. Large chunks of sample are missing around its base and the size of the fracture surfaces indicate that these pieces were removed intact.

The two samples of hyper-pure slip cast fused silica were almost completely lost during the test. Only approximately 5% of the samples remain. The low density sample (1.87 g/cc) was well below the density level at which fused silica is normally fabricated, i. e. 1.96 g/cc. The other sample was more dense than normal at 2.02 g/cc. Neither sample had been surface sealed or resin impregnated. No detailed explanation can be given as yet for the poor erosion resistance of this material. It should be made clear however, that this material is being developed for its high reflectivity properties and not for its strength, density or erosion resistance. The investigators felt that erosion data on this material would be of value as it does represent a purity level not achieved before in slip cast fused silica.

CONCLUSIONS

Hot pressed silicon nitride was shown to have unexcelled rain erosion resistance when tested through 610 meters of rain a MACH 5.5. The dielectric properties of this materials are acceptable and suitable for tactical missile radome and rain cap applications.

The SiAlON material also showed no surface erosion or cracking after seld testing. Its dielectric properties are suitable for radome applications and this material was sintered as opposed to hot pressed which makes it extremely attractive from a "cost of fabrication" aspect.

Sintered silicon nitride, either with MgO or a rare earth added as a sintering aid exhibited excellent erosion resistance but did crack catastrophically during the test. The dielectric properties of these materials are well within the design limits for radomes even with a substantial amount of additives. These materials are also sintered rather than hot pressed. Further refinements in the fabrication of this material should show it to be a prime candidate for high performance flight applications.

Reaction sintered silicon nitride showed poor erosion resistance at MACH 5.5 through 610 m of rain at an angle of 22.5°. Higher density and correspondingly higher strength samples may show improved performance.

Hyper-pure slip cast fused silica at densities of 1.87 and 2.02 g/cc showed very poor erosion resistance.

Continued studies on the erosion resistance and dielectric properties of new and unique ceramic materials is warranted as major developments are made quite frequently and data must be obtained on these materials as quickly as possible. Data such as is presented here may help to stimulate further developments in sintering silicon nitride with radome applications as the foremost objective rather than optimizing high temperature and fatique properties for turbine engine applications as is now the case.

REFERENCES

1. Letson, K. N. and P. A. Ormsby, "Rain Erosion Sled Tests of Radome Materials at MACH 5", RL-76-19, U. S. AMIRADCOM, Redstone Arsenal, Alabama, April, 1976.
2. Blome, J. C. et. al., "High Purity Silica Reflective Heat Shield Development", NASA CR-137617, McDonnell Douglas Astronautics Co., St. Louis, MO., October, 1974.
3. Messier, D. R. and P. Wong, " Silicon Nitride: A Promising Material for Radome Applications", AMMRC-TR-74-21, Army Materials & Mechanics Research Center, Watertown, MA., Deptember, 1974.

4. Gazza, G. E., "Sintered Silicon Nitride", in "Ceramics for High Performance Applications - II", Proceedings of the Fifth Army Materials Technology Conference, Newport, RI, March 1977. (to be published).

5. Waugh, J. S. and M. M. Jaremchuk, "Reaction Sintered Silicon Nitride Material Optimization for Radome Applications", AFML-TR-76-182 (CONFIDENTIAL), Air Force Materials Lab, WPAFB, OH 45433, November 1976.

6. Ruhmann, D. C., Pionke, L. J., Brandon, H. J. and R. E. Plummer, "Laser Hardened Aircraft Radomes", AFML-TR-77-12, (SECRET), Air Force Materials Lab, WPAFB, OH 45433, February 1977.

Table I. Processing and Physical Properties of Rain Erosion Samples

Sample	Fabrication	Additive	Major Phase	Density
Hot Pressed Si_3N_4	Cold Pressed & Hot Pressed	5% MgO	Beta-Si_3N_4	3.18g/cc
Sintered Si_3N_4	Cold Pressed & Sintered	- MgO	Beta-Si_3N_4	3.29
Sintered Si_3N_4	Cold Pressed & Sintered	Proprietary (rare earth)	Beta-Si_3N_4	3.31
SiAlON	Isostatically Pressed & Sintered	Proprietary	Proprietary	3.14
Reaction Sintered Si_3N_4	Isostatically Pressed & Sintered	3% Fe_2O_3	Beta-Si_3N_4	2.30
Hyper-Pure SCFS	Slip Cast & Sintered	None	Amorphous Fused Silica	1.87
Hyper-Pure SCFS	Slip Cast & Sintered	None	Amorphous Fused Silica	2.02

Table II. Results of Rocket Sled Rain Erosion Testing of Ceramic Radome Materials

Sample	Density	% Eroded	Comments
Hot Pressed Silicon Nitride	3.18g/cc	0.0%	No surface erosion or damage
Sintered Silicon Nitride	3.29	0.1%	No surface erosion; catastrophic cracking longitudinally and circumferentially
Sintered Silicon Nitride	3.31	0.4%	No surface erosion; catastrophic cracks longitudinally
SiAlON	3.14	0.0	No surface erosion of damage
Reaction Sintered Silicon Nitride	2.30	37.3%	Severe erosion; large segments missing
Hyper-Pure SCFS	1.87	96.0%	Sample nearly totally gone
Hyper-Pure SCFS	2.02	94.1%	Sample nearly totally gone
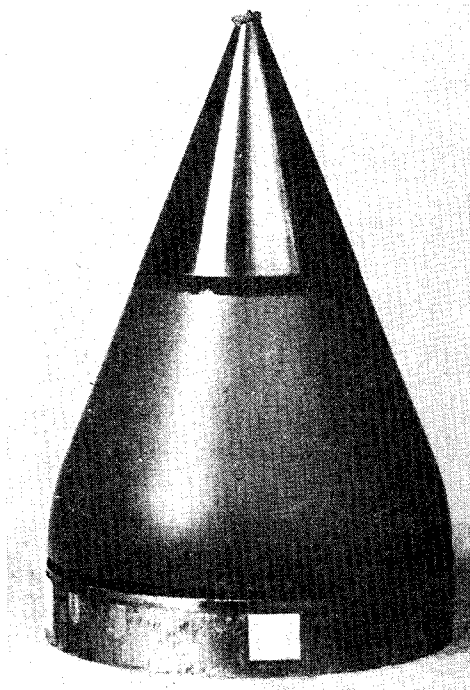
POST TEST RADOME SAMPLE - HOT-PRESSED SILICON NITRIDE   POST TEST RAIN CAP SAMPLE - HOT-PRESSED SILICON NITRIDE
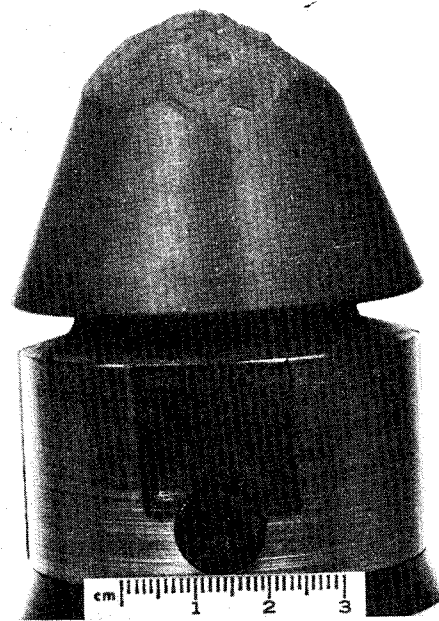
V = 1800 m/sec, 610-m Rainfield, Rain Rate = 67 mm/hr, Median Rain Drop Size - 1.4 mm, Normal Impact
Figure 1. HOT-PRESSED SILICON NITRIDE SLED TEST SAMPLES
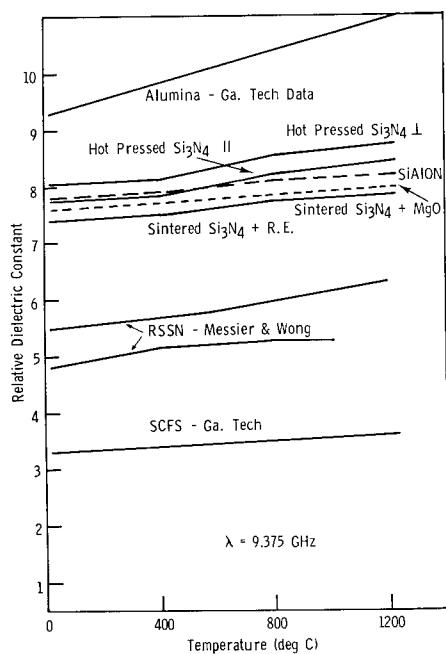
Figure 2. RELATIVE DIELECTRIC CONSTANT VERSUS TEMPERATURE FOR CANDIDATE RADOME MATERIALS
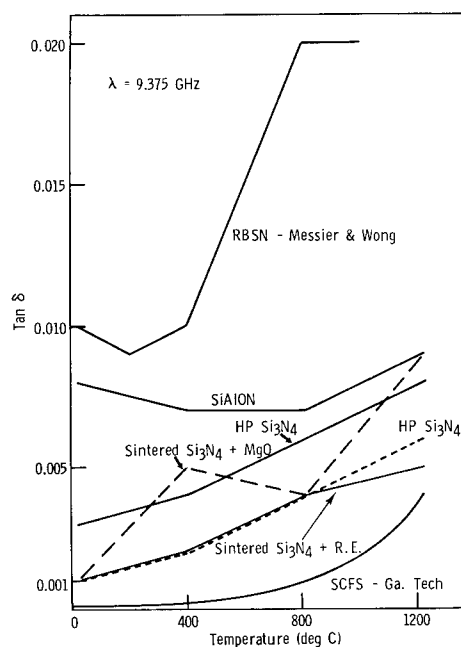
Figure 3. LOSS TANGENT VERSUS TEMPERATURE FOR CANDIDATE RADOME MATERIALS
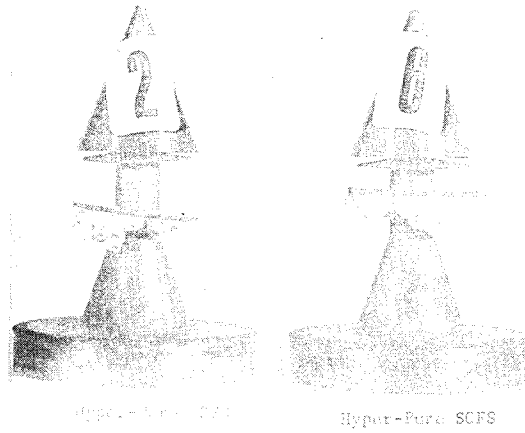
Figure 4. HYPER-PURE SLIP CAST FUSED SILICA SAMPLES - POST TEST:
1772 m/sec, 600 METER RAIN FIELD
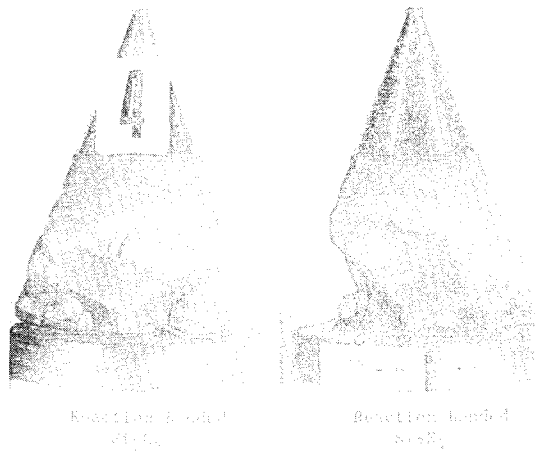
Figure 5. REACTION BONDED SILICON NITRIDE SAMPLE - POST TEST:
1772 m/sec, 600 METER RAIN FIELD
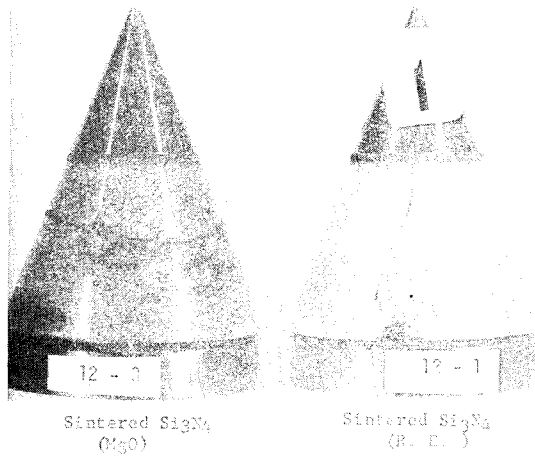
Figure 6. SINTERED SILICON NITRIDE SAMPLES - POST TEST:
1772 m/sec, 600 METER RAIN FIELD

124

THE DIELECTRIC PROPERTIES OF HOT PRESSED AND SINTERED β-SIALON

by
Peter L. Land
Air Force Materials Laboratory
Wright Patterson AFB, Ohio 45433
and
Stig Holmquest
United Technology Research Laboratory
East Hartford, Connecticut

Introduction

This paper describes the dielectric properties of some hot pressed and sintered sialons, and a comparison is made with the properties of experimental and hot pressed Si_3N_4. The sialons studied were mainly β-sialon, which has the β-Si_3N_4 structure, with up to 20% of J and minor amounts of other phases occurring in the Si-Al-O-N system. The phase diagram from Land et al. is shown in Figure 1. (1) The sialons having the best properties for use as a radome material were sintered from powder mixtures which were prepared by the General Electric Company under an Air Force Contract. (2)

Experimental

The hot pressed sialons and Si_3N_4 samples were prepared by heating in a graphite die to about $1800^{\circ}C$ under pressures which were varied from 800 to 3200 psi. The original purpose for these samples was CO_2 laser testing. The fragments from laser tested 1.25 inch diameter discs were used to make cylinders for the dielectric measurements at 24 GHz

The sintered sialons were prepared from powder mixtures which were subjected to ball milling with sialon balls for 72 hours to promote sintering. (2) The samples were fired at AFML at $1775^{\circ}C$ in an Al_2O_3 muffle tube under 25 psi N_2. Cylinders or discs of 3/8, 5, 8 and 1 inch diameter were used to obtain dielectric data at 8.5, 14 and 24 GHz.

The dielectric measurements were performed by William Westphal of the Massachusetts Institute of Technology using slotted line measurements or a dielectric filled cavity. One method was used to obtain data up to 800 $^{\circ}C$ and the other to still higher temperatures.

Futher information on sample preparation, measurement techniques and results are available in a Technical Report. (3)

Dielectric Properties

The chemical and phase composition and the density, along with the dielectric properties of the sialons and Si_3N_4 samples are tabulated in Reference 3. The conclusions from those tabulations are: (a) The dielectric constant increases as the amount of Si_3N_4 in β-sialon increases. This is demonstrated by Figure 2 where the dielectric constant was adjusted to that for theoretically dense material, (3) and plotted versus the Si_3N_4 content. (b) The dielectric constant appears to decrease slightly with increasing amounts of J-sialon. (c) There is a general trend for the dielectric constant to be high when the loss is high. (d) There is no clear correlation between impurity levels and dielectric properties. The dielectric constants of the hot pressed sialons

are between 7.5 and 8.5, and most loss tangents are between 0.0015 and 0.0040, and samples with no known difference in purity span both ranges. Most impurities would have entered with the Si_3N_4 since this is a major component and since the Al_2O_3 is purier. There was no evidence that the properties of the samples of sialon or Si_3N_4 from higher purity Sylvania or Plessey Si_3N_4 were different from those made from AME or Ventron Si_3N_4. (e) The dielectric loss of Norton Co. NC-350 was much higher than that of the sialons. (f) The dielectric constant of Norton Co. NC-132 was considerably higher than that of the sialons, as was the loss, and the properties changed as the sample was rotated through 90°. It is surmised that the cylindrical sample, which was cut from one slice of a pressed billet, had its axis oriented at approximately 90° to the hot pressing direction. (g) The dielectric properties of Si_3N_4 containing 5 w/o CeO_2 as a pressing aid were similar to those of hot pressed sialon.

The temperature dependence of the dielectric constant and loss tangent at 8.5 and 24 GHz for several samples are shown in Figures 3 through 6. The measurements on GE sialon at 8.5 GHz were made by the resonance method and the remainder were made by the standing wave method. The accuracy of the dielectric constant is approximately $\pm 1\%$ at 23 ^{O}C and $\pm 3\%$ below 1000 ^{O}C and that of the loss tangent is approximately $\pm 3\%$ at 23 ^{O}C and $\pm 5\%$ below 1000 ^{O}C.

Sample 2-1 was used for the variable temperature measurement because it had the highest loss tangent of the hot pressed sialons and 182-C was used be because it had a low loss tangent and was the puriest of the expreimental hot pressed sialons. M2 had the lowest loss and was probably the puriest of the hot pressed Si_3N_4 samples. NC-132 was used for comparison because it is well known.

The GE sialons had the lowest dielectric constant and loss tangent for the temperature range 0-800°C at 24 GHz and also at 8.5 GHz. The measurements at 8.5 GHz were extended to 1300°C by using the resonance method, and it was found that both the dielectric constant and loss tangent had marked increases with temperature beyond 1000°C. Below 1000 ^{O}C and at 8.5 GHz the dielectric constant changes by 8%/1000°C and at 24 GHz it changes by 5%/1000°C. The average temperature coefficients, $\Delta\epsilon/\epsilon\Delta T$, are 77 X 10^{-6}/^{O}C and 48 X 10^{-6}/^{O}C, respectively for 8.5 and 24 GHz. The dielectric loss changes below 1000°C were less than a factor of 2 except in the case of GE-129 at 24 GHz.

The dielectric properties at 8 and 24 GHz from this work are summarized in Table 1 along with those reported by others for Si_3N_4. The GE sialon dielectric loss is comparable to that of Georgia Tech. reaction sintered Si_3N_4, and the dielectric constant is lower if adjusted to theoretically dense material.

In reviewing previous work it was noted that Perry and Moules found a linear relation between the dielectric loss and the temperature coefficient (TC = $\Delta\epsilon/\epsilon\Delta T$) of the dielectric constant for the range TC = 3 to 120 ^{O}C^{-1}, Tan δ = 0.004 to 0.04, and T = 20 to 400 ^{O}C. In this work most of the curves except that for sample 2-1 have a similar shape and there is no suggested correlation between Tan δ and the temperature coefficient.

This work indicates that the dielectric constant for sialon decreases as Si and N are partially replaced by Al and O, and the lowest measured values are about 7.5 when adjusted to correspond to to theoretically dense material. We note however that Messier and Wong, (7) and also Torti and Richardson(10)

TABLE 1

A SUMMARY OF DIELECTRIC PROPERTIES FOR SIALON AND Si_3N_4

Sample	Reference	ρ (gm/cm^3)	Freq. (GHz)	ε	Tan δ X10^4	Temp. Range (°C)
20 Samples of HP sialon containing up to 5 w/o AlN or 21 w/o J	This work	2.99-3.14	24	7.4-8.1	9-44	23
GE sintered sialon 128	"	3.10	8	7.3-8.4	14-21	23-1000
	"	"	24	7.7-8.0	19-27	23-800
GE sintered sialon 129	"	3.10	8	7.4-8.4	15-26	23-1000
	"	"	24	7.7-8.0	16-40	23-800
GE sintered sialon 130	"	2.99	8	7.5-8.0	14-25	23-1000
	"	"	24	7.6-7.9	18-31	23-800
Norton RS Si_3N_4 NC-350	"	2.4	24	5.7-6.0	120-146	23
Norton HP Si_3N_4 NC-132-θ	"	3.2	24	8.25-8.59	40-56	23-800
" " " θ+90	"	3.2	24	8.45-8.77	67-84	23-800
M1, Hot Pressed AME Si_3N_4 + 4 w/o CeO_2	"	3.14	24	8.45	41	23
M2, HP Plessey Si_3N_4 + 5 w/o CeO_2	"	3.3	24	8.81	33	23
M3, HP Ventron (Alpha) Si_3N_4 + 5 w/o CeO_2	"	3.19	24	9.24	118	23
M4, HP Ventron (Alpha) Si_3N_4 + 6 w/o Y_2O_3	"	3.20	24	10.47	**370**	23
Georgia Tech. Experimental RS Si_3N_4	4	2.1-2.5	9.8	4.4-5.6	15-60	25-1000
Georgia Tech. Experimental RS Si_3N_4	5	2.2-2.5	9.8	5. - 6.	< 20	25-800
Raytheon RS Si_3N_4	6	2.13	8.5	5.15	4	23
Admiralty Materials Lab. RS Si_3N_4	6	2.45	8.5	5.4-6.3	36-67	23-1000
Hanes Stellite Si_3N_4	6	2.46	10	5.6	150-200	23-500
AMMRC Experimental RS Si_3N_4	7		10	5.5-9.8	100-2200	25-1100
Commercial HP Si_3N_4 labeled N, C and FM	7	3.0-3.2	10	6.5-9.0	30-500	25-1100
AMMRC RS Si_3N_4 Experimental	8	2.2,2.3	10	4.8-7.8	40-1300	
Si_3N_4 from Several Suppliers	9	2.1-2.6	9.4	4.8-8.3	50-1200	25-400

conclude that the dielectric constant for theoretically dense Si_3N_4 is about 7.5, while Walton (4) and Westphal (6) indicate it is above 8.5.

Conclusions

Table 1 shows that the dielectric properties of the sintered β-sialon made from GE powder mixtures are comparable to the best reported for Si_3N_4 when differences due to porosity are accounted for.

The dielectric constant of β-sialon decreases with Al and O content. The lowest measured value for theoretically dense material was 7.5, but the true value might be lower if the value for theoretically dense Si_3N_4 is 7.5.

The dielectric properties of the commercial hot pressed Si_3N_4, NC-132, like the mechanical properties, are anisotropic, with differences in the dielectric constant and loss of 2% and 50%, respec ively for a 90° rotation. This asymmetry may be common to hot pressing or other fabrication techniques which tend to produce preferred alignment of asymmetric crystallites. The NC-132 is probably unixial along the hot pressing direction which means that rays passing through a radome of this material would split into two components and thus reduce target resolution.

REFERENCES

1. P. L. Land, J. M. Wimmer, R. W. Burns and N. S. Choudhury, "Compounds and Properties of the System Si-Al-O-N," J. Am. Ceramic Soc., 61, No. 1-2, 56-60 (1978).
2. A. Gatti and M. J. Noone, "Methods of Fabricating Ceramic Materials," Final Report AFML-TR-77-135 (1977).
3. P. L. Land and S. Holmquest, "Evaluation of β-Sialon for Radome Applications, " AFML-TR-78-79(1978).
4. J. D. Walton, Jr., "Reaction Sintered Silicon Nitride for High Temperature Radome Applications, "Ceramics Bull., 53, No. 3, 255-258 (1974).
5. J. N. Harris, "Slip-Cast Reaction Sintered Silicon Nitride for Radome Applications," pp 72-76 , Proceedings of the Twelfth Symposium on Electromagnetic Windows, June 12-14, 1974, "State of Radome Technology" - 1974, Edited by J. N. Harris, Georgia Institute of Technology, Atlanta, Ga.
6. W. B. Westphal and A. Sils, "Dielectric Constant and Loss Data, " AFML-TR-72-39, April (1972).
7. D. R. Messier and P. Wong, "Silicon Nitride; A Promising Material for Radome Applications," pp 62-66, Reference 5.
8. D. R. Messier and P. Wong, "Effect of Processing Conditions on Microwave Dielectric Properties of Reaction-Sintered Silicon Nitride, " Proceedings of the Thirteenth Symposium on Electromagnetic Windows, Sept 21-23, 1976, Edited by H. L. Bassett and J. M. Newton, Georgia Institute of Technology, pp 3-8.
9. G. S. Perry and T. R. Moules, "Microwave Dielectric Properties of Silicon Nitride, pp 67-71, in Reference 5.
10. M. L. Torti and D. W. Richerson, "Properties of Hot Pressed Silicon Nitride, " Proceedings of the Eleventh Symposium on Electromagnetic Windows, 1972, N. E. Poulos and J. D. Walton. Jr., Georgia Institute of Technology, pp 9-11.

FIGURE 3. THE DIELECTRIC CONSTANT FOR β-SIALON AND Si_3N_4.

FIGURE 2. THE DIELECTRIC CONSTANT ADJUSTED TO THAT FOR THEORETICALLY DENSE β-SIALON VERSUS Si_3N_4 CONTENT.

FIGURE 1. A MOLE PRECENT PRODUCT OR QUASI-EQUILIBRIUM PHASE DIAGRAM OF THE SIALON SYSTEM.

129

FIGURE 6. THE DIELECTRIC LOSS VERSUS TEMPERATURE AT 8.5 GHz FOR GENERAL ELECTRIC SINTERED SIALONS.

FIGURE 5. THE DIELECTRIC CONSTANT VERSUS TEMPERATURE AT 8.5 GHz FOR THE GENERAL ELECTRIC SINTERED SIALONS.

FIGURE 4. THE DIELECTRIC LOSS FOR β-SIALON AND Si_3N_4.

130

THE EFFECT OF SOME FABRICATION VARIABLES ON THE DIELECTRIC PROPERTIES OF REACTION BONDED SILICON NITRIDE

by

G. S. Perry and J. H. Sant

Atomic Weapons Research Establishment (PE)
Aldermaston, Reading, RG7 4PR, Berks, UK

1. INTRODUCTION

Silicon Nitride is now a well established high temperature engineering ceramic which has considerable potential as a dielectric for radome applications. The dielectric properties were first described in 1964 (1) and since then silicon nitride as a radome material has been studied in the US (2,3,4,5) and the UK (6). This paper reports on a series of systematic studies on the effects of fabrication variables on the dielectric properties of reaction bonded silicon nitride.

2. EXPERIMENTAL

2.1 Factorial Design

The initial approach was to design a factorial experiment based upon six factors, each with a number of settings; Tables 1 and 2 give the details.

One thick and one thin specimen (isostatically pressed at 150MPa using water as a temporary binder) of the same material variant were included in each tube during a nitriding experiment. The number of possible variants of the other five factors is $4^2 \times 2^3 = 128 = 2^7$, and the experimental design used was a 1/4 - replicate of the 2^7 system in 4 blocks of 8. Each block consisted of 8 material/atmosphere combinations nitrided simultaneously.

2.2 Multitube Furnace

To enable 8 nitriding experiments to be carried out simultaneously a furnace was built with 8 alumina reaction tubes, each tube with the nitriding gas atmosphere independently variable. In each of the 4 nitriding experiments new tubes were initially conditioned at 1450° C for 3 hours before use. This furnace was used for all experiments.

2.3 Microwave Dielectric Measurements

All the dielectric measurements were made on circular specimens (0.9 in.) at a frequency of 9375 MHz using the shorted-line method. Duplicate measurements were made on specimens produced in the factorial experiments; initially the specimens were ground to the maximum length then re-measured after having the length reduced.

3. RESULTS

3.1 Factorial Experiment

Detailed results are given in Table 3. Statistical analysis showed that of the six factors examined, three only, source material, particle size, and firing schedule showed significant effects. These effects are summarized in Table 4, which shows that the high purity silicon, unlike the normal commercial material, responded markedly to a decrease in particle size, and that a general improvement in properties accrued from the incorporation of the 24th at 1450° C stage in nitriding.

The remaining variants - material and atmosphere additives and specimen thickness failed to yield significant effects.

3.2 Nitridation of Pure Silicon

In the first experiment a sample of < 5μm pure silicon powder showed a very high weight gain (65.8%) and yet some authorities would contend that pure silicon cannot be nitrided under the conditions used. Subsequent chemical analysis showed that the Fe content of the starting powder was 200 ppm and Atkinson et al (7) have suggested that this level would be sufficient to permit nitridation to proceed readily.

A further experiment was therefore carried out to establish, with more confidence, the role of iron in < 5μm pure silicon. Although the presence of $\frac{1}{2}$% H_2 in the nitriding gas was not found to be significantly beneficial it was included again because of the possibility that its effect may have been masked by the iron.

For this experiment high purity powder which has been classified to provide the < 5μm fractions was divided into two roughly equal parts and one portion was washed with 5M HC1 until no more iron was removed. The spectrographic analyses of the two silicon powders, before and after acid-washing, given in the following table shows substantial reduction in the Fe, Al and Mn contents, other elements remained essentially unchanged.

SPECTROGRAPHIC ANALYSIS OF PURE SILICON (ppm)

	Fe	Mg	K	Ca	Al	Ti	Mn	Na
Un-washed	1500	10	4	20	110	< 150	33	45
Washed	200	7	11	20	60	< 150	4	45

Details of the nitriding conditons, and of the results obtained, are shown in Table 5. Three specimens were nitrided at the same time at each condition.

The experiment was rather a small one and so the conclusions, in some respects, are not so clear. Thus there do not appear to be any systematic variations of dielectric constant resulting from the different treatments. It does appear, however, that the un-washed silicon gives a lower loss product than the acid-washed silicon.

132

4.   DIELECTRIC CONSTANT OF PARTIALLY NITRIDED SILICON

4.1   Dielectric Constant of Silicon

Throughout the short history of the measurement of the dielectric constant of silicon nitride it has often been stated that the presence of free silicon, usually at low concentrations, is responsible for the poor dielectric properties, in particular high values of ε and loss tangent.

Now the dielectric constant of pure silicon is about 11.7 at 10 GHz and the dielectric constant of fully dense silicon nitride is about 8.5. It follows therefore (without invoking any special theories of dielectrics) that the dielectric constant of a mixture of the two materials cannot exceed the value for silicon. The literature, however, contains many references to values often exceeding ε = 10 for silicon nitride with a density only 80% of the theoretical maximum.

Measurements were made of the dielectric constant of compacted compacted silicon powder obtained from different sources and the results are given in Table 6. The dielectric constant of the silicon was then calculated using the Lewin (8) and Looyenga (9) equations and the results show that the dielectric constant of commercial grades of silicon is 40 or more rather than the value of about 14 found for pure silicon. The reason for the high value obtained is likely to be due to the presence within the material of regions of higher conductivity, such as iron, in one form or another (10). It follows, therefore, that high dielectric constant in silicon nitride may be due to the presence of metallic impurities which have not reacted during nitridation. Some further experiments and analyses were therefore carried out in order to elucidate the nature of this effect.

4.2   Commercial Silicon

Dunstan and Wragg silicon was classified to < 5μm, divided into two parts, and one portion washed with 5M HCl until apparently free of Fe. Chemical analysis showed that the acid-washing reduced the iron content from 1.0% to 0.44%. Partial nitridation of compacts prepared from the two powders was carried out at 1250° C and 1350° C by nitriding at different times. Figure 1 shows a plot of weight gain against time.

This shows that the acid-washing treatment appears to delay the nitridation at the lower temperature but to have less effect at the higher temperature. As Figure 2 shows, whether washed or not, at the same degree of nitriding (assuming that the latter can be represented by the weight gain) the same dielectric constant is obtained.

4.3   Pure Silicon

A similar experiment was carried out on the < 5μm Alfa pure silicon powder studied in the earlier experiment. Discs of the acid-washed and un-washed silicon were partially nitrided at 1350° C for different times and the results are given in Figures 1 and 3. Data at the maximum weight gain from the first factorial experiment are also shown. On this material the effect of Fe on the kinematics of the nitridation are even more pronounced

than in the Dunstan and Wragg silicon in which the lack of effect of Fe may be ascribed to the high residual Fe level in the acid-washed material.

Figure 3 shows how the dielectric constant varies with the progress of nitriding, in the Alfa material, and brings out an additional effect associated with the higher iron content, namely an increase in dielectric constant. For the same degree of nitriding (weight gain) the dielectric constant of the washed material is lower: however, the difference decreases as nitriding proceeds, finally disappearing just as nitriding is complete.

This last, remarkable feature indicates that the influence of iron on the nitriding process, and the resultant evolution of electrical properties, is a complex one deserving further study. It is assumed, of course, that the critical difference between washed and un-washed silicon in this study lies in the Fe content.

5.   REFERENCES

(1)	W. M. Wells	Silicon Nitride as a Radome Material. Report UCRL 7795, May 1964
(2)	J. D. Walton	State of Hypersonic Radome Technology: Slip-Cast Fused Silica and Reaction Sintered Silicon Nitride. 3rd Colloque Fenetre Electromagnetique. Paris 1975, p381
(3)	D. R. Messier and P. Wong	Proceedings of the 12th Symposium on Electromagnetic Windows, Atlanta, Ga, p63
(4)	D. R. Messier and P. Wong	Proceedings of the 13th Symposium on Electromagnetic Windows, Atlanta, Ga. p3
(5)	J. N. Harris	An Investigation of Reaction Sintered Silicon Nitride as a Radome Material. Final Report. Georgia Institute of Technology, March 1975 (AD A019133)
(6)	G. S. Perry and T. R. Moules	Proceedings of the 12th Symposium on Electromagnetic Windows, Atlanta, Ga, p67
(7)	A. Atkinson, A. J. Moulson and E. W. Roberts	J.Am. Ceram. Soc. 59, 285 (1976)
(8)	L. Lewin	J. Inst. Elect. Eng. 94, 65 (1947)
(9)	H. Looyenga	Physica 31, 401 (1965)
(10)	R. W. Sillars	J. Inst. Elect. Eng. 80, 378 (1937)

TABLE 1

FIRST MULTIFACTORIAL EXPERIMENT

FACTORS AND SETTINGS

Factor	Settings
Silicon Material	Alfa (high purity) and Dunstan and Wragg (normal low-purity)
Silicon Particle Size	Fine ($< 5 \mu$m) and Coarse (30–100μm) (obtained by classifying)
Material Additive	Nil, 2% Fe_2O_3, 2% MgO, 2% C
Atmosphere Additive	Nil, $\frac{1}{2}$% H_2, $\frac{1}{2}$% O_2, $\frac{1}{2}$% H_2/O_2
Firing Cycle	(i) (24h x 1350°C) + (24h x 1450°C) (ii) 48h x 1350°C
Specimen Thickness	8 mm and 16 mm (approx)

TABLE 2

MATERIALS AND NITRIDING CONDITIONS

Silicon	Particle Size	Additives \ Gas \ Silicon	24h x 1350°C + 24h x 1450°C				48h x 1350°C			
			–	$\frac{1}{2}$%H_2	$\frac{1}{2}$%O_2	$\frac{1}{2}$%H_2/O_2	–	$\frac{1}{2}$%H_2	$\frac{1}{2}$%O_2	$\frac{1}{2}$%H_2/O_2
PURE (Alfa Products)	$< 5 \mu$m	Nil	1/2		4/5		2/2		3/6	
		Fe_2O_3		4/3						
		MgO								
		C				1/7		3/3		2/7
	30–100μm	Nil				4/7		2/3		
		Fe_2O_3		1/3						3/7
		MgO			1/5		3/2			
		C	4/2						2/6	
INPURE (Dunstan & Wragg)	$< 5 \mu$m	Nil		1/4						3/8
		Fe_2O_3				4/8		2/4		
		MgO	4/1						2/5	
		C				1/6	3/1			
	30–100μm	Nil			4/6		2/1			
		Fe_2O_3							3/5	
		MgO	1/1			1/8		3/4		
		C		4/4						2/8

Note: The pairs of numbers appearing in certain cells of the above table refer to firings and tube numbers; thus, 1/2 signifies that the experiment was carried out in the first of the four firings and in No 2 of the eight tubes. These numbers are used as sample identification in Table 3. Where cells of the table do not show sample numbers no test of the factor combination was carried, in accordance with the $\frac{1}{4}$ – replicate experimental design.

135

TABLE 3

RESULTS OF FIRST FACTORIAL EXPERIMENT

Sample	Weight Gain (%)	Density (g/ml)	ε_r	tan δ
1/1	58.3/60.3	2.45/2.50	6.71/6.00	0.015/0.009
1/2	65.8/64.2	2.05/2.02	4.51/4.39	0.004/0.004
1/3	53.4/40.1	2.17/2.09	86.7/26.9	0.080/0.225
1/4	61.0/62.6	2.01/2.01	4.47/4.36	0.003/0.004
1/5	1.0/68.5	– /2.58	– /6.42	– /0.059
1/6	55.7/57.6	1.99/2.02	4.55/4.86	0.009/0.017
1/7	61.9/59.5	2.06/2.02	5.60/5.39	0.056/0.028
1/8	60.8/56.5	2.44/2.43	6.82/5.53	0.013/0.005
2/1	32.1/37.9	2.05/2.13	22.5/17.4	0.323/0.134
2/2	60.2/62.7	2.04/2.05	4.52/4.40	0.007/0.006
2/3	19.1/19.2	1.89/1.89	104/38.7	0.057/0.127
2/4	60.1/61.2	2.03/2.02	4.55/4.33	0.011/0.009
2/5	13.3/60.7	1.69/1.74	4.43/4.92	0.107/0.003
2/6	9.1 /9.8	1.81/1.79	40.2/43.0	0.188/0.130
2/7	30.2/38.4	– /1.74	– /10.2	– /0.124
2/8	24.8/23.1	1.84/1.89	5.77/10.6	0.241/0.217
3/1	57.8/58.7	2.05/2.06	5.70/5.38	0.025/0.028
3/2	3.9/4.0	1.63/1.66	25.8/27.3	0.200/0.136
3/3	57.3/58.9	2.00/2.02	5.88/5.60	0.065/0.038
3/4	45.0/46.2	2.23/2.23	11.7/12.0	0.147/0.106
3/5	28.6/32.5	1.99/2.07	19.6/17.0	0.151/0.144
3/6	26.7/38.7	1.49/1.77	12.9/9.09	0.139/0.114
3/7	30.6/38.2	2.10/2.29	25.8/53.4	0.367/0.060
3/8	45.6/62.4	1.74/2.03	80.0/4.40	0.039/0.010
4/1	58.2/60.2	2.08/2.16	4.49/4.59	0.005/0.005
4/2	30.7/17.2	1.76/1.52	65.0/30.2	0.051/0.036
4/3	58.5/61.0	2.04/2.05	4.39/4.35	0.001/0.002
4/4	55.0/56.5	2.36/2.42	10.4/10.4	0.097/0.093
4/5	53.8/60.7	1.83/2.12	3.76/3.96	0.006/0.143
4/6	59.9/58.4	2.45/2.38	6.16/5.53	0.008/0.005
4/7	53.5/59.4	2.49/2.52	7.70/7.76	0.085/0.119
4/8	64.6/54.0	2.01/1.88	4.29/26.1	0.010/0.071

Notes: (i) For sample identification see footnote to Table 2

(ii) The pairs of numbers given for each result refer to the thin and thick specimens respectively.

TABLE 4

FIRST FACTORIAL EXPERIMENT

Property		Firing Cycle	
		48h x 1350°C	24h x 1350°C + 24h x 1450°C
WEIGHT GAIN (%)		37	55
DIELECTRIC CONSTANT		24.4	13.1
LOSS TANGENT		0.13	0.04
DENSITY (g/ml)		1.94	2.18

Property	Material — Size	Alfa	D&W
WEIGHT GAIN (%)	<5 μm	53	56
	30–100 μm	30	46
DIELECTRIC CONSTANT	<5 μm	8.3	10.7
	30–100 μm	42.1	14.1
LOSS TANGENT	<5 μm	0.05	0.02
	30–100 μm	0.11	0.09
DENSITY (g/ml)	<5 μm	1.94	2.00
	30–100 μm	2.05	2.25

Note: Following conventional practice, the property values in the above tables are averages over all levels of the non-relevant factors, namely those not shown in the column and row headings of the table in question.

TABLE 5

NITRIDATION OF ACID-WASHED < 5μm SILICON POWDER

Material	Nitriding Gas	Nitriding Schedule					
		24h/1350°+ 24h/1450°C			24h/1350° + 72h/1450°C		
		Density	ε	tan δ	Density	ε	tan δ
Unwashed < 5μm	$N_2 + \frac{1}{2}\%H_2$	2.023 2.003 2.004 (64.0)	4.43 4.36 4.35	0.003 0.002 0.003	* 2.045 2.097 (61.9)	4.53 4.65	0.003 0.003
	N_2	2.013 2.026 2.040 (63.1)	4.45 4.51 4.53	0.003 0.004 0.005	2.015 1.995 1.994 (62.7)	4.43 4.35 4.35	0.002 0.003 0.003
Acid-Washed < 5μm	$N_2 + \frac{1}{2}\%H_2$	1.931 2.087 2.072 (63.0)	4.10 4.65 4.58	0.017 0.017 0.003	2.045 2.052 2.074 (61.9)	4.43 4.48 4.49	0.002 0.003 0.003
	N_2	1.965 2.021 2.072 (63.2)	4.24 4.46 4.52	0.029 0.026 0.004	1.834 1.906 2.041 (63.2)	3.91 4.06 4.43	0.004 0.015 0.013

*Disc damaged during grinding

Note: the values (64.0) etc are the mean weight gains for the three specimens.

TABLE 6

DIELECTRIC CONSTANT OF SILICON

Material	Bulk Density (% Theory)	Measured Dielectric Constant	Estimated Dielectric Constant for Silicon	
			Ref (8)	Ref (9)
Alfa < 5 μm	46.3	4.32	15.5	13.1
Koch-Lights	49.4	10.7	42	41
BDH	54.7	12.6	58	40
Dunstan and Wragg	49.5	11.4	46	43

Fig 1

NITRIDATION OF < 5 μm ALFA SILICON AND D&W SILICON
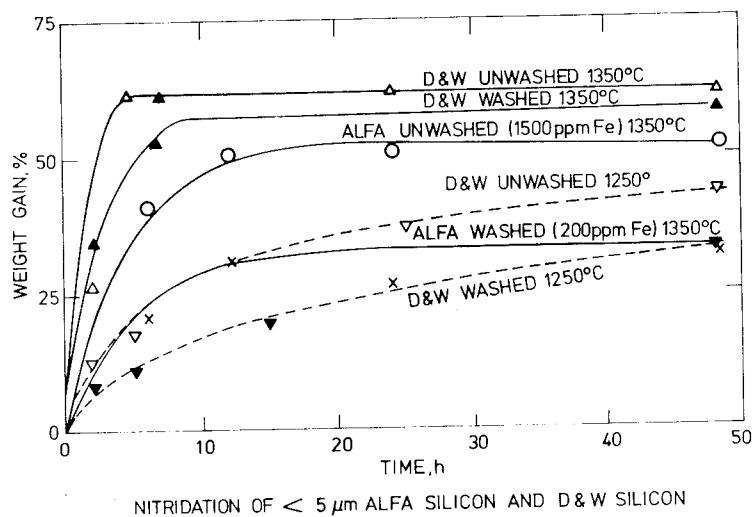
Fig 2
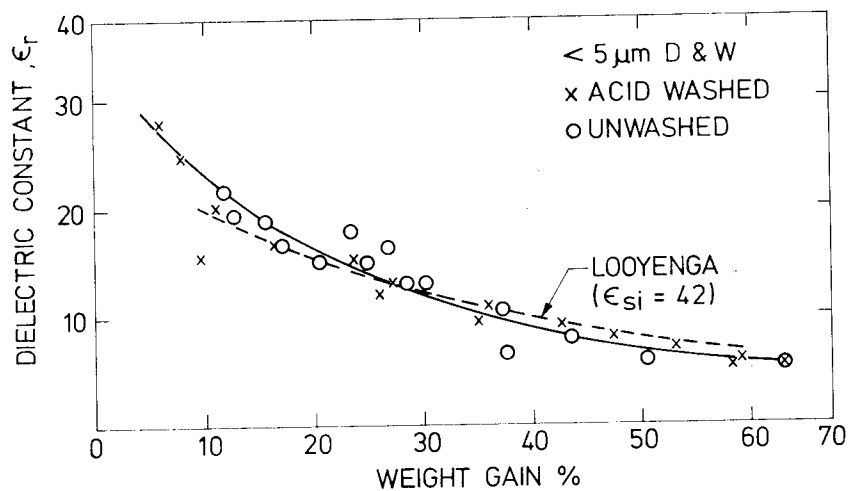
Fig 3
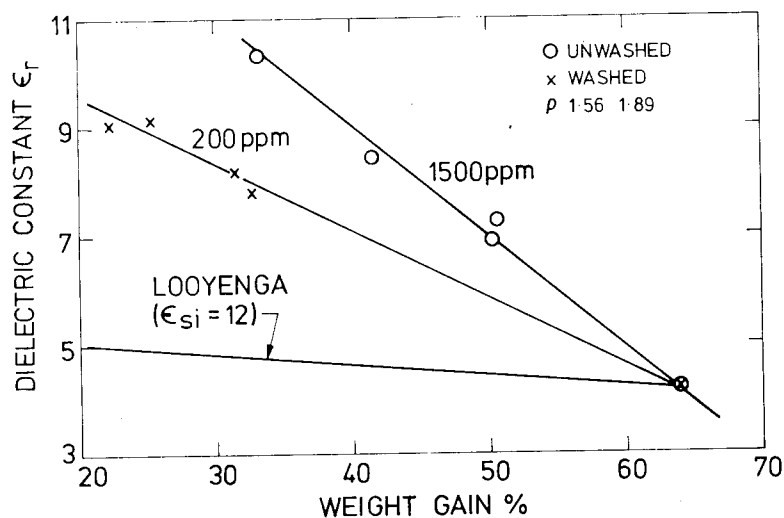
CERAMIC COMPOSITE RADOME MATERIALS

S. W. Freiman, R. W. Rice, P. F. Becher
W. J. McDonough and J. J. Mecholsky
Naval Research Laboratory
Washington, D. C. 20375

Future missiles are expected to operate at significantly higher Mach numbers and be subjected to greater acceleration than those currently employed. Such operation will subject missile radomes to much more severe inertial and aerothermal stresses than can be met by existing materials. In addition, all-weather requirements will necessitate the use of radome materials with improved erosion capabilities. New materials to meet these more demanding mechanical requirements must also have adequate dielectric properties under these more demanding environments.

Work performed at NRL has shown that one of the primary parameters needed for good thermal shock resistance under high heat flux conditions is a low thermal diffusivity. One of the ways to reduce thermal diffusivity is to introduce porosity into the material. It has been shown at this laboratory that Al_2O_3, for instance, containing approximately 20 v/o porosity is much more resistant to thermal stress fracture than theoretically dense Al_2O_3. However, the introduction of porosity also reduces the ablation resistance of the material and decreases its mechanical strength. For this reason, this approach was modified such that a second phase having a different thermal expansion coefficient and only limited bonding to the matrix was introduced into the body. It was hypothesized that the difference in thermal expansion coefficient between the two phases would cause the formation of microcracks localized around the second phase particles during a high thermal flux, such that these microcracks would sufficiently reduce thermal diffusivity to give increased thermal shock resistance. It was felt that localized microcracking would also inhibit crack propagation and failure due to rain drop impacts. A significant density of microcracks appeared necessary to be effective, yet to minimize strength reductions, it was considered important that the microcracks remain small and well separated. Therefore, since microcrack sizes are governed by the size of the particles causing them, small dispersed particles are required. It was also felt that the thermal stress and rain erosion resistance could be achieved while limiting strength losses by selecting parameters such that the microcracking be local to the second phase particles and occurs mainly in the vicinity of primary flaws under significant stress.

While a few other ceramic composites were considered and preliminary testing performed, the most promising systems ap-

peared to be an Al_2O_3 matrix with a second phase of 30-50 v/o
BN. Al_2O_3 was chosen as a matrix because of its high heat of
vaporization, good strength, good rain erosion resistance,
reasonable dielectric behavior and expected compatibility with
BN. BN was chosen as the dispersed phase because the large mis-
match in its thermal expansion coefficients from those of Al_2O_3
should allow the desired small microcrack formation around small
BN particles in the vicinity of stress concentrations. BN was
also chosen because of its excellent dielectric behavior.

Studies are underway to determine whether the performance
of these materials is due to mechanisms originally hypothesized.
The focus of this paper is instead to examine the behavior of
the bodies fabricated thus far as indicative of the potential
of this composite system for radome application. It should be
kept in mind that the system is still under development, and
may still be far from optimized.

Processing of the Al_2O_3-BN composites has been discussed
in more detail elsewhere.[1] Briefly, the composites were fab-
ricated by mixing the constituents in the form of fine powders
($Al_2O_3 \sim 0.5$ μm and fine BN flakes ~ 2 μm on an edge and 0.2 μm
thick) using isopropanol as a mixing agent. Wet milling re-
sulted in a more homogeneous composite than dry milling and pro-
vided more reproducible thermal shock resistance. After drying
the mixture, the powders were vacuum hot pressed at approxi-
mately 1900°C for thirty minutes to obtain dense ceramic-
ceramic composites. It has been found that the temperature at
which these composites are hot pressed is critical to the for-
mation of a good thermally shock resistant body. Lower hot
pressing temperatures resulted in much degraded behavior,
apparently due to the lack of bonding of the BN to the Al_2O_3
matrix at the lower temperatures.[1]

The thermal shock resistance of the composites was com-
pared to existing radome materials using a quench test in which
sets of flexural bars approximately 1/8" x 1/8" x 1" were
quenched into room temperature water from a furnace held at
different temperatures for each set of bars. The temperature
at which the initial strength of a material drops precipitously,
known as ΔTc, is a measure of the thermal shock resistance of
that material.

As shown in Fig. 1, the 70 v/o Al_2O_3 - 30 v/o BN as well
as the 50 v/o Al_2O_3 - 50 v/o BN both have excellent thermal
shock resistance compared to existing radome materials such as
Al_2O_3, pyroceram and even slip cast fused SiO_2, which is one of
the most thermally shock resistant materials available. It
should be noted that the thermal shock resistance of the Al_2O_3-
BN composites is also significantly better than that of reaction
sintered Si_3N_4, which is being developed for an improved radome.
Thermal shock testing has also been performed using a 15 kw
laser as a heat source in order to determine whether rapid

heating would change the ranking of these materials. The Al_2O_3-BN composites showed about a factor of 5 increased thermal stress resistance under these conditions compared to pyroceram and slip cast fused SiO_2, were a factor of 10 to 20 better than Al_2O_3, and also significantly better than reaction sintered Si_3N_4.

TABLE 1

Dielectric Properties of Candidate Radome Materials*

Material	Density g/cc	Dielectric Constant at 8-10 GHz	Loss Tangent
Al_2O_3	2.9	9.5	0.1
BeO	2.1	6.6	0.5
Slip Cast Fused Silica	2.6	3.3	0.4
Pyroceram 9606	2.45	5.7	0.2
Si_3N_4 (reaction sintered)		5.6	2.0
Hot pressed 70Al_2O_3-30BN	2.98	6.9	0.4
Hot pressed 50Al_2O_3-50BN	2.8	6.5	0.4

*Data from Bull. Am. Ceram. Soc. 53 (3), 255, 1974 (J. D. Walton, Jr.) except for Al_2O_3-BN composites which were measured at MIT through the courtesy of D. Evans, AFML.

It is seen in Table 1 that the dielectric properties of the Al_2O_3-BN composites are quite good compared to existing materials and as seen in Fig. 2, the strength and fracture toughness of the materials are comparable to or better than most of the existing radome materials.

Having established good thermal shock, strength and dielectric behavior of the Al_2O_3-BN composite bodies, the next area addressed was rain erosion resistance. Slip cast fused SiO_2 for instance, while having excellent thermal shock resistance, is quite soft and is unacceptable as a material that is carried under the wing of an aircraft, since flight through rain under successive missions would significantly erode the radome. In addition to the erosion at the subsonic level in captive flight, it is necessary to consider the erosion behavior during flight in the supersonic regime. For this reason, two sets of rain erosion tests were performed.[†] Lower velocity data was obtained using the AFML whirling arm rig at Mach .6 to Mach .8, while

---

[†]Both tests obtained through the courtesy of George Schmitt, Air Force Materials Laboratory, Wright-Patterson Air Force Base, Ohio.

supersonic rain erosion data was obtained on sled test facilities at Holloman AFB at Mach 4.0.[†]

The rain erosion resistance at 500 mph (Mach .7) of the Al_2O_3-BN composites depends on the BN concentration as shown in Fig. 3. As expected, those composites containing a higher percent of Al_2O_3 are more resistant to erosion than are the lower alumina content bodies. It can also be seen that all of the Al_2O_3-BN composites are superior in erosion resistance to slip cast fused SiO_2 which was almost completely destroyed after six minutes in the facility at 500 mph. Another comparison of the 70% Al_2O_3-30% BN composite with slip cast fused SiO_2 is shown in Fig. 4 at 400 mph. Almost no damage was observed on the composite material while again the slip cast fused SiO_2 was considerably eroded. Some tests were performed on 70% Al_2O_3-30% BN composite that had been plasma sprayed with a 10 mil thick Al_2O_3 coating. However, the coating spalled off quite early in the rain erosion test. While significantly better than that of slip cast fused SiO_2, the rain erosion resistance of the composites was in general inferior to that of both fortified and unfortified pyroceram and pure alumina, as would be expected. However, it does appear that the erosion resistance of these composites may be sufficiently high that they could be used as a radome material. Further, it is felt that the rain erosion resistance can be considerably improved by further development of the material, e.g. more homogeneous BN distribution and grading higher Al_2O_3 contents near the surface.

TABLE 2

Rain Erosion Material Evaluation*

Material	Mean Depth of Penetration Rate MDPR (cm/sec)
Impregnated slip cast fused silica	1.19
Pyroceram 9606	1.0
Reaction sintered silicon nitride	0.25
70% Al_2O_3-30% BN	0.12

*Materials compared at Mach 4.0 in Holloman sled test facility. Specimens at 60° to rainfield of 3-4 in/hr.

The erosion resistance of the 70% Al_2O_3-30% BN composite was even more favorable at Mach 4 (Table 2). In this case, the depth of penetration rate for this material was approxi-

mately an order of magnitude lower than that of slip cast fused SiO_2 and significantly lower than that of both Pyroceram and reaction sintered Si_3N_4. Thus, the rain erosion resistance of the 70% Al_2O_3-30% BN composite is significantly better than that of slip cast fused SiO_2 at both subsonic and supersonic velocities. At the former the composite may not be as good as Pyroceram or Al_2O_3.

Work is now underway to improve the erosion resistance of these composites by a grading technique in which the outer surface of the composite is made to contain a higher percent alumina than does the rear surface. This technique should give a harder outer surface and, therefore, a greater erosion resistance, while maintaining the good thermal shock properties of the lower alumina content bodies. Work is also continuing on developing more practical processing techniques. In this respect, use of additives, e.g. to give liquid phase densification are being investigated in order to reduce the hot pressing temperature and make a more formable body, or preferably produce a body that can be sintered rather than hot pressed. In addition, sol-gel techniques are being applied to produce more homogeneous bodies or bodies containing more controlled heterogeneous structures. It is expected that these efforts should lead to improvements in the effectiveness of this composite system as a radome for future missile systems.

In conclusion, it appears that the Al_2O_3-BN composite system, especially the composition 70% Al_2O_3-30% BN, which in part represents a tradeoff between the greater thermal shock resistance of BN and the better erosion resistance of the Al_2O_3 is an excellent prospect for a new radome material. The thermal shock resistance, dielectric properties, mechanical strength and rain erosion resistance of these composites are all good to excellent.

REFERENCES

1. "Thermal-Structural Ceramic Composites," R. W. Rice, P. F. Becher, S. W. Freiman and W. J. McDonough, Proc. of Conference on Composites and Advanced Materials, Cocoa Beach, Florida, Jan. 1978.

ΔT_c: Temperature from which sample is rapidly quenched (in H_2O) to 25°C to cause loss in strength at 25°C.
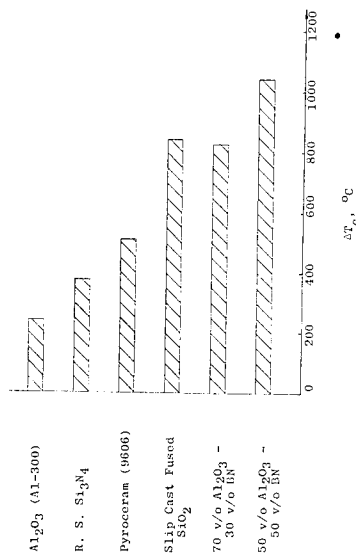
Fig. 1. Thermal shock resistance of radome materials obtained by a quenching test. A larger T_c indicates greater resistance to failure from thermal stresses.

Al₂O₃ (Al-300)

R. S. Si₃N₄

Pyroceram (9606)

Slip Cast Fused SiO₂

70 v/o Al₂O₃ - 30 v/o BN

50 v/o Al₂O₃ - 50 v/o BN

Slip Cast SiO₂ (7)

R. S. Si₃N₄ (25)

Pyroceram 9606 (30)

Al₂O₃ (Al-300) (45)

Al₂O₃ - BN Composites (30)

Strength, MN/m² (ksi)

Fracture Toughness, MN/m³/²

Fig. 2. Comparison of the flexural strength and fracture toughness of existing and proposed radome materials.

60% Al₂O₃ - 40% BN   70% Al₂O₃ - 30% BN   85% Al₂O₃ - 15% BN

SLIP CAST FUSED SILICA   PYROCERAM-FORTIFIED   Al 300 Al₂O₃

Fig. 3. Rain erosion resistance of radome materials at 500 mph. AFML whirling arm rig, 1" hr rainfield, 1.8 mm drops. All specimens except SCFS run 10 min. SCFS stopped after 6 min.
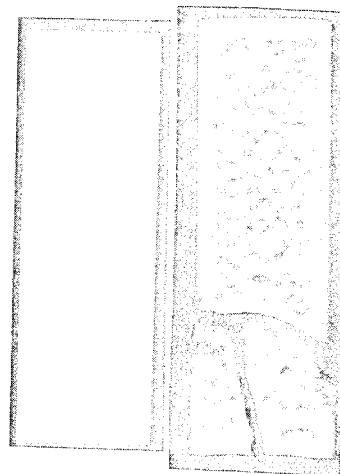
Fig. 4. Comparison of lower velocity rain erosion (10 min at 400 mph) of slip cast fused silica (bottom) with that of 70% Al₂O₃-30% BN (top) AFML whirling arm rig, 1" hr rainfield, 1.8 mm drops.

NEW POLYURETHANE COATINGS FOR
RADOME APPLICATIONS

BY

J.F. Moraveck and P.W. Sherwood

CAAP CO., INC.
Huntington, CT 06484

ABSTRACT:

The necessity of moisture to effect a cure in standard MIL-C-83231 polyurethane coatings has seriously limited its use in dry areas or at facilities not having controlled environments.

A development effort over the past two years at the CAAP CO Laboratory has resulted in polyurethane coating formulations which have satisfied the initial performance requirements of MIL-C-83231 and MIL-C-83445 Specifications for black, Type I, black antistatic, Type II and non-yellowing white radome coatings. Unique about these coatings systems, is the ability to apply the coatings rapidly under non-controlled environments. The curing mechanism does not require moisture to effect a cure and void-free coatings of 10-12 mils thickness can be applied in less than four hours.

Electrical performance, rotating arm evaluation and property data are presented. Effects of accelerated conditionings on property performance are described.

INTRODUCTION:

Protective radome coatings development efforts funded by the Air Force Materials Laboratory in the late 1960's identified a class of moisture curing polyurethane formulations that exhibited superior rain erosion resistance as measured on various rotating arm apparatus. These formulas were further developed into useful radome coatings currently being used by the military and commercial airlines. Military Specifications, MIL-C-83231, based on black pigmented polyurethane coatings was issued in August 1969 and MIL-C-83445, based on non-yellowing white pigmented coatings was issued in June 1974.

Although the application of the MIL-C-83231 and MIL-C-83445 moisture curing polyurethane formulations are difficult, the superior performance of these coatings over the neoprene rain erosion coatings was reason enough for their eventual acceptance as the state-of-the-art radome coatings.
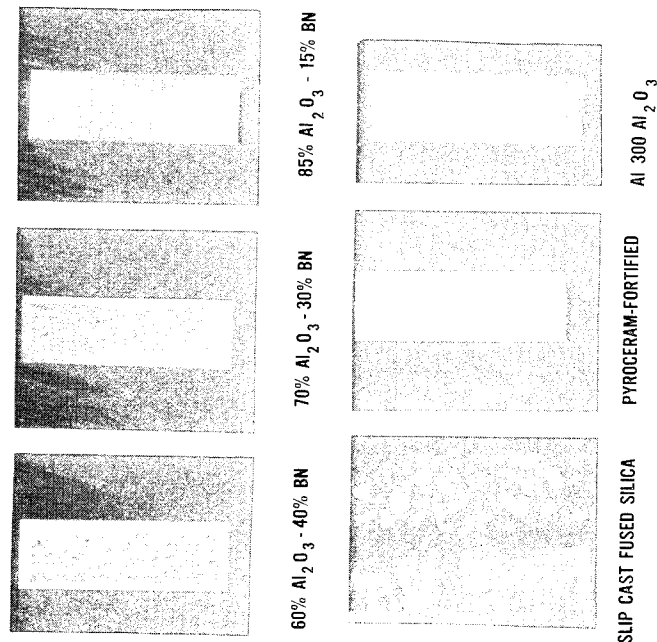
At best these moisture curing coatings are difficult and tedious to apply even under controlled environments. Under optimum conditions the coating application requires 8 to 12 hours to apply 10-12 mils of coating thickness. Between 45 and 60 minutes are necessary between coat applications at 70°F

147

and a 40% minimum relative humidity before the next coat can be applied. Static build-up during spraying causes dust and lint bumps that are unsightly; too fast an application causes bubbling and pinholing; and typically the coatings have an orange-peel appearance.

A development effort was initiated at the CAAP CO Laboratories early in 1975 to design protective radome coatings which could be applied rapidly under ambient conditions, that did not require moisture to effect a cure and could be applied by painters with minimum supervision or technical experience.

Extensive formulating with polyols, isocyanates, catalysts and curing agents has identified a particular non-moisture curing, two component polyurethane formulation that can be applied in successive coats at 10 to 30 minute intervals. A void-free coating of 12 to 14 mils thickness can be applied in less than four hours to a typical radome in paint facilities not having controlled environments.

COATING COMPOSITION:

The CAAP CO polyurethane coatings currently under evaluation as protective coatings for radomes, antennas and leading edges, are characterized as two component polyurethane coatings composed of solution prepolymers and a reactive curing agent solution.

The vehicle portion of the coating is an isocyanate terminated prepolymer prepared from a selected combination of polyols and aliphatic isocyanates in either a xylene based solvent system or a non-photochemically reactive solvent system. The reactive vehicles are pigmented in the usual manner to provide color stable, non-yellowing polyurethane coatings.

The curing agent solution used with the CAAP CO polyurethane vehicles is characterized as a simple amine, such as used in epoxy curing agents, which has been modified and deactivated. The curing agent, when mixed with vehicle, does not react until applied. A typical curing mechanism occurs after application with the isocyanate terminated prepolymer portion of the coating, resulting in chain extension and crosslinking to produce an elastomeric rain erosion resistant coating.

These coatings are being evaluated as candidate MIL-C-83231 black Type I and Type II polyurethane coatings and MIL-C-83445 non-yellowing white polyurethane coatings.

ROTATING ARM EVALUATIONS:

The candidate vehicles, curing agents, primers and epoxy glass laminate airfoil specimens were submitted to Wright Patterson Air Force Base, AFML/MXE personnel, along with instructions for application of the coatings. Airfoil specimens, 18 for each type or class of coating being qualified, were coated by AFML personnel per qualification procedures.

Six specimens were sent to Florida for six months outdoor weather exposure, six were tested after a 10 day ambient cure and six were tested following the ambient cure plus a thermal exposure of 225°F for 24 hours.

The AFML rotating arm test results for the CAAP CO ambient control and thermal aged airfoil specimens along with the specification requirements are listed in Table 1.

The average time to failure is the numerical average of the individual test times of the six specimens tested to failure or for a maximum of 180 minutes for each type, class or conditioning. Exposure of the substrate (penetration of the coating) constitutes a failure and the time to failure is recorded.

As can be seen from Table 1, the performance of the CAAP CO coatings exceed the requirements. In the case of the ambient controls, no failures occurred in the Type I or Type II coated specimens -- all survived 180 minutes. Only one of the six specimens of the Class 1 white coating failed to survive the 180 minutes test time and it failed after 150 minutes exposure.

The average times to failure of the thermally aged specimens are somewhat less than the ambient controls but still exceed the requirements.

The remaining airfoil specimens are being weathered at 45° to the South exposure in Florida and will be tested after the six months exposure.

FILM PROPERTY EVALUATION:

Effects of accelerated conditioning on film physical properties were used as a relatively rapid means of evaluating the performance of the coatings.

Humid aging at 120°F and 95% relative humidity for 30 days was used to evaluate the reversion resistance of the coatings and Weather-O-Meter conditioning for 500 hours was used to evaluate the UV and humidity resistance of the coatings.

The physical properties of the candidate CAAP CO coatings were measured after Humid Age and Weather-O-Meter conditionings and compared to ambient controls in Tables 2, 3, and 4.

The Weather-O-Meter conditioning increases the tensile modulus and tensile strength slightly as compared to the unexposed ambient controls, while Humid Aging causes a slight reduction in modulus and tensile.

The film properties are only slightly affected by accelerated conditionings, however, the rotating arm performance might be affected. Samples for rotating arm evaluation were not subjected to Weather-O-Meter or Humid Age conditioning.

149

ELECTRICAL PERFORMANCE:

One way power transmission measurements were measured at 9.375 GHz per MIL-C-83231 requirements by the Brunswick corporation on 2' x 2' dopler panels coated with 12-14 mils of the candidate CAAP CO coatings. Results of radar transmission, surface resistivity, dielectric and loss tangent measurements are listed in Table 5.

Dielectric and loss tangent measurements were made on solid one-half inch thick plugs of the various coatings and an unpigmented clear resin at 9.375 GHz.

The results are consistent with coatings currently being used as radome coatings and exceed the specification requirements.

Other pertinent CAAP CO coating data are listed in Table 6.

CONCLUSIONS:

Based on initial test results, the polyurethane coatings developed at CAAP CO offer improved performance as well as ease of application. These products should be approved for use as radome and antenna coatings as soon as the Florida weathering has been completed and results tabulated.

These products are currently available in development quantities for evaluation from CAAP CO., Inc., P. O. Box 2066, Huntington, Connecticut 06484.

TABLE 1

ROTATING ARM EVALUATIONS

AFML APPARATUS

SPECIFICATION	AVERAGE TIME TO FAILURE		
	REQUIREMENTS		RESULTS
MIL-C-83231 TYPE I			B-274 COATING
10 DAY AMBIENT CURE	120 MINUTES		180 NO DAMAGE
AFTER 24 HRS. @ 225°F	120 MINUTES		146 EROSION
AFTER 6 MOS. FLORIDA WEATHERING	120 MINUTES		--
MIL-C-83231 TYPE II			B-274/ASP108 COATING
10 DAY AMBIENT CURE	100 MINUTES		180 NO DAMAGE
AFTER 24 HRS. @ 225°F	100 MINUTES		180 NO DAMAGE
AFTER 6 MOS. FLORIDA WEATHERING	100 MINUTES		--
MIL-C-83445 CLASS 1			CW-4 COATING
10 DAY AMBIENT CURE	75 MINUTES		175 EROSION
AFTER 24 HRS. @ 225°F	75 MINUTES		134 EROSION
AFTER 6 MOS. FLORIDA WEATHERING	75 MINUTES		--

EPOXY FIBERGLASS SUBSTRATES - 12 MILS OF COATING OVER MIL-P-15328 PRIMER
TESTED AT 500 MPH AND 1 INCH PER HOUR SIMULATED RAINFALL WITH 1.8 mm
DIAMETER DROPS.

TABLE 2

FREE FILM PHYSICAL PROPERTIES
CAAP CO B-274 BLACK
RAIN EROSION COATING

	FILM PROPERTIES		
	CONTROL	HUMID AGE	WEATHER-O-METER
TENSILE PSI	3300	2800	3800
ELONGATION %	450	470	440
TENSILE MODULUS PSI			
100%	220	210	250
200%	300	290	370
300%	470	430	630

FORMULATION

CAAP CO B-274 VEHICLE AND CURING AGENT
5 MIL DRY FILM THICKNESS
1 HOUR APPLICATION TIME

CONTROL	14 DAYS AMBIENT
HUMID AGE	30 DAYS @ 120°F + 95% RELATIVE HUMIDITY
WEATHER-O-METER	500 HOURS, ATLAS WEATHER-O-METER

TABLE 3

FREE FILM PHYSICAL PROPERTIES
CAAP CO ASP108 ANTISTATIC
RAIN EROSION COATING

	FILM PROPERTIES		
	CONTROL	HUMID AGE	WEATHER-O-METER
TENSILE PSI	3200	3200	3100
ELONGATION %	435	440	430
TENSILE MODULUS PSI			
100%	370	320	300
200%	540	520	520
300%	930	900	900

FORMULATION

CAAP CO ASP 108 VEHICLE AND CURING AGENT
5 MIL DRY FILM THICKNESS
1 HOUR APPLICATION TIME

CONTROL	14 DAYS AMBIENT
HUMID AGE	30 DAYS @ 120°F + 95% RELATIVE HUMIDITY
WEATHER-O-METER	500 HOURS, ATLAS WEATHER-O-METER

TABLE 4

FREE FILM PHYSICAL PROPERTIES
CAAP CO CM-4 WHITE
RAIN EROSION COATING

	FILM PROPERTIES		
	CONTROL	HUMID AGE	WEATHER-O-METER
TENSILE PSI	3800	3000	4400
ELONGATION %	355	355	365
TENSILE MODULUS PSI			
100%	360	350	400
200%	770	600	800
300%	1850	1300	1800

FORMULATION

CAAP CO CM-4 VEHICLE AND CURING AGENT
5 MIL DRY FILM THICKNESS
1 HOUR APPLICATION TIME

CONTROL 14 DAYS AMBIENT
HUMID AGE 30 DAYS @ 120°F + 95% RELATIVE HUMIDITY
WEATHER-O-METER 500 HOURS, ATLAS WEATHER-O-METER

TABLE 5

ELECTRICAL PROPERTIES
CAAP CO POLYURETHANE COATINGS

	CLEAR	TYPE I BLACK	TYPE II BLACK	CLASS I WHITE
RADAR TRANSMISSION (9.375 GHz)				
CONTROL		95%	96%	96%
6 MONTH FLORIDA		95%	93%	-
DIELECTRIC CONSTANT (9.375 GHz)	3.036	3.065	-	3.75
LOSS TANGENT (9.375 GHz)	0.069	0.068	-	0.068
SURFACE RESISTIVITY (MEGOHMS)			2-5	

TYPE I PER MIL-C-83231 - CAAP CO B-274
TYPE II PER MIL-C-83231 - CAAP CO B-274 PLUS ASP108 ANTISTATIC TOPCOAT
CLASS I PER MIL-C-83445 - CAAP CO CM-4

TABLE 6

CAAP CO COATING PROPERTY DATA

	B-274 BLACK	ASP108 BLACK ANTISTATIC	CM-4 NON-YELLOWING WHITE
VEHICLE PROPERTIES			
NON-VOLATILE CONTENT	40%	55%	40%
WEIGHT PER GALLON	7.9 LBS.	8.2 LBS.	8.2 LBS.
VISCOSITY	200-500 CPS	1000-2000 CPS	200-500 CPS
ACCELERATED STORAGE (4 DAYS @ 120°F)	PASSES	PASSES	PASSES
POT LIFE (GREATER THAN)	4 HOURS	4 HOURS	4 HOURS
COVERAGE (SQ. FT./GAL./MIL)	360	500	380
SHELF LIFE (MINIMUM)	12 MONTHS	12 MONTHS	12 MONTHS
FILM PROPERTIES			
FILM DENSITY	1.12 g/cc	1.17 g/cc	1.25 g/cc
180° PEEL STRENGTH			
MIL-P-15328 PRIMER	10 LBS. PEEL		7 LBS. PEEL
MIL-P-23377 PRIMER	12 LBS. (Cohesive Film Failure)		12 LBS.
FLUID RESISTANT			
ALCOHOL		EXCELLENT	
TT-S-735 TYPE III		EXCELLENT	
JP-4		EXCELLENT	
MIL-A-8243 DEICER		EXCELLENT	
MIL-H-5606		EXCELLENT	
MIL-C-5769 CLEANER		EXCELLENT	
XYLENE/TOLUENE		GOOD	
KETONES		POOR	
SKYDROL		POOR	
ESTERS		GOOD	
HYDROCARBONS		GOOD	
WATER		NO EFFECT	

CAMOUFLAGE COLORED RAIN-EROSION RESISTANT, ANTI-STATIC COATINGS FOR RADOMES

C. L. Price, Jr.
General Dynamics Corporation
Fort Worth Division
Fort Worth, Texas

Introduction

Camouflaged colored rain erosion resistant, anti-static coatings are now a reality. No longer is it necessary to be limited to black coatings in order to dissipate static electricity charges which build up on radome rain erosion coatings. Through the efforts of the Air Force Materials Laboratory, the CAAP Company and Avco Systems Division, colored anti-static coatings are feasible. This development was first used on an operational F-16 nose radome.

Background

When aircraft are flown through atmospheric dust, ice crystals, or snow-flakes, frictional charging of the airframe results. Virtually all clouds above 20,000 feet are composed of ice crystals with cirrus clouds being prolific sources of electrification. Flying aircraft through such charging conditions causes electrification of the airframe until the charge and discharge rates are equal. Discharges of the electrical buildup occur from the aircraft extremities. If sufficient charging takes place, corona breakdown at the extremities will occur, and the resultant broadband noise is a major cause of radio interference when flying in weather. Plastic or dielectric surfaces will be charged at a rate that is different than the airframe owing to electrical isolation. Electrical discharges, or streamering, occurs when such surfaces are sufficiently charged with respect to the metal airframe. These streamer discharges are also a source of trouble causing electromagnetic interference in radio and radar systems. In some cases, the discharges can be so great that small delaminated areas will appear in the radome wall as the discharge arcs from the outer to inner surfaces of the wall.

To eliminate radio and radar noise interference problems as well as to provide safety both to the airplane and personnel, most all large radome surfaces are coated with an anti-static material over the rain erosion coating. One case has been documented whereby a person suffered cardiac arrest from contacting a radome without an anti-static coating on an airplane which had just landed. Reference (1) reports on a flight test where an eight mile error in the localizer offset resulted from static charging of the aircraft. Other cases of EMI have been reported on aircraft which did not have anti-static coatings on large radome surfaces.

Until this latest development, anti-static coatings for radomes have used carbon black loading to dissipate static charges and therefore color matching of the coating to the airframe color scheme has not been possible.

Camouflage Coating Development

Camouflage colored rain-erosion resistant, anti-static coatings evolved during the process of developing thermal flash resistant coatings by the

Air Force Materials Laboratory. While protection could be provided by using black carbon loaded vehicles over white rain erosion coatings, the greater need was for a compatible white anti-static coating over white rain erosion. Under AFML contract F33615-76-C-5210, performed by the Avco Systems Division, such a coating system was developed using a proprietary Avco conductive fiber material in a fluoroelastomer vehicle supplied by the CAAP Company (Reference (2)). It was found that only the fluoroelastomer material allows the fibers to be conductive; other materials (i.e. polyurethane) insulate the fibers. With this development, colored anti-static coatings became a reality.

F-16 Camouflaged Radome

In the Spring of 1977 General Dynamics contacted Mr. J. F. Moraveck of the CAAP Company in regard to coating a F-16 nose radome with a gray camouflage rain-erosion resistant, anti-static fluoroelastomer coating. It was determined that such a coating could be applied. Therefore, plans were made to select a F-16 radome and electrically test the unit at the Brunswick Corporation, first with its original black MIL-C-83231 Class II polyurethane, and again after recoating with the gray fluoroelastomer material. This plan was implemented and electrical data was obtained on a deliverable F-16 radome with its MIL-C-83231 Class II black polyurethane coating. The black coating was then stripped from the radome and the radome was shipped to Avco for application of the gray coating by Mr. J. F. Moraveck of the CAAP Company.

Up to this time, only flat panels had been sprayed with conductive fluoroelastomer coatings. The F-16 nose radome was the first unit to have such a coating applied. Reference (2) describes the process whereby the radome was sprayed with a gray base fluoroelastomer over a two day period allowing an overnight cure of the first seven mils of coating. The surface area of the radome is approximately 30 square feet and seven gallons of the fluoroelastomer vehicle were required to obtain 12 mils of coating thickness.

The gray base was next overcoated with a conductive fiber containing gray fluoroelastomer, colored to match number 36270 gray per FED-STD-595. An airless spray gun was used for this application as it was found that conventional spray guns became easily clogged requiring constant back flush to unclog the orifice. Surface resistivities between .5 and 15 megohms were obtained with one application of conductive fibers and was measured with a conventional ohmmeter approximately 20 minutes after the conductive fiber coating was applied. An additional top coat of gray fluoroelastomer was used to seal-in the fibers and resistivities of 3 to 10 megohms were measured on the cured coating by means of a 500 volt megohmeter.

Figure 1 shows a close-up view of the radome surface highlighted to show the conductive fiber pattern. Figure 2 is an overall view of the radome with gray coating.

The gray coated radome was returned to the Brunswick Corporation where an electrical re-test was conducted. No wall corrections were made to the radome so that differences in electrical performance between the black polyurethane and gray fluoroelastomer coatings could be evaluated. Table I lists the

electrical performance of the radome with its black polyurethane coating and also with its gray fluoroelastomer coating. Test results indicate minor differences in electrical performance for the two coatings. Although transmission efficiency measurements show the most change, the radome exceeded minimum specification requirements. The gray coating thickness was measured by Brunswick and found to be somewhat thinner than the original black coating. This was felt to be a significant factor in the lower transmission efficiency measured. Average beam deflection errors between black and gray radomes were found to be small, almost within the repeatability measurements of the test system. Average sidelobe level differences were also found to be small and considered to be within repeatability measurements.

Erosion Resistance and Weathering Evaluation

Rain-erosion resistance performance testing of the gray fluoroelastomer coating both with and without conductive fibers was conducted on the rotating arm rain test apparatus at the Air Force Materials Laboratory (Reference (2)). Table II shows the results of two sets of four specimens. The first group was coated with 12 mils of gray fluoroelastomer rain-erosion resistant coating without conductive fibers. The second set was coated with 12 mils of the gray fluoroelastomer with a topcoat containing conductive fibers. The data spread of "test times to failure" are normal for this type of test and are due to variations in coating thickness, minute imperfections in coating and substrate, etc. As of this writing, a military specification has not been released for fluoroelastomer rain erosion coatings. However, the average time to failure for the bare fluoroelastomer indicates that it meets the same requirements as established for polyurethane coatings. The anti-static top coating reduces the rain resistance approximately 20% below the requirement for polyurethane anti-static coatings but its average life of approximately 80 minutes is considered satisfactory. Work is still in progress under Contract F33615-76-C-5210 to optimize the topcoat fluoroelastomer composition to increase its rain erosion resistance.

Flat panel weathering tests over a six months period have been completed by the CAAP Company on gray fluoroelastomer samples. No change has been found in the resistivity of the anti-static coating and no loss was noted in transmission efficiency.

Summary

The gray camouflaged F-16 nose radome has been flying since late fall 1977. As of this writing, no operational problems have been encountered.

The principal advantage of this new coating development, and its flight testing on an operational radome, is that the F-16 nose radome is the fore-runner of a new class of radomes using anti-static colored coatings tailored for specific applications.

Acknowledgements

material. Also, Mr. J. L. Moe, General Dynamics Fort Worth Division for his assistance in the area of EMI and electrification. Appreciation is also extended to the Brunswick Corporation for the electrical test data.

References

(1)   Truax, R. L. and Robb, J. D., "ILS/VOR Navigation and Approach Errors from Precipitation Static Interference", AFAL-TR-72-325-1972 Conference on Lightning and Static Electricity.

(2)   Moraveck, James F., "Erosion Resistant, Anti-static Thermal Flash Resistant Polymeric Coatings" AFML-TR-77-204.

TABLE I - RADOME ELECTRICAL PERFORMANCE COMPARISONS FOR GRAY VS BLACK COATINGS

ELECTRICAL PERFORMANCE PARAMETER	FREQUENCY	TEST RESULTS		
		BLACK	GRAY	DIFFERENCE
Average power transmission efficiency in 30° cone about nose	F_L F_0 F_H	80.4% 81.2 82.6	76.0% 79.5 81.2	-4.4% -1.7 -1.4
Average power transmission efficiency for remainder of radome	F_L F_0 F_H	89.8% 90.5 90.4	85.5% 87.6 89.2	-4.3% -2.9 -1.2
Maximum beam deflection within $\pm 10^\circ$ of nose	F_L F_0 F_H	3.7MR 3.3 3.7	3.9MR 3.6 3.8	+0.2MR +0.3 +0.1
Maximum beam deflection $\pm 30^\circ$ to $\pm 60^\circ$	F_L F_0 F_H	5.0MR 4.8 5.0	4.8MR 4.8 4.7	+0.2MR 0 -0.3
E-plane pattern sidelobe level average increase from peak of main lobe	F_0	7.8dB	6.3dB	-1.5dB*
H-plane pattern sidelobe level average increase from peak of main beam	F_0	9.7dB	9.5dB	-0.2dB*

NOTES
F_L - Lowest frequency of the radar band
F_0 - Middle   "   " "   "   "
F_H - Highest   "   " "   "   "
* - Minus indicates improved result

TABLE II. - AFML ROTATING ARM EVALUATION TEST RESULTS

AFML SPECIMEN NUMBER	COATING	SUBSTRATE	POST CURE	TEST TIME MINUTES	TYPE OF FAILURE
8251	GRAY FLUOROELASTOMER WITH NO CONDUCTIVE FIBERS (12 MILS)	LAMINATE	AMBIENT	135	EROSION
8252				115	EROSION
8253				135	EROSION
8254				180	NO DAMAGE
8255	GRAY FLUOROELASTOMER BASE WITH TOP-COAT CONTAINING CONDUCTIVE FIBERS (12 MILS)	LAMINATE	AMBIENT	100	EROSION
8256				65	EROSION
8257				75	EROSION
8258				50+	NOT FAILED

156

FIGURE 1 - CLOSE-UP VIEW OF FLUOROELASTOMER COATED
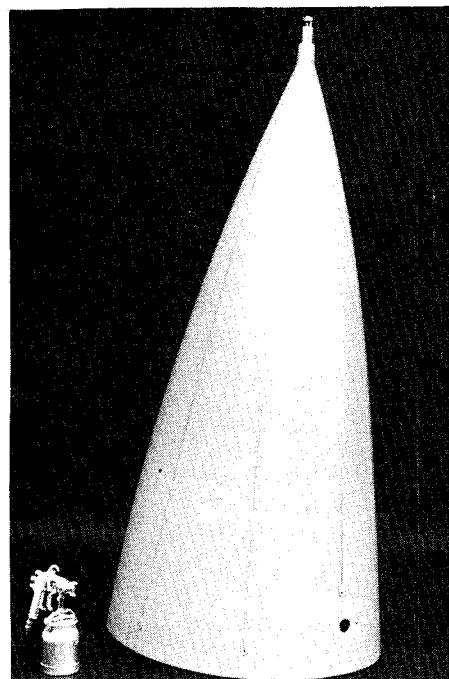F-16 NOSE RADOME

FIGURE 2 - GRAY FLUOROELASTOMER RAIN-EROSION RESISTANT
ANTI-STATIC COATED F-16 NOSE RADOME

157

POLYURETHANE TAPE EROSION BOOTS

BY

KENNETH W. FOULKE
NAVAL AIR DEVELOPMENT CENTER
WARMINSTER, PENNSYLVANIA 18974

SUMMARY

Rain erosion has been a chronic problem for naval aircraft radomes for the last 30 years. Protective coatings have been used historically to reduce the problem. NAVAIRDEVCEN is currently using a new protective technique of applying a boot made of 3M polyurethane tape. The boot is a protective sheet that is shaped in the form of the radome and is applied over and bonded to the surface of the radome in one piece. The polyurethane tape boot concept has been used successfully on A-6 and A-7 nose radomes. It provides the protection of polyurethane elastomer without the application and maintenance problems associated with the sprayed polyurethane.

INTRODUCTION

The fiberglass dielectric materials from which radomes are constructed are poor in resistance to rain erosion. The neoprene protective coating, developed in the late 1940's, was used exclusively until the early 1970's and in some cases is still used today. The neoprene coating exhibited superior erosion resistance to the uncoated fiberglass radomes. Preformed neoprene boots have been used for many years. The A-3 and A-4 aircraft have used them since the mid 1960s.

In the late sixties polyurethane elastomeric coatings, which exhibit far superior rain erosion resistance than the neoprene coating, were introduced. Currently used on many Navy aircraft radomes, polyurethane elastomer is still the most erosion resistant dielectric coating for radomes.

The sprayed polyurethane coating creates problems for fleet maintenance because it is difficult to handle during application and removal. Due to gases released during the spraying cure cycles, the application must be performed in specially equipped paint areas. The coating requires about 15 hours to apply and 72 hours to cure. To strip the coating, special strippers that must be used under controlled conditions are required. Due to the difficult handling condition and the health and safety factors, the polyurethane coating cannot be used at the organizational levels of naval aircraft maintenance.

Operational Experience

The A-7 nose radome has experienced erosion problems since its inception. The radome was originally designed with only a 2 to 3 mil coat of polyurethane paint. To improve the performance, NAVAIRDEVCEN proposed the application of a polyurethane erosion protection coating. Before any coating could be applied, the electrical performance had to be checked to assure the coating would cause no degradation in the electrical performance.

Under a NAVAIRDEVCEN contract, four A-7B nose radomes were chosen from aircraft about ready for overhaul at the NAVAIREWORKFAC, Jacksonville, Florida. These radomes had been in service for at least two years since their last overhaul, and their condition varied from very good to poor. The radomes were sent to the Brunswick Corporation, Marion, Virginia, where they were electrically tested using the same tests and procedures applied to new A-7 radomes.

After completion of the initial tests, the radomes were returned to NAVAIREWORKFAC, Jacksonville, where they were stripped and repaired according to normal repair procedures. However, instead of refinishing them with standard polyurethane paint, two of the radomes were coated with Astrocoat RM-115W polyurethane rain erosion resistant elastomer. The other two radomes were sent to NAVAIREWORKFAC, Norfolk, where polyurethane tape boots were installed. All four radomes were sent to Brunswick for retest.

Table I shows the comparison of the test results before and after repair and installation of the rain erosion protective coating. The tests show that either the sprayed polyurethane elastomer or the polyurethane tape boot could be used without affecting radar performance.

Once it had been verified that the boot created no degradation of the radar performance, fleet evaluation was initiated to determine the value of the boot on in-service aircraft. A boot was made at NAVAIRDEVCEN and applied to the A-7 stationed there. After over two years in service the boot is completely undamaged. It looks as good as the day it was applied.

For additional service life experience, boots were installed on fleet aircraft. Twelve boots were fabricated and sent to the Naval Air Station, Lemoore, California. Six boots were applied to aircraft of VA-22 and six were applied to aircraft of VA-94. The boots were installed by organization level personnel with no problems. These aircraft were then deployed to the Western Pacific Fleet. The boots were monitored continously for six months while the aircraft were in service. At the end of that period the radomes had experienced no erosion problems or damage. Based on this experience the decision was made to install boots on all A-7 aircraft. This is being done currently.

POLYURETHANE TAPE BOOT FOR EROSION PROTECTION

Early Use of Polyurethane Tape in Sheet Form

In the early 1970's the 3M company developed polyurethane film backed with a pressure sensitive adhesive. Fleet experience with the use of the tape on the leading edges of wings and bomb racks had shown excellent erosion protection. NAVAIRDEVCEN experimented with the tape to determine its applicability as an erosion protection for radomes. The tape, designated SJ8561, was found to have a dielectric constant of 2.81 and a loss tangent of 0.035. These values are comparable to those of neoprene and slightly lower than those of the sprayed polyurethane elastomer. Based on the experience, rolls of 2 inch and 4 inch wide tape were included in the Radome Repair Kit developed by NAVAIRDEVCEN.

Use of the tape on operational aircraft over the past 6 years has shown excellent results in preventing rain erosion. The tape was tested by George Schmitt on the rotating arm at the Air Force Materials Laboratory, Wright-Patterson Air Force Base, where it was found to be more erosion resistant than neoprene, epoxy paint, polyurethane paint or the base laminate but not as resistant as the sprayed polyurethane elastomer. The failure of the tape, when it occurred, was always in the adhesive bond which caused the tape to tear. A 3M improved-adhesive tape will be tested by George Schmitt during 1978.

Development of the Boot Technique

Although the tape works well on flat or simply curved surfaces, it will not stretch to fit extreme compound curvatures. Harold Sommerfleck of NAVAIREWORKFAC, Materials Laboratory experimented with the tape to develop a technique of using it on compound curves. He developed a method of vacuum forming the tape into a boot and then installing the boot on a radome. The SJ8561 tape is backed with a paper liner and is supplied in rolls up to 4 feet wide. To thermal form the tape, the paper liner has to be removed and the boot formed inside out. 3M, working on Sommerfleck's effort, produced the tape with a polyethelyene liner that could be thermal formed with the boot. This tape is designated SJ8661X. Jack Hickman of NAVAIRDEVCEN modified the forming method slightly by stretch molding the boot instead of vacuum forming it. This makes the process easier and does not require a vacuum facility.

A boot cannot be formed in one piece over a pointed or sharp edged radome such as the F-4, F-14 or F-18 nose radomes. It has to be drawn too deeply and thus becomes too thin. A boot can be made for radomes of this type, but it requires a seam.

Boot Forming and Installation Process

Currently, a program is being conducted by NAVAIRDEVCEN to put boots on all P-3 wing tip radomes. The process illustrated is similar for any boot.

The radome on which the boot will be applied can be used for the mold. A frame slightly larger than the base of the radome is constructed (figure 1). A sheet of the tape is clamped in the frame and then placed in an oven at 350°F for 1 to 1½ minutes. The frame is removed from the oven and tape is stretch formed over the radome (figure 2). The tape is then allowed to cool in this position forming the finished boot. Stretch forming this way creates a boot with the greatest thickness in the nose region, the area of worst erosion with slightly thinner sides where the erosion is less severe.

When the boot is ready to be applied, the polyethelyene liner is removed. A solution of two to three level teaspoons of a non-ionic detergent (e.g., Dreft, Vel or Surf) in one gallon of water or a 50%-50% solution of isopropyl alcohol and water is put on the adhesive side of the boot to deaden the adhesive. Enzyme detergents should not be used because they permanently deaden the contact adhesive.

The radome surface is prepared for the installation by removing all irregularities and discontinuties from the surface. If the tape is allowed to bridge gaps or dents its elastic memory will cause lifting. After the radome is filled it can be painted with polyurethane or epoxy paint which must dry at least 15 hours before application of the boot. The radome surface should be scuff sanded and then wet with the detergent solution.

The boot is placed on the prepared radome and floated into the correct position. Then the boot is squeegeed from the center towards the edges using light overlapping strokes to smooth out the film (figure 3). The boot is dried with a rag and then resqueegeed with firm overlapping strokes. All water and blisters must be worked out. If any air bubbles are present that cannot be squeegeed out, a small puncture should be made with a pin in the film at one end of the bubble and the entrapped air pressed out.

After all bubbles have been removed and the boot has been firmly bonded, the radome should be allowed to dry for 24 hours at room temperature or in an oven at 150°F for 2 to 3 hours to dry out any residual water and to cure the contact adhesive.

When the radome is thoroughly dry, the boot should be trimmed off at the desired place with a razor blade. Then the edges should be sealed with an edge sealer such as 3M decal edge sealer NR-3M-3950. The radome is then ready for operation use (figure 4).

If the boot is damaged or has to be removed for some other reason, it can be stripped off using just a knife or razor blade. To facilitate the removal, an edge of the boot should be lifted and a solvent such as acetone, MEK, toluene or isopropyl alcohol should be applied to the area between the boot and the radome. This will soften the adhesive and make the stripping easier.

The A-6 nose radome experiences the same type of erosion problem as the A-7 nose radome. At about the same time as the A-7 program was started a program was initiated by NAVAIREWORKFAC, Norfolk, for the A-6 aircraft. Electrical tests performed on A-6 radomes by Brunswick showed that the polyurethane boot did not degrade the radar performance. A pilot program was started on fleet aircraft. Boots were applied to several A-6 aircraft in 1974. After 876 flight hours in extreme dry heat, damp, cold, rain and hail environments the polyurethane boot showed no signs of erosion or damage.

During October 1977, two A-6E aircraft stationed at the Naval Air Station, Oceana, encountered heavy rain and hail during a routine flight. One A-6E had a polyurethane boot with paint applied to prevent the yellowing that is common with polyurethane elastomers. The other aircraft's radome was covered with neoprene rain erosion coating. The aircraft with the boot received minor paint erosion damage that required about two hours maintenance time. The other aircraft received major damage to the radome requiring 72 hours of maintenance time. From this experience, the Commander of the Naval Air Force, US Atlantic Fleet has recommended immediate retrofit of all A-6 aircraft with the polyurethane boot.

CONCLUSION

The 3M SJ8661X tape can be easily heat formed into a boot to fit compound curved surfaces. Using a detergent water solution to deaden the contact adhesive the boot can be floated onto the radome surface, cured at ambient room temperature and is ready for flight in less than 24 hours. The installation can be done by fleet organization level personnel with no special tools or safety requirements. Electrical testing showed the boot had no greater effect on antenna patterns than either the neoprene coating or the sprayed polyurethane elastomer rain erosion coating. Since fleet experience has shown the boot to have excellent erosion resistance, all Navy A-6 and A-7 aircraft are being retrofit with these erosion protective boots. Currently P-3 aircraft are being retrofit with boots for the wing tip radomes.

ACKNOWLEDGEMENTS

The technique of thermal forming the 3M SJ8661X polyurethane tape and the application procedure were developed by Harold Somerfleck of the Naval Air Rework Facility, Norfolk, Virginia.

TABLE I SUMMARY OF A-7B NOSE RADOME ELECTRICAL PERFORMANCE

Specification: LTV Specification 204-15-13G Revised per LTV TWX 37 Dated 10-5-67
Test Procedure: BTP-802-124-001 (12-9-64 as Revised by LTV TWX 37 (10-5-67)

Test   Results

Specification Item	Requirement	Polyurethane Boot		Polyurethane Boot		Polyurethane Coating		Polyurethane Coating	
		Initial Test	Following Coating	Initial Test	Following Coating	Initial Test	Following Coating	Initial Test	Following Coating
Minimum Power Transmission	83.1%	78.0%	82.0%	65.0%	76.5%	66.0%	65.5%	77.0%	77.2%
Average Power Transmission	75.0	86.5%	88.6%	75.9%	81.1%	79.9%	81.8%	84.2%	85.7%
Maximum Beam Deflection Area 1, 0 thru +30° Roll	2.5 mr	3.2 mr*	2.4 mr	5.8 mr*	2.2 mr	5.2 mr*	4.0 mr*	7.0 mr*	3.1 mr*
Maximum Beam Deflection Area 1, +30 thru +45° Roll	4.0 mr	2.6 mr	1.9 mr	6.2 mr*	1.8 mr	4.5 mr*	4.0 mr	4.4 mr*	1.6 mr
Maximum Beam Deflection Area 2, 0 thru +30° Roll	5.0 mr	9.6 mr*	6.8 mr*	6.7 mr*	3.1 mr	8.4 mr*	11.2 mr*	3.8 mr	4.1 mr
Maximum Beam Deflection Area 2, +30 thru +45° Roll	10.0 mr	1.8 mr	1.8 mr	5.0 mr	2.7 mr	5.2 mr	7.7 mr	1.2 mr	1.5 mr
Maximum Error Rate Area 1, 0 thru +45° Roll	1 mr/deg	0.5 mr/deg	0.5 mr/deg	1.1 mr/deg*	0.6 mr/deg	0.6 mr/deg	0.35 mr/deg	0.65 mr/deg	0.5 mr/deg
Maximum Error Rate Area 2, 0 thru +30° Roll	1 mr/deg	0.7 mr/deg	0.7 mr/deg	0.9 mr/deg	0.85 mr/deg	1.05 mr/deg	0.7 mr/deg	0.5 mr/deg	0.4 mr/deg
Maximum Error Rate Area 2, +30° thru +45° Roll	1.2 mr/deg	0.6 mr/deg	0.75 mr/deg	0.65 mr/deg	0.75 mr/deg	1.0 mr/deg	0.6 mr/deg	0.5 mr/deg	0.3 mr/deg

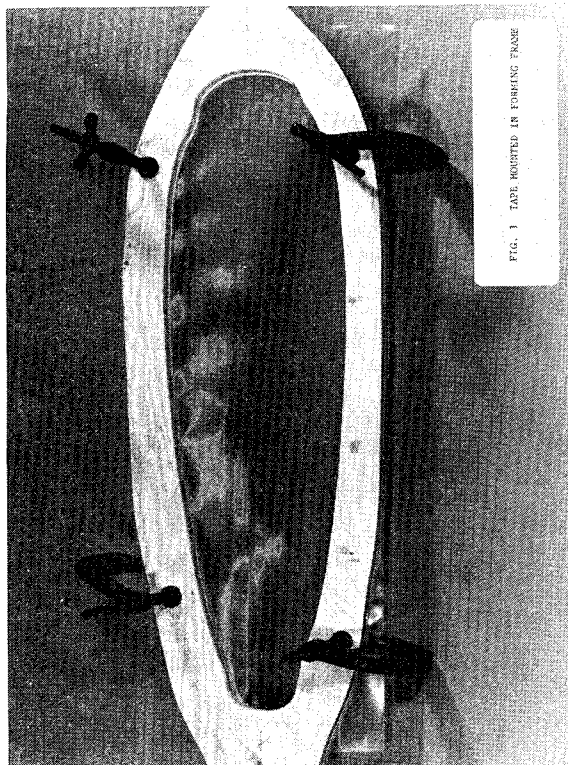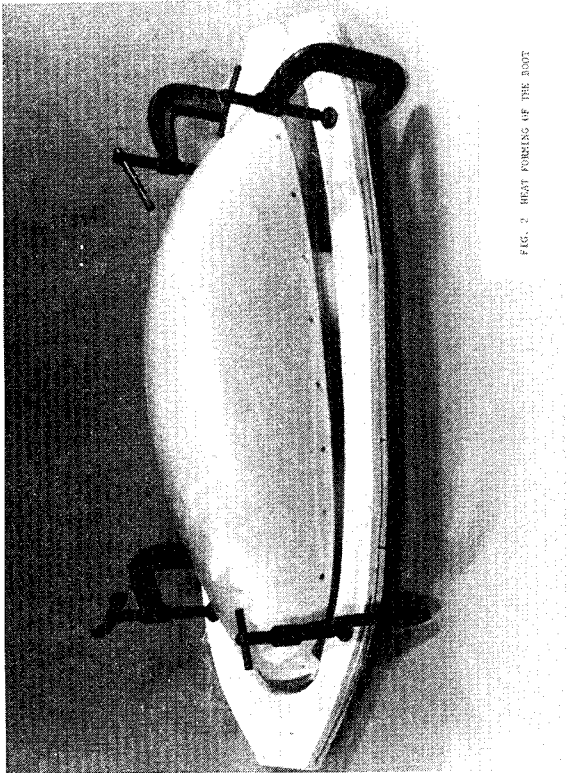* Indicates performance below specification requirements.

FIG. 2 HEAT FORMING OF THE BOOT

FIG. 4 FINISHED BOOT INSTALLED ON THE RADOME
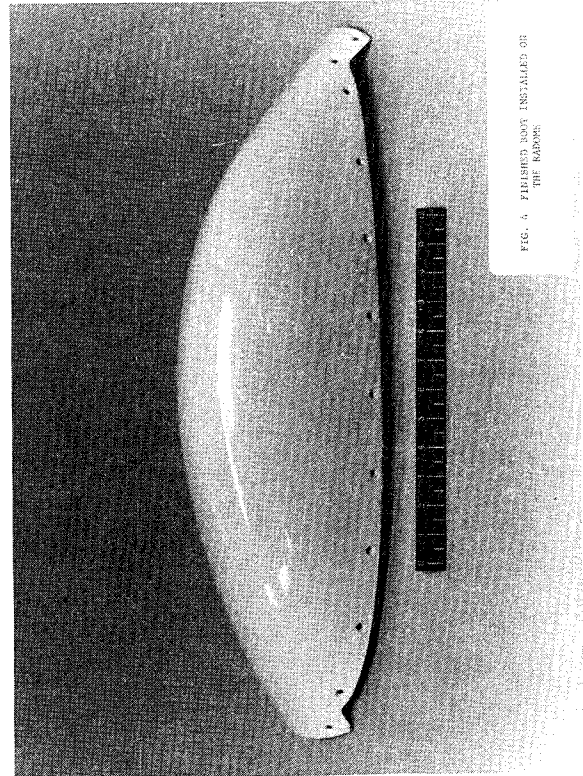

FIG. 1 TAPE MOUNTED IN FORMING FRAME

FIG. 3 SQUEEGING THE FINISHED BOOT IN PLACE

RADOME TEST STAND MEASUREMENT COMPENSATION

Irving Kanter

Raytheon Company, Missile Systems Division
Bedford, Massachusetts 01730

ABSTRACT: Single gimbal-axis radome test stands introduce an unwanted roll of the radome about its longitudinal axis when one attempts to measure the boresight error at a compound yaw and pitch gimbal angle. An expression for this induced roll is developed which may be used to compensate the measurements.

ANALYSIS: In computing boresight error we assume that the missile seeker antenna tracks the target perfectly, i.e., that the boresight axis of the antenna lies along the Poynting vector of the incident electromagnetic radiation. Consider a right handed Cartesian coordinate system i_A, j_A, k_A centered at the antenna (Figure 1) with j_A and k_A along the magnetic, H, and electric, E, fields respectively. For a given radome shape an arbitrary elemental area on the surface of the radome is specified in terms of its location with respect to a coordinate system i_R, j_R, k_R fixed to the radome. For convenience we assume that these two systems coincide when the radome is ungimbaled.

Assume that the seeker's two-axis gimbal system is such that in flight the radome gimbals first about k_A through a yaw angle, Y, then about the subsequent j axis through the pitch angle, P. The response of a surface element to the incident radiation can be calculated provided we know the orientation of the surface element in the antenna coordinate system (A). This will be found in terms of the orientation of the surface element in the radome coordinate system (R) since we know the transformation of coordinates which takes system R into system A.

Consider a vector (x_1, y_1, z_1) whose coordinates are transformed into (x_2, y_2, z_2) when system 2 is obtained from system 1 by rotation about k_1 through an angle θ. The coordinates in the 2 system are given in terms of those in the first system by

$$\begin{bmatrix} x \\ y \\ z \end{bmatrix}_2 = \begin{bmatrix} \cos\theta & \sin\theta & 0 \\ -\sin\theta & \cos\theta & 0 \\ 0 & 0 & 1 \end{bmatrix} \begin{bmatrix} x \\ y \\ z \end{bmatrix}_1 = \begin{bmatrix} x_1 \cos\theta + y_1 \sin\theta \\ -x_1 \sin\theta + y_1 \cos\theta \\ z_1 \end{bmatrix} \tag{1}$$

We note that z goes through unchanged; each new component consists of its old component times $\cos\theta$ and a coupled term which is the cross component times $\pm\sin\theta$. (In this case since i_2 lies between i_1 and j_1 (for $\theta < \Pi/2$) the x component picks up the plus coupling term). This information is succinctly conveyed by means of the schematic in Figure 2.

Flight: Figure 3 shows the gimbaled R system and the reference A system. A surface element on the radome specified by the vector $(V)_R$ has coordinates in the A system given by $(V)_A$ and determined by the indicated schematic in Figure 3. Thus

$$x_A = (x \cos P - z \sin P) \cos Y + y \sin Y$$
$$y_A = y \cos Y - (x \cos P - z \sin P) \sin Y \qquad (2)$$
$$z_A = z \cos P + x \sin P$$

In particular, the coordinate vectors of the R system are given in the A system by

$$i_R = (1, 0, 0)_R = (\cos P \cos Y, -\cos P \sin Y, \sin P)_A$$
$$j_R = (0, 1, 0)_R = (\sin Y, \cos Y, 0)_A \qquad (3)$$
$$k_R = (0, 0, 1)_R = (-\sin P \cos Y, \sin P \sin Y, \cos P)_A$$

Test: We measure the electromagnetic response of the radome in laboratory axes i_L, j_L, k_L. The radome is mounted on a test stand so that i_R coincides with i_L. The radome can be rotated about i_L, but because of mechanical constraints the test stand can be gimbaled about only the single axis, k_L. We start with the horn axes antenna axes and ungimbaled radome axes coinciding with the laboratory coordinate axes. We first rotate the horn, the antenna and the radome through angle θ about i_L. The R system goes into the A system as indicated in Figure 4. Next the horn and antenna are fixed and the test stand (radome) is gimbaled about k_L through angle ϕ. The final radome (R) coordinate axes are expressible in terms of the antenna (A) coordinate axes by noting that the angle between k_A and k_R is ϕ while that between k_R and k_L is θ. The schematic in Figure 4 yields the equations

$$x_A = x \cos \phi + (y \cos \theta - z \cos \theta) \sin \phi$$
$$y_A = [(y \cos \theta - z \sin \theta) \cos \phi - x \sin \phi] \cos \theta$$
$$+ (z \cos \theta + y \sin \theta) \sin \theta \qquad (4)$$
$$z_A = (z \cos \theta + y \sin \theta) \cos \theta - [(y \cos \theta - z \sin \theta) \cos \phi$$
$$- x \sin \phi] \sin \theta$$

In particular the radome coordinate axes are given in the antenna system by

$$i_R = (1, 0, 0)_R = [\cos \phi, -\sin \phi \cos \theta, \sin \theta \sin \phi]_A$$
$$j_R = (0, 1, 0)_R = [\cos \theta \sin \phi, \cos^2 \theta \cos \phi$$
$$+ \sin^2 \theta, \sin \theta \cos \theta (1 - \cos \phi)]_A \qquad (5)$$
$$k_R = (0, 0, 1)_R = [-\sin \theta \sin \phi, \sin \theta \cos \theta (1 - \cos \phi),$$
$$\cos^2 \theta + \sin^2 \theta \cos \phi]_A$$

To find the laboratory angles θ, ϕ which corresponds to a set Y, P of yaw and pitch angles we equate components of i_R in the same A system of (3) and (5); thus

$$\cos \phi = \cos P \cos Y$$
$$\sin \phi \cos \theta = \cos P \sin Y \qquad (6)$$
$$\sin \phi \sin \theta = \sin P$$

168

or

$$\phi = \tan^{-1}\left(\sqrt{\frac{\tan^2 Y}{\cos^2 P} + \tan^2 P}\right)$$

$$\theta = \tan^{-1}\left(\frac{\tan P}{\sin Y}\right)$$
(7)

Plots of ϕ, θ versus Y, P are given in Figure 5. They do not tell the whole story however. By proper choice of θ, ϕ in (7) we can ensure that i_R in the laboratory has the same orientation in terms of the incident E and H fields as does i_R in flight. However, in flight the missile may be roll stabilized. Since the surface thickness of the radome does not in general possess circular symmetry about the radome's longitudinal (i_R) axis, we must calculate any roll induced by the test stand. Since the negative sine of the roll angle, ψ, is given by the scalar product of j_R in flight and k_R on the test stand we calculate this scalar product in the same A coordinate system, i.e., j_R from (3) and k_R from (5). Thus

$$\sin \psi = \sin Y \left[\sin \theta \sin \phi\right] - \cos Y \left[\sin \theta \cos \theta (1 - \cos \phi)\right] \qquad (8)$$

When (7) is employed we obtain

$$\psi (Y,P) = \sin^{-1}\left(\frac{\sin Y \sin P}{1+\cos Y \cos P}\right) = \sin^{-1}\left[\frac{\sin\theta \cos\theta (1-\cos\phi)}{\sqrt{1 - \sin^2\theta \sin^2\phi}}\right]$$
(9)

$$= \Psi (\theta, \phi)$$

We note that when making principal plane measurements, P = 0 or Y = 0, (θ = 0 or θ = $\Pi/2$), there is no induced roll. For a compound gimbal angle measurement however, we must, using (7), first calculate the θ, ϕ which corresponds to the desired Y, P orientation. Then using (9), unroll the radome (or the horn and antenna) before measuring the boresight error. We note in passing that ψ (Y, P) is invariant with respect to interchange of yaw and pitch. The induced roll is shown in Figure 6.
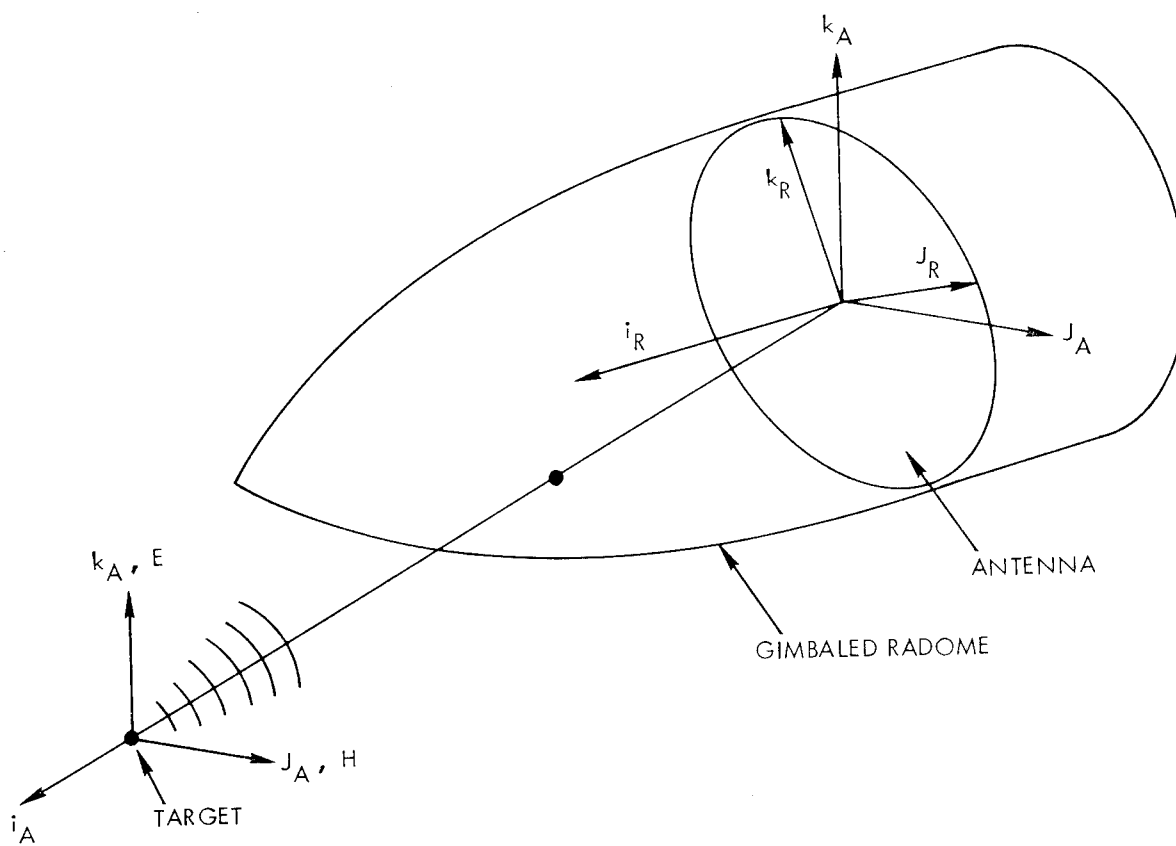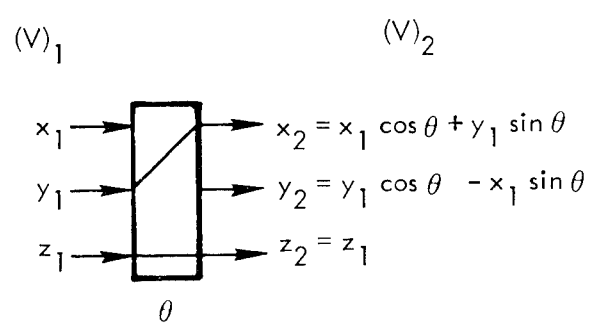
Figure 1.   Radome - Target Geometry

$$(V)_1 \qquad\qquad (V)_2$$

$x_1 \rightarrow$ ▭ $\rightarrow x_2 = x_1 \cos\theta + y_1 \sin\theta$

$y_1 \rightarrow \qquad \rightarrow y_2 = y_1 \cos\theta - x_1 \sin\theta$

$z_1 \rightarrow \qquad \rightarrow z_2 = z_1$

θ
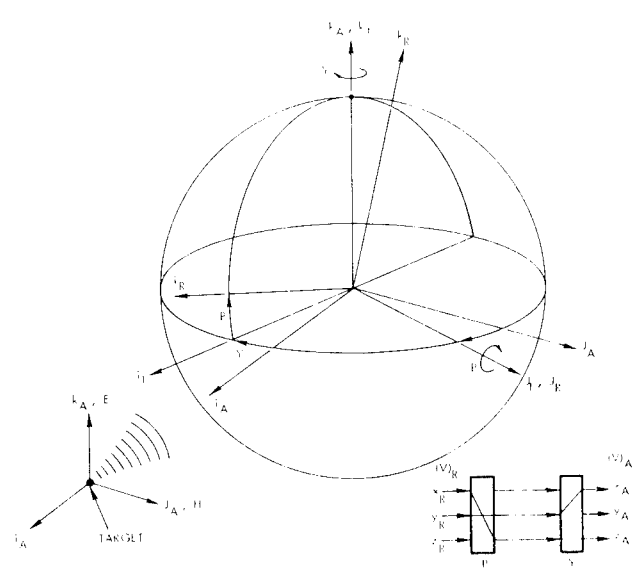
Figure 2.   Coordinate
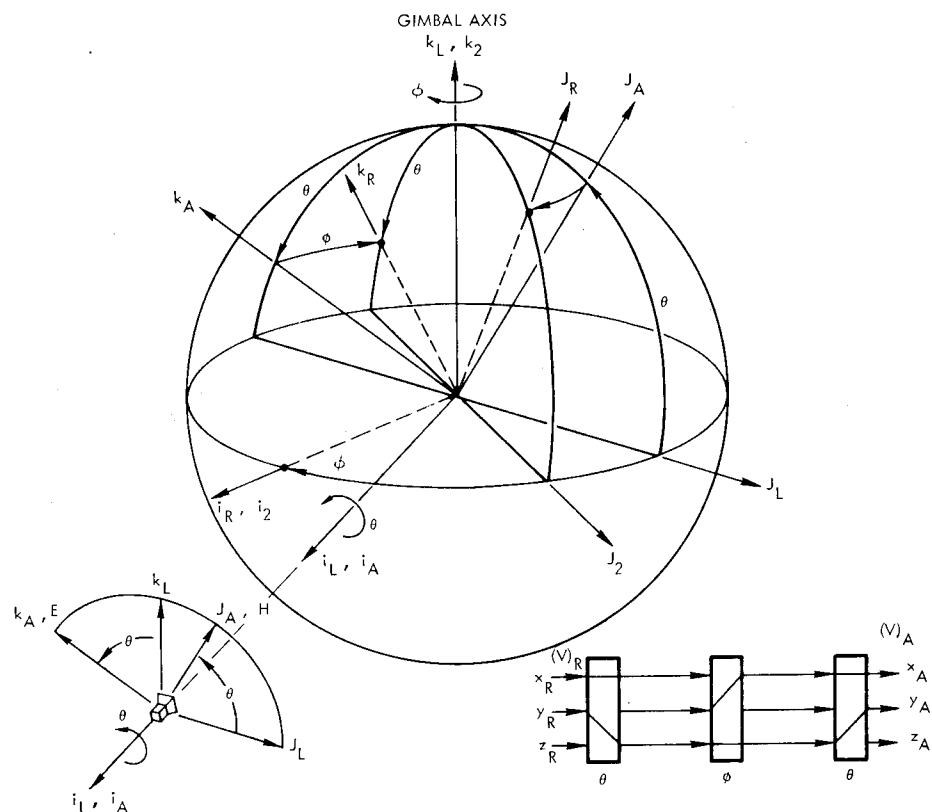Transformation Schematic

Figure 3.   Flight Gimbaling
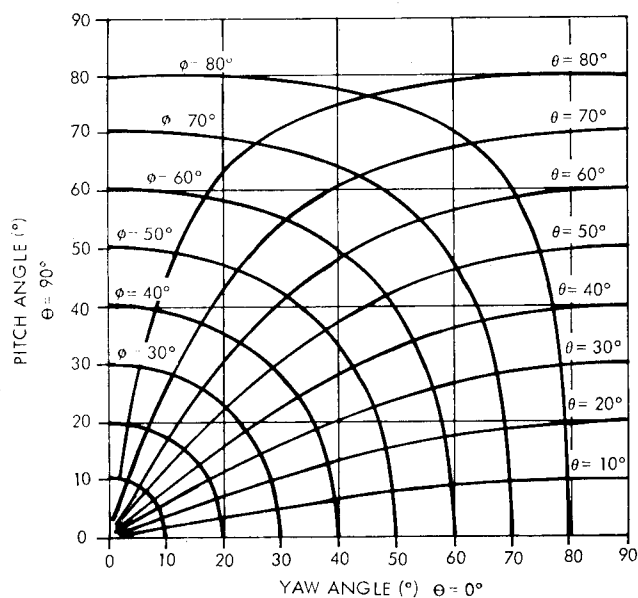
Figure 4. Test Stand Gimbaling

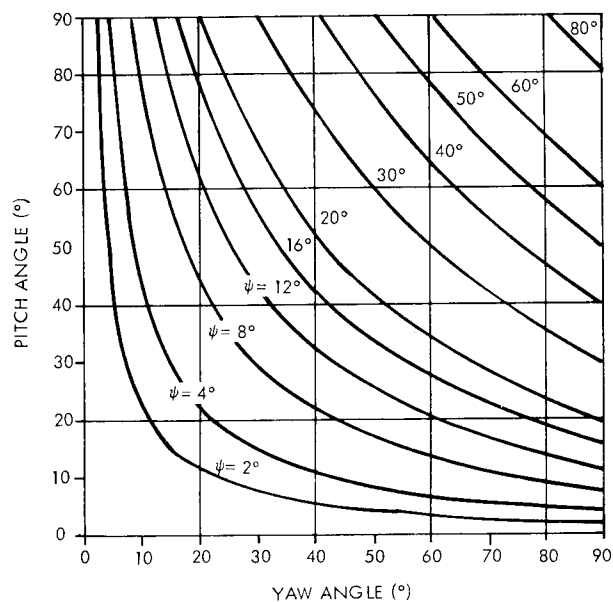Figure 5. Mapping Between Single-Axis Test Stand Angles and Compound Gimbal Angles

Figure 6. Radome Roll Induced By Single-Axis Test Stand Measurement as a Function of Compound Gimbal Angle

171

AUTOMATED RADOME TEST FACILITY

T. Dowling, M. Cerullo, C. S. Ward, A. R. Chinchillo
Raytheon Company, Missile Systems Division
Bedford, Massachusetts 01730

SUMMARY

The Automated Radome Test Facility permits the rapid collection of the large amounts of data necessary to characterize completely a radome's performance. An 8:1 measurement time improvement was obtained compared to manual measurement, and human setup errors were virtually eliminated. The collected data (approximately 115,000 data points) can be immediately processed and displayed in sophisticated formats which expedite the design and development process.

The availability of a general purpose computer in the system enables immediate on-the-scene simulation of radome computer compensation methods on actual measured radome data.

Also, the facility can be used to supplement a manufacturing plant's testing capacity to verify the adequacy of manufacturing methods and process modifications via rapid testing of pilot production lots.

BACKGROUND AND MOTIVATION

Boresight error, which is caused by a radome's complex curvature, must be measured as a function of antenna yaw-pitch gimbal angles, polarization and frequency. These measurements typically require the collection of 115,000 data points to characterize completely a radome's performance and thereby permit thorough design tradeoffs. Otherwise, if fewer measurements were used in the design modification cycles required for radome optimization, the result would be improved radome performance in the measured planes at the expense of degradation in nonmeasured areas, which is unsatisfactory.

In the manual measurement system, the data collection took nine days per dome and since many parameters must be accurately set for each measurement sequence, there was significant potential for human error. After these data were gathered, they were sent to a data processing center for digitizing. These digitized data were then processed on a central computer to produce the outputs required by the designer.

All of the above led to lengthy delays in radome design and thus to the decision to design a computer-controlled radome test facility. This facility eliminated most of the measurement and data reduction delays and also resulted in significantly more accurate and repeatable data.

OVERALL DESCRIPTION

The automated facility is a highly effective combination of hardware, software, and a dedicated computer arranged as shown in Figures 1 and 2 to accomplish full radome electrical characterization automatically. The following capabilities are automated via computer control:

- System Calibration
- BSE Measurement
- Data Processing
- Data Displays

Key advantages resulting from this automation are:

- Large quantities of data (i. e., 115,000 BSE values per dome) are measured quickly in nine hours, instead of nine days by manual methods.
- Accuracy of the data is improved due to the virtual elimination of human error in the adjustment of the many different test conditions; i. e., radome roll angle, receive antenna roll angle and transmit horn polarization angle.
- Data are processed in the dedicated computer immediately after completion of tests to provide radome design engineers with prompt information for decision making.
- Processed data are displayed at the facility in a variety of formats, such as 3-D contour plots and cumulative distribution plots (see examples below), which simplify and expedite the engineer's evaluation of candidate designs.

The above capabilities in measurement and data processing can be exploited to provide: 1) immediate simulation of radome computer compensation methods using actual measured data; 2) additional test capacity to supplement that of a manufacturing plant for verifying the adequacy of manufacturing methods and process modifications via rapid testing of pilot production lots.

It is also noteworthy that the interaction of the test operator with the computer is straightforward and requires no special training in programming or the like. For instance, Figure 3 shows a typical sequence of computer questions and test operator responses by which comprehensive radome tests are performed. Computer questions in Figure 3 (shown in rectangles) are displayed on a video console, and operator responses (shown in ovals) are typed in at the same console. The flow of events in Figure 3 accomplishes three basic functions: 1) definition of tests to be performed; 2) calibration of system; and 3) data measuring and recording.

EXAMPLES OF DATA DISPLAY FORMATS

Three examples of the convenient display formats available at the facility are the following: 1) BSE versus gimbal angle plot; 2) 3-D BSE contour plot; and 3) cumulative BSE slope distribution plot. Figure 4 is a typical plot of measured BSE versus gimbal angle drawn up by an automatic plotter that is linked to the computer for displaying data recorded on magnetic tape. Figure 5 is a more comprehensive 3-D display of BSE for all the look angles of interest over the entire surface of the dome. This display is available immediately after tests are completed, and it provides the radome designer with a prompt, convenient overview of the entire performance of the dome. For instance, radome symmetry and localized trouble spots can be assessed, and comparisons against performance specifications can be made quickly for the whole dome.

Figure 6 represents a typical plot of the cumulative distribution of BSE slopes for the full dome. This format is particularly useful to the missile systems engineer for calculating probability distributions of miss distance and probability of kill. This distribution curve is automatically drawn after the computer does the following processing: 1) transform the BSE data from test station (polar) gimbal angle coordinates to missile pitch - yaw coordinates; 2) calculate and store BSE slopes for all look angles of interest; and

3) sort and "bin" all slopes according to amplitude and polarity. A convenient single parameter for summarizing an entire radome's performance is also shown in Figure 6, namely R_t, which describes the BSE slope range containing 90 percent of all slopes.

CONCLUSIONS

Radome BSE tests and data displays are now made much faster, more accurately and more comprehensively with Raytheon's Automated Radome Test Facility than was possible with previous manual methods. The benefits are: 1) a significant improvement in radome design capability; and 2) major cost reductions for radome testing.
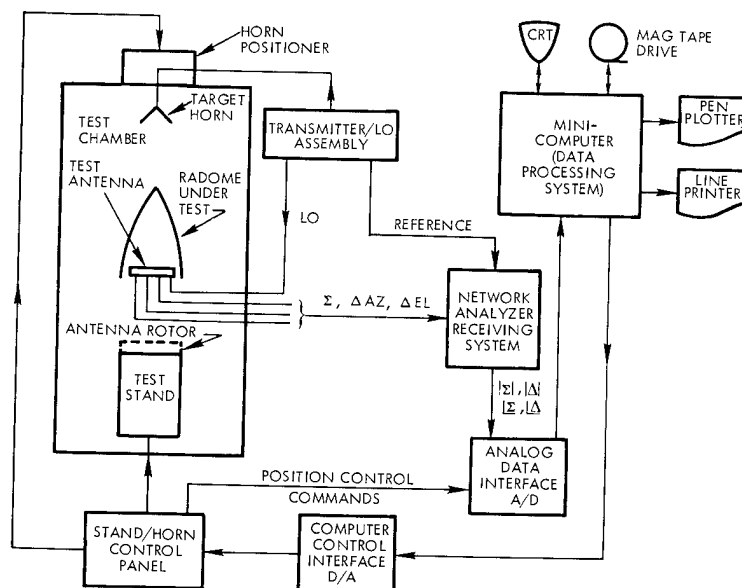

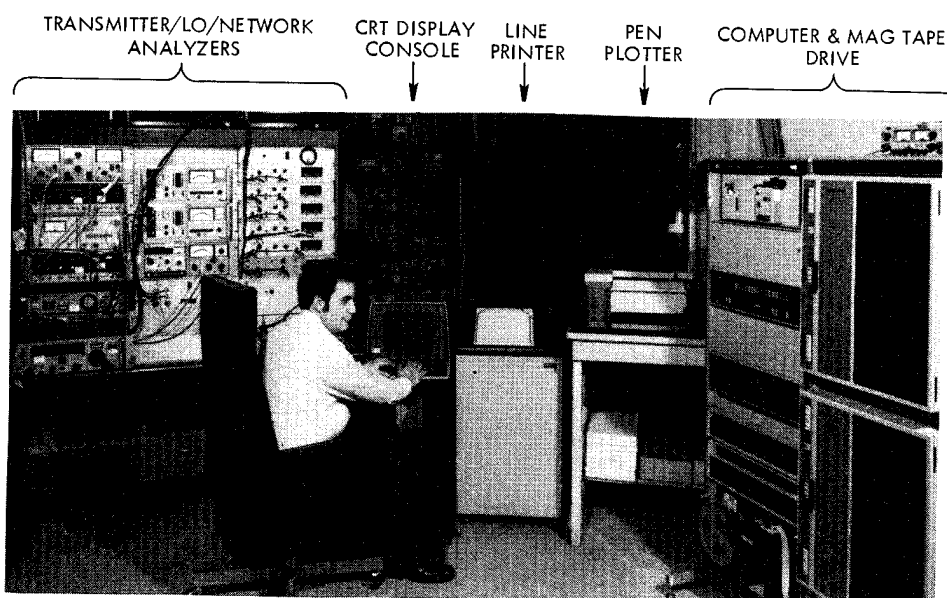Figure 1 - Block Diagram of Automated Radome Test Facility

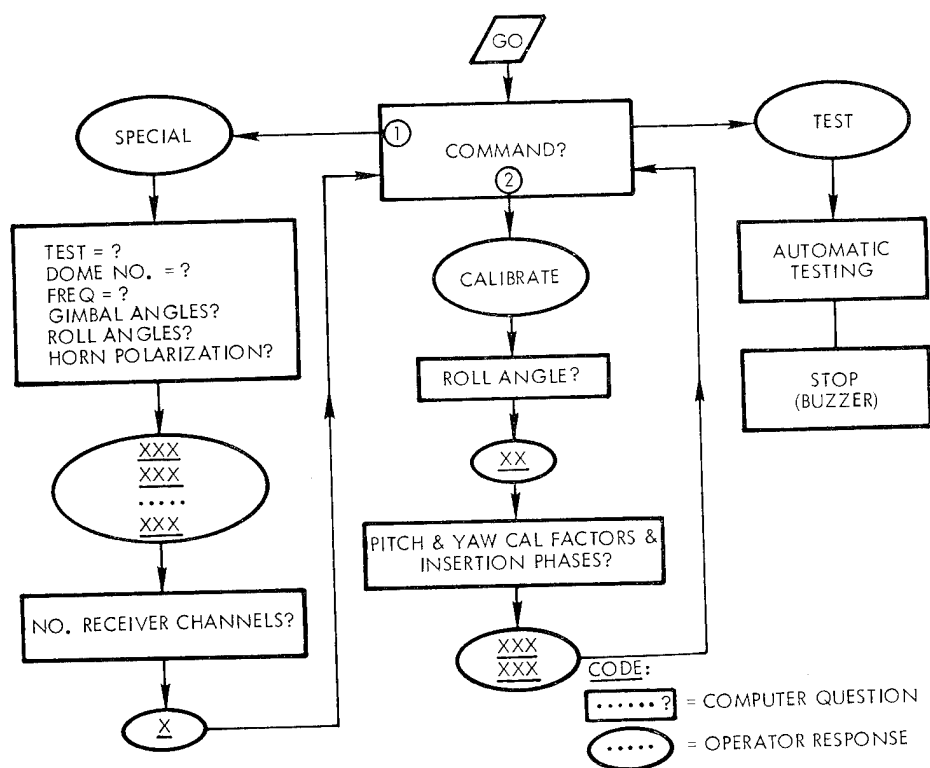Figure 2 - Photo of Key Hardware in Automated Radome Test Facility
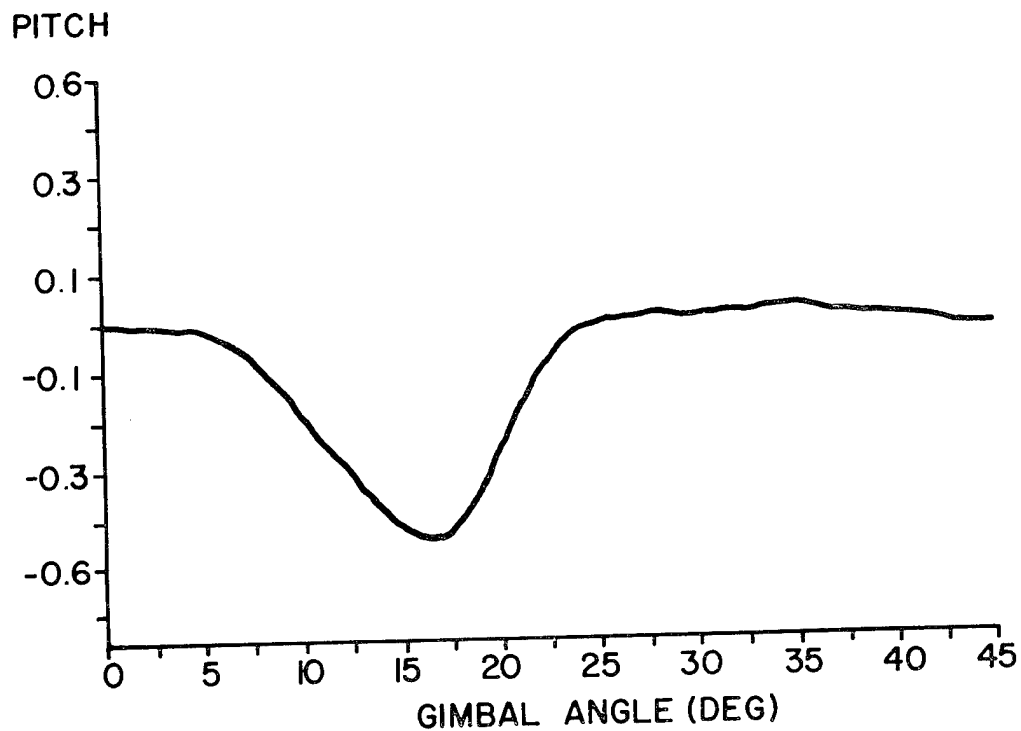
Figure 3 - Operator Interaction with Test Station

PITCH

GIMBAL ANGLE (DEG)

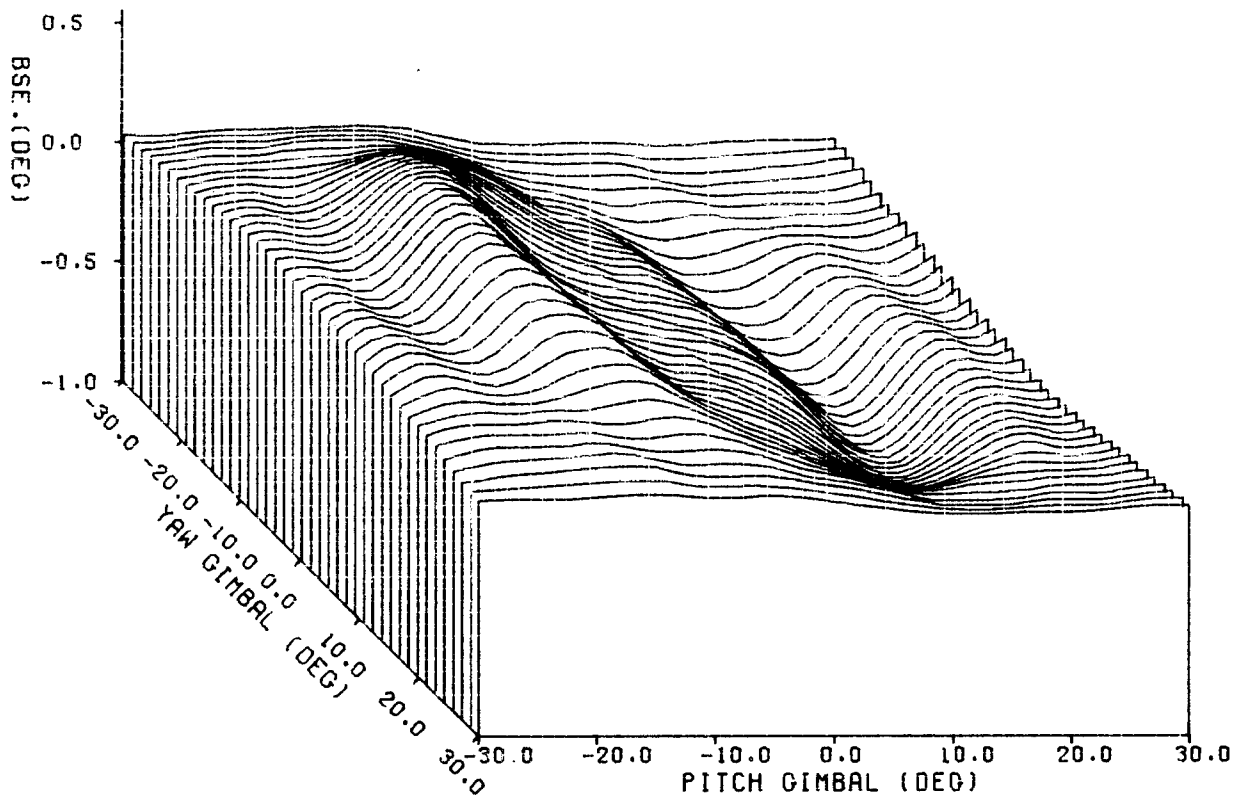Figure 4 - BSE Versus Gimbal Angle by System Pen Plotter

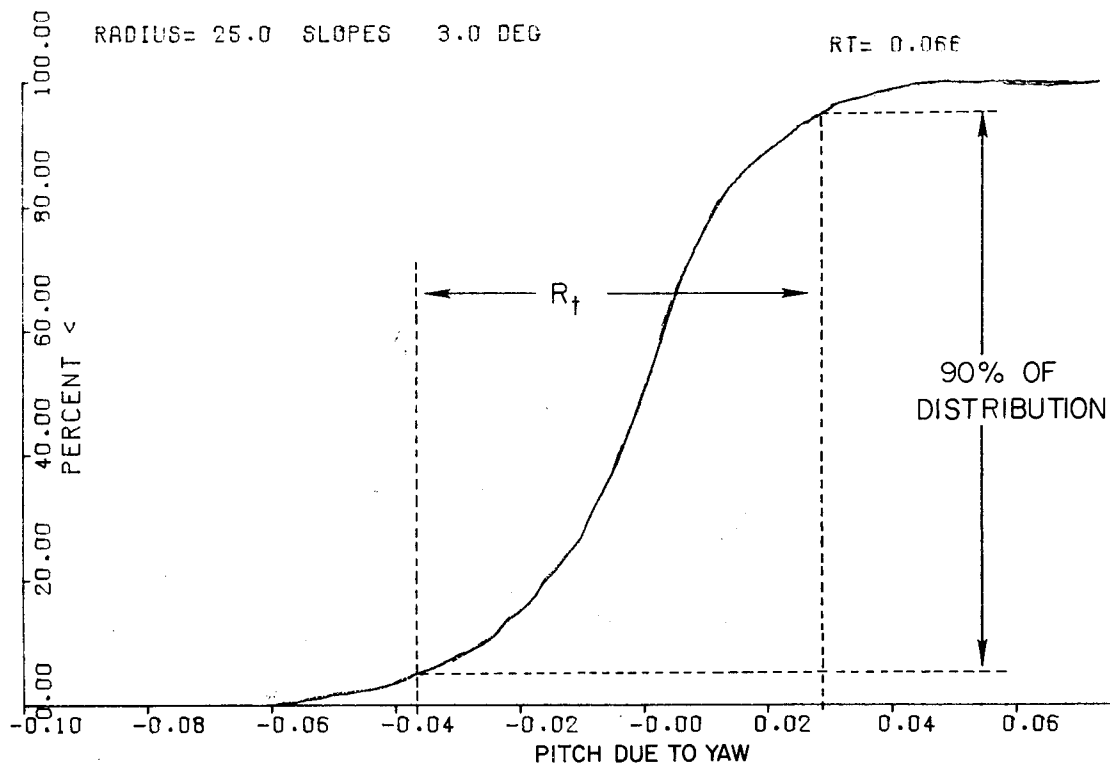Figure 5 - 3-D Contour Plot of Pitch BSE

Figure 6 - Cumulative Distribution of BSE Slopes

177

DEVELOPMENT OF A RESONANT METAL RADOME

W. R. Bushelle, McDonnell Douglas Astronautics Company - St. Louis, MO
L. C. Hoots, Brunswick Corporation, Marion, VA
R. M. Van Vliet, Air Force Materials Laboratory, WPAFB, OH

INTRODUCTION

Although the concept of resonant metal radomes is not new, there has been renewed interest in their study because of their potential for overcoming disadvantages inherent in conventional radomes, such as susceptability to lightning damage and static charge build-up. Also, a resonant metal radome offers reduced radar cross section and electromagnetic pulse (EMP)/electromagnetic interference (EMI) attenuation. Finally, the resonant metal radome concept affords the radome designer a new set of design options not available with conventional radomes. For example, the potential exists that metallic radome designs may be a solution to the radome problems associated with hypersonic flight, such as rain erosion and thermal shock, or the solution to future design requirements such as laser hardening and IR signature reduction.

The program was conducted under the sponsorship of the Air Force Materials Laboratory, Contract Number F33615-76-C-5157.[1] The electrical slot pattern designs were supplied by the Ohio State University ElectroScience Laboratory, under contract to the Air Force Avionics Laboratory.[2]

The objective of the program was to develop and demonstrate a technique for applying a slotted metallic coating to polymeric radomes. The Lockheed Jetstar (C-140) nose radome was selected to be covered with the slotted metallic coating. The C-140 radome is 21 inches long and 28 x 34 inches at the base and has an A-sandwich wall construction of E-glass/epoxy skins and a nylon/phenolic honeycomb core. The C-140 radome is designed to operate at X-band frequencies (9.375 GHz).

DEVELOPMENT OF FABRICATION TECHNOLOGY

Several methods were identified and developed for providing an adherent and uniform slotted metallic coating for radomes. An approach combining two

of these methods was selected for metallizing the demonstration radomes. The approach involved: (1) electroforming a nosecap for the highly doubly curved region of the radome nose and adhesively bonding it to the radome and (2) adhesively bonding etched copper foil pieces to the remaining less highly curved surfaces.

The nosecaps were electroformed on a planographic mandrel. The mandrel was made of stainless steel which had been drop hammer formed in a matched metal die. The mandrel was cleaned, passivated, and spray coated with photoresist. A doubly curved transparency, made by a technique developed in this program, was used to image the photoresist with the required slot pattern. The photomasked mandrel was spray etched with ferric chloride until the slot pattern was 0.008 inches deep into the 0.020 inch thick mandrel. The etched mandrel was then stripped of remaining resist and recleaned. The recessed slots were filled with Teflon and sanded smooth. The entire mandrel was polished to provide a smooth conductive surface upon which to electrodeposit the copper nosecap. The mandrel was placed in a plating bath and copper was deposited to a thickness of 0.005 inches. Note: The copper did not deposit on the Teflon filled slots because the plating process is electrolytic and the Teflon is a dielectric. The electroformed, slotted copper part was then released from the mandrel (Figure 1), and adhesively bonded onto the radome. Of the various fabrication approaches identified and studied during the program, this electroforming method is considered to have the most potential for use in quantity production of resonant metal radomes. However, in this study the process was used only for the manufacture of the nosecap because of the high cost of fabricating a planographic mandrel for the full radome. In actual production, this cost would be amortized over an entire production run, making this a practical and preferred manufacturing method.

The remainder of the radome was covered with etched 0.005 inch thick copper foil. The etched foil was cut into triangles and laid out on the radome surface in an arrangement which allowed the entire radome to be covered with slotted copper (Figure 2). The slot design used on these radomes was developed at the Ohio State University ElectroScience Laboratory (OSU) and consisted of a periodic array of tripolar slot elements like those shown in Figure 3. Three variations of this design were employed in order to uniformly cover the radome surface. Since periodicity of the pattern is important for

good electrical performance, the edges of the copper foil triangles were serrated so that they interlocked with one another. This allowed the tripolar slot elements to overlap, minimizing interruptions in the periodicity of the slotted array along the seams of the foil triangles (Figure 4). All of the copper (i.e. both nosecap and foil triangles) was adhesively bonded to the radome. Finally the radome was overcoated with an 0.020 inch thick polyure-thane rain erosion coating (per MIL-C-83231).

ENVIRONMENTAL TEST PROGRAM

A testing program was conducted to determine which fabrication method, type of metal, kind of adhesive, and metal foil thickness was most resistant to the environmental effects of concern to radome designers, i.e., lightning, rain erosion, precipitation static, temperature/humidity/altitude cycling, sunshine, and solvent exposure. The following is a summary of those test results:

o Lightning tests indicated that a 0.005 inch slotted copper coating could protect the radome substrate and enclosed antenna from damage in a 200,000 amp lightning strike, which is in the upper one percentile of natural occurring lightning strikes.

o Rain erosion testing performed at the Air Force Materials Laboratory Whirling Arm Facility demonstrated that the bonded copper fabrication method, when overcoated with a 0.020 inch thick polyurethane rain erosion coating, was sufficiently resistant to rain erosion so that in service, a significant number of flight hours could be accumulated before the radome's rain erosion coating would require refurbishment.

o Precipitation static (p-static) tests were conducted in the MDC Blown Dust P-static simulator, which demonstrated that a grounded metallic coating eliminates p-static associated noise below ambient noise conditions, even when overcoated with 0.020 inches of polyurethane rain erosion coating.

o A series of additional environmental tests, commonly specified in radome procurement specifications, were also performed. The tests, conducted in conformance with MIL-STD-810, included: temperature/ humidity/altitude cycling; sunshine exposure; solvent resistance; and because of the metallic coating, corrosion resistance testing. All

resonant metal radome specimens tested demonstrated at least as much resistance to these effects as conventional radomes.

ELECTRICAL EVALUATION

In order to conveniently assess the performance of the slot design, and the radome wall configuration resulting from the selected fabrication technique, numerous flat panels were fabricated and tested. The flat panels were tested for transmission efficiency and insertion phase delay (IPD) at incidence angles from 0 to 60°.

The panels were tested with various slot patterns both with and without rain erosion coatings. Otherwise the panels were, in general, all very similiar. The effects of a 0.020 inch thick rain erosion coating on transmission and resonance as determined from the flat panel tests can be seen in Figure 5. The resonant frequency is shifted downward nearly a gigahertz because of the presence of the dielectric coating. Figure 5 also shows that bandwidth can be narrowed by altering slot leg width. Out of band transmission measurements which were conducted demonstrated the value of the resonant metal radome for attenuating EMP/EMI. Optimum sizing of the slots was never achieved so that the A-sandwich substrate and metallic coating were always resonant at different frequencies, i.e. stagger tuned. Even so, transmission efficiencies of 87% were achieved without rain erosion coating and 84% with the erosion coating. One panel assembled as an unbalanced A-sandwich (unequal skin thicknesses) had a transmission efficiency of nearly 89% without the rain erosion coating. This indicates that optimization of the total metallic radome wall, i.e., substrate and slotted metal coating, holds potential for additional improvement in performance beyond that achieved in this program.

The specific slot design used on the demonstration radomes had an overall average transmission of 77% (all incidence angles and polarizations) in the flat panel tests. Due to time constraints, it was necessary to proceed with fabrication of the demonstration radomes before the optimum dimensions of the slot elements could be exactly determined.

The completed radomes, which had the same wall design as the flat panels were tested for transmission efficiency, boresight error and antenna patterns. Table I summarizes performance of the demonstration radomes. The overall average transmission efficiency of the demonstration radomes was 77% at

resonance (8.875 GHz). It should be noted that this is identical to the data for the flat panel tests of the same configuration. There was a 2.8 dB increase in the sidelobe levels for the H-plane case and a 5.3 dB increase for the E-plane case over the free space levels for the antenna alone. Boresight errors at resonance were on the order of 7 to 10 milliradians.

CONCLUSIONS

The electrical performance of the demonstration radomes was excellent in terms of agreement with the flat panel test results. Average transmission of the two radomes was equal (to within approximately 3%) to that of the flat panel which incorporated the slot pattern exactly like that used on the radomes, at all three test frequencies. While an improved design could alter the comparison, the degree of conformance was impressive. This indicates that the inevitable compromises necessary to adapt a periodic array to a doubly curved radome can be tolerated. Therefore, the single most important goal of the program, development of a fabrication method was achieved.

To improve electrical performance, the stagger tuning of the slotted metal array and the substrate must be eliminated by optimally sizing the slots. In addition, the substrate should be designed specifically for use with the slotted metal coating, rather than adapting an existing radome design. With these steps the achievement of 90% overall average transmission is seen as readily achievable. Experience has shown that when transmission efficiency is improved the other aspects of performance, boresight and antenna patterns, are also improved. The results of this work indicate that resonant metal radomes are very near to being a practical design alternative to conventional all dielectric radomes.

REFERENCES:

1. Bushelle, W. R., Hoots, L. C., "Exploratory Development of Resonant Metal Radomes," Air Force Materials Laboratory Report AFML-TR-78-XXX, May 1978.

2. Kornbau, T. W., Munk, B. A., "Design of a Metallized Radome for the C-140 Aircraft," Ohio State University Report 4346-4, July 1977.
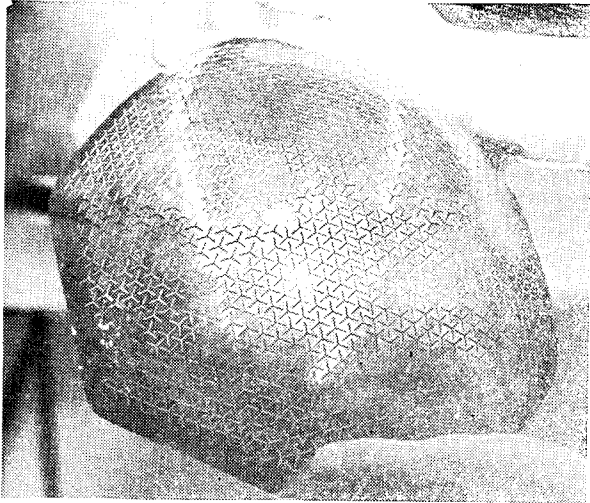
FIG. 1. ELECTROFORMED COPPER NOSECAP
FOR THE DEMONSTRATION RADOME

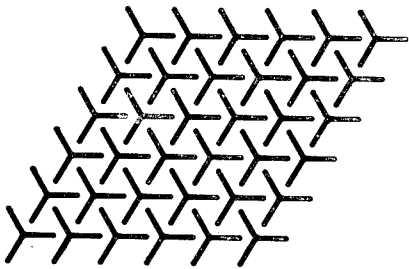FIG. 2. DEMONSTRATION RADOME
COMPLETELY METALLIZED

FIG. 3. TYPICAL SLOT ELEMENTS LIKE
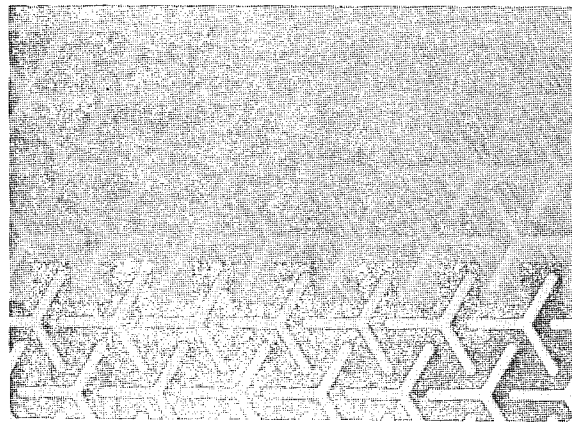THOSE USED ON DEMONSTRATION
RADOMES

FIG. 4. DETAIL OF INTERFACE BETWEEN
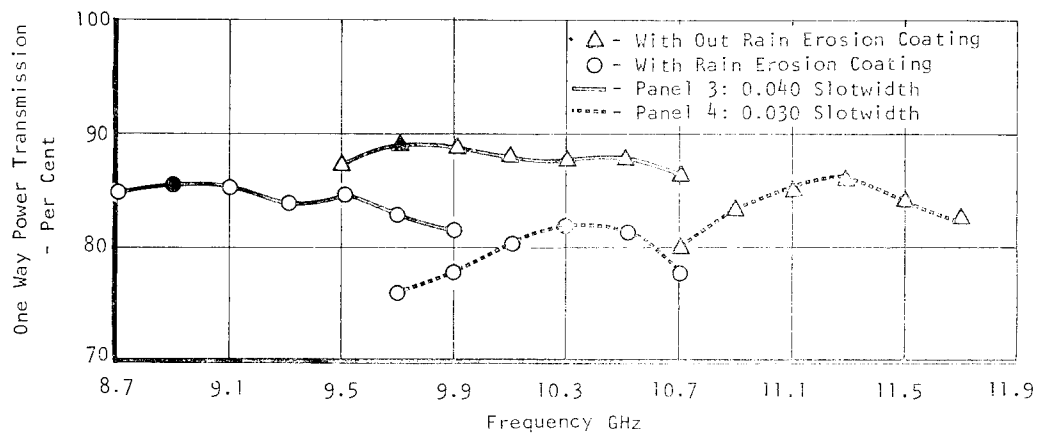FOIL TRIANGLES SHOWING
SERRATED EDGES AND OVERLAP-
PING SLOTS

FIG. 5. EFFECTS OF RAIN EROSION COATING ON RESONANT FREQUENCY

184

TABLE I - PERFORMANCE SUMMARY FOR RESONANT METAL RADOMES

Radome: Freq. (GHz):	S/N 1			S/N 2			UNMETALLIZED
	8.570	8.875 (RESONANCE)	9.375	8.570	8.875 (RESONANCE)	9.375	9.375 (RESONANCE)
Power Transmission, % - Average - Minimum	72.6 68.5	77.6 68.5	68.6 59.0	74.1 68.5	76.0 72.5	68.0 61.5	90.0 85.0
Beam Deflection, Max., mr - Nose Area - Outside Area	6.8 7.4	6.9 7.8	8.8 10.1	9.2 9.0	10.2 9.2	10.6 12.4	NA NA
Beam Deflection Rates of Change, Max, mr/deg.	0.50	0.68	1.20	0.76	0.80	1.22	NA
Pattern Beamwidth Increase, Max., % - H-Plane - E-Plane	10 15	* *	* *	6 15	6 *	* 10	≤10 ≤10
Max. Sidelobe Level with Dome, dB - H-Plane - E-Plane	-20.8 -18.5	-25.9 -19.8	-19.1 -16.8	-20.5 -18.3	-25.0 -19.5	-20.5 -19.5	(8.875 GHz) -24.8 -21.8

Notes:
(1) mr - milliradians.
(2) Beam Deflection Rates Averaged over 5 Segments.
(3) * For Beamwidths without change (to test accuracy), or decreases in beamwidth.
(4) Sidelobe Levels for Antenna Alone at the three frequencies:
      H-Plane -21.6/-27.8/-20.8 dB
      E-Plane -20.8/-24.8/-23.1 dB

185

COMPARITIVE MEASUREMENTS ON ANTENNAS AND RADOMES USING COMPACT AND CONVENTIONAL ANTENNA RANGES

Mr. C. McCartney, Mr. S. W. Waterman

British Aerospace, Dynamics Group, Stevenage, Hertfordshire, England

1. INTRODUCTION

All test ranges which are intended to be used for measurement of the far field performance of an antenna have the fundamental requirement that the electromagnetic field in the region of the antenna under test should be a plane wave, i.e., constant amplitude and phase. Various approaches are used which attempt to produce an approximation to a plane wave and are generally known as conventional test ranges, being either free space ranges or reflection ranges. The deviation from plane wave over a given test aperture reduces as the wavelength and range length increase. Conventional ranges need therefore large areas of real estate free from interfering obstacles. The magnitude of the problem is increased if the measurement has to include a radome (and also associated hardware, e.g., pitot), since the size of the test aperture required has to include the swept area of the radome.

The prime advantage of a compact test range is the reduction of the length of the range to such an extent that large test apertures become possible in an indoor environment. A measurement programme has been carried out which has demonstrated that a compact test range can be used for radome measurements over a wide range of frequencies.

2. SMALL SCALE TEST RANGE

To demonstrate the suitability of the compact test range for radome measurements a small scale compact range was built. The range consists of a positioner placed in the near field of an offset fed parabolic reflector and the whole range enclosed in a simple anechoic chamber. The feeds were of the corrugated horn type which have good circular symmetry over a wide frequency range. Measurements of amplitude and phase of the field in the test aperture were made and the edge shape of the reflector was modified to reduce the ripples in the test aperture. For 50% of the projected area of the reflector the variation in amplitude was reduced to 1 dB and $\pm 10^{0}$ in phase in X band. This gave a test aperture of approximately 600 mm in diameter with a range length of 1.5 m. An equivalent conventional range would have a length of 24 m at X band, and that has a 22^{0} systematic phase variation which is much worse than a pseudo-random 10^{0} variation.

3. COMPARITIVE MEASUREMENTS

Measurements were carried out on the compact range and a conventional range at C, X and Q band for three types of antenna/radome combinations.

3.1. C band measurements

The antenna consisted of a four dipole element linear array which has sum and difference outputs and was mounted in an ogive shaped solid radome but offset from the radome axis. The swept diameter of the radome was equal to the width of the compact range reflector and the width of the antenna was 1/6th the reflector width. Figure 1 shows the difference channel polar diagram measured on a conventional range of length 7.6 m and on the compact range at 1.5 m for antenna set angles of 0° Azimuth and 0° Elevation. Figure 2 shows the measured aberration due to the presence of the radome for the same test ranges. Good agreement is demonstrated between the conventional and compact test range results. If only the antenna dimensions are considered then the conventional range length of 7.6 m corresponds to a range of 16 D^2/λ and if the full swept diameter of the radome is considered, the conventional range length is 0.5 D^2/λ.

3.2. X band measurements

These measurements were carried out on a 200 mm diameter single plane monopulse antenna and an elliptical shaped sandwich type radome. The swept diameter of the radome being 450 mm. The conventional range length was 4.5 m (equivalent to $3D^2/\lambda$ for the antenna and $0.6D^2/\lambda$ for the swept radome). Figure 3 shows the sum channel polar diagrams as measured on the conventional and compact ranges the range length in the latter case being 2 m. Measurements have been carried out on the compact range lengths of between 1.5 and 3.5 m. Table 1 lists the measured side lobe levels for various range lengths.

Table 1

Range length (m)	Side Lobe Level (dB)			
	A	B	C	D
1.5	23.0	21.3	18.0	12.2
2.0	23.2	23.0	17.8	12.0
2.5	22.5	22.0	17.0	11.0
3.0	23.0	22.0	17.2	11.3
3.5	23.0	22.4	17.5	11.8
Conventional 4.5	22.5	22.3	16.5	10.8

Null depths measured on the compact site were lower than the conventional site and coupled with the measured lower side-lobes indicates that the aperture field is a better approximation to a plane wave in the compact range case.

Figure 4 compares the measured aberration due to the radome for the conventional range length of 4.5 m and compact range length of 2 m. Again this shows good agreement. The offset in the aberration curves is due to slight asymmetry in the radome.

3.3. Q band measurements

For Q band measurements a standard waveguide horn was mounted inside a thin wall ellipsoidal shaped radome and measurements taken on a conventional range at various range lengths from 3.5 to 7 m and on the compact test range at ranges from 1.5 to 2.3 m. Figure 5 compares the measurements of the main lobe with the horn axis at 30° to the radome axis for conventional range length of 7 metres ($4 D^2/\lambda$ for the antenna and compact site length of 1.5 m showing reasonable agreement. For the same antenna/radome geometry the radome produces a reflection lobe structure at approximately 55° off the radome axis. The angular position of the measured reflection lobe is a function of antenna set angle, test antenna type, radome shape (all of which are fixed in this case) and the flatness of the test aperture field. From Figure 6 it is seen that the position of the reflection lobe as measured on the conventional range approaches the compact range measured position as the conventional range length is increased. This indicates that the phase of the compact range is flatter than the conventional range of $4 D^2/\lambda$.

4. EFFECT OF THE CHAMBER WALLS

Throughout the measurements the compact range was housed in a simple anechoic chamber consisting of a rectangular room lined with radar absorbing material normally used for measurements in X band and above. The position of one side wall was varied to ascertain the effect of the close proximity of the wall to the test aperture. This was most effectively carried out by observing the effect of the wall on low level sidelobes as the test antenna was moved through a range of site lengths from 1.5 to 2.3 m (the main lobe of the antenna points at the side wall). The effect of the reflected energy off the sidewalls is to introduce a variation in measured side lobe level as the test antenna moves through the field. For side walls only 0.5 m from the edge of the reflector, a 34 dB side lobe varied by $\pm$ 3 dB and with the wall at 1.5 m the variation is only $\pm$ 0.5 dB.

5. ADVANTAGES OF THE COMPACT RANGE

The advantages of the compact range over conventional ranges are broadly as follows:-

   i) Independent of $2 D^2/\lambda$ range criterion (as required for a typical conventional range)

   ii) Greater test aperture field phase purity than given by $2 D^2/\lambda$ range.

   iii) Greatly reduced real estate requirements

iv) Can be made visual and radiation secure.

v) Increased utilisation - independent of weather.

Although the conventional range lengths used in the measurement programme are short enough for indoor anechoic chambers, the site lengths required for typical aircraft antennas and radomes would preclude the use of indoor conventional sites whereas the compact range required can be readily accommodated in an indoor facility.

A comparison of costs of the two approaches is dependent on the dimensions of the test ranges required. However taking a typical large antenna/radome combination which requires a test aperture diameter of 2 m working in X band, then with the $2 D^2/\lambda$ criterion, the conventional range length is 300 m. For 50% utilisation of a compact reflector, the size of the offset paraboloid is 4 m x 4 m. Working on this basis a cost comparison can be made between conventional outdoor range and a compact range. The non-recurring costs are estimated based on the following items:-

Conventional Outdoor	Compact in Door
a) Platform and building to house antenna/radome positioner	a) Building and air conditioning
b) Transmitter Tower	b) Compact reflector manufacture and installation
c) Radar absorbing material and fences.	c) Absorbing material to cover internal walls.

The recurring costs per annum for operating the sites are based on the following:-

Conventional Outdoor	Compact Indoor
a) Ground rent for area 300 m x 50 m	a) Ground rent for area 15 m x 6 m
b) Labour (2 men required for safety regulations on high platform)	b) Labour 1 man
c) Loss of interest in non-recurring costs	c) Loss of interest on non-recurring costs

On this basis the compact site becomes cost effective in 4 years (assuming no time is lost due to bad weather for the conventional case).

A second comparison is made between a small compact range and a conventional indoor test site. For example a test aperture size of 0.5 m working a X band requires a convention range length of 15 m (assuming a $2 D^2/\lambda$ range) and a compact reflector size of 1 m x 1 m.

190

The non-recurring costs are estimated on the following:-

Conventional Range	Compact Range
a) Building 20 m x 6 m x 6 m	a) Building 4 m x 3 m x 4 m
b) RAM 1400 pieces	b) Air conditioning
	c) Compact reflector
	d) RAM 150 pieces

The annual running costs for the compact range are again lower than the conventional but the ratio is not so great as for larger sites as both indoor ranges only require one operator and the real estate areas are lower.

The compact range offers a cost effective solution with the added advantage for large test apertures the facility is independent of weather conditions.

6. CONCLUSIONS

By comparison measurements in C, X and Q bands it has been demonstrated that a compact test range can be utilized for polar diagram and aberration measurements of antenna and radomes and is cost effective. Additional advantages of the compact range include visual and radiation security together with independence from bad weather.

7. ACKNOWLEDGEMENTS

We wish to acknowledge the support and assistance offered by MOD(PE) UK through the programme and the useful collaboration given by Queen Mary College, London.
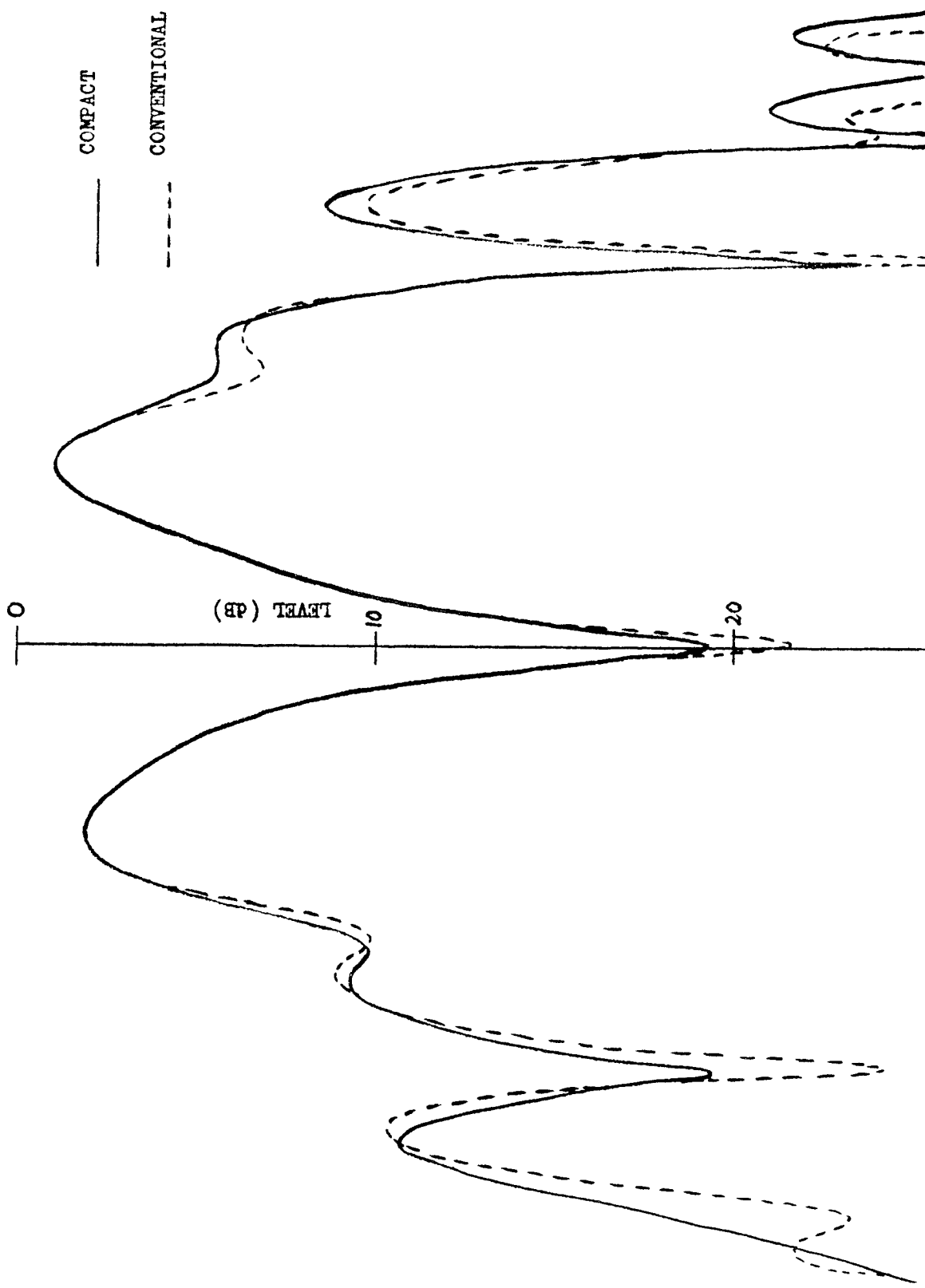
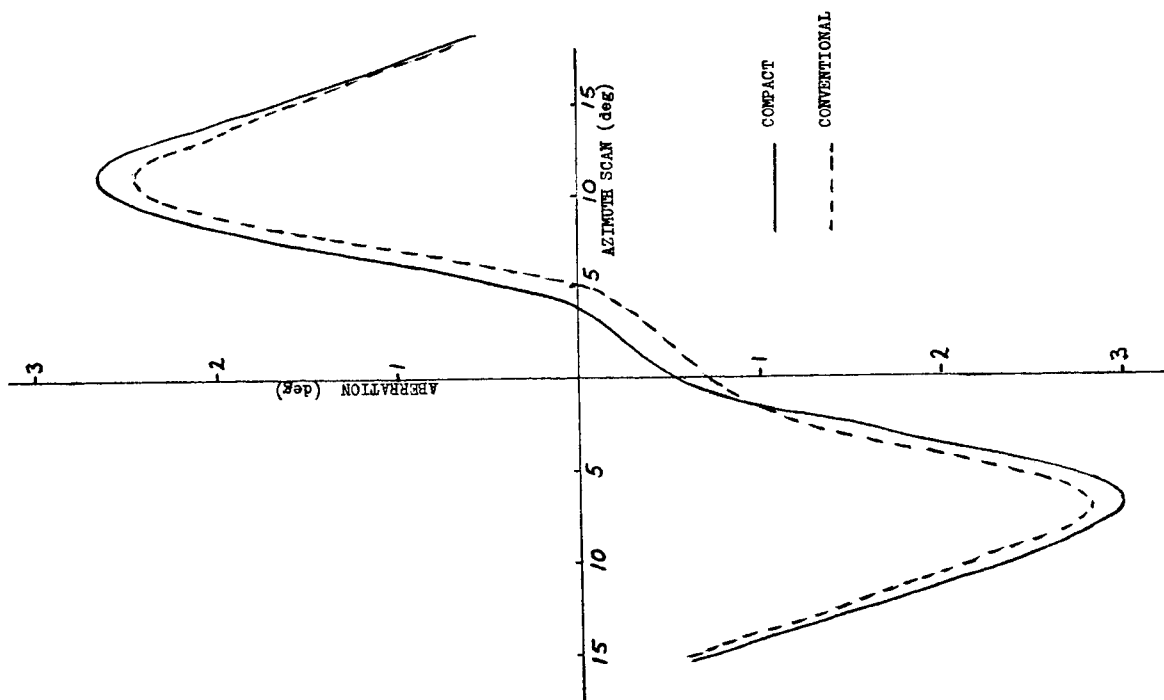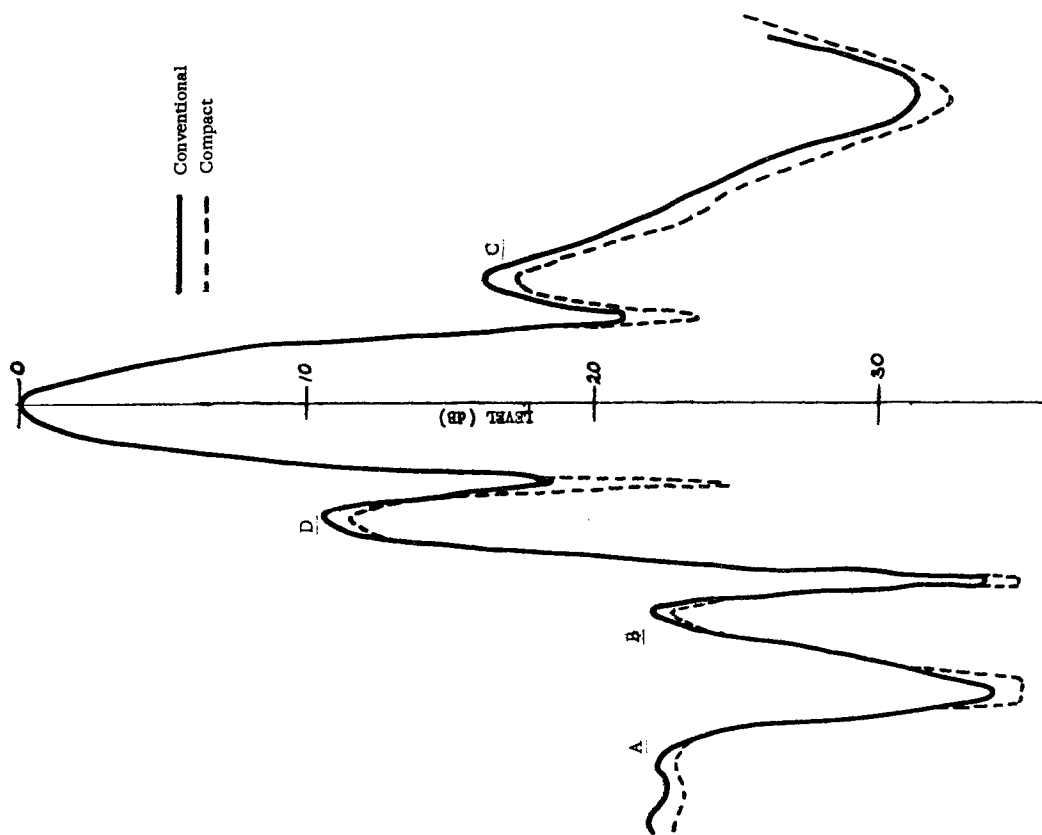FIGURE 1   DIFFERENCE CHANNEL POLAR DIAGRAM FOR C-BAND ANTENNA

FIGURE 3 SUM CHANNEL POLAR DIAGRAM FOR X-BAND ANTENNA

FIGURE 2 C-BAND RADOME ABERRATION
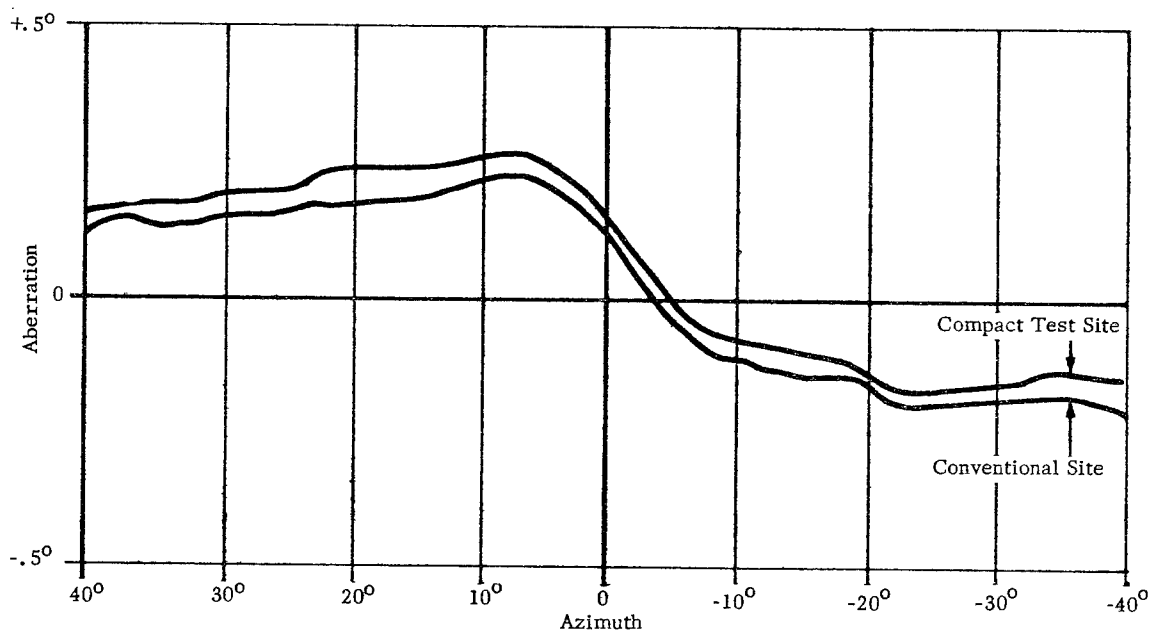
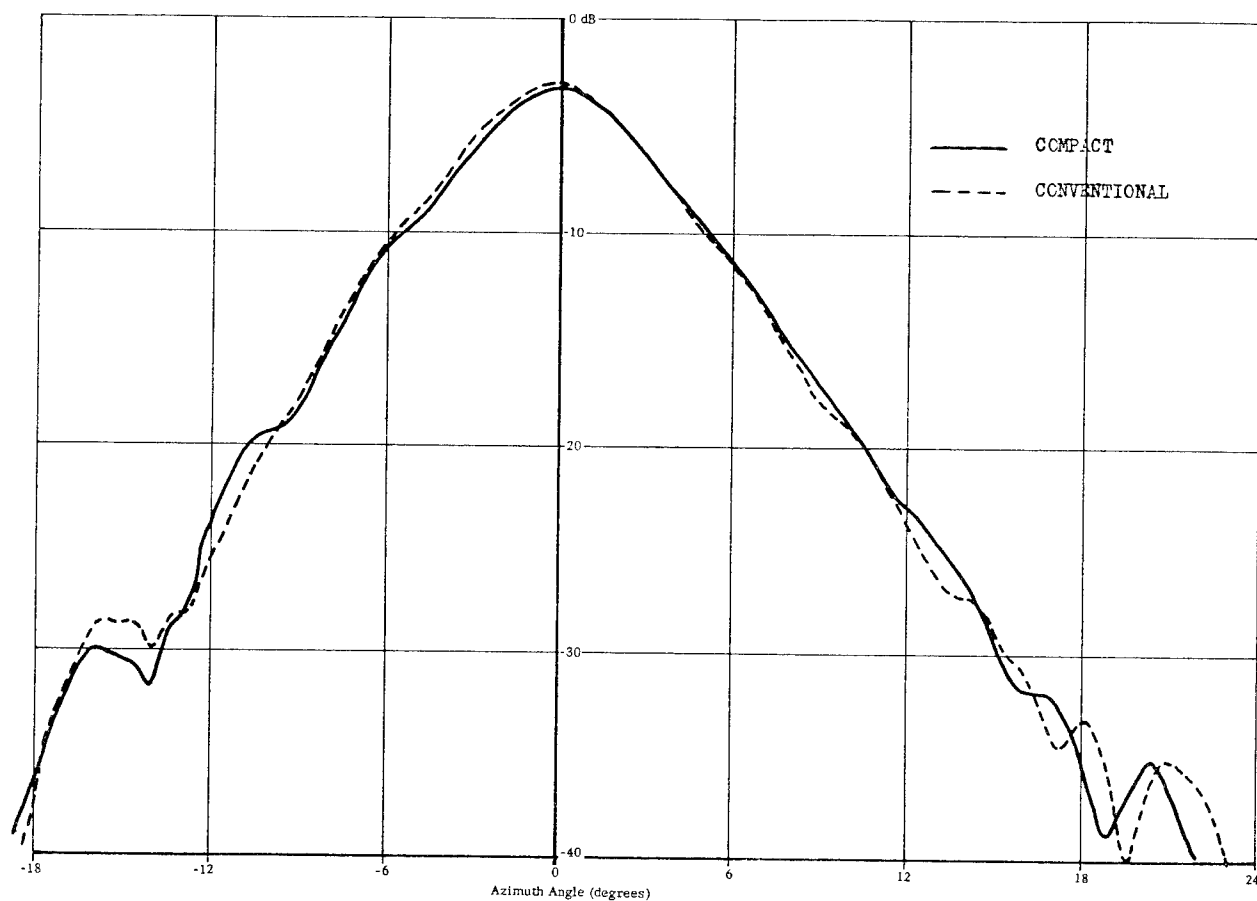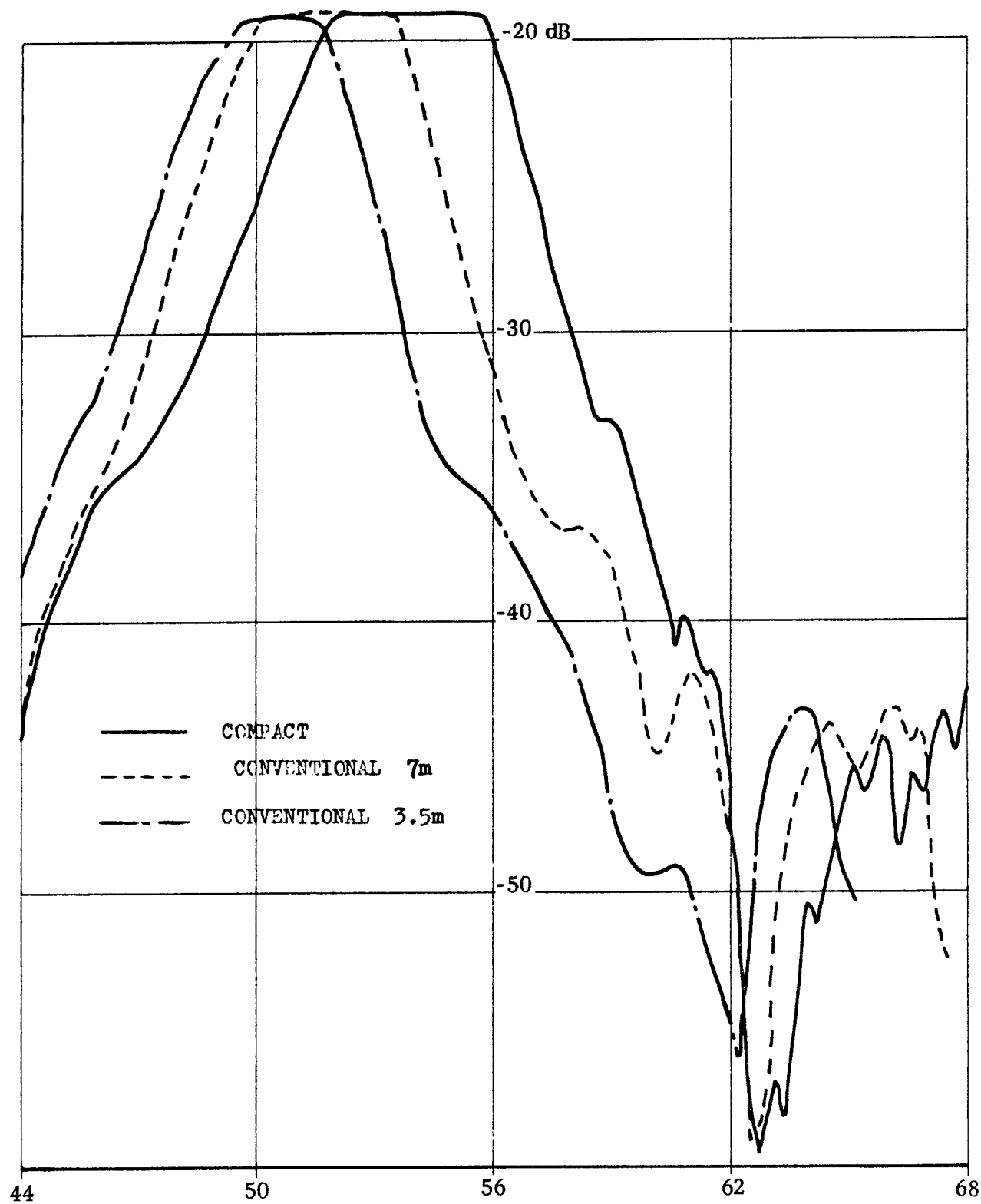FIGURE 4   BORESIGHT ERROR COMPARISON

FIGURE 5   HORN AND RADOME MAIN LOBE (Q-BAND)

194

FIGURE 6   REFLECTION LOBE COMPARISON

195